8-2004

# Effect of Microfissures on Corrosion Performance and Mechanical Properties of Austenitic Stainless Steel Weld Metals

Yan Cui
*University of Tennessee - Knoxville*

To the Graduate Council:

I am submitting herewith a dissertation written by Yan Cui entitled "Effect of Microfissures on Corrosion Performance and Mechanical Properties of Austenitic Stainless Steel Weld Metals." I have examined the final electronic copy of this dissertation for form and content and recommend that it be accepted in partial fulfillment of the requirements for the degree of Doctor of Philosophy, with a major in Materials Science and Engineering.

Carl D. Lundin, Major Professor

We have read this dissertation and recommend its acceptance:

Raymond A. Buchanan, Peter K. Liaw, David C. Joy

Accepted for the Council:
Dixie L. Thompson

Vice Provost and Dean of the Graduate School

(Original signatures are on file with official student records.)

To the Graduate Council:

I am submitting herewith a dissertation written by Yan Cui entitled “Effect of Microfissures on Corrosion Performance and Mechanical Properties of Austenitic Stainless Steel Weld Metals”. I have examined the final electronic copy of this dissertation for form and content and recommend that it be accepted in partial fulfillment of the requirements for the degree of Doctor of Philosophy, with a major in Materials Science and Engineering.

Carl D. Lundin

Major Professor

We have read this dissertation
and recommend its acceptance:

Raymond A. Buchanan

Peter K. Liaw

David C. Joy

Accepted for the Council:

Anne Mayhew

Vice Chancellor and Dean of
Graduate Studies

(Original signatures are on file with official student records)

# Effect of Microfissures on Corrosion Performance and Mechanical Properties of Austenitic Stainless Steel Weld Metals

**A Dissertation**

**Presented for the**

**Doctor of Philosophy**

**Degree**

**The University of Tennessee, Knoxville**

**Yan Cui**

**August 2004**

## DEDICATION

This dissertation is dedicated to my wife and daughter

Hui Liu

and

Yimeng Cui

who have been my best friend, and have always understood and supported me.

This dissertation is also dedicated to my parents

Mr. Zhiqian Cui

and

Mrs. Shaohua Chen

who have given me love, support and educational opportunities, and have always encouraged me in my life.

## ACKNOWLEDGEMENTS

The author sincerely acknowledges his major advisor, Dr. Carl D. Lundin, for his inspiration, guidance and support through this investigation. Sincere appreciation is also extended to the committee members, Dr. Raymond A. Buchanan, Dr. Peter K. Liaw and Dr. David C. Joy for their academic advice and encouragement.

The financial support provided through the Welding Research Council (WRC) is gratefully acknowledged. Expert advice from Dr. Damian J. Kotecki is especially acknowledged. The author appreciates the assistance from Lincoln Electric Company, ESAB and Hobart for supplying the experimental electrodes.

The author would also like to thank the faculty, staff, members of the mechanical shop, electronic shop, purchasing and electronic shops in the Materials Science and Engineering Department at the University of Tennessee, Knoxville, for their assistance. Especially, the author would like to express his appreciation to Dr. John R. Dunlap and Greg Junes for their performance and assistance during the metallographic examination.

The author sincerely expresses his thanks to Dr. Peng Liu, Dr. Gang Zhou, Dr. Lijia Chen, Dr. Hongbo Tian, Mr. Yulin Lu, Mr. Greg Batten and Mr. Vasudevan Hariharan for their generous and cooperation.

## ABSTRACT

It is generally recognized that hot cracking or microfissuring is one of the main concerns in austenitic stainless steel welding. Microfissures formation can be attributed to the presence of liquid film along the grain boundaries near the bulk solidus temperature under a sufficient strain to rupture the liquid film. Microfissures can be controlled to a certain extent by attention to consumable composition, purity, and welding technique, but they cannot be uniquely eradiated in real weld application. The occurrence of the microfissures can be the cause of weld rejection and may induce property degradation of the weld metal. With the increase of utilization of heavy section of austenitic stainless steel, the microfissures have been raised concern in the application of industries.

In this study, eight kinds of commercial and modified electrodes provided by Lincoln Electric Company, ESAB and Hobart were used to produce fissure-containing and fissure-free welded coupons for extracting the samples for this investigation. The modified electrodes, E308L, E316L, E308H and E316H, are those electrodes which Ferrite Numbers are around zero to produce microfissures for the investigation. Except these electrodes, some of the pads from the earlier projects entitled "Fissure Bend Test" and "Weld Metal Fissuring Tendency of Kro-Kay 316-15" were also used because of the pads with the different microfissuring levels. All of the commercial and modified electrodes used in this research fall within the AWS A5.4 specification.

The shielded Metal Arc (SMA) welding process was used to produce bead-on-plate weld deposits for microfissure evaluation by Fissure Bend Testing and Dye Penetrant Testing methods. Microfissures distributed along grain boundaries and are almost uniform on the top of the pad surface along welding direction. Microfissures show typical hot cracking characteristics, smooth surface with cellular dendritic solidification pattern, revealed by scanning electronic microscopy (SEM).

The corrosion performance of these weld deposits with different microfissure densities was evaluated by pitting and crevice corrosion testing in ferrite chloride solutions. Critical Pitting Temperature (CPT) and Critical Crevice Corrosion Temperature (CCT) were used to detect corrosion behavior of these weld deposits. In addition, cyclic polarization testing in 3.5% sodium chloride solution was also conducted to evaluate the corrosion behavior in terms of $E_{pit}$ and $E_{prot}$. The corrosion testing results showed that microfissures provided the pitting corrosion sites and degraded pitting and crevice corrosion resistance of austenitic stainless steel weld metals. CCT and CPT are a function of the microfissure level. With an increase in microfissure level a decrease in CPT and CCT is noted and microfissures have a more significant effect on CPT than CCT. Pits preferentially initiated at the tips of microfissures for fissure-containing samples and in overlapped region for fissure-free samples. When 308L is compared to 316L, the 316L deposits are superior with regard to CPT and CCT at the same microfissure level. The ferrite content does not appear to influence CPT and CCT at the same microfissure level. E316H deposits have the highest

$E_{pit}$, $E_{prot}$, followed by E308H, E316L, and E308L. The corrosion behavior obtained from cyclic polarization testing follows in the same order and is consistent with the immersion CPT and CCT results. Based on the immersion CPT and CCT methodologies and the cyclic polarization techniques it is clear that the use of the cyclic polarization testing is to be recommended for optimum definition of the effect of fissures on corrosion.

Room temperature pre-strain tension and standard tension tests were performed to determine the 0.2% offset yield strength, tensile strength, percent elongation, and percent reduction in area for the weld metals with and without microfissures. It is apparent that microfissures can affect the ductility of 316L and especially of 308L and there is little effect on strength properties.

High-cycle tension-tension fatigue testing with a 0.1 stress ratio at a frequency of 20 Hz (load control at ambient temperature) was conducted on 308L and 316L stainless steel weld metals with and without microfissures. The load in the range of 204 to 476 MPa for fatigue testing is based on the yield strength of each material. The results of such tests from a number of different stress levels was plotted to obtain a stress-life curve (S-N curves). The fatigue testing results showed that microfissures act as stress raisers in the weld metals and greatly decrease the fatigue properties of E308L and E316L weld metal samples. The initiation of failure for microfissure-containing samples is linked to the microfissures which show hot cracking characteristics; a smooth flowed pattern on the fissure surface.

The creep testing was conducted on constant load creep frames with a three-zone furnace with the power level for each zone being independently adjustable. Loading is uniaxial tension with a constant load throughout the test. Different stress levels between 70 to 240 MPa were used together with a range of temperature (550-700°C) for creep testing of the E308H and E316H weld deposits. The creep test results revealed that modified E316H with 0 FN even having microfissures (fissure-containing deposits) have superior creep resistance, followed by commercial E316H and E308H, the modified 308H with 0 FN (fissure-containing) samples showed the poorest performance. This means that the effect of microfissues on creep property of E316H and E308H are quite different. Significant carbides of the $M_{23}C_6$ type evolved from modified 308H and 316H weld coupons with FN approximately 0 after creep testing. The majority of the carbides in modified 316H (FN = 0) in the range of 0.2-0.4 μm distributed as a chain of discrete globular $M_{23}C_6$ along the substructure and grain boundaries while the carbides in modified E308H weld coupon (FN = 0) as distributed randomly. Sigma phase was detected in commercial 316H and 308H samples during creep test. More sigma phase was formed in commercial E316H weld deposits than commercial E308H because of the difference in Molybdenum content. Sigma phase is more detrimental for creep performance than microfissures for 316H. Carbides evolved in a chain effectively retard the movement of dislocations which results in the higher creep properties for E316H fissure-containing sample than fissure-free. Microfissures degrade the creep properties for 308H deposits because they provide the propagation paths for

secondary cracking caused during the creep testing and do not show the effect of modified 316H fissure-containing samples where carbides formed and strengthen the grain boundaries thus improving the creep strength. Secondary cracking caused by sigma phase is more detrimental for commercial 316H deposits than microfissures because brittle sigma can easily initiate cracks. More sigma phase formed in 316H than 308H during creep testing due to the effect of Molybdenum. The test results for commercial 308H and 316H are consistent with the database for 308 and 316 welds.

To characterize the microstructure, optical light microscopy (OLM), scanning electron microscopy (SEM), energy dispersive spectroscopy (EDS), X-ray diffraction (XRD), and transmission electric microscopy (TEM) were used.

## TABLE OF CONTENTS

## LIST OF TABLES

## LIST OF FIGURES

# CHAPTER 1
# INTRODUCTION

Austenitic stainless steels constitute the largest stainless family in terms of alloy type and usage. They were developed for use in various corrosive conditions in the temperatures ranging from cryogenic to elevated. Austenitic stainless steels are iron-based alloys that contain a minimum of approximately 11%Cr which is used to prevent corrosion in corrosive atmospheres. The alloys achieve their stainless characteristics through the formation of an adherent surface film composed of chromium-rich oxide. This oxide forms and heals itself in the presence of oxygen. Other elements added to improve particular characteristics of the alloys include nickel, molybdenum, copper, titanium, aluminum, silicon, niobium, nitrogen, sulfur, and selenium. Carbon is present in amounts ranging from less than 0.03% in austenitic grades and to over 1.0% in certain martensitic grades.

Austenitic stainless steels are generally regarded as readily weldable materials without the risk of cracking and with considerable tolerance for variations in welding conditions. However, fully austenitic weld deposits may contain microfissures in single pass welds and in underlying weld runs reheated by subsequent passes in multipass welds. These microfissures tend to occur along solidification grain boundaries and often appear to cross interpass

boundaries. The occurrence of the microfissures can be the cause of weld rejection and may induce property degradation of weld metals.

Microfissures occur primarily in ferrite-free areas along grain boundaries in the HAZ of previously deposited weld that shows a low ductility region. This region is usually the initial location for microfissure occurrence when the weld has a low Ferrite Number (FN), under a high imposed strain that exceeds the strain tolerance of the structure. Furthermore, delta ferrite has a beneficial effect in reducing or preventing microfissuring in austenitic stainless steel weldments. Delta ferrite in the austenitic stainless steel weld plays a dual role. On the one hand it reduces the susceptibility of the weld to hot cracking and on the other hand it affects the creep properties for long-term service at elevated temperatures. Microfissures can be controlled to a certain extent by attention to consumable composition and purity, and welding technique, but they cannot be uniquely eradicated in real weld application because ferrite distribution is not uniform. Thus, ferrite level and microfissures or cracks in austenitic materials generally cause the most alarm when the weldment properties are being considered such as strength, toughness, corrosion resistance, and long-term service at elevated temperatures.

In order to conduct a comprehensive study to understand the corrosion, fatigue and creep behavior of weld deposits containing microfissures and to quantify the effects of microfissures in each of these areas – “Effect of Microfissures on Corrosion Performance and Mechanical Properties of Austenitic Stainless Steel Weld Metals”, sponsored by Welding Research Council Stainless

and High Alloys Committee-have been conducted at the University of Tennessee.

In conjunction with this research, a state-of-art literature review on microfissures effect on corrosion and mechanical properties was accomplished. Characteristics of microfissures, regular testing techniques, and the effect on corrosion and mechanical properties were addressed.

# CHAPTER 2
# LITERATURE REVIEW

.

## 2.1 Microfissuring

### 2.1.1 Definition

A weld metal microfissure is usually regarded as a crack-like separation occurring in the weld metal [2, 3] which may not be observed except by metallographic examination [1, 2, 4]. Metallographic examination is often the only method to reveal microfissures underlying (reheated) weld beads (liquation cracks and ductility dip cracks) [4, 5]. Ultrasonic evaluation appears to be generally unsuitable for the detection of microfissures, although some efforts have been successfully implemented [5]. Microfissure in stainless steels can be caused by a grain boundary liquation mechanism, induced by low melting point inclusions [6], or microcavities which expand and form microfissures during cooling [2] (shown in Figure 2.1) (all Figures located in Appendix) or upon reheating of underlying weld passes by subsequent weld passes which induces a form of grain boundary liquation [7].

### 2.1.2 Microfissure Appearance and Location

Most of the microfissures observed in austenitic stainless steel welds are narrow in width and disconnected [8] exhibiting primarily disc-like shaped [9]. It is recognized that austenitic stainless steel weld metal

are susceptible to microfissuring in the fusion zone of a single-run weld, base metal HAZ, and weld metal HAZs in a multipass welds [10]. Many researchers have observed that the microfissures rarely initiate in the root layers of the multipass welds, but they tend to form in the upper layers of the weld in the locations related to the sequence of depositing the upper layers of beads in the weld. This may be related to the fact that the thermal and mechanical restraints in the upper layers are generally of a tensile natural and greater compared to those in the root layers [11]. Cracks, as distinguished from microfissures, may still be found in root passes that are located at base metal interfaces, such as where the weld pass fuses backing and the parent metal.

### 2.1.3 Microfissure Fracture Morphology and Size

Honeycombe and Gooch [12] observed three different fracture morphologies in Types 310 and 316 stainless steel. Two are termed “rumpled” and “smooth” types. “Rumpled” surfaces as shown in Figure 2.2(a) indicate extensive liquation. The smooth surface is seen to reveal a dendritic structure (Figure 2.2 (b)) which indicates that liquation has occurred but to a more limited extent than the “rumpled type”. The third type which also shows a smooth surface reveals no evidence of liquation, but only plastic deformation and some discrete solid particles (Figure 2.2(c)). Microfissures, with liquation evidence, occurred at a temperature near the bulk solidius of the alloy and result from partial fusion of thin layers along the grain boundaries. Microfissures with no

evidence of liquid phase formation, appear to be formed at slightly low temperature.

Lundin [9] summarized the nature and morphology of microfissures in austenitic stainless steel weld metals:

a). The microfissure occurs primarily along the grain boundaries in the HAZ of a previously deposited pass.

b). The microfissuring tendency in the HAZ of deposited pass is enhanced by multiple thermal cycling produced by a number of subsequent weld runs.

c). Microfissuring is invariably more prone to form in ferrite-free areas.

d). The size distribution of microfissures determined by light metallography at 200X reveals that the average microfissure length in Type 308 stainless steel weld metal is 0.1 mm. The size distribution is graphically shown in Figure 2.3 [13].

### 2.1.4 Microfissuring Mechanism

The microfissuring mechanism in stainless steel is associated either with melting along grain boundaries (liquation) or by insufficient hot ductility [1, 4, 8, 9, 15, 16, 17, 18, 19, 20] and in some cases it can be attributed to both of them [20].

1). HAZ liquation Cracking

The majority of microfissures are formed by a liquation mechanism at a temperature close to the bulk solidus. Microfissures occur in the

presence of liquid film along grain boundaries near the bulk solidus temperature under a sufficient strain to rupture the liquid film.

2). Ductility-Dip Cracking

Ductility-dip Cracking results from a loss in ductility occurring over a temperature range well below bulk solidus temperature. This low ductility region has been termed the “Hazard HAZ” by Lundin [15] and exists in the underlying weld metals near the fusion line of an overlapping weld bead. The “Hazard HAZ” is enriched “in harmful” elements such as S, P, Si in the grain boundaries and this decreases the ductility when compared to the surrounding areas. The microfissures occur if the strain imposed on the weld exceeds the strain tolerance of this local microstructural region. The extent (width) of the “Hazard HAZ” is dependent upon the ferrite potential of the welding consumable used and the thermal conditions induced by welding. Figure 2.4 shows a schematic representation of two temperature ranges for two primary cracking mechanisms [21].

Microfissures are more likely to form when phosphorus and sulfur levels are higher (more than 0.015%P and 0.015%S), when high heat inputs are used during welding, and when the weld metal $\delta$-ferrite content is low (<3%) [22].

The primary mechanism for microfissuring in fully austenitic stainless steel weld metals involves liquation which plays the dominant role in microfissure formation. This phenomenon is the basis for most hot cracking theories applied to austenitic stainless steel weld metals. Thus, primary attention in the formation of microfissures should be directed to liquation, which can occur in the fusion

zone, base metal or deposited metal reheated to near the bulk solidus temperature by deposition of a subsequent weld bead [18]. Hot cracking, microfissuring and solidification cracking [23] in austenitic stainless steels, have been one of the most investigated phenomena in stainless steel welding. A significant number of papers related to this subject have been published in the last few decades. Several important observations have been made and several significant conclusions about hot cracking, microfissuring susceptibility have been drawn. Several theories of hot crack formation have been summarized [24]: 1) Shrinkage-brittleness theory; 2) Strain theory; 3) Boland theory; 4) Critical speed (strain-rate) theory; 5) Grain boundary sliding theory. The predominant theory of hot cracking is attributed to the formation of low-melting phases in the solidifying weld metal and in the heat-affected zone, under the action of shrinkage stresses and restraint imposed on the joint [1, 10, 23, 25, 26, 27]. It has been well recognized that delta ferrite, when present in a certain critical level in austenitic stainless steel weld metals, can be an efficient indication for mitigation of microfissuring. Figure 2.5 shows a relationship between ferrite content and microfissure tendency [14]. Austenitic stainless steels of varying compositions apparently requires a different minimum ferrite content to prevent microfissuring. The beneficial effects of delta ferrite in reducing or preventing microfissuring in austenitic stainless steel weldments were first reported in the early 1940's. Initial work by Boland [2] and Hull [28] indicated that austenitic stainless steel welds and castings, which were estimated to contained 5-10 percent delta ferrite provided optimum resistance to

microfissuring in a variety of austenitic stainless steel alloys. During the last 20 years, a significant number of studies have been undertaken to determine the relationship between weld ferrite content, solidification behavior and microfissuring susceptibility. A unifying observation from these studies shows that it is not the absolute level of weld metal ferrite that is important with respect to cracking resistance but rather the manner in which the weld metal solidifies [27, 29, 30, 31, 32]. When primary solidification occurs as delta ferrite, cracking resistance is far superior to the situation when primary solidification occurs as austenite. In the former case, much of the ferrite formed during solidification transforms to austenite via a solid -state reaction that occurs on cooling to ambient temperature. In austenitic stainless steel, this transformation generally produces an as-welded microstructure containing from 3 to 20 vol-% Ferrite Number (FN). A variety of ferrite morphologies that have been reported in austenitic/ferritic weld metal and they are primarily a function of composition and the resultant ferrite content [33].

## 2.2. Beneficial Effect of Primary Ferrite Solidification

The beneficial effects of primary ferrite solidification in reducing or preventing hot cracking in austenitic stainless steel weldments are summarized as follows:

1). When welds solidify in a primary ferrite solidification, there is no γ-γ or δ-δ boundary during the solidification interval, and austenite-ferrite phase boundaries are not wetted by the last traces of liquid. Delta ferrite formed from the residual liquid cannot entirely prevent γ-γ boundary formation [34]. Kujanpaa, et al. [25] described the similar point at which ferrite along HAZ grain boundaries, inhibits wetting by liquid films and limits diffusion of impurity elements. Another important effect of ferrite formation along austenite grain boundaries is the restriction of grain growth [25].

2). The solidification mode not only controls the initiation of solidification cracks, but also influences propagation [34].

a). Upon solidifying in a primary austenitic mode, an extensive liquid film on the solidification γ-γ boundaries will be developed to enhance the initiation of microfissures and will be aggravated by the presence of solutes, which depress the melting point, such as sulfur. On the other hand, for the primary ferrite solidification mode, no δ-δ solidification boundaries forms and the initiation of a solidification crack inhibits.

b). In the primary austenitic mode, grain boundaries are straight and offer an easy propagation path for microfissures. In primary ferrite mode, grain boundaries are eliminated by a three-phase reaction and lead to more irregular γ-δ phase boundaries which act as crack arrests. Finally, the backfilling of cracks by liquid is found to be easier in the primary ferritic solidification mode than in the primary austenitic mode.

3). The higher solubility of harmful impurities in ferrite than that in austenite results in less segregation during primary ferrite solidification than that in primary austenite solidification [35, 36, 37, 38].

4). The temperature range in which the ductility is decreased to the greatest extent, ranges from approximately 1800°F (982°C) to the bulk solidus temperature. The “Hazard HAZ” region in the ferrite-containing welds is generally narrower than in the fully austenitic weld metals. Therefore, the probability of fissuring in the weld HAZ in fully austenitic welds is higher than in ferrite-containing welds [39].

5). When solidification occurs as austenite, the as-welded microstructure will be either fully austenite, or contain a small amount of ferrite along solidification grain and subgrain boundaries. The level of ferrite produced under primary austenite solidification conditions is generally estimated to be less than 3 FN in austenitic stainless steels [40].

## 2.3 Effects of Cooling Rate on Ferrite

Weld cooling rate has a significant influence on the room temperature microstructure in austenitic stainless steel weld metal. Vitek and David investigated the ferrite content and ferrite composition of Type 308 austenitic stainless steel welds in the cooling rate range of 0.16 to 693°C/s. It was found that as the cooling rate is increased, the amount of residual ferrite at room

temperature is increased as shown in Figure 2.6 [41]. Conversely, slow cooling has the effect of lowing the ferrite amount.

Elmer used electron-beam surface melting method to rapidly solidify several stainless steel alloys at cooling rates between 7°C/s to 7.5X106 °C/s and developed the relationship between the solidification mode and the residual ferrite content with the variation of cooling rate. They concluded that the primary solidification mode determines whether the ferrite content will increase or decrease with cooling rate. The residual ferrite content of primary-austenite solidified alloys decreases with increasing cooling rate wheres the residual ferrite content of primary-ferrite solidified alloys increases with increasing cooling rate. This is because the higher amount of original ferrite that solidifies from the melt and the reduced amount of transformation that occurs at high rates. Figure 2.7 shows this general behavior. But there are some exceptions (1) when ferrite transforms to austenite by a massive transformation in fully-fully-ferrite-solidified alloys and (2) an alloy changes its mode of solidification from primary-ferrite at low cooling rates to primary-austenite at high cooling rate [42]. Lippold used the microstructure resulting from rapid solidification of austenitic stainless steels to construct a microstructural “map” as a function of solidification rate and composition. Figure 2.8 represents a preliminary attempt to rationalize the variety of microstructures observed in austenitic stainless steel welds. It can also be used to predict the susceptibility of austenitic stainless steels to solidification microfissuring when considering both composition and welding process variables. Weld solidification cracking would be highest in the regions

designated A and AF. These regions are essentially a projection of the crack-susceptible envelopes predicted by Suutala and modified Suutala diagrams where will be discussed later [29].

## 2.4 Relationship Between Solidification Mode and Microstructure

There have been extensive discussions in the literatures, on whether austenitic stainless weld metals solidify primarily as delta ferrite or as austenite [32, 34, 37, 42, 43]. The solidification mode and consequently the room temperature microstructure are dependent on the content of the austenite and ferrite forming elements. The Solidification modes can be classified [1, 32] as A, AF, FA, and F (shown in Figure 2.9).

1). Mode A or AF (Figures 2.8a, 2.8b, and 2.9a).

If $Cr_{eq}/Ni_{eq} \leq 1.48$, there can be either a fully austenitic structure (mode A) or an austenitic structure containing a minor amount of $\delta$-ferrite (AF mode).

2). Mode FA (Figures 2.8c, 2.8d, 2.9c and 2.9d)

If $1.48 \leq Cr_{eq}/Ni_{eq} \leq 1.95$, the primary phase is $\delta$-ferrite and furthermore, in the final stage of solidification, some eutectic $\delta$-ferrite formed (FA mode).

3). Mode F (Figures 2.8e and 2.9b).

If $Cr_{eq}/Ni_{eq} \geq 1.95$, the morphologies of $\delta$-ferrite which are typically lathy structures are observed. At higher Creq/Nieq ratio, a widmanstatten austenite structure can also form in welds that solidify as single-phase ferrite. Figure 2.10

shows the solidification mode for this composition range. Micrographs of the three-dimensional structure of several weld ferrite morphologies are shown in Figure 2.11[1]. Small amounts of ferrite along solidification cell boundaries of a primary austenite structure are shown in Figure 2.11a. This cellular-appearingsolidification structure is characteristic of welds that solidify as austenite and results primarily from the microsegregation of chromium and, to a lesser extent, nickel along the solidification cell boundaries. Depending on alloy composition and welding conditions, final solidification may occur as eutectic of ferrite and austenite. Figures 2.11b and 2.11c show ferrite along cell cores of primary ferrite structures. Figure 2.11d shows acicular ferrite or Widmanstatten austenite in a structure that solidified completely as ferrite.

Kujanpaa, et al summarized the results of trans-varestraint tests arranged in order of increasing the $Cr_{eq}/Ni_{eq}$ ratio on hot cracking (Figure 2.12) [32]. It is to be noted that the austenitic or austenitic-ferritic solidified welds are prone to solidification cracking. The results also show that the single phase ferrite solidification increases cracking susceptibility. The best resistance to solidification cracking is found in welds which have solidified in the ferritic-austenitic mode.

## 2.5 Primary Phrase Prediction

A number of diagrams can be used to predict the primary solidification structure based on the weld metal composition. Four microstructure prediction diagrams have found the widest application. These include the Schaeffler

diagram, the DeLong diagram, and the Welding Research Council (WRC) diagrams (WRC-1988 and WRC-1992).

### 2.5.1 Schaeffler Diagram

The Schaeffler diagram [46] employs a relationship among alloy elements that promote the formation of ferrite (chromium-equivalent, $Cr_{eq}$, elements) and elements that promote the formation of austenite and the suppression of ferrite (nickel-equivalent, $Ni_{eq}$, elements). Using both of the chromium and nickel equivalents calculated from the composition of a given weld metal, the weld metal ferrite can be estimated as shown in Figure 2.13. Experience has shown that the Schaeffler diagram is reasonably accurate for conventional 300-series stainless steel SMR weld deposits. It is of limited use when less conventional compositions are used and a high level of nitrogen is present.

### 2.5.2 DeLong Diagram

DeLong developed a new diagram [47] that covers a more restricted composition range and includes the effect of nitrogen. Specifically, a nickel equivalent of 30%N was added. In the DeLong diagram, shown in Figure 2.14, the FNs for alloy 308, 308L, and 347 coated electrodes are similar to those in Schaeffler, but the 309, 316, and 317 alloy families have FNs that are about two to four times higher. Generally, the DeLong diagram provides a better correlation with GTAW and GMAW weld metals than the Schaeffler diagram, because it allows for nitrogen pick-up.

### 2.5.3 WRC Diagrams

The DeLong diagram has been considered to have underestimated the ferrite content of weld metal with high manganese contents and has overestimated the FN of high alloyed weld metals. Consequently, the Welding Research Council (WRC) funded work and collected data for the development of a new, more accurate diagram, known as the WRC-1988 diagram. The diagram (shown in Figure 2.15) covers a broader range of compositions than the DeLong diagram and removes the two errors noted above [48]. A modification of the WRC-1992 diagram, which added a coefficient for copper to the Nieq, was first proposed by Lake in 1990. This modification and an extension of the Creq and Nieq axes were incorporated into the most recent constitution diagram, the WRC-1992 diagram shown in Figure 2.16. Its extended axes permit graphical estimation of the ferrite content of weld metal over a wider range and for prediction of ferrite when dilution occurs in dissimilar metal welding. It is considered more accurate in predicting ferrite content for many weld metals [49].

## 2.6 Measurement of Weld Metal Ferrite

Weld metal ferrite content can either be predicted using constitution diagrams or be measured using instruments that take advantage of the ferromagnetic characteristics of the feritic phase. A number of instruments are

commercially available for determining the ferrite content of weld, including the Magne Gage, Severn Gage, and Feritscope. The Severn Gage and Feritscope are particularly applicable for use in the field or on the production floor. The ferrite scope is also useful in measuring ferrite on narrow width welds. Calibration procedures for magnetic measurement techniques are recommended in AWS A4.2. When using constitution diagrams the agreement between the predicted and measured weld metal ferrite content is strongly dependent on the accuracy of the chemical analysis [1].

## 2.7 Effects of Elements on Hot Cracking or Microfissuring

Hot cracking or microfissuring susceptibility is highly dependent on the solidification mode, and presence of impurities. For some materials, such as fully austenitic stainless steels and nitrogen-bearing stainless steels, a primary ferritic solidification mode may not occur. In such cases, the levels of impurity and minor elements may critically determine the cracking behavior.

### 2.7.1 Effect of Sulfur and Phosphorous

Rozet et al. investigated the effect of sulfur and phosphorous on the tensile properties and the soundness of 15%Cr-35%Ni weld metal. The results shows that sulfur and phosphorous both have great influence on hot-cracking susceptibility, as shown in Figure 2.17. With increasing amounts of either of these elements, above the commercial limit of about 0.025%, weld fusion zone

cracking occurs during welding, and the tensile strength and elongation both decrease as microfissures will be present in the all-weld-metal tensile specimens [50]. Similar results were obtained from an investigation on 25%Cr-20%Ni weld metal [2]. The most detrimental effects are caused by elements which combine with iron to form low-melting compounds as FeS (1190°C) and Fe3P (1166°C), which can form low-melting eutectics such as FeS-Fe (988°C) and Fe3P-Fe (1050°C), Ni3S2–Ni (637°C) and Ni3P-Ni3 (875°C). These liquation related compositions easily wet and spread along grain boundaries and lead to conditions which are more sensitive to microfissuring [40]. The effect of sulfur is non-linear. Sulfur is considered, by some, to have twice the effect of phosphorous on hot cracking [36].

The relationship between microfissuring susceptibility and sulfur plus phosphorous content is best illustrated in the diagram shown in Figure 2.18 devised by Suutala et al [51] based on weldability test data generated using conventional arc welding processes, (primarily gas tungsten arc welding (GTAW). At low sulfur plus phosphorus (S+P) levels (less than 100 ppm) cracking susceptibility is low over a wide range of composition. At higher (S+P) levels, comparable to these commonly encountered in austenitic stainless steels, cracking susceptibility undergoes a sharp transition at a $Cr_{eq}/Ni_{eq}$ ratio of 1.48. It is interesting to note that when delta ferrite is the primary solidification phase, high (S+P) contents can be tolerated. This diagram clearly demonstrates the efficacy of solidification control and/or reducing impurity

content for preventing weld solidification cracking in austenitic stainless steels. $Cr_{eq}$ and $Ni_{eq}$ Suutala used are: $Cr_{eq}$=%Cr+%Mo+1.5%Si+0.5%Nb, $Ni_{eq}$+%Ni+30%C+0.5%Mn. Recently, several studies involved high-energy density, low-energy input processes such as electron beam welding (EBW) and laser beam welding (LBW) have shown that the solidification behavior predicted by Suutala is inaccurate when solidification rates, and subsequent cooling rates, are extremely high [29, 52]. A modified-Suutala diagram is plotted based on the metallographic assessment of cracking susceptibility in terms of $Cr_{eq}/Ni_{eq}$ and (S+P+B) content in Figure 2.19a. This diagram has been modified from the one originally proposed by Suutala [53] by the addition of boron as an embrittling impurity element. Figure 2.19b shows another modified Suutala diagram using WRC-1988 equivalents. These two modified Suutala diagrams can be used to determine weld solidification cracking susceptibility in austenitic stainless steels under rapid solidification conditions. Under rapid weld solidifications, alloys with a Creq/Nieq exceeding 1.7 in Figures 2.19a (Suutala equivalents) and 1.65 in Figure 2.19b (WRC-1988 equivalents) would be expected to be resistant to cracking [29].

### 2.7.2 Effect of Silicon and Carbon

Silicon and carbon affect hot cracking. Increasing silicon content promotes fissuring, whereas increasing carbon content reduces fissuring sensitivity [2]. The harmful effect of silicon can be summarized as following: 1). The formation of low melting point silicate films at the grain boundaries can

influence solidification cracking. 2). With increasing silicon content, the liquid/solidus interval is widened and the material becomes more susceptible to solidification/liquation cracking [54-57]. Figure 2.20 shows the influence of silicon. Fissures present in tensile specimens at about 0.60% silicon, and become more numerous when the amount of silicon increases [50].

Silicon should be maintained below 0.3%. With such low Si other deoxidants may be necessary and, as most parent austenitic stainless steels contain more than 0.3% silicon, the effects of dilution must be considered [17].

The effect of carbon in the 15%Cr-35%NI weld metal, at various silicon levels, is shown in Figure 2.21. It is to be noted that the tensile strength increases to a maximum and then decreases. If the silicon is greater than 0.60%, elongation decreases because fissures are present in the weld deposit unless carbon is increased added [50].

It was reported by McCowan that, although the addition of carbon is beneficial in reducing the risk of hot cracking, it reduces ductility when added to the parent metal, and may cause further embrittlement in service at elevated temperature due to the carbide precipitation [48]. Gooch and Honeycombe suggest that Carbon should be below 0.1% for normal corrosion resistant consumables [17].

Rozet et al [50] also have shown that increasing carbon content at constant silicon concentration reduces cracking susceptibility. Figure 22 shows the combined effect of these two elements on a 15Cr-35Ni weld deposits with low

sulfur and phosphorous contents. For this and other fully austenitic weld deposits the carbon content should exceed (0.22)(Si%wt)1/2 to reduce microfissures at a low levels [48].

### 2.7.3 Effect of Manganese

It was found that manganese reduced microfissuring with the optimum content being between 2 and 6% [3, 20, 35, 36, 58]. Figure 2.23 shows the relationship between hot cracking in weld pads and manganese content [56]. Adding Mn to form MnS instead of FeS is usually beneficial and this beneficial effect reflected the reduction in the “harmful” effect of sulfur by forming MnS type sulphides of relatively high melting temperature. It should, in fact, be noted that FeS and its eutectics freezes at lower temperatures than the Manganese sulfide [3]. For austenitic stainless steels, the ratio of manganese to sulfur must exceed a certain value to avoid hot cracking (about 35 in the case of fully austenitic steel) [54]. A new fissure-resistant filler metal, 20Cb-3LR, was developed to replace standard fillers: AWS ER-320 and E-320 for welding carpenter 20Cb-3 stainless steel, a columbium-stabilizer austenitic alloy. The composition of this new filler metal is similar to that of ER-320 except the manganese and carbon contents, manganese increasing from 0.40% max to 1.8% and carbon decreasing from 0.07% max. to 0.025%. This filler metal withy increasing manganese demonstrates much better fissure resistance than AWS ER320, AWS ER NiCrMo-1, and AWS ERNiCrMo-3 in the circular-groove weldability test [59]. However, manganese had a potentially harmful effect on corrosion resistance,

particularly in moderately oxidizing conditions when passivity has broken down and the material has become active.

In the presence of copper, however, manganese is detrimental because of the formation of low-melting-point ternary Ni-Mn-Cu sulfide and the reduction of the solubility of copper in austenite with increased manganese content, and the segregation of a low-melting-point Cu-rich phase to the weld metal sulificate boundaries. In the absence of copper, however, manganese mitigates the detrimental effect of sulfur [3].

### 2.7.4 Effect of Nitrogen

Nitrogen is usually considered to have a detrimental effect on the weldability of austenitic stainless steels through its reduction in ferrite potential. The reduced ferrite content is associated with the change in the solidification mode from the primary ferritic to austenitic mode resulting from the strong austenite stabilizer [60]. Figure 2.24 shows the effect of the nitrogen content on the delta ferrite content of deposited metal of type Cr18-Ni9-Ti [61]. Apparently line 3 in Figure 2.24 (adapted reference 61) is incorrectly plotted. The true position of line 3 is near line 2. This probable error does not affect the conclusion concerned the effect of nitrogen. Figure 2.25 shows the effect of nitrogen addition in the shielding gas on the number of fissuring in stainless steel welds [62]. Nitrogen contents above 0.02% in niobium-containing steels significantly decrease the hot cracking resistance significantly [40]. While nitrogen is

restricted by its solid solubility to about 0.2%, higher nitrogen contents are likely to cause porosity [57]. Some studies on welds in 25Cr-20Ni type steels found nitrogen to have advantageous effect. Increasing the nitrogen content improved the hot cracking resistance of a fully austenitic stainless steel (25%Cr-20%Ni) which contains no niobium [63]. Lee has also found that the addition of nitrogen (from 0.047 to 0.12%) has lowered hot cracking susceptibility in the fully austenitic 316 stainless steel weld metals. This is due to a decreased solidification substructure size from an average of 18 μm to 14 μm when the nitrogen content increased from 0.047 to 0.12%. This is also due to the decreased brittle temperature range (BTR), because of decreased liquidius and solidus isothermals [64].

### 2.7.5 Effect of Niobium

Thomas and Messler reported in their literature review that the main purpose of niobium in stainless steel is to form a carbide (NbC, $Nb_4C_3$) preferentially to that of carbide, which reduces the free carbon to a level below which no chromium carbide form a continuous precipitate in grain boundaries, thus avoiding depletion of the region of chromium and avoiding intergranular corrosion [18]. But niobium tends to increase the susceptibility to hot cracking of fully austenitic weld metal by segregation at grain boundaries during welding [65]. The segregation found in the study of the weldability of nuclear grade austenitic stainless steel 316NG is Nb(C, N)-austenite eutectic which is enriched

in the last solidifying liquid and formed low melting microconsitituents and /or eutectics along the solidication/interdendritic boundaries after cooling below the solidus [66]. Boland thought, with the low Nb contents, hot cracking cannot form because of the small amount of liquid present. Increasing the Nb content increases cracking tendency owing to increase in the freezing range. In large quantities it results in the formation of ferrite, which tends to prevent cracking [3]. Some researchers pointed out that decreasing the Nb level reduces the volume of terminal eutectics which contribute to fissuring. The consequently narrower effective melting range would generally be associated with improved resistance to solidification cracking (though eutectics can also be associated with self-healing/backfilling of incipient solidification cracks) [12]. Niobium should be below about 0.3% [57].

### 2.7.6 Effect of Oxygen

Lundin and Chow [10] noted that oxygen appears to increase the adverse effect of sulfur, and by oxidizing Al, Ti, Si, Cr, and other ferrite formers, results in a low ferrite weld metal which can become fully austenitic and be more prone to microfissuring.

### 2.7.7 Effect of Boron

Boron is usually regarded as having a deleterious effect on liquation cracking in the base metal weld heat-affected zone. Its segregation to grain boundaries reduces the melting temperature of the grain boundary region and

accelerated the grain boundary liquation, causing microfissures to form. Boron is considered to segregate to high energy random grain boundaries to promote intergranular liquation [67]. Boron should be limited to 0.001% for Type 321 and Alloy A286, or 0.0045% for Type 316 [68].

### 2.7.8 Effect of Molybdenum

Molybdenum is considered beneficial in regard to microfissuring and while precise quantitative comment is not possible, the optimum Mo content is mostly in the order of 2.5-3% [51]. Figure 2.26 shows the effect of the molybdenium content on the delta ferrite content of the weld metal of type OKH16N6M2 [61].

### 2.7.9 Effect of Rare Earth Metal (REM) (Mish Metals)

Lee claimed that addition of REM (0.017%) to 347 appears to have a beneficial effect on weld metal solidification cracking and weld metal HAZ liquation cracking, provided the weld metal solidification in a primary ferritic mode. A REM addition was found to be ineffective for reducing liquation cracking in the base metal HAZ, unlike the cases in the fusion zone and weld metal HAZ behavior [64].

## 2.8 Effect of Other Factors on Microfissures

### 2.8.1 Effect of Welding Conditions on Microfissures

Gooch and Honeycombe [8] concluded that welding current has little effect on microfissuring, with reduced current being slightly beneficial. Both travel

speed and heat input appear to have minor effects. No specific effect of arc voltage was identified, but the results indicate that the microfissuring can be affected by the welder technique because variation in arc length can result in changes in deposit chemistry. Neither preheating or interpass temperature nor joint restraint of fit-up have a major effect on microfissuring. Increasing the size of the electrode used decreases the degree of microfissuring [55].

There is a striking difference between the microfissuring results from GTA and SMA welding and from GMA and SA welding [69]. The latter two processes are clearly more susceptible to microfissuring in the HAZ and to ductility dip cracking.

### 2.8.2 Effect of Multiple HAZ Thermal Cycle on Microfissures

Since the occurrence of a single weld metal HAZ experience does not produce myriads of microfissures as does multiple thermal cycling, it is clear that the strain tolerance of the weld deposits grain boundary is significantly reduced by multiple thermal effects. Figure 2.27 shows the number of microfissures as a function of HAZ exposures [39].

Lundin summarized the attributes of this phenomenon [10].

1). Enhanced segregation due to continued partitioning of harmful trace elements to the grain boundaries followed by liquation and rupture under strain.

2). Additional strengthening of the matrix by thermally-induced precipitate reaction as is the case for some ductility-dip incidences. The increased strength

of the matrix may cause strain accumulation in the degraded grain boundary microstructure region thus leading to rupture.

3). Strain-induced precipitation leading to a strong matrix and the subsequent accumulation of strain in degrade microstructural region.

4). The simple accumulation of thermal and restrain strains over a range of temperatures produced by continued thermal cycling causing the strain tolerance of the grain boundary microstructural region to be exceeded.

The effect of multiple weld metal HAZ thermal cycles appears to be the most influential factor in the gamut of microfissuring in austenitic stainless steel weld metal, even though liquation plays a decisive role in the majority of microfissuring occurrence.

## 2.9 Microfissuring Test Methods

### 2.9.1 Fissure Bend Test

Fissure bend test was originally developed and evaluated for determining the microfissuring tendencies of SMA deposited, and was later extended to evaluate GTA and GMA deposited filler metals and the results closely correlated with fabrication experience [39]. The fissure bend test has the favorable features desired in the weldability test because it is economical, easy to conduct, reproducible and capable of evaluating fissuring in multipass weldments. So it is widely used in investigation the susceptibility of fissuring of austenitic stainless

steel weld [70]. The applied strain in Fissure Bend Test not only opens up existed microfissures, but also makes more visible at low magnification.

The Fissure Bend Test employs a multirun, double-layer, weld pad to permit the evaluation of fissure on relatively undiluted weld metal. The weld pad is welded by SMA, or GTA or GMA process on a rigidly clamped ½" base plate as twelve 8" long stringer bead, six beads to each layers. The pad is then ground to produce a smooth surface for examination. The Ferrite Number of the deposit is determined on the ground surface. Examination of the pad for fissuring is conducted both before and after bending.

Fissure evaluation is performed in the center 100 mm of each specimen. This evaluation is a two-step process: (1) fluorescent penetrant testing to detect surface indications, (2) binocular microscopic examination of these indications, to count and measure their length and verify that they are indeed microfissures. The pad bent to an included angle of 120°, and the entire fissure evaluation process is repeated on the bent specimen surface [71].

Lundin proved that the original weld metal microfissures were opened but not increased in length the extensive bending strain and thus the microfissures not only did not propagate but they became blunted during deformation upon bending [10]. Further, no microfissures were created during bending. The Fissure Bend Test was determined to be the most useful procedure for characterizing the microfissuring sensitivity of welded metal. There is a good

comparability among microfissure sensitivity, longitudinal bent test LBT and the modified Varestraint-transvarestraint Test [6, 7].

### 2.9.2 Volumetric Microfissure Determination Test

Kotecki employed a “Volumetric Microfissure Determination Test” [73] based on examination of a fixed volume of weld metal by radiography after tensile elongation to open microfissures. Figure 2.28 shows the original joint geometry of mild steel base metal used for the test groove weld and the two butter layers which are deposited over the joint faces before welding the test deposit. The joint is restrained by a 25 mm thickness plate and all welding is performed with a slight weave technique operating at 140 amperes, DC electrode, and 150°C interpass temperature. The joint length is about 320 mm. After welding, a flat longitudinal reduced section tensile specimen, 65 mm long, 6.5 mm in thickness and 25 mm wide, is machined from the joint about 1mm below the original plate surface. The specimen is tested at three elongations (3.3% elongation at each increament). The total strain from the three extensions was about 10%. Radiograph was used to show the microfissures. It was considered that radiography of a flat longitudinal weld tensile specimen strained to about ten percent elongation can effectively detect microfissure.

### 2.9.3 Varestraint Test

Varestraint Test, developed in the early 1960's by Lundin and savage [74], met the "ideal" test requirements, economical preparation, efficient testing, sensitivity to small changes in a test variable, reproducibility of results, free of variation due to human factors and universal application to all welding process. Although a number of changes in the Varestraint test techniques have occurred during the past decades, the basic concepts and advantages of the original version did not change. These methods for hot cracking and microfissuring have been utilized by researchers [13, 53, 60, 65, 68, 75-78] world-wide for the past decades. In the original Varestraint, the weld is supported parallel to the long specimen dimension, beginning neat the unsupported end. When the arc approaches the point marked "A" in the Figure 2.29, the force is applied at the unsupported end and the specimen is bent downward rapidly to conform to the radius of curvature of the top surface of the interchangeable die-block "B". Meanwhile, the arc travels steadily onward and is subsequently interrupted in the run off area "C".

Figure 2.30 is a schematic representation showing the typical relationship between the observed hot cracking and the location of the weld puddle at the instant of application of the augmented-strain. Microfissuring in the weld heat-affected zone is normally observed only in the region of the heat-affected-zone at either side of the location of the weld puddle at the instant the augmented-strain is applied. Therefore, where metallographic examination is to be performed, a

section corresponding to the dashed rectangular area in Figure 2.30 is removed and subjected to suitable metallographic preparation [75].

The following criteria have been used to evaluate the varestraint test results: cracking thereshold strain, combined crack length, maximum crack length and average crack length, brittle temperature range and critical strain rate. The maximum crack length criterion provided a better discrimination for evaluation the weld metal and base metal HAZ cracking sensitivity when compared with the total crack length and threshold strain criteria [65]. These criteria can be used for ranking and understanding of the hot cracking and microfissuring susceptibility of materials, but no single criterion can rank all materials or explain the entire range of behavior. Lundin [75] in his discussion of interpretation of the Varestraint test results (criteria), concluded the “the data, especially the total crack length and cracking threshold strain criteria, has to be statistically related to the chemical analysis of the material, and then elements responsible for behavior (cracking) differences can be uniquely identified “, indication the combined criteria of the total crack length and threshold strain is the best criteria for understand hot cracking, microfissuring susceptibility of materials.

### 2.9.4 Spot Varestraint Test

The second generation of Varestraint testing evolved with the Spot-Varestraint test colloququially known as the Tig-A-Ma-Jig, which was designed mainly for testing the hot cracking and microfissuring susceptibility of thin sheet

material [69]. It maintains the desirable features of the original varestraint test and additionally permits the use of smaller specimens. In this test, the specimen is subjected to a gas tungsten arc spot weld thermal cycle to establish approximately steady-state thermal conditions. As the arc current is interrupted, an augmented strain is applied to the specimen by bending and either solidification cracks or HAZ cracks can be formed. The schematic test method is shown in Figure 2.31. Lundin reported that the threshold stress criterion provided the best discrimination of hot cracking susceptibility for the sigmajig test [79].

The major conceptual difference between the Spot-Varestraint and the basic Varestraint test is related to the thermal history of the weld region. In the conventional test, the augmented strain is applied as an actual weld bead is being deposited. In the Spot-Varestraint, the strain is applied to a region surrounding a stationary spot. The fusion hot cracking sensitivity for the modified 316, 316NG and 347NG with both the Varestraint and Sigmajig tests show a similar trend [76], and the same ranking for the test materials [61].

### 2.9.5 SICO (Strain Induced Crack Opening) Testing

SICO testing was developed by Dynamic System Inc. using Gleeble physical simulation and can be used to evaluate microfissures in a multipass weldment of austenitic stainless steels and Ni-base alloys [12, 81]. SICO test specimen of 10mm diameter by 86 mm long are cut form the transverse of a

multipass weld coupon with the weld fusion zone located at the specimen midspan, as shown in Figure 2.32 (a). Figure 2.32 (b) shows the beads sequence. The specimens are clamped in the Gleeble thermal-mechanical simulator in copper grips. The specimen is heated to a test temperature (1000°C to 1300°C) at a heating rate similar to that of an actual welding cycle and then compressed to different strains with a rate adequate to avoid any substantial microstructural changes. The mcirofissures initiate at the equatorial surface of the bulge zone shown in(shown in Figure 2.32(c)).

The onset of cracking is judged at a 30X magnification to search for microfissuring in the bulge zone in the midspan of the specimens using different levels of applied strain. All the tests are conducted in argon, and the hot deformed specimens are conduction cooled naturally in the water-cooled copper grips. SICO method can also be used to evaluate microfissure susceptibility of different materials by measuring nil strength and critical secondary tensile strains to fracture as a function of temperature in multipass welds of high alloy austenitic stainless steel and Ni-based alloys.

## 2.10 Effect of Microfissure on Austenitic Stainless Steel Properties

Microfissures can be controlled to a certain extent by attention to consumable composition and purity, and welding technique, but they are not

uniquely eradicated in actual weld application. Increasing the amounts of ferrite in the weld metal, the microfissuring tendency quickly diminishes and is eventually eliminated at a ferrite level which may vary from 3 FN to 6 FN, a high nominal ferrite content does not ensure uniform distribution throughout the weld metal [15]. Gunia and Ratz report that a weld metal having an average of 2.8% ferrite may actually vary in ferrite content from 0.3 to 8.1% [82]. Thus, it may not be possible to guarantee freedom from microfissuring in multipass welds. It is essential, therefore, to determine the significance of these microfissure defects relative to service performance.

### 2.10.1 Effect of Microfissure on Mechanical Properties

In 1940s, Campbell, and Thomas indicated that weld deposits with microfissures reduced the tensile properties of 25Cr-20Ni weld metal. With the increased utilization of heavy section stainless weldments, microfissures in multipass welds in austenitic stainless steels have raised concerned involving mechanical and corrosion performance degradation in recent years.

Campbell and Thomas showed that microfissures in 25Cr-20Ni weld metal reduced tensile strength and ductility [2]. While other researchers reported that results obtained from the austenitic stainless steel weld metal with microfissures have no significant effect on the tensile properties of welded joints. Neither have the microfissures significantly affected metal ductility [7, 12, 49, 61].

### 2.10.2 Effect of Microfissures on Fatigue Properties

Fatigue failure is invariably associated with a stress concentration and possibly weld defects. However, there have been conflicting opinions regarding the significance of weld metal with microfissures in austenitic stainless steel on fatigue behavior. In weld deposited claddings, Wylie et al [83] found that microfissures had no effect, while Baggerud [84] observed a substantial loss in fatigue strength due to microfissures.

Honeycombs and Gooch investigated the fully austenitic welds with more extensive microfissures than would be expected in practice and found that fatigue crack initiation took place preferentially from the weld toe, but not from the microfissures. They also showed that, with dressed welds, microfissures may become critical in influencing fatigue crack initiation. However, in practice, stainless steel welds will relatively seldom be dressed to improve their fatigue resistance. In the general case, it can be concluded that microfissures would have no significant effect on the fatigue behavior of undressed welds [85]. Bauer and Wilken drew a similar conclusion that weld defects reduce the fatigue life, but for defect sizes below 0.4 mm, the reduction was not significant [86]. Fatigue crack initiation sites were microfissure, specimen corners, and acceptable weld defects (such as small nonmetallic inclusions with no apparent dominance of one discontinuity over another). But the low-cycle fatigue tests indicated that the microfissures are no more detrimental to the fatigue strength than other geometrical effects or nonmetallic inclusions [1, 9].

The researchers evaluated the effect of microfissures on the fatigue life of austenitic stainless steel welds at high and low ferrite count. The results of the evaluation indicated that there is no significant difference in fatigue life between two weldments [9, 87].

### 2.10.3 Effect of Microfissures on Corrosion Performance

Microfissures provide easy initiation sites for crevice attack particularly in chloride-containing environments, and thus drastically reduce the corrosion resistance of a weldment. Stainless steels are more susceptible to crevice corrosion than to pitting. However, microfissure-crevice corrosion is often mistakenly interpreted as self-initiated pitting. As microfissures are often invisible to the naked eyes their existence can be explained by the unexpectedly poor pitting performance of weldments made with filler metals of apparently similar general composition [88].

Microfissuring related corrosion in austenite stainless steel weldments containing 4 to 6% Mo is best avoided with the use of nickel-base ERNiCrMo-3, filler metals, which is very resistant to crevice attack [22].

In practical situations requiring control of the ferrite content in austenitic stainless steel weld metals, a decision will be necessary whether to use partially ferritic weld metal with possible loss of corrosion resistance, toughness etc., or to specify fully austenitic deposits that may suffer microfissuring.

### 2.10.4 Effect of Microfissures on Creep Properties

Creep failure was not believed to be significantly affected by the presence of pre-existing defects. The examples of service failures are usually relative to either overheating or to very long time effects [71].

Lundin reported in his review that the weld discontinuities are not influential in high temperature creep and stress rupture for austenitic materials if microstructure alteration in service does not degrade the ductility [70]. The microfissures induced by welding only influence the crack growth and propagation process if they are located in an area impaired by creep or fatigue [89].

## 2.11 Summary

From the review of currently available information, the follow conclusions are obtained:

1). It is recognized that austenitic stainless steel weld metals are susceptible to microfissuring in the fusion zone during weld solidification and underlying pass weld metal heat affected zones subsequent pass

deposit, especially in primary austenitic solidification mode with high sulfur and phosphorous contents.

2). The delta ferrite solidification mode has a beneficial effect on reducing and preventing microfissuring in austenitic stainless steels weld metals.

3). In some cases, the levels of impurity and presence of minor elements may critically determine the microfissuring behavior.

4). Microfissures have deleterious effects on corrosion performance, a small effect on fatigue and creep properties, and little effects on tensile strength, or toughness.

5). Ductility can indeed be adversely affected by microfissures based on the work of Campbell and Tomas [2]

# CHAPTER 3
# MATERIALS AND EXPERIMENTIAL PROCEDURES

## 3.1 Materials Evaluation

### 3.1.1 Materials used in the experiments

A total of 17 different weld deposits, 6 E308L, 7 E316L, 2 E308H and 2 E316H, were used in this investigation. Eight types of modified E308L, E316L, E308H, and E316H electrodes with 3.2 mm diameter, with a ferrite content in the weld metal at the 0 FN level, were especially manufactured by Lincoln Electric Company, ESAB and Hobart for this project. Except the new pads welded by these electrodes, those from the earlier projects entitle “Fissure Bend Test ” (1976) and “Weld Metal Fissuring Tendency of Kryo-Kay 316-15” were also used in this study because these weld pads provided differing microfissure levels (and concomitant different ferrite content). The identification of the new pads is labeled based on the electrode type and classification (C: commercial, M: modified). Figures 3.1 and 3.2 show the weld pads selected from the previous project. The compositions of the weld deposits are shown in Table 1 (All Tables located in Appendix B). It is to be noted that the compositions for all of the materials (Table 1) fall within the AWS A5.4 specification. The base metal used in all tests is 304 stainless steel cut from bar stock. The coupon size of the sample prior to welding is 230 mm long, 50 mm wide and 13 mm thick, as shown in Figure 3.3

### 3.1.2 Welding

To assist in maintaining proper position and alignment of the first stringer bead, a guide line was punched on the base plate. After the first stringer bead was deposited, the arc, for secondary passes, was directed into the previous bead to minimize dilution from the base metal. Before welding, the plates were clamped on each end to a heavy backing fixture to prevent deformation. Three test coupons were clamped in the clamping fixture, as shown in Figure 3.4(a). Three-layer (six beads to each layer) weld pads were produced using Shielded Metal Arc (SMA) welding to permit the evaluation of microfissuring in relatively undiluted weld metals. The weld pad configuration for the Fissure Bend Test are schematically shown in Figure 3.4(b). The welding parameters are shown in Table 2.

### 3.1.3 Surface Preparation

With the pads still in the clamping fixture, the surface was milled using a 0.254 mm depth of cut on each pass until the surface was clear of almost all irregularities. The pad surface was ground on a surface grinder using a twelve pass sequence with the first eight passes each removing 0.0254 mm. and the final four passes each removing 0.0127 mm.

After grinding, the specimens were removed from the clamping fixture and washed in the ultrasonic cleaner with methanol to remove all traces of cutting fluids.

### 3.1.4 Microfissure Evaluation

Test pad evaluation was performed over the center 4” of each specimen using dye penetrate testing. Apply a light coating of the fluorescent onto the weld pad surface. Allow a penetration time of 15 min. to permit the penetration to soak into all microfissures and other surface discontinuities. Remove the penetrant by rinsing the weld pad for 30 s with remover. Dry each specimen under a warm air dryer. Allow a developing time of 10 min to permit the penetrant to exude from fissures and other surface discontinuities and then inspect the pad under a standard black light in a dark area. The indications of discontinuities will fluoresce with a brilliant yellow-green light in the darkness. Count and circle with water-soluble ink all linear indications in the center 100 mm of the pad. These indications generally denote microfissures. Inspect each of these linear indications at 50X, then count and measure the length of those indications verified as fissures. Bend the specimens to an included angle of 120 degrees in a fixture. The results showed that many microfissures were observed in Modified M308L, M308H, M316L and M316H, and no microfissures were present in the commercial E308L, E308H, E316L and E316H weld pads. Typical morphology detected using dye penetrant testing is shown in Figure 3.5.

### 3.1.5 Ferrite Number Measurement

Ferrite Number is a specific term to describe the ferrite content, the measured ferrite content is not designated as the ferrite percentage but as the ferrite number, in short FN. In 1974, the measurement of ferrite in normally

austenitic stainless steel weld metals was standardized by the American National Standards Institute/American Society (ANSI/AWS) A4.2 specification in terms of magnetically determined Ferrite Number, rather than the metallographically determined “volume percent ferrite”. Ferrite Number has been found to be very reproducible, which is the main advantage for its use in standardization. Ferrite Number approximates the “volume percent” at level below 8FN. Above this level, deviation occurs, where the FN value exceeds the actual volume percent ferrite.

The Ferrite Number was determined in the center 100mm region of the ground pad, using a 15 intersection grid layout, with the Feritscope, as shown in Figure 3.6. The Ferrite Numbers are also determined from the cooperations plotted in the Schafller diagram based on the Chromium and Nickel equivalents calculated from the chemical compositions. The average Ferrite Numbers of previous and current experimental deposits measured and calculated are shown in Table 1. The Ferrite Numbers from both methods match well.

### 3.1.6 Microfissure Level and Distribution

The bend fixture shown in Figure 3.7 was used to perform the Fissure Bend Test on weld coupons to determine the microfissure distribution. The milled and surface ground weld pads were bent in tension to an angle of 120 degrees for detecting the microfissures present across the center 100 mm of the pad surface for evaluation of microfissuring tendency. An average microfissure density of 40, 12, 4, 7.9 and 5.9 per $cm^2$ was determined for modified E308L, E316L (Lincoln), F316L (Hobart), E308H, and E316H pads, meanwhile no

microfissures were present in the commercial E308L, E316L, E308H, and E316H weld pads. In addition, the microfissure distribution was also determined on the top surface of the pad along the welding direction. Samples were extracted from the unbend samples (85X10mm$^2$) (in Figure 3.8) and they were ground and polished to 0.05 μm and electrolytically etched with 10% oxalic acid. The distribution of microfissures on the pad surface was determined by fissuring counting and noted to be relatively uniform along pad surface, as shown in Figure 3.9. Figures 3.10 and 3.11 are typical photomicrographs of modified E316H and E308L pad surfaces along the welding direction before Fissure Bend Test.

### 3.1.7 Microfissure Morphology

(1). Optical Evaluation

A number of metallographic samples were extracted from both bent and unbent locations in the M308L test pads (surface and transverse sections) for optical evaluation. Metallography was undertaken in order to locate and characterize the microfissures present. The samples were polished to 0.05um and then etched electrolytically with 10% oxalic acid to reveal the microstructure. Figures 3.12 and 3.13 show typical photomicrographs of microfissures in a transverse section of M308L bent section. The microfissures occur along grain boundaries and are open to the surface of the weld pad (at the top of the figures). However, not all of the microfissures intersected to the surface and thus were contained within the weld pad beneath the surface. Figure 3.12 (a) shows some

of the microfissures appearing entirely within the weld deposit but beneath the surface. Note that they are clearly located along grain boundaries. Some microfissures cross the interpass boundary as shown in Figures 3.12 (b), while others terminate near the interpass boundary as shown in Figures 13 (a) (b). Figure 3.14, a photomicrograph obtained from the top surface of a M308L specimen, clearly shows that the microfissures occurred along grain boundaries. Further, the microfissures tend to occur preferentially along grain boundaries which cross or are near the interpass boundaries.

(2). SEM Evaluation

A sample extracted from bent M308L for SEM evaluation is shown in Figure 3.15. Figure 3.16 shows the fracture surface morphology revealed by SEM. Figure 3.16 (c) shows position A in Figure 3.16 (b) at higher magnification and reveals a ”smooth” flowed appearance, as a result of the liquid film which was on the surface at the time of crack formation. The “smooth” surface with cellular dendritic solidification pattern is clearly noted. These features show typical hot cracking characteristics.

## 3.2 Specimen Preparation

### 3.2.1 Preparation of Immersion Corrosion Testing

3.2.1.1 Corrosion Test Media

The selection of a proper corrosion test solution is the key for successfully screening the corrosion behavior of weld deposits with and without microfissures.

To ensure the CPT and CCT obtained from the pitting immersion corrosion testing below 85°C based on the ASTM G48-99 requirement, a group of candidate solutions were initially evaluated: 3.5 wt% and 6 wt% NaCl with 0.1g of $Fe_2(SO_4)_3$ $4H_2O$ (modified artificial seawater solutions) and 1%, 3% and 6 % $FeCl_3$ solutions. It was determined that the best solution for CPT and CCT determination is a 1% $FeCl_3$ solution for E308L weld deposits, 3% $FeCl_3$ solution for E316L weld deposits, and 6% $FeCl_3$ for E318H and E316H weld deposits.

3.2.1.2. Corrosion Test Specimens

A 13 mm X13 mm coupons (for CPT test) and 25.4 mm X25.4 mm (for CCT test) were extracted from the weld pads. Before corrosion testing, the samples were ground and polished to 0.05μm and electrolytically etched with 10% oxalic acid.

3.2.1.3. Evaluation Criteria for Pitting and Crevice Corrosion

After a 24 hour corrosion test period (pitting or crevice corrosion) at a given temperature, the corrosion samples were evaluated optically at 100X. Pitting was considered to occur when two or more pits were observed at 100X. For crevice corrosion, the formation of “interconnected pits” under the edge of the TFE blocks was used to define crevice attack.

### 3.2.2 Preparation of Cyclic Polarization Testing

3.2.2.1 Test Specimen

13 mm X13 mm samples extracted from the weld pads with and without microfissures were mounted in epoxide resin. Before testing, the samples were polished to 0.05μm and electrolytically etched with 10% oxalic acid and then the sample edges were sealed.

3.2.2.2 Test solution

3.5% sodium chloride in the deaerated conditions.

3.2.2.3 Test Temperature

22°C

3.2.2.4 Test Apparatus and conditions

Test cell and a computer controlled EG & G model 263A potentionstat were used in the tests. The test cell uses a saturated (KCl) silver/silver-chloride reference electrode. All potentials were converted to the standard hydrogen electrode (SHE) scale.

### 3.2.3 Preparation of Mechanical Testing Specimen

A total of 8 different weld deposits, 2 E308L, 2 E316L, 2 E308H and 2 E316H, were employed. The compositions of all the weld deposits meet the AWS A5.4 specification, as shown in Table 1. The base metal used in

all tests is 304 stainless steel. Before welding coupons for tensile sample extraction, 304L base plates were clamped on each side to a heavy welding fixture to prevent distortion. Shielded metal-arc welding was used to produce the weld pads with the welding parameters shown in Table 2. Figure 3.17 shows the weldment preparation for tensile test. All-weld-metal specimens with a gage section diameter of 6.35 mm and a gage length 25.4 mm for tensile test was extracted, as shown in Figure 3.18, along the longitudinal direction of the fusion zone. Figure 3.19 shows the microfissure morphologies distributed in the transverse section shown in Figure 3.17.

### 3.2.4 Preparation of Fatigue Testing Specimen

#### 3.2.4.1 Weldment Preparation

Four types of commercial and modified E308L and E316L electrodes were used to produce microfissure-free and microfissure-containing weldments. The base metal used in the tests is 304 stainless steel. The compositions of the weld deposits are shown in Table 1. Before welding, two plates were clamped to a heavy backing fixture to prevent distortion which can occur in welding. All welding was accomplished with the same welding conditions, 110 amperes, 203 mm/min. travel speed and max. 94 °C interpass temperature. All-weld-metal test specimens for fatigue testing were extracted along the longitudinal direction from the weld coupon. Figure 3.20 shows a schematic drawing of the weld coupon and the configuration of the fatigue sample.

### 3.2.5 Preparation of Creep Testing Specimen

Before welding, the plates were clamped on each side to a heavy backing fixture to prevent excessive distortion. All welding was accomplished with the same welding conditions as those for the electrode evaluation. Figure 3.21 (a) shows the procedure of weldment preparation for creep coupon from initial joint preparation, joint after buttering, completed joint, and sample extraction. All weld-metal test specimens for creep testing were extracted along the longitudinal direction from the coupon. The creep sample geometry is shown in Figure 3.21 (b). Figure 3.22 illustrates microfissure morphologies on a transverse section of modified E316H coupon, no microfissures were present in the commercial E308H and E316H weld coupons.

### 3.2.6 Preparation of TEM Specimen

The sample for TEM evaluation extracted from the transverse section of creep sample after creep test, at 45 degree along the loading axis. A thin plate was sectioned from the location to be examined. The sectioned plate was ground to approximately 0.5 mm in thickness. Then, the 3 mm diameter discs have been made by using a hand punch machine. The discs were mechanically polished to approximately 100$\mu$m before conduction chemical thinning. Finally, the polished specimens were chemically thinned till a tiny hole has been generated at center of the specimen. The chemical thinning was performed by using a type Tenupol-3 dual jet electrolytic polishing equipment with a solution of 5% perchloric acid in acetic acid.

The conditions for chemical thinning are:

Current: 0.8-1.4 A

Voltage: 20-30 V

Flow Rae: 0.17 $m^3$/hour

Temperature: 25°C

### 3.2.7 Preparation of X-ray Diffraction Specimen

To further verify the sigma phase and precipitation, an X-ray diffraction apparatus was employed to carry out the analysis. An electrolytic precipitate exaction technique was used to obtain the precipitates from commercial and modified E308H and E316H samples before and after creep testing. To extract particles, a known weight of a sample was placed into 10% HCL + 90% methanol solution with a constant voltage of 8 volts referred to the platinum electrode. A centrifuge was used to separate the particles from the solution. The particles collected from the solution were cleaned using high purity methanol. Then the particles were ready for X-ray diffraction. The particles extracted are weighed again and the ratio of the weight percentage of the precipitate to the matrix is obtained from the following formula [90]. The results of electrolytic extraction of particles from weld deposits are shown in Table 8.

$R=[M_r/(M_i-M_f)]X100$,

Where:

$M_i$ = initial mass of sample,

$M_f$ = final mass of sample after extraction and cleaning,

$M_r$ = mass of residue

R = residue, mass %.

The X-ray diffraction (XRD) spectra were obtained in a Philips X'pert Pro Diffractioner at 45 kV and 40 mA. Diffraction patterns are acquired from samples in a step mode with 0.02 deg. step ($2\theta$) and 4 seconds per point over diffraction angles from 30 to 60 deg. The information from X-ray examination was recorded in the form of intensity as function of $2\theta$.

Careful sample preparation was necessary for produce the x-ray diffraction samples. The powder was mixed with some glue which was x-ray checked to be without sharp peaks (amorphous material). The mixture was placed on a piece of glass which was also x-ray checked and should no sharp peaks. The information from x-ray examination was recorded in the form of intensity as function of $2\theta$. Each peak was carefully checked and analyzed.

## 3.3 Experimental Procedures

### 3.3.1. Corrosion Testing

3.3.1.1 Pitting Corrosion Testing for CPT (ASTM G48) [91]

The CPT was used as a base to compare the pitting resistance of the weld pad deposits. To determine the CPT, immersion corrosion tests were performed on 1/2" square weld pad samples. The test solution was 1% ferric chloride for E308L, 3% ferric chloride for E316L, and 6% ferric chloride for E308H and

E316H weld deposits. The CPT is defined as the lowest temperature at which two or more pits are observed by optical microscopy at 100X. A 5 C° test temperature increment was used in CPT testing.

3.3.1.2 Crevice Corrosion Testing for CCT (ASTM G48) [91]

For crevice corrosion testing, the CCT was determined to evaluate the crevice corrosion resistance. To determine the CCT, immersion corrosion tests were performed on 1" square weld pad samples. Two TFE blocks were fastened to the sample surface with O-rings as shown in Figure 3.23. This crevice assembly was then immersed in the test solution, 1% ferric chloride for E308L, 3% ferric chloride for E316L, and 6% ferric chloride for E308H and E316H samples, which was preheated to the test temperature. The immersion corrosion tests were conducted in a water bath (as shown in Figure 3.24) with a temperature control accuracy of ±1 C°. The corrosion samples were inspected after 24 hours.

The CCT was determined to be the lowest temperature at which the formation of "interconnected pits" under the surface of TFE-fluorocabon blocks was observed. The test temperature increment was 5 C°.

3.3.1.3 Cyclic Polarization Test Procedure

a. Before performing the cyclic polarization test, the oxygen level was reduced by bubbling Nitrogen at a rate of 150 $cm^3$/min. for 1/2 hour and then the sample was allowed to corrode "freely" for about 1 hour until stabilized at $E_{corr}$.

b. After $E_{corr}$ stabilization, the potential scan began at 50 mV (initial potential) below the established $E_{corr}$. The scan rate was 0.17mV/s. The reversing current density was set at 0.001A/cm$^2$.

### 3.3.2 Mechanical Testing

#### 3.3.2.1 Pre-strain tension tests

Pre-strain tension tests of the weld metals with and without microfissures were performed at room temperature. Before tensile testing, the samples were ground and polished to 0.05 μm surface finish and lightly electrolytically etched with 10% oxalic acid to reveal the microstructures and microfissures, as shown in Figure 3.25. The numbers of the microfissures on the modified and commercial polished and etched surfaces were 10 and 0, respectively. Pre-strain testing was applied to each sample at 180 MPa (approximate 50% of yield strength) to open the microfissures and enable comparison with fissures observed under the optical microscope before full tension testing. The pre-strain rate was $5X10^{-5}$ /sec.. During the pre-strain process, the samples were still in the elastic region. After releasing the pre-strain load, the samples were observed under the optical microscope to count the microfissures. The fissure counts were similar in comparison of those before and after pre-strain testing. The samples were then tested until fracture occurred.

3.3.2.2 Standard Tensile Testing

Room temperature tensile tests of weld metal with and without microfissuress are performed. Values determined from the test included the 0.2% offset yield strength, tensile strength, percent elongation, and percent reduction in area.

### 3.3.3 Fatigue Testing

All of the specimens were ground to a uniform surface finish of 800-grit to remove any surface irregularities prior to fatigue testing. Then, tension-tension fatigue testing with a 0.1 stress ratio was conducted in a computer-controlled Material Test System (MTS) servohydraulic testing machine operated at a frequency of 20 Hz under load control at ambient temperature. The load in the range of 204 to 476 MPa for fatigue testing is based on the yield strength of each material. The results of the tests for a number of different stress levels are plotted to obtain a stress-life curve (S-N curves). Figure 3.26 shows the servohydraulic fatigue test equipment.

### 3.3.4 Creep Testing

The creep testing was conducted in constant load creep frames. Each frame contains a three-zone furnace with the power level for each zone being independently adjustable. Each furnace is controlled by a Leeds and Northrup Electromax III controller which utilizes a chromel-alumel thermocouple to monitor

the temperature at the center of the middle zone. All furnaces were profiled and the zone profile over the specimen gage length is ±1F°.

Each specimen is mounted in a testing fixture and suspended within the creep frame furnace as shown in Figure 3.27. A chromel-alumel thermocouple wired to the center of the specimen gage length is connected to a digital temperature recorder which, in turn, is used to monitor the temperature of the specimen during testing. To minimize the convection of air through the furnace, both the top and bottom orifices of the furnace were packed with ceramic wool. At the beginning of each test, the specimens are heated to the desired temperature and stabilized before any load is applied. Loading is in uniaxial tension with a constant load throughout the test. In addition to temperature, specimen extension, measured by a dial gauge attached to the testing fixture, is also recorded as a function of time. Different stress levels between 70 to 240 MPa were used together with a range temperature (550-700°C) for creep testing of commercial and modified E308H and E316H weld deposits.

# CHAPTER 4
# EXPERIMENTAL RESULTS AND DISCUSSION

## 4.1 Corrosion Performance

### 4.1.1 CPT & CCT

Table 3 presents the CPT and CCT results for all tested materials. The CPT and CCT for fissure-containing samples are lower than those for fissure-free samples. The maximum differences in CPT observed are 75C°, 80C°, 75C° and 85C° for E308L, E316L, E308H and E316H between fissure-containing and fissure-free samples. Meanwhile the maximum differences in CCT are 25C°, 45C°, 20C° and 5C° for E308L, E316L, E308H and E316H between fissure-containing and fissure-free samples. The result shows that microfissures have a no more significant effect on CPT than CCT. Figures 4.1 and 4.2 present the corrosion test results (CPT and CCT) as a function of Ferrite Number together with the corresponding microfissure counts for E308L and E316L weld deposits. The CPT, CCT and Fissure Density for weld deposits from E308L-A to E308L-F are labeled in Figure 4.1 as A to F, respectively. In general, the greater the Ferrite Number in the weld deposits, the lower the microfissuring tendency will be, which results in a higher CPT or CCT for E308L deposits. In addition, the CPT is generally higher than the CCT for the weld deposits without microfissures. The sample surface condition (roughness) has a significant effect upon corrosion behavior. The “smoother” the surface, the greater the resistance to corrosion attack. It should be recalled that the corrosion samples used for both CPT and

CCT were ground, polished to 0.05μm, and etched before the corrosion testing. It should be noted that, for the samples with microfissures, the microfissures provide a great level of "roughness". Thus, it is believed that the corrosion behavior is dominated by the corrosion conditions associated with the tips of microfissures and not the bulk sample surface roughness per se. Because crevice corrosion occurs on the surface under the TFE-fluorocarbon block, the polished surface tends to enhance the crevice corrosion resistance. However, when microfissures are present, crevice attack forms by interconnected pits initiated at the tips of microfissures. As a result, the CPT will be less than the CCT when a corrosion sample contains microfissures greater than 0.27 microfissures/$cm^2$ and 0.5 microfissures/$cm^2$ for 308L.

There is no significant decrease in CPT or CCT at the higher ferrite levels, as was apparent for E308L. In general, the conditions for crevice corrosion testing are more severe than for pitting. Therefore, one would expect that the CPT would be greater than the CCT for samples without microfissures, which is generally the case for this study. For the commercial 308L-F (FN=7.3) fissure-free samples the value of CCT is even lower than that of the fissure-containing samples (FN=0.70). This is probably caused by the difference of chemical composition. From the chemical compositions listed in Table 1, the Mn content for commercial E308L-F is low in comparison with the other deposits. As a result, the chemical composition may dominate corrosion behavior and override the effect of fissures. Thus, Mn may have significant effect on crevice corrosion resistance. Figures 4.3-4.6 show typical pitting morphologies after a 24-hour

pitting corrosion test in $FeCl_3$ solution.

### 4.1.2 Cyclic Polarization Testing

Particular attention is to be focused on two features on the cyclic polarization behavior. One is $E_{pit}$, (breakdown potential). The more noble this potential, the less susceptible the alloy is to the initiation of localized pitting attack. The other feature is the protect potential ($E_{prot}$) at which the hysteresis loop is completed on the reverse polarization scan. The more electropositive the potential at which the hysteresis loop is completed (close to $E_{pit}$), the less likely that propagation of pits will occur over a range of potential below $E_{pit}$.

Table 4 shows the average values of $E_{pit}$ and $E_{prot}$ from different test results conducted on the same weld pad (fresh surface for corrosion testing each time). It is evident that the E308L deposits have the lowest average $E_{pit}$ and $E_{prot}$, followed by E308H and E316L, E316H shows the highest $E_{pit}$ and $E_{prot}$. Comparing the fissured and fissure-free deposits in each group, it is evident that in most cases the fissure-free samples show higher values of $E_{pit}$ and $E_{prot}$ than fissure-containing samples.

Figures 4.7-4.10 show typical cyclic polarization curves presented in the form of E (SHE potential) versus $mA/cm^2$ (current density) for E308L, E316L, E308H and E316H deposits with and without microfissures. $E_{pit}$ and $E_{prot}$ for E308L and E316L were also summarized in Figures 4.11-4.12.

In Figure 4.7 (E308L), $E_{pit}$s of fissure-containing samples, M308L,308L-A and 308L-B, are between 221-336 mV, meanwhile, those of fissure-free samples,

308L-C, 308L-D and C308L, are between 371 and 527 mV. With the decrease of microfissure densities from M308L, 308L-A, 308L-B to 308L-C (40 to 0 microfissure/cm$^2$), $E_{prot}$s are increase from –73 to 230 mV, which means that the corrosion surface becomes more easy to form the repassive films to prevent the existed pits to propagate. However, with the increase of $E_{pit}$s for 308L-D and C308L, $E_{prot}$ began to decrease, even lower than the lower fissure densities samples E308L-A and E308L-B. Which can be attributed to the disadvantages of the cyclic polarization testing method (discuss in the following paragraph).

In Figure 4.8 (E316L), $E_{pit}$s of M316L and F316L with higher fissure density are very low (around 400 mV). The $E_{pit}$s of those with lower microfissure densities16L-A, 316L-B and KK316L are very high and in the same level with the fissure-free 316L-D, and higher than fissure-free C316L. From Figure 4.8, it is very obvious that $E_{pit}$ can be divided into two groups based on the manganese content shown in Table 1-2, higher fissure-density samples M316L and F316L as well as fissure-free C316L are in the same $E_{pit}$ level because of their manganese contents are in the same level, meanwhile, lower fissure-density 316L-A, 316L-B, and KK316L are in the same $E_{pit}$ level with fissure-free 316L-D, they have the same manganese contents.

It is very clear for commercial and modified 308H and 316H shown in Figures 4.9-4.10 that fissure-containing 308H and 316H show the lower $E_{pit}$ and $E_{prot}$ than fissure-free, respectively, and $E_{prot}$ of 308H fissure-containing is lower and 316H fissure-containing is near the fissure-free, respectively. This can be attributed to the disadvantage of cyclic polarization testing method.

Based on the above the fissure-free samples are more corrosion resistant than fissure-containing samples. The order (from higher to lower potential) of $E_{pit}$ and $E_{prot}$ is E316H, followed by E308H, E316L, and then E308L, thus the corrosion resistance order is E316H, followed by E308H and E316L, then E308L, which is consistent with the pitting and crevice corrosion results.

One phenomena should be considered in cyclic polarization testing, certain value of current density should be set for curve to come back. In comparison with the “pitting scan” of the different materials in the same testing condition, the “pitting scan” should shift more left in the coordination axes for more corrosion resistant material compared with those of less corrosion resistance. This means that more noble material has a long way to go to reverse and reach the value of $E_{prot}$. If the material has an excellent corrosion resistance, $E_{pit}$ will be high. After scan reaches $E_{pit}$, the current density increases abruptly and the sample undergoes a long path to reverse and reach $E_{prot}$. Therefore, the corrosion testing condition for more noble material will be more severe than less corrosion resistance sample. Thus, this sample experiences a long time in the severe corrosion conditions and the initial pits were forced to undergo a long time to propagate. So there is such a possibility for more corrosion resistant material that the scan cannot close because the pits are so large that it is not available to form the repassive film again. That does not mean the sample will be corroded in the open circuit condition.

The cyclic polarization curve of KK316L in Figure 4.8 belong to this case. It exhibits excellent corrosion resistance in terms of higher $E_{pit}$ and higher $i_{passive}$

(the curve shifts more left than others), however, the loop is open. Based on the regular way to process such curves, extend both of the curves from the beginning and end until they intersect at one point. The potential corresponding to this point is regarded as $E_{prot}$ of this material. It will be very low and is a negative value for KK316L. Which means this material will be corroded in the open circuit condition. Actually, KK316L proved to be an excellent corrosion resistant material in terms of CPT (80°C) and CCT (75°C) in immersion corrosion testing in 3% $FeCl_3$ solution.

Cyclic Polarization Testing method is not comprehensive to evaluate the corrosion behavior when $E_{prot}$ is considered in the case that there are large differences of anodic current density with polarization potential between the materials compared.

### 4.1.3 Corrosion Sites

Figures 4.13-4.14 show the typical pitting morphologies of fissure containing 316L samples after pitting immersion testing in 3% $FeCl_3$ solution at CPT, 65°C for 316L-A and 1°C for M316L. It is to be noted that pitting preferentially occurs at the microfissures. Microfissures provide the pitting corrosion sites and degrade pitting corrosion resistance of austenitic stainless steel weld metals.

Figure 4.15 shows the initial pitting location at the fusion line of C316L in pitting immersion corrosion testing at CPT (65C). With an increase in temperature to 80°C, more significant pits appear in the overlapped HAZ, as

shown in Figure 4.16, and it is almost pit free away from this region. This illustrates that these are susceptible (preferential) locations for corrosive attack. The phenomena can be caused by two factors, one is the specific characteristic of the overlapped HAZ, and the other one is the difference in microstructures and properties between overlapped and un-overlapped HAZ that results in “galvanic corrosion”.

More segregation can occur in the overlapped HAZ region due to multiple thermal cycling, which would be reflected in microstructural characteristics of the overlapped HAZ. Grain boundary movement caused by the thermal cycling in this region provides for more grain boundaries acting as sites for impurity atoms and this results in more segregation sites. The corrosion problem commonly associated with welding of austenitic stainless steels is related to the chemical segregation, therefore, overlapped regions are usually the weakest sites to resist corrosion attack in the weld metal. For the multi-run welds, each subsequent weld thermal cycle effectively affects a part of the previous weld metal (HAZ) which results in two different adjacent regions, microstructure that changed in the overlapped high temperature region and microstructures that are not altered (low temperature HAZ). The differences in properties and microstructural morphologies between these two regions can result in different corrosion sensitivities and may promote preferential galvanic attack.

Figures 4.17-4.20 show the typical morphologies of E316L and E316H fissure-containing samples before and after pitting immersion testing. It is to be noted that pitting preferentially occurs at the tips of microfissures during corrosion

testing. This can be attributed to the easy formation of occluded cells at the tip or narrow regions of microfissures that results in highly concentrated corrosion product cations that hydrolyze to create a locally aggressive acidic environment [92]. For fissure-free samples, the initial pitting location is along the fusion line in the overlapped HAZ, as shown in Figures 4.21-4.22 showing the pitting location after cyclic polarization testing.

### 4.1.4 Preferential Austenite Attack

It is generally accepted that delta ferrite, when present in small amounts in the austenite matrix, has been shown to be detrimental to pitting resistance by providing favorable sites for pitting initiation in the weld metal. The corrosion problems commonly associated with welding of austenitic stainless steels are related to both precipitation effects and chemical segregation. The “cast” solidified fusion zone microstructure of a weld is always subject to segregation during solidification. Thus, it is important to investigate the corrosion behavior related to the segregation of weld metal in order to consider its effects on the practical welding of stainless steels. There are some differences in segregation for the different solidification modes of the weld metal, so it is not comprehensive to regard the initial corrosion site as always from the ferrite.

Figures 4.23-4.26 show the typical pitting morphologies after pitting immersion testing for different weld deposits in the initial pitting locations at the CPT, 65°C and 75°C (3% $FeCl_3$ for 316L-A and B respectively), and 75°C (6% $FeCl_3$) for 316H. It is very clear that the initial corrosion attack is in austenite as

opposed to ferrite. This can be attributed to the increased micro-segregation and coring in the cellular dendritic microstructure in the weld metal that results in the formation of chromium-depleted in the cell cores. In austenitic stainless steels, the primary phase of solidification may be either austenite or ferrite, which is dictated predominantly by composition. Four solidification modes for the solidification of castings and weld metals, A, AF, FA and F (A-austenite, F-ferrite), were established by Suutala and Moisio. The WRC-1992 diagram is the most accurate diagram for predicting the final microstructure and solidification mode based on the chemical composition in terms of $Cr_{eq}/Ni_{eq}$. For the standard chemical composition of 316 electrodes met the requirement of AWS A5.4 specification, the value of Creq/Nieq are found in the region of AF solidification mode. Figure 4.27 shows the schematic representation of crystal segregations and the distribution of chromium and nickel within dendrites during the AF mode solidification of an austenitic weld metal alloy according to Cieslak, Ritter and Savage [91]. It is to be noted that for the primary austenite solidification, the cores of the cellular dendrites are depleted in chromium and nickel relative to the normal composition, and chromium segregates more highly than nickel. The mechanism of corrosion protection for stainless steel is the formation of a passive film to separate the metal from the surrounding atmosphere. Chromium is the essential element in forming this passive film and nickel is effective in promoting repassivation. When these two elements are at a low levels, the passive film is rather weak in its resistance to corrosion attack.

### 4.1.5 Manganese Content

In many aspects, manganese plays an important role in austenitic stainless steels and high nickel base alloys. Many researchers recognized that the addition of manganese to fully austenitic stainless steels has a favorable effect on hot cracking resistance.

It is well known that the conventional reason for adding manganese to austenitic stainless steels is deoxidation and sulfur control. Approximately 1.5%Mn is used both as an austenite stabilizer and as a sulfur and silicon compound former. The beneficial effect of manganese is to interact with sulfur in stainless steels to reduce the “harmful” effect of sulfur by forming MnS type sulphides of relatively high melting temperature. The morphology and composition of these sulfides can have substantial effects on corrosion resistance, especially pitting resistance. Manganese is considered to be a detrimental effect on the pitting resistance because of the formation of manganese sulfide. Manganese sulfide inclusions are active anodic sites at a stainless steel surface in presence of aqueous chloride solutions.

Let’s recall the CPT and CCT results shown in Figure 4.1, with the increase of Ferrite Number so as to decrease the microfissure density, CPT and CCT increase gradually from point A to E and just decrease slightly at point F (C308L) for CPT, however, the CCT at point F drops greatly, and even lower than point A (fissure-containing). It is to be noted from Table 1.1, the manganese contents in the samples represented by point B, C, D, and E are in the same level, around 1.6%, and A and F in the same level (0.6%)(A is fissure-containing

and F is fissure-free). Let's analyze the representative points A, E and F. Crevice corrosion testing results show that CCTs for 308L-A, 308L-E and 308L-F are 40°C, 55°C and 20°C, respectively. The main difference in 308L-A and 308L-F is the FN (FN=0 for 308L-A, FN=7.3 for 308L-F) and their Mn contents are in the same level (0.6%); the main difference in 308L-E and 308L-F is the Mn content (1.66% for 308L-E and 0.61% for 308L-F) and their FNs are not in the large difference (FN=6.0 for 308L-E and FN=7.3 for 308L-F). Even though 308L-F is fissure-free sample, its CCT is 20°C lower than fissure-containing 308L-A which can be attributed to the difference in Ferrite Number. It is generally accepted that delta ferrite, when present in small amounts in the austenite matrix, has been shown to be detrimental to pitting resistance by providing favorable sites for pitting initiation in the weld metal. The CCTs difference in 308L-E and 308L-F is 35°C, which can be caused by difference in manganese content. When the Ferrite Number in the similar level, higher manganese content shows higher crevice corrosion resistance.

For 316L, the commercial 316L also contains lower manganese content (0.71%) and are even lower than fissure-containing M316L (0.82%), but because of the molybdenum added (2.42%) and lower FN (FN=4.76), commercial 316L still shows the higher crevice resistance.

The CCTs are 75°C and 85°C for commercial 316H and modified 316H, respectively. The microfissures seem not affect CCT. Figures 4.28-4.29 shows typical surface morphologies of 316H after crevice corrosion testing at CCT. It is

to be noted that the crevice corrosion attack occurred at 75°C for commercial 316H, however, for modified 316H, the crevice attack did not begin at 75°C up to 85°C. Molybdenum content in both samples is in the same level (2.2%) and the manganese content in modified 316H (1.23%) is even lower than commercial 316H (1.6%). Therefore, under the containing of molybdenum content, manganese shows a little effect on CCT and the low level FN is beneficent on CCT for 316H.

The difference in chemical compositions between 308 and 316 welding deposits is the Mo content. As the Mo added in 316 welding deposits, it greatly increases the pitting potential. In this case, those samples with lower Mn content did not appear any differences in corrosion resistance. In addition, because there is no presence of Mo in 308 welding deposits, Mn plays a much more important role in resisting the corrosion attack. For the lower Mn content samples without microfissures, the CCT is even lower than that microfissure-containing sample with higher Mn content. So Mn is very important element to affect the crevice corrosion resistance for stainless steels, especially for 308 welding deposits. Manganese is considered to be a detrimental effect on the pitting resistance because of the formation of manganese sulfide. While the added molybdenum can suppress the active sites via formation an oxy-hydroxide or molybdate ion.

## 4.2 Tensile Testing

### 4.2.1 Standard Tensile Testing

Room temperature tensile tests of weld metal with and without microfissuress are performed. Values determined from the test included the 0.2% offset yield strength, tensile strength, percent elongation, and percent reduction in area. It is apparent from the test results shown in Table 5 that all of the properties of commercial 308L fissure-free samples are similar to the modified 308L fissure-containing samples. The same similarities were obtained for commercial 316L and modified 316L. The results from the 308L weld deposits indicated that the weld metals presence of microfissures has no significant effect on the properties in tensile test.

Figure 4.30 shows the samples of modified E308L and E316L before and after the tensile testing. Fissures are clearly observed on the sample fracture surfaces and on the gage length surface after the tensile tests. Figure 4.31 demonstrates that the morphologies of fracture surfaces of modified E308L and E316L, 50 and 10 microfissures respectively observed under 100X on the fracture surfaces. The fracture of modified E308L exhibited a flat transverse break bounded by a narrow shear lip, meanwhile, modified E316L exhibited a classic cup-and cone rapture. From the test results it is shown that microfissures have little effect on the mechanical properties defined by a tensile test.

### 4.2.2 Pre-strain Tensile Testing

Pre-strain tension tests of the weld metals with and without microfissures were performed at room temperature. Before tensile testing, the samples were ground and polished to 0.05 μm surface finish and lightly electrolytically etched with 10% oxalic acid to reveal the microstructures and microfissures, as shown in Figures 4.32 and 4.33. The numbers of the microfissures on the modified and commercial polished and etched surfaces were 10 and 0, respectively. Pre-strain testing was applied to each sample at 180MPa (approximate 50% of yield strength) to open the microfissures and enable comparison with fissures observed under the optical microscope before full tension testing. The pre-strain rate was $5X10^{-5}$ /sec.. During the pre-strain process, the samples were still in the elastic region. After releasing the pre-strain load, the samples were observed under the optical microscope to count the microfissures. The fissure counts were similar in comparison of those before and after pre-strain testing. The samples were then tested until fracture occurred. Properties determined from the tests included the 0.2% offset yield strength, tensile strength, percent elongation, and percent reduction in area. It is apparent from the test results that the yield strength of modified 308L is similar to that of commercial 308L with only 60MPa difference in ultimate strength, but the ductility is lower than for commercial 308L, as summarized in Table 6. The results from the 308L weld deposits indicate that the presence of weld metal microfissures has a deleterious effect on the ductility for 308L, but virtually little effect on yield and ultimate tensile strength. These can be attributed to the basic mechanical properties of stainless steel, high

ultimate strength and relative low yield strength. Since the high strength and excellent ductility of stainless steels, microfissures did not show much of an effect on ultimate strength in the tensile testing. When the load exceeds a value corresponding to the yield strength, the sample undergoes plastic deformation. With increase of the deformation, the sample begins to neck locally. Because of the fissures in the fissure-containing samples decrease the cross section of the sample to withstand the load subjected to the sample. The sample fractured in the plastic deformation region of the tensile test and shows reduced ductility compared to the commercial fissure-free samples.

## 4.3 Fatigue Behavior

### 4.3.1 Typical S-N Curve

All of the test results are listed in Table 7. Figures 4.34 and 4.35 shows the S-N curves of commercial and modified E316L and E308L weld-metal fatigue samples. As seen from the Figure 4.34, at the stress amplitude of 374 and 408 MPa, the fatigue life reaches about $10^7$ cycles (fatigue limit) for commercial E316L, meanwhile, only 206,818 and 98,946 cycles were exhibited by modified E316L. The slope of both curves shows a large difference, which reflects the large difference in fatigue behavior. General fatigue failure can be regarded as three stages, material yield to produce fissures, fissures propagate, and fracture. Because of the pre-existing microfissures in the cross section of the samples, they greatly reduce the incubation time to produce microfissues so as to shorten

the fatigue life. This is reflected in the S-N curve; the fatigue properties of fissure-containing E316L are lower than those of fissure-free samples. The S-N curves of commercial and modified E308L in Figure 4.35 shows the similar results with Figure 4.34.

### 4.3.2 Metallurgical Evaluation

Figures 4.36 and 4.37 show the typical fracture surface of modified and commercial E316L samples. Both fractures exhibited a flat transverse break with obvious beach marks over a large area of the fracture surface bounded by a narrow shear lip. The crack initiations sites can be identified following the radial lines back to the point of convergence, A for modified E316L and C for commercial E316L. Figures 4.36 show the failure initiation site of modified E316L. Figure 4.36 (c) shows location A in Figure 4.36 (b) at higher magnification. This location shows a typical characteristic of hot cracking morphology, “a smooth flowed pattern”, which means these cracks were produced at elevated temperatures. It is evident that the initiation is caused by these microfissures. Fatigue initiation and propagation along the microfissures is thus related to weld solidification. Microfissures act as stress raisers and significantly decrease the fatigue properties. At higher magnification, the fatigue striations for modified E316L sample were easily observed as shown in Figures 36(d) (e). Figure 4.37 (a) (b) shows the morphology of commercial E316L crack initiation site C. There are many fissures in the origin without any characteristics of hot cracking under higher magnification. Thus indicates secondary cracking.

After the secondary cracks have nucleated and propagated to a finite size, they become a macroscopic stress raiser and control the fracture direction. Striations can also be observed at higher magnification. The conflicting options regarding the significance of weld metal with microfissures were obtained from the observations of the weldments failed in service. When additional defects which caused more stress concentration compared to microfissures, the failure preferred to occur in that location instead of microfissure; otherwise, microfissures are the initial failure location. Our test results from all-weld-metal samples

## 4.4 Creep Behavior

### 4.4.1 Typical Creep Curves (Strain vs. Time to Rupture)

Figure 4.38 illustrates typical creep curves (strain vs. time to rupture) for fissure containing and fissure-free E316H samples under the same testing conditions, 117 MPa and 660°C. Both curves match well up to 1700 hours, then the fissure-containing specimen exhibits more secondary creep. The creep rate increases rapidly in the tertiary region that starts at approximately 2% creep strain in both specimens. However, the time to rupture for fissure-containing modified 316H is 1000 hours greater than commercial 316H fissure-free sample.

### 4.4.2 Creep Rupture Behavior

The analysis of creep test results was conducted using the Larson-Miller Parameter technique as shown in Figures 4.39, 4.40 and 4.41 (Stress Level vs.

LMP). It is apparent that the creep properties of modified E316H (microfissure-containing) are superior to the commercial E316H (microfissure-free) samples; meanwhile modified E308H (fissure-containing) sample shows lower creep properties than commercial E308H (fissure-free) sample. The data obtained in the study is overlayed on the stainless steel weld metal data base as shown in Figure 4.42. This depiction indicates that fissures in modified E316H deposits are not influential in affecting creep behavior. Furthermore, microstructure can play an important role on creep behavior.

### 4.4.3 Metallurgical Evaluation

Samples for microstructure evaluation were extracted from fractured creep specimens and ground and polished to 0.05μm surface finish and electrolytically etched with potassium hydroxide to reveal the morphology of the microstructure. The etchant selection is considered to be sensitive in revealing sigma phase (colored) in austenitic stainless steel weld metals which have experienced long-term service at elevated temperature. The most successful etchant for revealing sigma phase is an electrolytic etchant containing potassium hydroxide (KOH-$H_2O$) solution under a controlled (DC) current density and the etchant time. The solution preferentially etches sigma (relative to the austenitic grain boundaries) the color of which color varies from yellow to reddish-brown under the optical microscope. Such characteristic colors and contrast made sigma phase identification [92].

Figures 4.43 and 4.44 show the microstructural morphologies of modified

308H samples before and after creep testing. Before and after creep testing, the microstructure of modified 308H is austenite (FN = 0). The cracking shown in Figure V-11 may be the combination of microfissures and secondary cracking. For commercial 308H, the as–deposited microstructures are austenite with ferrite, austenite with ferrite and sigma after creep testing as shown in Figures 4.45 and 4.46.

Figures 4.47 and 4.48 show the microstructure of modified 316H. Before creep testing, the microstructure is all austenite (FN=0); during testing, carbides evolved in the vicinity of the substructure and grain boundaries.

For commercial 316H (FN=4.7), the microstructure is austenite with ferrite before creep testing and austenite with ferrite and sigma (deduced from morphology and color etching) after creep testing, as shown in Figure 4.49 and 4.50 . The sigma phase is distributed along the substructure and grain boundaries and shows reddish-brown under the microscope.

SEM microstructural morphology of commercial and modified E316H samples after creep testing is presented in Figures 4.51 and 4.52 as a back scattered image. The typical microstructure includes the coarse irregular-shaped secondary phase like the "islands" in the matrix in Figure 4.51 and the dark globular particles in Figure 4.52. The majority of the globular particles form, in modified E316H, along the substructure and grain boundaries and exhibit a size in the range of 0.2-0.4$\mu$m while the size of the particles within the matrix is around 0.6 $\mu$m. EDS analysis was performed at location A for the irregular-shaped secondary phase and location B for matrix. The EDS spectra presented

in Figure 4.53 for locations A and B, respectively. The EDS results show that the irregular-shaped secondary phase contains higher Cr as compared to the matrix. In addition, the fact that these irregular shape secondary phases were stained red by potassium hydroxide etching, indicates that these are $\sigma$ phase. Aluminum oxide presented shown in Figure 4.53 (Al and O peaks) was involved from the polishing process with aluminum powder. This can be deduced from the chemical composition (less aluminum content) and further proved by the latter X-ray diffraction pattern (no aluminum peak appears again).

The EDS spectra for particles (location C) and matrix (location D) for modified E316H was shown in Figure 4.54. There is some difference in Mo content, 3.36 wt% in particle and 1.8 wt% in matrix (equal to the content in the chemical composition).

### 4.4.4 X-ray Diffraction

The X-ray diffraction (XRD) spectra were obtained in a Philips X'pert Pro Diffraction at 45 kV and 40 mA, as shown in Figure 4.55. Diffraction patterns are acquired from samples in a step mode with 0.02 deg. step ($2\theta$) and 4 seconds per point over diffraction angles from 30 to 60 deg. The information from X-ray examination was recorded in the form of intensity as function of $2\theta$. The X-ray spectra of the particles extracted from pre- and post-creep modified and commercial 308H and 316H samples are shown in Figures 4.56-4.69. It is evident that $Cr_{23}C_6$ is the dominant precipitate with a few MnS inclusions for both of the samples before creep testing. After creep testing most particles are $Cr_{23}C_6$

and an amount of σ-FeCr was observed in the commercial 316H sample. This agrees with the metallographic examination on this sample. No σ-FeCr was found in commercial E308H samples due to an insufficient amount particles to be detected using X-ray diffraction.

### 4.4.5 Mechanism Analysis

According to the results on particles extracted from weld deposits of modified E308H and E316H (FN = 0), the ratio of extracted particle weight (the ratio of the particle weight to the weight dissolved in electrolytic precipitate extraction) for these two deposits pre-and post-creep testing are in the same level, around 0.2% and 1%, respectively. The precipitate ratio after creep testing is much greater than that before, which means that a significant amount of carbides evolved during creep testing. The carbides in modified E316H are distributed in chains and those in modified E308H are distributed at random. For commercial E308H and E316H, the extracting ratios are quite different. Because of molybdenum added in E316H, more carbides formed in weld deposits for E316H than E308H before creep testing. After creep testing, more sigma phase formed in E316H than E308H which results in the large difference in extraction ratio for both of these commercial weld deposits.

It is to be noted that microfissures decrease creep resistance for E308H because of the propagation paths provided by fissures and the reduced benefit effect of the randomly distributed carbides. However for commercial E316H, sigma phase formed along the grain boundaries due to the higher ferrite and Mo

content (the extent of sigmatizion is greater than for commercial 308H). Since the sigma phase is hard and brittle it promotes secondary cracking between the sigma phase and austenite in the matrix under the stress. For modified E316H (fissure-containing), carbides are distributed in a chain of discrete globular $M_{23}C_6$ at the sub-structure and grain boundaries. This morphology benefits creep-rupture life.

The mechanisms causing creep are complex and not fully understood, but dislocation climb is thought to be important. To observe the morphology related to carbides and dislocation, a Hitachi 800H type transmission electron microscope was employed. Figure 4.60 shows the typical TEM microstructural morphology of modified E316H after creep testing under 70 MPa, 700°C and 4560 hours. From the metallurgraphy evaluation and particle extraction ratio, the concentration of the evolved carbides in the modified E316 creep sample is high. At such high concentrations, the precipitates may interact with the dislocation cooperatively rather than individually. Dislocations are multiplied and locked by the fine precipitate formed in austenite, as shown in Figure 4.60(a). It is evident that bonding of dislocation to the precipitates will be much stronger than it would be to an "atmosphere". The precipitates nucleated at dislocations and most effectively retard slip. With increasing plastic deformation, the intersection of dislocations with each other grows to form network as a forest of dislocations. Because of the particles in the forest, any slip dislocation does not travel far before it intersects other dislocations passing through its slip plane at various angles. The particles make the movement of the entangled dislocations through

the lattice more difficult. When part of the dislocation in the forest locked, it is hard to move entire network. Which results in the density of dislocation on one side of a particle wall is higher than the other side, as shown in Figure 4.60 (b). Thus, carbides in modified E316H samples serve two principal functions. First, prevent or retard dislocation sliding. Second, fine carbides are precipitated in the matrix and strengthen the grain boundaries. It is not quite understood why carbides distributed in a chain of discrete globular particles in the E316H weld metal, but in a random in E308H weld deposits when both of their FNs are 0. Compared to the effect of microfissures and sigma phase in E316H and E308H weld deposits, it is concluded that secondary cracking caused by sigma phase is a main factor in affecting creep properties for E316H deposits, and the microfissures compared to E308H deposits.

Ferrite Number measurements were made from commercial E308H and E316H samples after the creep testing. The Larson Miller Parameter shows a linear relationship with Ferrite Number after creep testing, as shown in Figure 4.61. The results show that the longer the testing time, the lower the ferrite content. It is evident that with an increase in time ferrite transforms to sigma phase for commercial E308H and E316H samples. It is to be noted that more sigma phase formed in commercial 316H than 308H based on the ferrite remaining in the creep samples after testing. Even though the creep properties of commercial 316H still exhibits a slightly higher creep rupture-strength than 308H.

# CHAPTER 5
# CONCLUSIONS

## A. Materials Evaluation

1. The microfissure distribution was determined for modified and commercial E308L, E316L, E308H and E316H weld pad deposits using dye penetrate test and Fissure Bend Test.

2. It was found that microfissures are distributed relatively uniform over the evaluation length. The average microfissure density was determined as microfissures per $cm^2$ for modified E318L, E316L, E308H and E316H weld deposits, respectively. No microfissures were found on commercial E308L, E316L, E308H and E316H weld deposits.

3. The microfissure morphology, evaluated using optical microscopy and scanning electronic microscopy, shows the characteristic of hot cracking.

## B. Corrosion Behavior

1. Pitting corrosion testing and crevice corrosion testing were performed in terms of CPT and CCT to evaluate the corrosion resistance of fissure-containing and fissure-free samples in ferrite chloride solutions.

2. CPT and CCT are a function of the microfissure level. With the increase in microfissure level a decrease in CPT and CCT is noted for both 308L and 316L samples.

3. When 308L is compared to 316L, the 316L deposits are superior with regard to CPT and CCT at the same microfissure level. The ferrite content does not appear to influence CPT and CCT at the same microfissure level.

4. The corrosion performance of E308L, E316L, E308H and E316H weld deposits with and without microfissures were evaluated by cyclic polarization testing in 3.5% sodium chloride solution under deaerated conditions. The test results reveal the cyclic polarization behavior of these materials in terms of $E_{pit}$ and $E_{prot}$.

5. $E_{pit}$ and $E_{prot}$ of fissure-free samples are higher than fissure-containing, which reflects more corrosion resistance.

6. E316H deposits have the highest $E_{pit}$ and $E_{prot}$, followed by E316L, E308H and E308L. The corrosion behavior follows in the same order and is consistent with the immersion CPT results.

7. Based on the immersion CPT and CCT methodologies and the cyclic polarization techniques it is clear that the use of the cyclic polarization testing is recommended for optimum definition of the effect of fissures on corrosion.

8. Cyclic polarization testing method is not comprehensive to evaluate the corrosion behavior when $E_{prot}$ is considered for the different materials with large differences of anodic current density and $E_{pit}$.

9. The corrosion test results from immersion corrosion testing and cyclic polarization testing reveal that pitting preferentially initiates at the tips of microfissures for fissure-containing samples and along the fusion line as well as in the overlapped HAZ for fissure-free samples.

10. Preferential corrosion attack, observed during immersion testing in ferric chloride and cyclic polarization testing in 3.5% sodium chloride, was from austenite instead of ferrite.

11. Manganese content has a quite different effect on 308 and 316, a great effect on CCT than CPT for 308L and 308H, and little effect on 316L and 316H.

### C. Mechanical Behavior

1. Tensile testing and pre-strain tensile testing of E308L and E316L weld deposits with and without microfissures were carried out. The result shows that microfissures can affect the ductility of 316L and especially of 308L and there is little effect on strength properties.

2. The fracture of modified E308L exhibited a flat transverse break bounded by a narrow shear lip, meanwhile, modified E316L exhibited a classic cup-and cone rupture.

### D. Fatigue Behavior

1. Fatigue testing of E308L and E316L weld metal samples with and without microfissures was conducted. Microfissures act as stress raisers in the weld metals and greatly decrease the fatigue properties of E308L and E316L weld metal samples.

2. The fracture evaluation in SEM shows that the failure initiation site in microfissure-containing sample was from the microfissures with hot cracking characteristic, and from secondary cracking for fissure-free sample.

## E Creep Behavior

1. The creep test results reveled that modified E316H with 0 FN (fissure-containing deposits) have superior creep resistance, followed by commercial E316H and E308H, the modified 308H with 0 FN (fissure-containing) samples showed the poorest performance.

2. $M_{23}C_6$ carbides evolved from modified E308H and E316H weld coupons after creep testing when their Ferrite Numbers are 0 in as-welded samples. The majority of the carbides in modified 316H (FN = 0) in the range of 0.2-0.4$\mu$m distribute in a chain of discrete globular $M_{23}C_6$ along the sub-structure and grain boundaries while the carbides in modified E308H weld coupon (FN = 0) distribute in a random order.

3. Sigma phase can be detected in commercial E316H and E308H samples after creep test. More sigma phase formed in commercial E316H weld deposits than commercial E308H because of the difference in molybdenum content.

4. Carbides evolved in a chain effectively retard the movement of dislocation which results in the higher creep properties of modified E316H fissure-containing sample than fissure-free. Fissure-containing modified E308H has a lower creep strength than fissure-free commercial sample because of the propagation paths provided by fissures and the reduced effect on the randomly distributed carbides.

5. Creep strength of austenitic stainless weld metals is as a function of ferrite: secondary cracking caused by sigma phase (high ferrite content) is a main factor in effecting creep properties for E316H deposits, and the microfissures to E308H deposits (low ferrite content).

6. The test results for commercial E308H and E316H are consistent with the database for 308 and 316 welds.

7. Ferrite Number shows a linear relationship with Larson Miller Parameter after creep testing.

# CHAPTER 6
# FUTURE WORK

1. Develop austenitic stainless steel electrodes with low ferrite content and high hot cracking resistance.

2. Modeling the effect of secondary cracking on creep behavior of austenitic stainless steel weld metals at elevated temperature for a long term service.

# REFERENCES

1. J. R. Davis, Stainless Steels, ASM Specialty Handbook, 1996.

2. H. C. Campbell and R. D. Thomas, Jr, “The effect of alloying elements on the tensile properties of 25-20 weld metal,” Welding J., November 1946, 760s-768s.

3. J. C. Boland and R. N. Younger, “Some Aspects of Cracking in Welded Cr-Ni Austenitic Steels,” British W. J., Jan. 1960, pp. 22-59.

4. Leonard P. Conner, Welding Handbook, Volume 1, Welding Technology, Eight Edition, Third Printing, 1991, pp. 360.

5. Klaus Wilken and Horst Kleistner, “The Classification and Evaluation of Hot Cracking Tests for Weldments,” Welding in the world, 7/8, pp. 37-48, 1990.

6. “Review of experience with the longitudinal bend test (LBT) for microfissuring susceptibility of deposited weld metal,” Welding in the World, July/August 1995, pp.307-326.

7. Helmut Thielsch, “Examination of Type 316 Stainless Steel Weld Deposits for Microfissuring and Delta Ferrite Contents for the Oconee Nuclear Power Station,” Duke Power Company, Technical Report, No., 1057, Dec., 23, 1972.

8. T. G. Gooch and J. Honeycombe, “Welding Variables and Microfissuring in Austenitic Stainless Steel Weld Metal,” Welding J., August 1980, 233s-241s.

9. H. C. Burghard, E. B. Norris, A. G. Pickett, and P. D. Watson, “Investigation of the Properties of Type 316 Stainless Steel Weldments Containing Austenitic Microfissures,” Technical Report, August 15, 1971.

10. C. D. Lundin and D. F. Spond, "The Nature and Morphology of Fissures in Austenitic Stainless Weld Metal," Welding J., 55 (11), 356s-367s (1976).

11. C. D. Lundin and C. P. D. Chou, "Hot Cracking Susceptibility of Austenitic Stainless Steel Weld Metals," WRC Bulletin, 289, Nov. 1983.

12. W. C. Chen, S. T. Mandzies, and A. W. Marshall, “Microfissure Susceptibility Study of A Multipass Weldment Using SICO Testing,” Trends in Welding Research, Proceedings of the 5th International Conference, pp.739-744.

13. J. Honeycombes and T. G. Gooch, “Microcracking in Fully Austenitic Stainless Steel Weld Metal,” Metal Construction and British Welding Journal, September, 1970, pp. 375-380.

14. C. D. Lundin, W. F. DeLong, and D. F. Spond, “Ferrite-fissuring Relationship in Austenitic Stainless Steel Weld Metals,” Welding J. 54(8) pp. 241s-246s, 1975

15. C. D. Lundin and C. P. D. Chou, “Fissuring in the “Hazard HAZ” Region of Austenitic Stainless Steel Welds,” Welding J., April, 1985, pp.113s-118s.

16. Helmut Thielsch, "Cracks and microfissures-base meals," Welding Engineer, June 1967, pp. 80-85.

17. T. G. Gooch and J. Honeycombe, “Microcracking in Fully Austenitic Stainless Steel Weld Metal,” Metal Construction, Sep.1970, pp.375-380.

18. R. David Thomas, Jr. and Robert W. Messler, Jr., "Welding Type 347 Stainless Steel," WRC Bulletin 421—May 1977.

19. R. G. Baker, “Weld Cracking—A Modern Insight,” British W. J., June 1968, pp. 283-295.

20. R. G. Baker and R. P. Newman, “Cracking in Welds,” Metal Construction and British Welding Journal, Feb. 1969, pp. 1-4.

21. B. Hemsworth, T. Boniszewski, and N. F. Eaton, “Classification and Definition of High Temperature Welding Cracks in Alloys,” Metal Construction and British Welding Journal, Feb. 1969, pp. 5-15.

22. Metals Handbook, Nine Edition, Volume 13, Corrosion, pp. 348-349.

23. Robert W. Messler, Jr., “Joining of Advanced Materials,” 1993, pp. 272.

24. C. D. Lundin and S. Katayama, “Review of weldment hot cracking,” Technical Report.

25. J. C. Lippold and W. F. Savage, “Solidification of Austenitic Stainless Steel Weldments: Part III-The Effect of Solidification Behavior on Hot Cracking Susceptibility,” Welding J., Dec. 1982, 388s-396s.

26. J. C. Lippold, and W. A. Baeslack III and I. Varol, “Heat Affected Zone Liquation Cracking in Austenitic and Duplex Stainless Steels," Welding J., Jan. 1992, 1s-14s.

27. H. Fredriks and L. J. van der Toorn, "Hot Cracking in Austenitic Stainless Steel Weld Deposits," British Welding J., April 1968, pp.178-182.

28. F. C. Hull, “Effect of Delta Ferrite on the Hot Cracking of Stainless Steel,” Welding J., 46(9): 339s-409s, 1967.

29. J. C. Lippold, “Solidification Behavior and Cracking Susceptibility of Pulse-Laser Welds in Austenitic Stainless Steels,” Welding J., June 1994, 129s-139s.

30. V. Shankar, T. P. S. Gill, S. L. Mannan and S. Sundaresan, “Evaluation of Hot Cracking in Nitrogen-bearing and Fully Austenitic Stainless Steel Weldments,” Welding J., May 1988, 193s-201s.

31. M. J. Cieslak, A. M. Ritter, and W. F. Savage, "Solidification Cracking and Analytical Electron Microscope of Austenite Stainless Steel Weld Metal," Welding J., Jan. 1982, 1s-8s.

32. V. P. Kujanpaa, N. J. Suutala, T. K. Takalo and T. J. I. Moisio, "Solidification Cracking-estimation of the susceptibility of austenitic and austenitic-ferrite stainless steel welds," Metal Construction, June 1980, pp. 282-285.

33. Kujanpaa, V. P., David, S. A., and White, C. L. "Characteriztion of Heat-affect Zone Cracking in Austenitic Stainless Steel Welds," Welding J., 66 (8): 221s-.

34. V. P. Kujanpaa, S. A. David and C. L. White, “Formation of Hot Cracks in Austenitic Stainless Steel Welds—Solidification Cracking,” Welding J., August 1986, 203s-212s.

35. J. A. Brooks, A. W. Thompson, and J. C. Willams, “A fundamental Study of the Beneficial Effects of Delta Ferrite in Reducing Weld Cracking,” Welding J., March 1984, 71s-83s.

36. V. P. Kujanpaa, “Effects of Steel Type and Impurities in Solidification Cracking of Austenitic Stainless Steel Welds,” Metal Construction, Jan. 1985, pp. 22-28.

37. P. Bilmes, A. Gonzalez, C. Llorente, and M. Solari, “Effect of Ferrite Solidification Morphology of Austenitic Stainless Steel Weld Metal on Properties of Welded Joints,” Welding Research Abroad, Vol. XLIII No. 2, Feb. 1997, pp.18-29.

38. H. Tamura, T. Onzawa, A. Takasaki, and T. Takatori, “Effect of Ferrite on Low Temperature Toughness of Type 316L Austenitic Stainless Steel Weld Metal,” Welding Research Abroad, Vol. XXXVI No. 10, Oct. 1990, pp.2-8.

39. C. D. Lundin, C. P. D. Chou and C. J. Sullivan, “ Hot Cracking Resistance of Austenitic Stainless Steel Weld Metals,” Welding J. August 1980, 226s-232s.

40. T. Ogawa and E. Tsunetomi, “Hot Cracking Susceptibility of Austenitic Stainless Steel,” Welding J., March 1982, 82s-93s.

41. J. M. Vitek and S. A. David, "The Effect of Cooling Rate on Ferrite in Type 308 Stainless Steel Weld Metal," Welding J., May 1988, 95s-102s.

42. J. W. Elmer, S. M. Allen and T. W. Eager, “The influence of cooling rate on the ferrite content of stainless steel alloys,” Proceedings of the 2nd international conference on trends in welding research, Gatlinburg, Tennessee, USA, 14-18, May, 1989.

43. S. A. David, J. M. Vitek, and T. L. Hebble, “Effect of Rapid Solidification on Stainless Steel Weld Metal Microstructures and Its Implications on the Schaeffler diagram,” Welding J., 1987, 66(10): 289-s.

44. N. Suutala, T. Takalo, and T. Moisio, “The Relationship Between Solidification and Microfissure in Austenitic and Austenitic-Ferritic Stainless Steel Welds,” Metallurgical Transactions, April 1979, pp. 512-514.

45. S. A. David, “Ferrite Morphology and variations in Ferrite Content in Austenitic Stainless Steel Welds,” Welding J., Vol. 60, 1981, pp. 63s-71s.

46. A. L. Schaeffler, “Constitution diagram for stainless steel weld metal,” Metal Process, Vol. 56 (No. 11), 1949, pp. 680-680B.

47. W. T. DeLong, “Ferrite in austenitic stainless steel weld metal,” Welding J., Vol. 53 (No. 7), 1974, pp. 273s-286s.

48. C. N. McCowan, T. A. Siewert, and D. L. Olson, “Stainless steel weld metal: Prediction of Ferrite content,” WRC Bulletin 342, Welding Research Council, 1989.

49. D. J. Kotecki and T. A. Siewert, “WRC-1992 Constitution Diagram for Stainless Steel Weld Metals: A Modification of the WRC-1998 Diagram,” Welding J., Vol. 71 (No. 5), 1992, pp. 171s-178s.

50. David Rozet, Hallock C. Campebell and R. David Thomas, Jr., “Effect of Weld Metal Composition on the Strength and Ductility of 15%Cr-35%Ni Welds,” Welding J., Octomber 1948, pp. 481s-491s.

51. T. Takalo, N. Suutala and T. Moisio, “Austenitic Solidification Mode in Austenitic Stainless Steel Welds, “Metall. Trans., Vol. 10A, 1979, pp. 1173-1181.

52. Nakao Y., Nishimoto, K. and Zhang, W., “Effect of Rapid Solidification by Laser Surface on Solidification Modes and Microstructures of Stainless Steels,” Trans., JWS, 1988.

53. Kujanpaa, V., Suutala, N., Takalo, T., and Moisio, T. “Correlation Between Solidification Cracking and Microstructure in Austenitic and Austenitic-ferritic Stainless Steel Welds,” Welding Research Int., 9(2):55, 1979.

54. J. F. Lancaster, “Meatallurgy of Welding,” Third edition 1980, pp. 184.

55. D. M. Haddrill, and R. G. Baker, “Microcracking in Austenitic Weld Metal,” British Welding. J., August 1965, pp. 411-419.

56. S. Polgary, “The Influence of Silicon Content on Cracking in Austenitic Stainless Steel with Particular Reference to 18Cr-8Ni Steel,” Metal Construction, 1969, 93-97.

57. T. G. Gooch and J. Honeycombe, “Microcracking in Fully Austenitic Stainless Steel Weld Metal,” Metal Construction, March 1975, pp. 1-7.

58. J. Honeycombe and T. G. Gooch, “Effect of Manganese on Cracking and Corrosion Behavour of Fully Austenitic Stainless Steel and Weld Metal,” Metal Construction and British Welding Journal, 456-460, 1972.

59. K. B. K. Joseph, “New Stainless Filler Withstands Hot Cracking,” Welding Design & Fabrication, Septemper, 1980, pp. 103-105.

60. C. D. Lundin, V. Osorio, C. H. Lee and R. Menon, “Weldability of Nuclear Grade Stainless Steels,” Final Report, September 1986.

61. N. M. Novozhilov, et al, "On the Austenitising and Ferritising Effect of Elements in Austenitic Ferritic Weld Metals," Welding Research Abroad, Vol. XXVI No. 3, March 1980, pp. 60-62.

62. C. P. Chou and I. T. Chen, “Effect of Nitrogen on the Weldability of austenitic Stainless Steel Weld Metals,” Proceedings of the 2th International Conference on Trends in Welding Research, Gatlimburg, Tennessee, USA, 14-18 May 1989.

63. Y. Arata, F. Matsuda and S. Saruwatan, "Solidification Crack Susceptibility in Weld Metals of Fully Austenitic Stainless Steels (Report II)," Welding Research Abroad, Vol. XXIV No 1, Jan. 1978.

64. C. H. Lee, “Weldability and Microstructure Analysis of Nuclear Grade Austenitic Stainless Steel,” Ph. D Dissertation, The University of Tennessee, Knoxville December 1988.

65. T. Ogawa and K. Suzuki, and T. Zaizen, “The Weldability of Nitrogen Containing Austenitic Stainless Steel: Part II-Porosity, Cracking and Creep Properties,” Welding J., July 1984, 212s-223s.

66. C. D. Lundin, C. H. Lee and Y. P. Qiao, “Weldability and Hot Ductility Behavior of Nuclear Grade Austenitic Stainless Steels,” Final Report, December 1988.

67. H. Guo, M. C. Chaturvedi, and N. L. Richards, “Effect of B on Microfissing Susceptibility of Inconel 718,” Trends in Welding Research, Proceedings of the 5th International Conference, pp.763-768.

68. Thomas, R. D. Jr, ”HAZ Cracking in Thick Section of Austenitic Stainless Steel-Part II,” Welding J., 63 (12), 1984, pp. 335s-368s.

69. R. D. Buchiet, C. E. Jaske, and R. W. Bennett, "Laboratory Studies of Type 316 Stainless Steel Weldmental from Maine Yankee Reactor Coolant Systems," Sept. 17, 1971.

70. W. Lin, T. W. Nelson, J. C. Lippold and W. A. Baeslack III, “A Study of the HAZ Crack Susceptibility Region in Alloy 625, “Proceedings of the 3rd International Conference on Trend in Welding Research, Gatlimburg, Tennessee, USA, June 1-5, 1992.

71. C. D. Lundin, C. D. Delong, W. T., and Spond, D. F., "The Fissure Bend Test," Welding J., 55(6), 145s-151s (1976).

72. K. Wilken, “Investigation to Compare Hot Cracking Tests-Externally Loaded Specimen,” IIW Document: IX-1945-99.

73. Kotecki J. Damian, “Volumetric Microfissure Determination in Fully Austenitic Stainless Steel Weld Metal,” IIW Document IX-H-302-94.

74. W. F. Savage and C. D. Lundin, “The Varestraint Teat,” Welding J., 1965, 44(10): 433s-442s.

75. C. D. Lundin, A. G. Lingenfelter, G. E. Grotke, G. G. Lessmann and S. J. Matthews, “The Varestraint Tests,” WRC Bulletin 280, August 1982.

76. C. D. Lundin, C. Y. P. Gill and W. Ren, “The Hot Ductility and Hot Cracking Behavior of Modified 316 Stainless Steels Designed for High Temperature Service,” ORNL/Sub/88-07685/01, July 20, 1989.

77. J. C. Lippold, “Weld Cracking Mechanisms in Austenitic Stainless Steels,” Proceedings of a Conference Sponsored by the Joining Division of American Society for Metals, New Orleans, Louisiana, 16-18 Nov. 1988.

78. C. D. Lundin and C. Y. P. Qiao, “Weldability of Modified 800H Alloy,” Technical Report, ORNL/Sub/88-07685/04, June 1994.

79. C. D. Lundin, C. Y. P. Qiao, C. H. Lee and C. M. Goodwin, “Evaluation of Hot Cracking Susceptibility of Nuclear Grade Austenitic Stainless Steel by Four Hot Cracking Test Methods, “Proceedings of the 2th International Conference on Trends in Welding Research, Gatlimburg, Tennessee, USA, 14-18 May 1989.

80. H. S. Ferguson, “Dynamic Thermal,” 2nd Edition, Dynamic System, Inc., 1987.

81. Welding Research Council, High Alloys Committee Meetings Minutes of May 18, 2000, Rensselaer Polytechnic Institute, Troy, NY.

82. R. Gunia and G. Ratz, “The Measurement of Delta Ferrite in Austenitic Stainless Steels,” WRC Bulletin, No. 132 August 1968.

83. R. D. Wylie, McDonald, J. Jr., and A. L. Lowenberg, “Weld Deposited Cladding of Pressure Vessels,” British Welding Journal, pp. 78-93, Aug. 1965.

84. A. Baggerud, A proceedings on “Welding Dissimilar Metals,” Droitwich, May 1969, Welding Institute.

85. J. Honeycombes and T. G. Gooch, “The Effect of Microfissures Upon the Mechanical Properties of Austenitic Stainless Steel Weld Metals,” Metal Construction and British Welding Journal, April, 1973, pp.140-147.

86. Sigrid Bauer and Notre Ref, “Influence of Microcracks in Welds in Fully Austenitic Materials and Nickel-base alloys,” Doc. IX-H-247/91.
87. T. A. Whipple, H. I. McHenry and D. T. Read, “Fracture Behavior of Ferrite-Free Stainless Steel Welds in Liquid Helium, “Welding J., April 1981, 72s-78s.

88. Andrew Garner, “How Stainless Steel Welds Corrode, ”Metal Progress, Vol. 127 (No. 5) April 1985, pp. 31.

89. C. D. Lundin, “ Grant-in-aid Request To Evaluate the Effect of Microfissures on the Mechanical Properties of Austenitic Stainless Steel Weld Metals,” Proposal, April 1997.

90. ASTM Designation: E963-95, Standard Practice for Electrolytic Extraction of Phase from Ni and Ni-Fe Base Superalloys Using a Hydrochloric-Methanol Electrolyte.

91. M. J., Cieslak, A. M. Ritter and W. F. Savage, “Solidification Cracking and Analytical Electron Microscopy of Stainless Steel Weld Metals,” Welding J., 61, Suppl., 1s-8s (1982).

92. Lokanath Patel, "The Effect of Carbon on the Formation of Sigma phase in Austenitic Stainless Steel," Master Thesis, The University of Tennessee, 1981, p81.

# APPENDIXES

# APPENDIX A: TABLES

Table 1.1 Chemical Compositions of E308L Weld Deposits

| Element | EM308L | E308L-A | E308L-B | E308L-C | E308L-D | EC308L | AWS Specification |
|---|---|---|---|---|---|---|---|
| C | 0.020 | 0.020 | 0.024 | 0.025 | 0.022 | 0.030 | 0.04 |
| Mn | 0.63 | 1.62 | 1.64 | 1.55 | 1.66 | 0.61 | 0.5-2.5 |
| P | 0.032 | — | — | — | — | 0.025 | 0.04 |
| S | 0.021 | — | — | — | — | 0.019 | 0.04 |
| Si | 0.33 | 0.38 | 0.37 | 0.32 | 0.41 | 0.30 | 0.9 |
| Cr | 18.19 | 18.40 | 18.48 | 19.05 | 19.09 | 18.86 | 18.0-21.0 |
| Ni | 10.78 | 10.80 | 10.97 | 10.05 | 10.32 | 10.09 | 9.0-11.0 |
| Mo | 0.07 | — | — | — | — | 0.05 | 0.75 |
| N | 0.10 | — | — | — | — | 0.11 | — |
| Nb | <0.01 | — | — | — | — | <0.01 | — |
| Ta | 0.01 | — | — | — | — | <0.01 | — |
| Cu | 0.12 | — | — | — | — | 0.04 | 0.75 |
| Ti | 0.035 | — | — | — | — | 0.012 | — |
| V | 0.085 | — | — | — | — | 0.10 | — |
| Co | 0.10 | — | — | — | — | 0.02 | — |
| W | 0.02 | — | — | — | — | 0.01 | — |
| Al | — | — | — | — | — | 0.01 | — |
| B | — | — | — | — | — | <0.001 | — |
| FN | 0.22 | 0.7 | 2.6 | 4.7 | 5.5 | 7.3 | — |

Note:

M308L: Modified E308L, from Lincoln Electric Company

308L-A: AP-5-08L-A-2, 1976 Fissure Bend Program

308L-B: AP-5-08L-B-2, Fissure Bend Test Program

308L-C: AP-5-08L-C-2, Fissure Bend Test Program

308L-D: AP-5-08L-D-1, Fissure Bend Test Program

C308L, Commercial E308L, Lincoln Electric Company

FN: Ferrite Number

Table 1.2 Chemical Compositions of E316L Weld Deposits

| Element | M316L | F316L | 316L-A | 316L-B | 316L-D | KK316L | C316L | AWS Specification |
|---|---|---|---|---|---|---|---|---|
| C | 0.031 | 0.042 | 0.035 | 0.038 | 0.037 | 0.021 | 0.026 | 0.04 |
| Mn | 0.82 | 0.812 | 1.85 | 2.24 | 1.87 | 2.28 | 0.71 | 0.5-2.5 |
| P | 0.038 | 0.016 | 0.008 | 0.022 | 0.015 | 0.024 | 0.021 | 0.04 |
| S | 0.021 | 0.005 | 0.015 | 0.010 | 0.010 | 0.010 | 0.006 | 0.03 |
| Si | 0.32 | 0.632 | 0.40 | 0.48 | 0.46 | 0.32 | 0.29 | 0.9 |
| Cr | 17.36 | 18.635 | 17.88 | 17.30 | 18.60 | 18.02 | 17.34 | 17.0-20.0 |
| Ni | 12.89 | 12.998 | 13.07 | 12.40 | 11.64 | 13.64 | 12.00 | 11.0-14.0 |
| Mo | 2.26 | 2.041 | 2.15 | 2.25 | 2.12 | 2.23 | 2.42 | 2.0-3.0 |
| N | 0.10 | — | 0.047 | 0.044 | 0.047 | 0.044 | 0.029 | |
| Nb | <0.01 | — | — | 0.01 | — | — | — | |
| Ta | <0.01 | — | — | 0.01 | — | — | — | |
| Cu | 0.14 | 0.130 | — | 0.08 | — | — | 0.13 | 0.75 |
| Ti | 0.016 | 0.019 | — | 0.018 | — | — | — | — |
| V | 0.055 | 0.083 | — | 0.065 | — | — | — | — |
| Co | 0.07 | — | — | 0.13 | — | — | — | — |
| W | 0.02 | — | — | 0.07 | — | — | — | — |
| Al | — | 0.026 | — | — | — | — | — | — |
| | | | | | | | | |
| FN | 0.17 | 0.34 | 0.38 | 1.17 | 7.62 | 1.2 | 4.4 | — |

Note:

M316L: Modified E316L, Lincoln Electric Company

EF316L: Modified E316L, Hoboart

E316L-A: TM-6-16L-A-2, Fissure Bend Program

E316L-B: TM-2-16L-B-2, Fissure Bend Test Program

E316L-D: TM-2-16L-D-1, Fissure Bend Test Program

KK: Kryo-Kay 316L, “Weld Metal Fissuring Tendency of Kryo-Kay 316L-15”

C316L, Commercial E316L, Lincoln Electric Company

FN: Ferrite Number

Table 1.3 Chemical Compositions of E308H and E316H Weld Deposits

| Element | Commercial 308H | Modified 308H | Commercial 316H | Modified 316H | AWS Specification (E308H) | AWS Specification (E316H) |
|---|---|---|---|---|---|---|
| C | 0.074 | 0.057 | 0.054 | 0.065 | 0.04-0.08 | 0.04-0.08 |
| Mn | 1.23 | 0.93 | 1.6 | 1.23 | 0.5-2.5 | 0.5-2.5 |
| P | 0.037 | 0.037 | 0.028 | 0.038 | 0.04 | 0.04 |
| S | 0.010 | 0.010 | 0.006 | 0.011 | 0.03 | 0.03 |
| Si | 0.39 | 0.29 | 0.44 | 0.43 | 0.9 | 0.9 |
| Cr | 18.74 | 17.59 | 18.76 | 17.40 | 18.0-21.0 | 17.0-20.0 |
| Ni | 10.69 | 10.70 | 12.02 | 13.47 | 9.0-11.0 | 11.0-14.0 |
| Mo | 0.24 | 0.25 | 2.34 | 2.22 | 0.75 | 2.0-3.0 |
| N | 0.13 | 0.25 | 0.040 | 0.13 | — | — |
| Nb | 0.01 | <0.01 | 0.01 | 0.01 | — | — |
| Ta | <0.01 | <0.01 | <0.01 | <0.01 | — | — |
| Cu | 0.24 | 0.24 | 0.21 | 0.15 | 0.75 | 0.75 |
| Ti | 0.016 | 0.015 | 0.01 | 0.02 | — | — |
| V | 0.086 | 0.072 | 0.07 | 0.096 | — | — |
| Co | 0.13 | 0.13 | 0.21 | 0.06 | — | — |
| W | 0.01 | 0.02 | — | 0.02 | — | — |
| Al | 0.01 | <0.01 | — | 0.01 | — | — |
| B | <0.001 | <0.01 | — | <0.001 | — | — |
| | | | | | | |
| FN | 5.7 | 0 | 4.5 | 0 | — | — |

Note:

EM308HL: Modified E308H, from ESAB

Commercial E308H, from ESAB

Commercial E316H, from ESAB

Modified E316H, from ESAB

Table 2. Welding Conditions

| Current (A) | Voltage (V) | Travel speed (mm/min.) | No. of layers | Interpass Temp. (°C) | Heat Input (kJ/mm.) |
|---|---|---|---|---|---|
| 95 | 23 | 203 | 3 | 94 | 0.7 |

Table 3 Corrosion Test Results and Microfissure Density on Test Pad surface

| Sample ID | FN | Fissure Density Fissures/cm$^2$ | CPT (°C) | CCT (°C) | Solution |
|---|---|---|---|---|---|
| M308L | 0.22 | 40 | <0 | 40 | 1% $FeCl_3$ |
| E308L-A | 0.70 | 1.6 | 10 | 50 | 1% $FeCl_3$ |
| E308L-B | 2.55 | 0.27 | 10 | 50 | 1% $FeCl_3$ |
| E308L-C | 4.7 | 0 | 65 | 55 | 1% $FeCl_3$ |
| E308L-D | 6.0 | 0 | 75 | 65 | 1% $FeCl_3$ |
| C308L | 7.3 | 0 | 65 | 20 | 1% $FeCl_3$ |
| $M316L_1$ | 0.17 | 12 | <0 | 35 | 3% $FeCl_3$ |
| $M316L_2$ | 0.34 | 4.0 | 30 | 75 | 3% $FeCl_3$ |
| TM-6-16L-A-2* | 0.38 | 0.5 | 65 | 75 | 3% $FeCl_3$ |
| TM-12-16L-A-2* | 0.47 | 0.5 | 65 | 75 | 3% $FeCl_3$ |
| TM-2-16L-B-1* | 0.86 | 0.16 | 75 | 65 | 3% $FeCl_3$ |
| TM-6-16L-B-1* | 1.17 | 0.16 | 75 | 70 | 3% $FeCl_3$ |
| Kryo-Kay-316L* | 1.2 | 0.12 | 80 | 75 | 3% $FeCl_3$ |
| C316L | 4.76 | 0 | 65 | 85 | 3% $FeCl_3$ |
| TM-2-16L-D-1* | 7.62 | 0 | 80 | 75 | 3% $FeCl_3$ |
| M308H | 0 | 7.9 | <0 | 5 | 6% $FeCl_3$ |
| C308H | 5.7 | 0 | 75 | 25 | 6% $FeCl_3$ |
| M316H | 0 | 5.9 | <0 | 80 | 6% $FeCl_3$ |
| C316H | 4.5 | 0 | 85 | 75 | 6% $FeCl_3$ |

Note:

1. The sample IDs with * in Table 2 are followed previous project named "Fissure Bend Test" and "Weld Metal Fissuring Tendency of Kryo-Kay316L-15.
2. The pads TM-6-16L-A-2* and TM-12-16L-A-2*, TM-2-16L-B-1* and TM-6-16L-B-1* were welded by the different labs using the same kinds of electrodes named E316L-A and E316L-B respectively in Table 1-2.
3. The electrodes used for Kryo-Kay-316L and TM-2-16L-D-1 are KK316L and E316L-D respectively in Table 1-2.

Table 4. Summary of Cyclic Polarization Test Results

| Sample ID | $E_{pit}$ | Average error | $E_{prot}$ | Average error | $E_{corr}$ | Average error |
|---|---|---|---|---|---|---|
| M308L | -35 | 74 | -326 | 14 | -375 | 99 |
| 308L-A | 72 | 16 | -68 | 31 | -229 | 11 |
| 308L-B | 72 | 18 | -99 | 25 | -231 | 14 |
| 308L-C | 143 | 77 | -23 | 11 | -142 | 33 |
| 308L-D | 127 | 25 | -66 | 28 | -247 | 15 |
| C308L | 130 | 3 | -139 | 57 | -206 | 32 |
| M316L | 158 | 33 | -114 | 8 | -244 | 3 |
| F316L | 171 | 49 | -63 | 46 | -234 | 19 |
| 316L-A | 600 | 4 | -137 | 36 | -237 | 77 |
| 316L-B | 720 | 169 | -85 | 31 | -208 | 8 |
| Kryo-kay 316 | 568 | 26 | No Eprot | | -211 | 53 |
| 316L-D | 557 | 82 | -20 | 21 | -202 | 18 |
| C316L | 182 | 22 | -51 | 22 | -255 | 14 |
| M308H | 69 | 63 | -277 | 3 | -280 | 33 |
| C308H | 589 | 56 | -72 | 18 | -69 | 35 |
| M316H | 299 | 70 | -152 | 30 | -192 | 16 |
| C316H | 930 | 68 | -147 | 75 | -228 | 17 |

Table 5. Tensile Test Results

| Specimen ID | 0.2% Yield Strength, ksi | Ultimate Tensile Strength, ksi | % Elongation in 4d | % Reduction in Area |
|---|---|---|---|---|
| C316L | 61.5 | 81.1 | 31.3 | 53.8 |
| M316L | 59.6 | 82.1 | 34.4 | 57.5 |
| C308L | 58.6 | 81.8 | 46.9 | 54.3 |
| M308L | 56.2 | 77.3 | 31.3 | 54.8 |

Table 6. Pre-strain Tensile Test Results

| Specimen ID | 0.2% Yield Strength, ksi | Ultimate Tensile Strength, ksi | % Elongation in 4d | % Reduction in Area |
|---|---|---|---|---|
| C316L | 64.8 | 80.6 | 50 | 54.1 |
| M316L | 61.0 | 81.9 | 45 | 51.3 |
| C308L | 56.2 | 82.2 | 56 | 62.3 |
| M308L | 53.0 | 72.6 | 25 | 30.3 |

Table 7. Fatigue Test Results

| Specimen ID | Dynamic Stresses | | Fatigue Life, Cycles | Remarks |
|---|---|---|---|---|
| | Maximum, ksi | Minimum, ksi | | |
| C316L | 75 | 7.5 | 96331 | failed |
| | 70 | 7.0 | 53508 | failed |
| | 65 | 6.5 | 214973 | failed |
| | 65 | 6.5 | 186016 | failed |
| | 60 | 6.0 | 10000000 | Did not fail |
| | 55 | 5.5 | 10000000 | Did not fail |
| M316L | 65 | 6.5 | 87478 | failed |
| | 60 | 6.0 | 98946 | failed |
| | 55 | 5.5 | 206818 | failed |
| | 50 | 5.0 | 371567 | failed |
| | 45 | 4.5 | 355180 | failed |
| | 40 | 4.0 | 625216 | failed |
| M308L | 45 | 4.5 | 48649 | failed |
| | 40 | 4.0 | 323934 | failed |
| | 35 | 3.5 | 286495 | failed |
| | 30 | 3.0 | 970358 | failed |
| C308L | 65 | 6.5 | 10000000 | Did not fail |
| | 75 | 7.5 | 40603 | failed |

Table 8. Results of Electrolytic Extraction of Particles from Weld Deposits

| Material | Mi (g) | Mf (g) | Mr (g) | R (%) |
|---|---|---|---|---|
| M316Hbf | 10.1990 | 5.4798 | 0.0114 | 0.242 |
| M316Haf | 0.5760 | 0.1114 | 0.0050 | 1.076 |
| C316Hbf | 19.9467 | 13.4184 | 0.0383 | 0.587 |
| C316Haf | 2.1004 | 0.2789 | 0.0360 | 1.976 |
| M308Hbf | 3.7304 | 2.3709 | 0.0040 | 0.294 |
| M308Haf | 1.9611 | 0.1319 | 0.0200 | 1.093 |
| C308Hbf | 4.7813 | 1.3351 | 0.0027 | 0.078 |
| C308Haf | 1.8859 | 0.1695 | 0.0093 | 0.542 |

# APPENDIX B: FIGURES

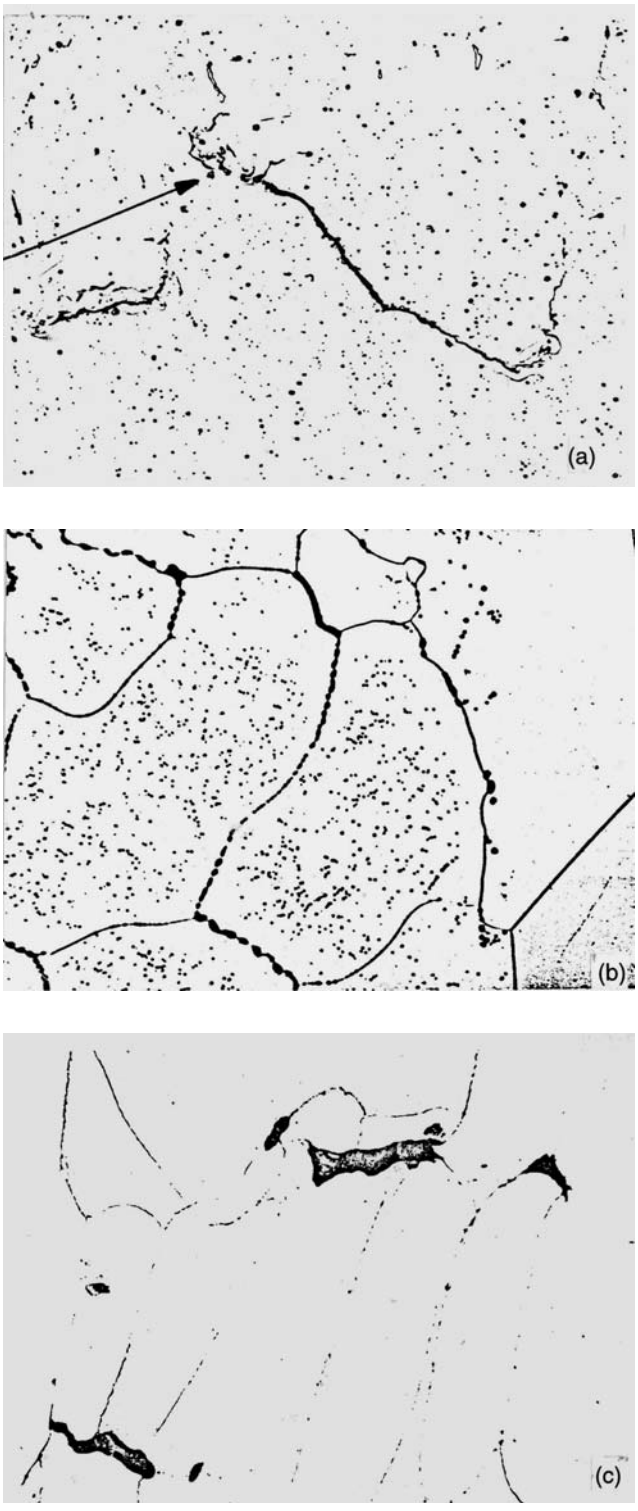


Figure 2.1 Microfissure types of indication of stainless steels,
(a) Liquated grain boundaries; (b) Voids expand into microfissures;
(c) Inclusion [7].

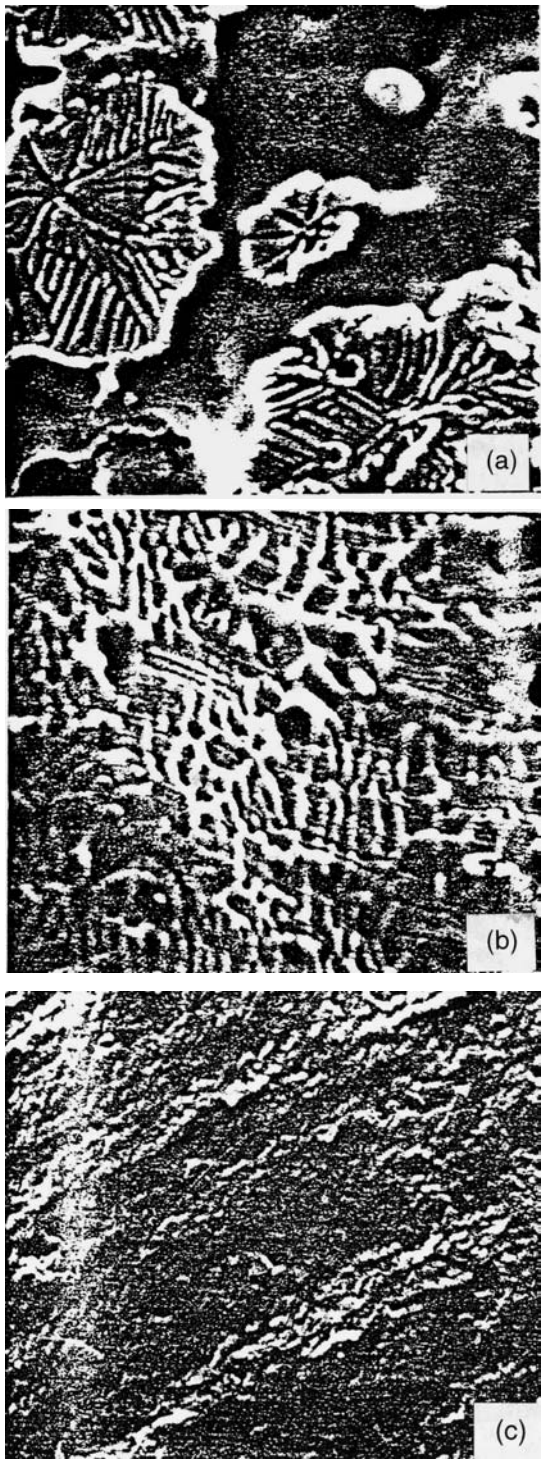


Figure 2.2 Three different microfissure fracture morphology for austenitic stainless steel weld metal, (a)-2400X; (b)-2800X, (c)-240X [12].

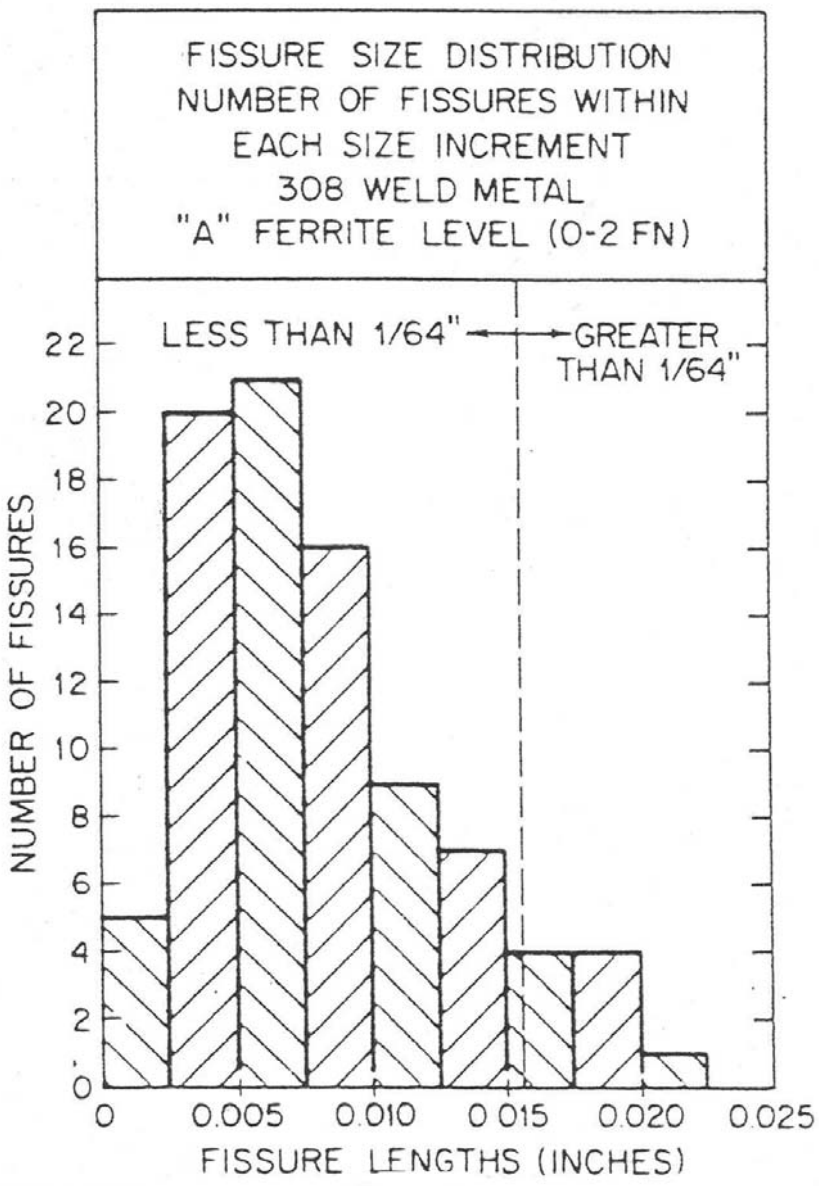


Figure 2.3 The distribution of microfissure size in 308 weld metal [13].

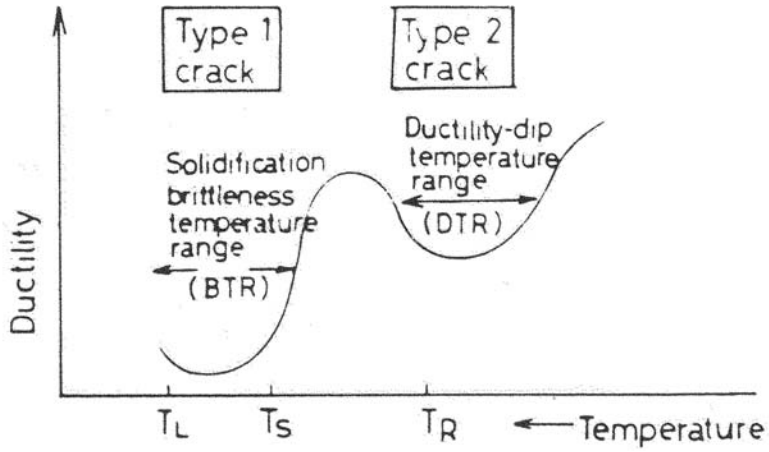


Figure 2.4 Schematic representation of ductility curve of weld metal at high temperature [21].

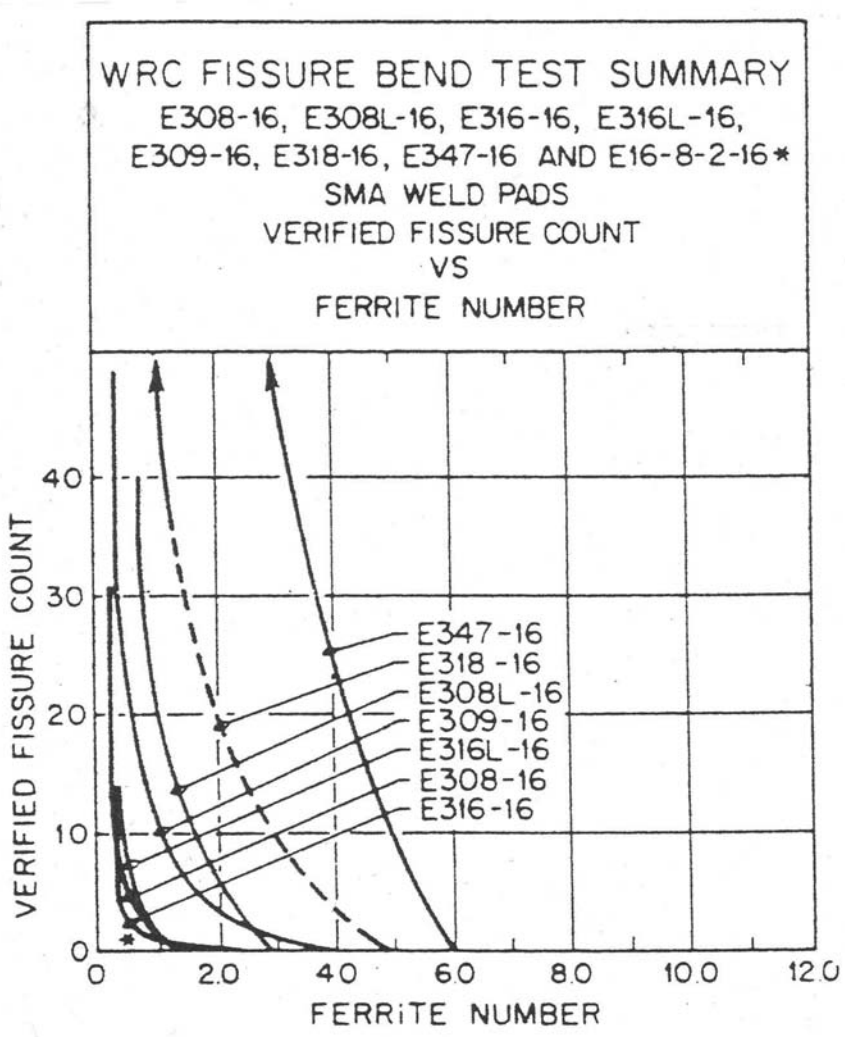


Figure 2.5 The relationship between ferrite content and fissure density [14].

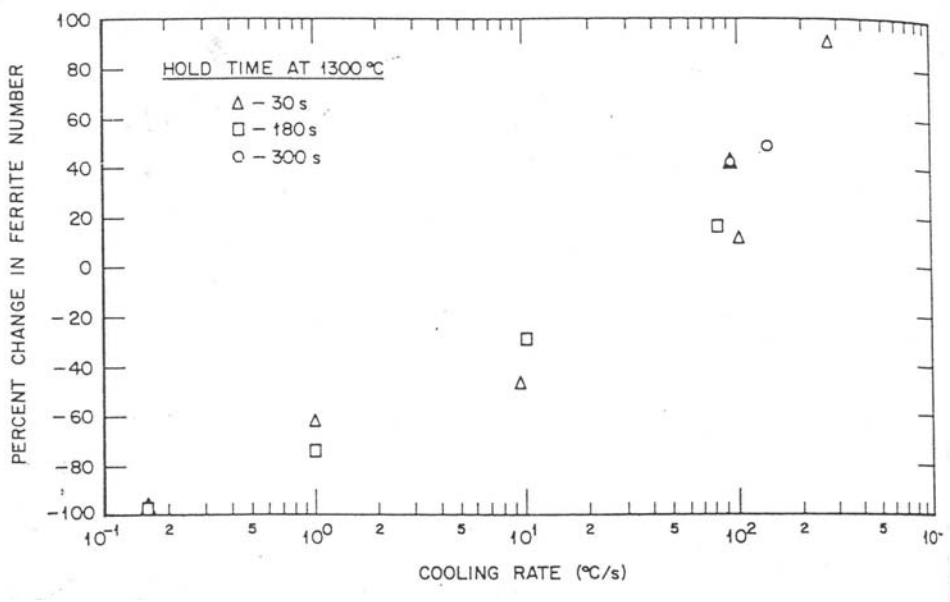


Figure 2.6 Percent change in Ferrite Number as a function of cooling rate from 1300°C.

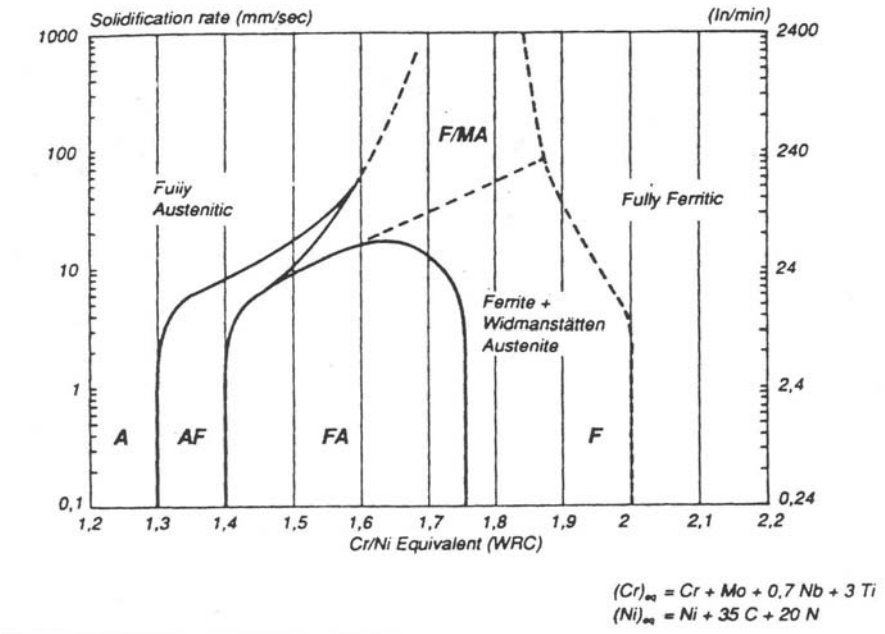


Figure 2.7 Preliminary microstructural map for austenitic stainless steel welds as a function of solidification growth rate [29].

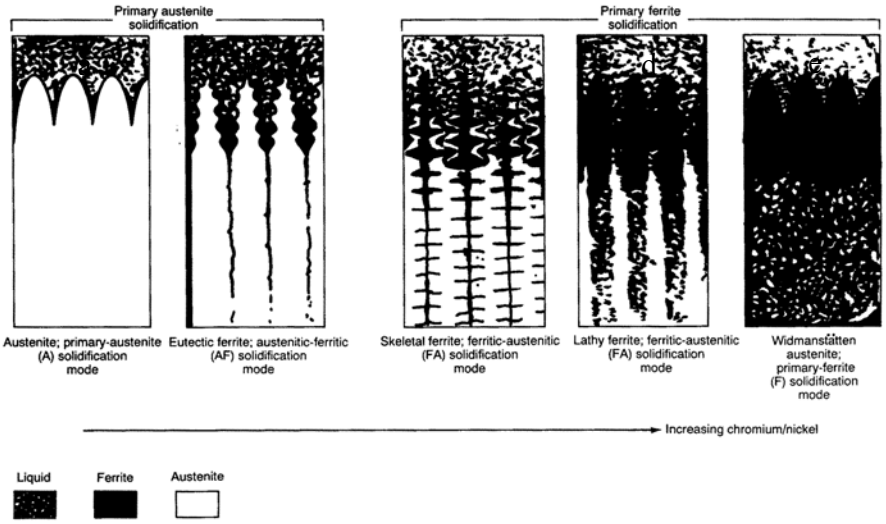


Figure 2.8 Schematic showing solidification and solid-state transformation behavior of welds with increasing $Cr_{eq}/Ni_{eq}$ ratios [29].

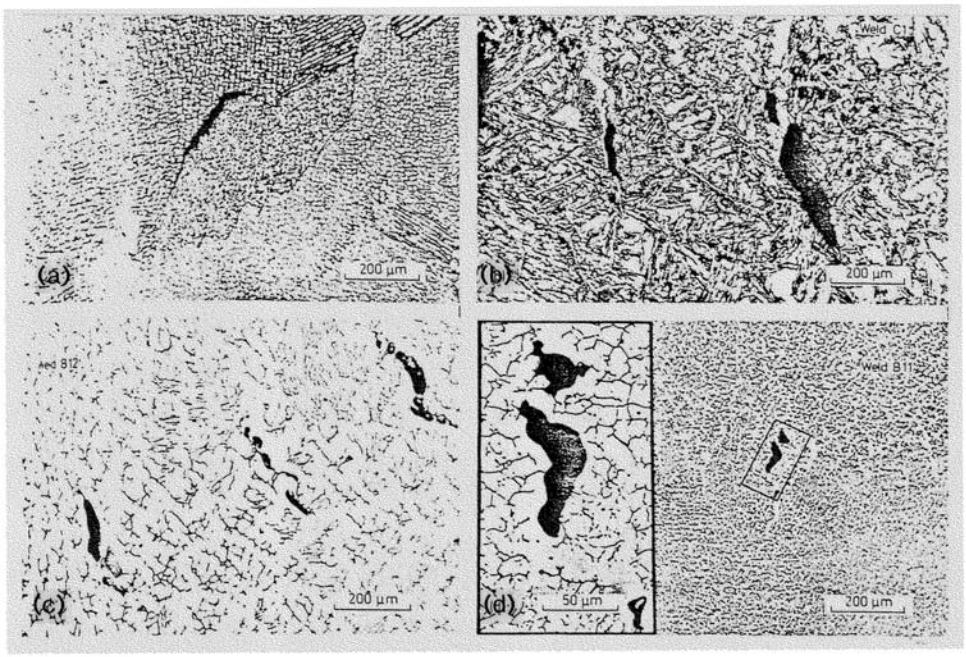


Figure 2.9 Solidification cracks
(a) Intergranular-austenitic or austenitic solidification;
(b) Intergranular-single phase ferritic solidification;
(c) Intergranular-ferritic-austenitic solidification;
(d) Transgranular-ferritic-austenitic solidification [32].

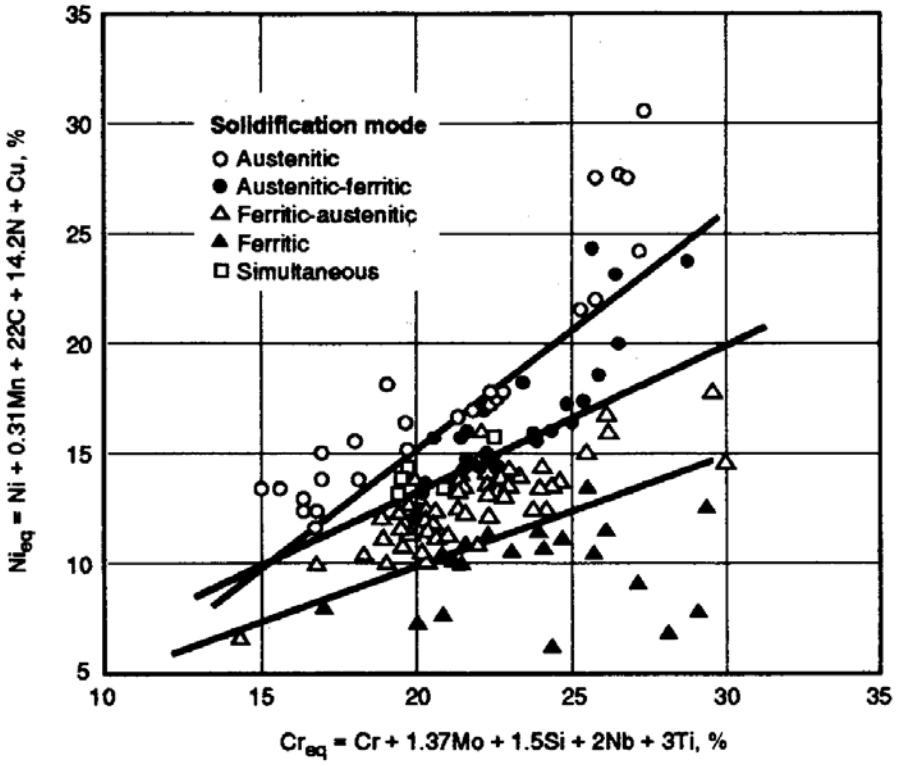


Figure 2.10 Solidification mode (experimental) for variety of compositions, compared on basis on $Cr_{eq}/Ni_{eq}$ ratio [1].

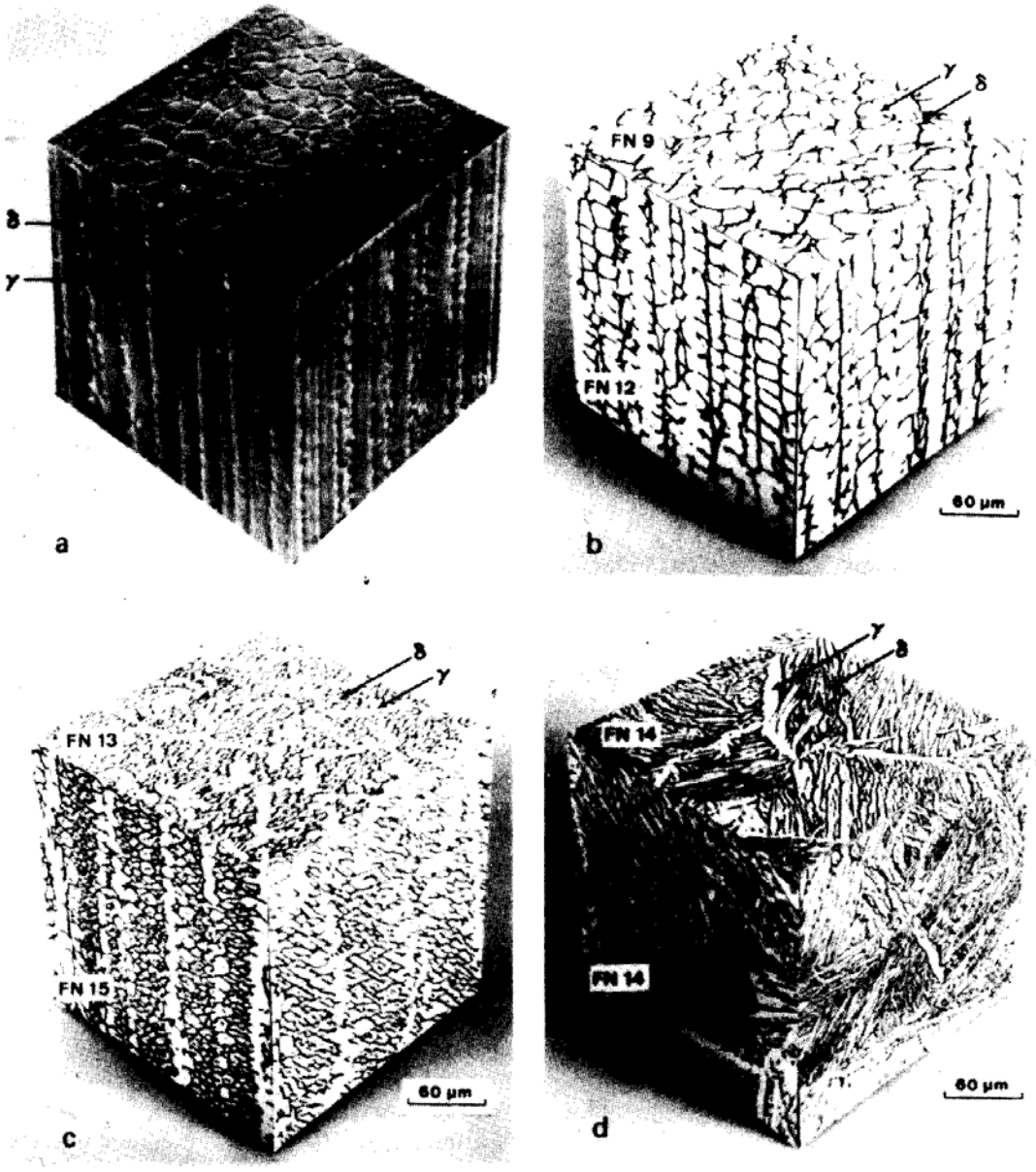


Figure 2.11 Three dimensional views of typical austenitic stainless steel weld morphologies [1].

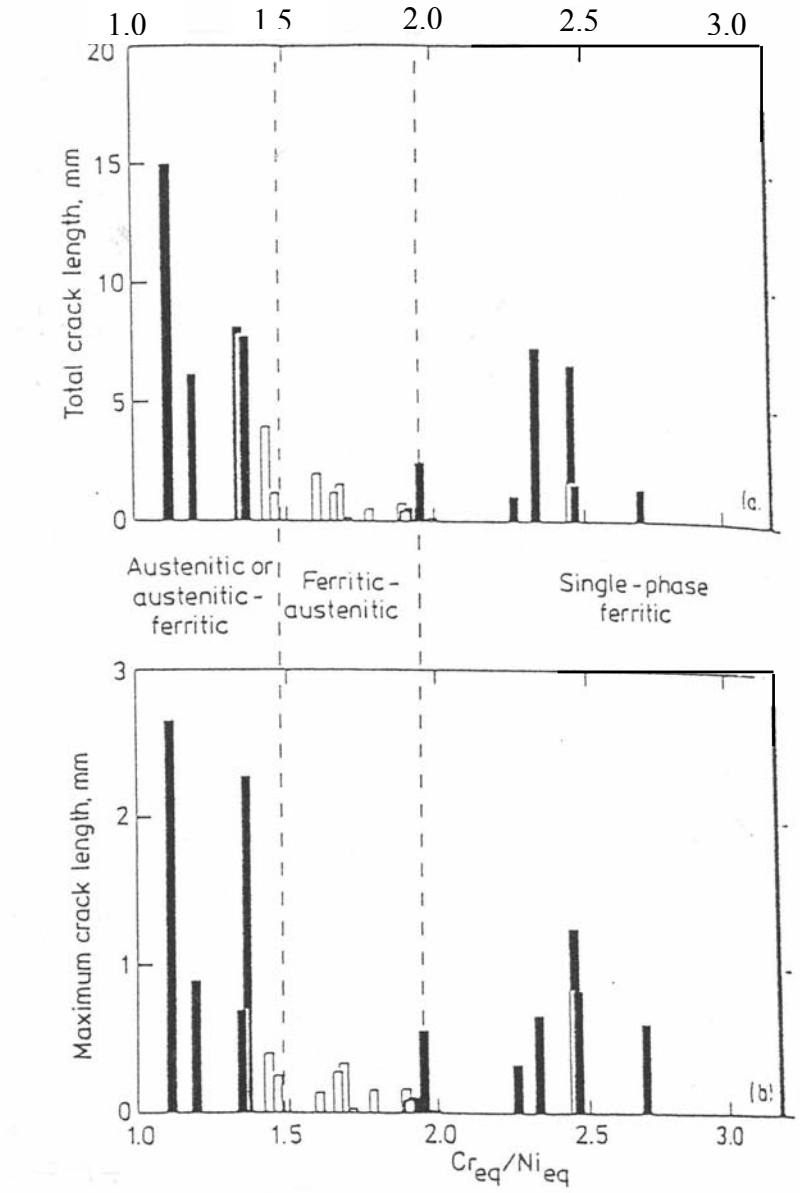


Figure 2.12 Result of trans-varestraint tests arranged in increasing order of the ratio $Cr_{eq}/Ni_{eq}$ for stainless steel weld metal [32].

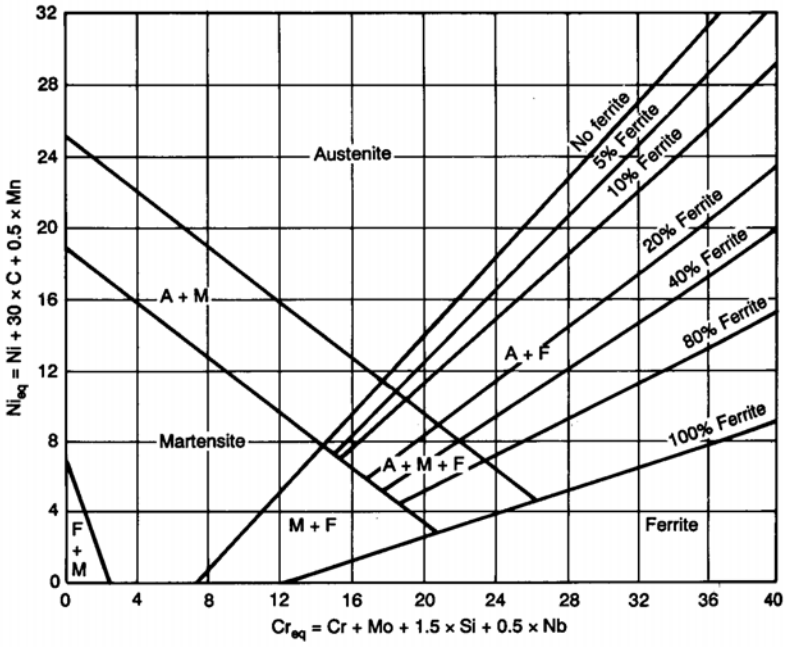


Figure 2.13 Schaeffller constitution diagram of stainless steel weld metal [43].

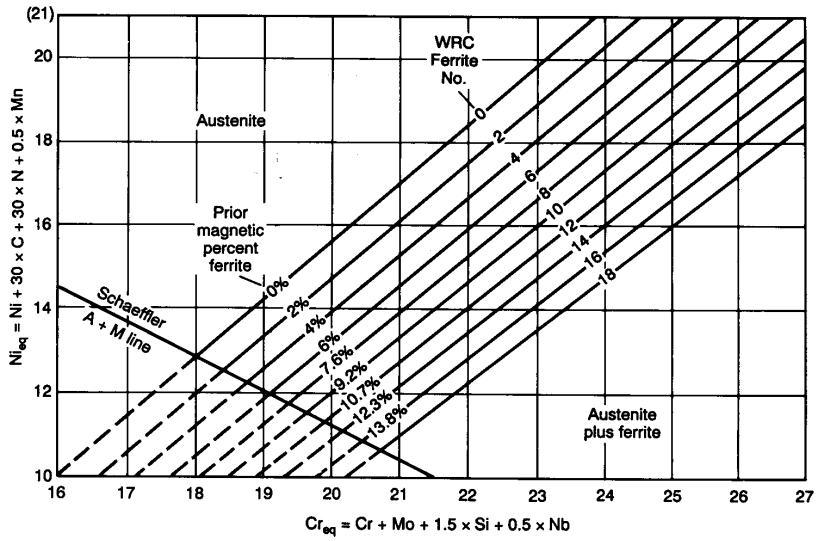


Figure 2.14 DeLong constitution diagram for stainless steel weld metal [44].

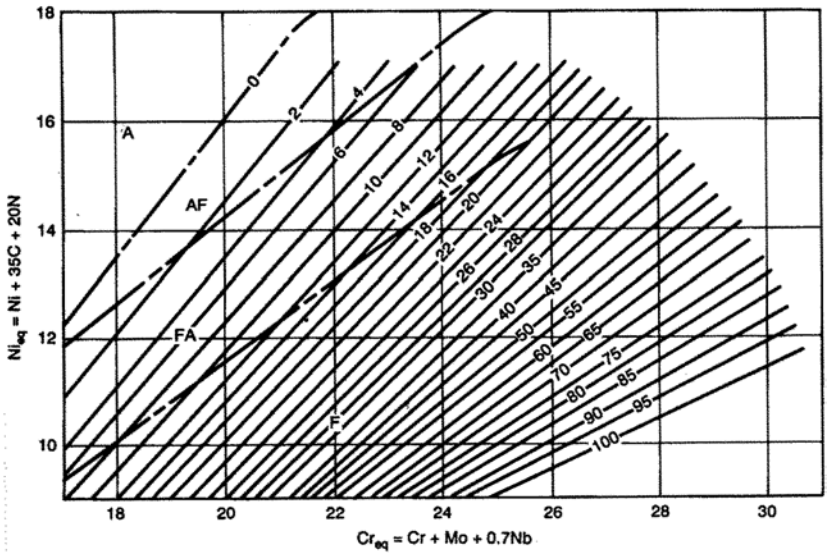


Figure 2.15 WRC-1988 diagram, including solidification-mode boundaries [48].

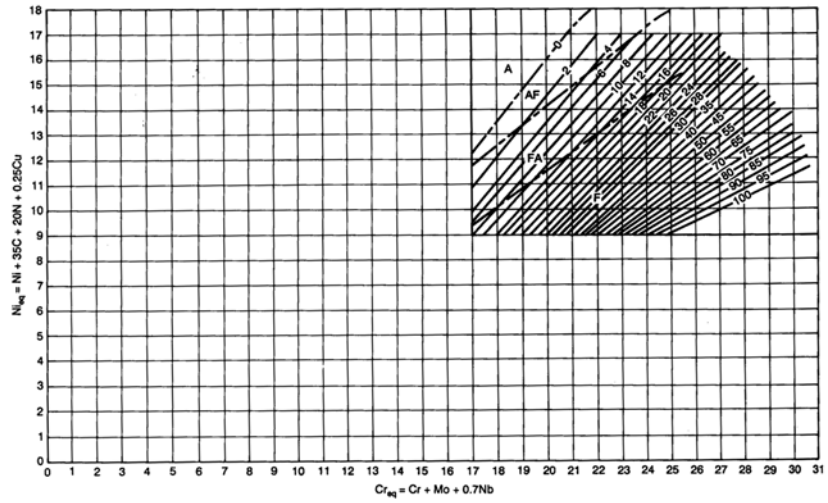


Figure 2.16 WRC-1992 diagram with expanded scale for dilution calculations [49].

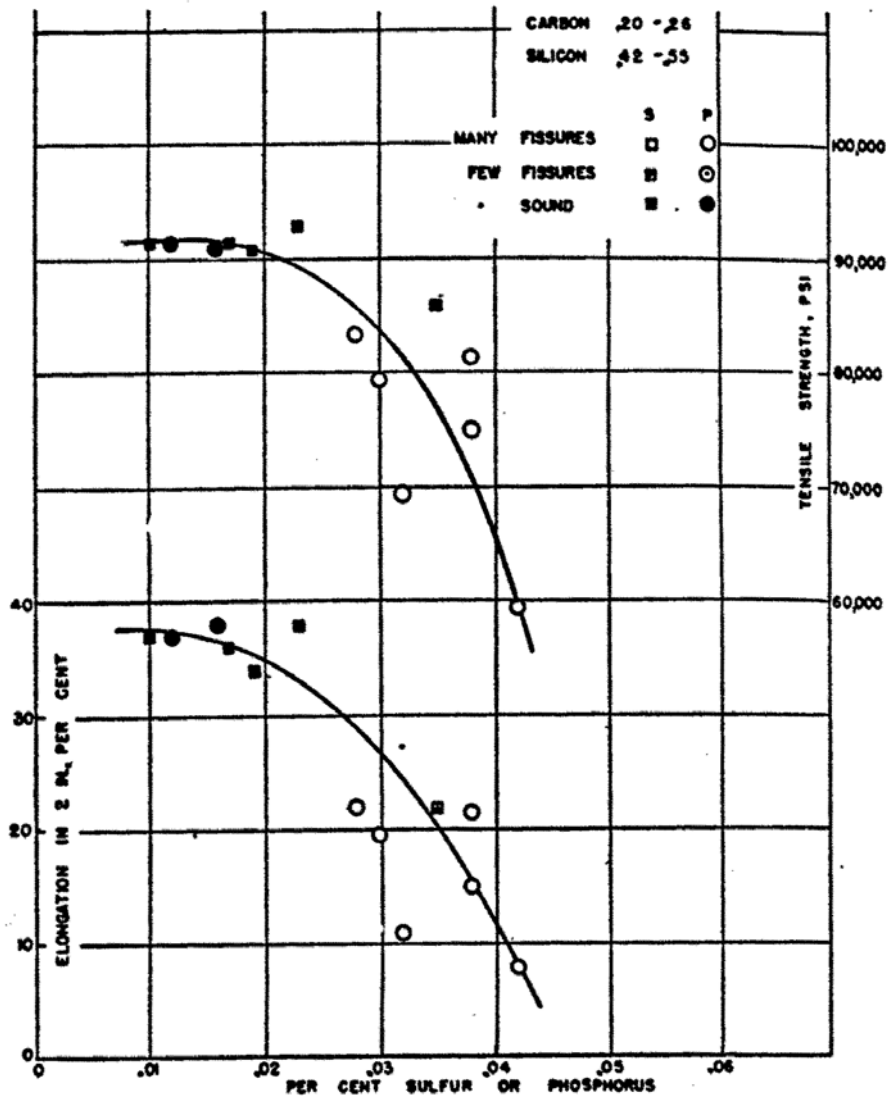


Figure 2.17 Effect of sulfur and phosphorous on elongation and tensile strength of 15%Cr-35%Ni Weld metal [48].

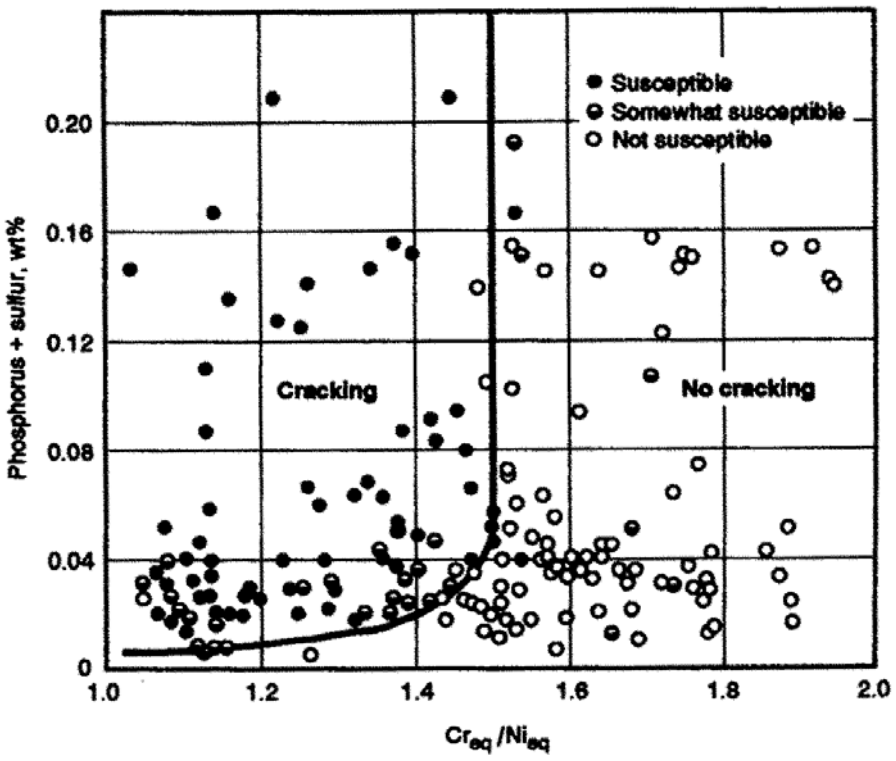


Figure 2.18 Relationship between solidification cracking susceptibility and $Cr_{eq}/Ni_{eq}$ ratio [43].

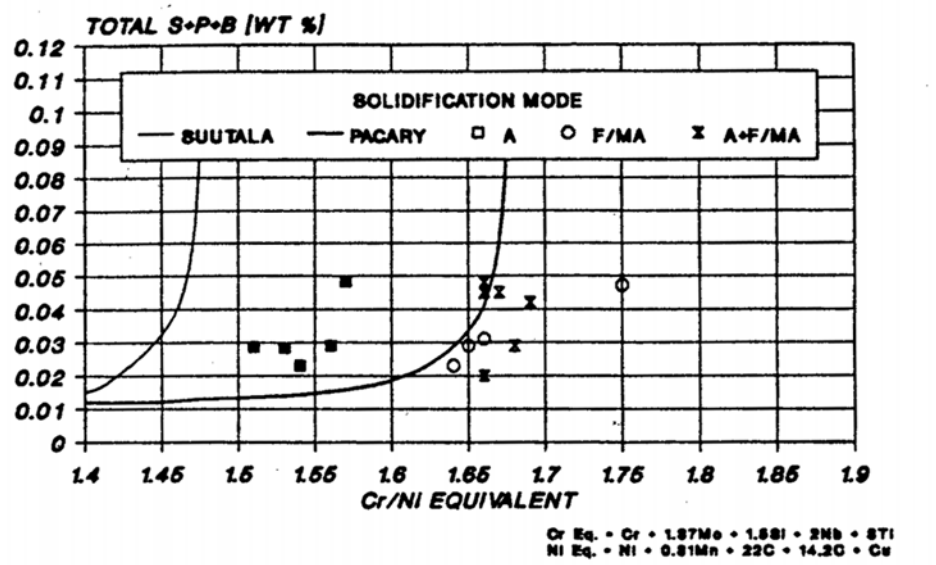


(a)

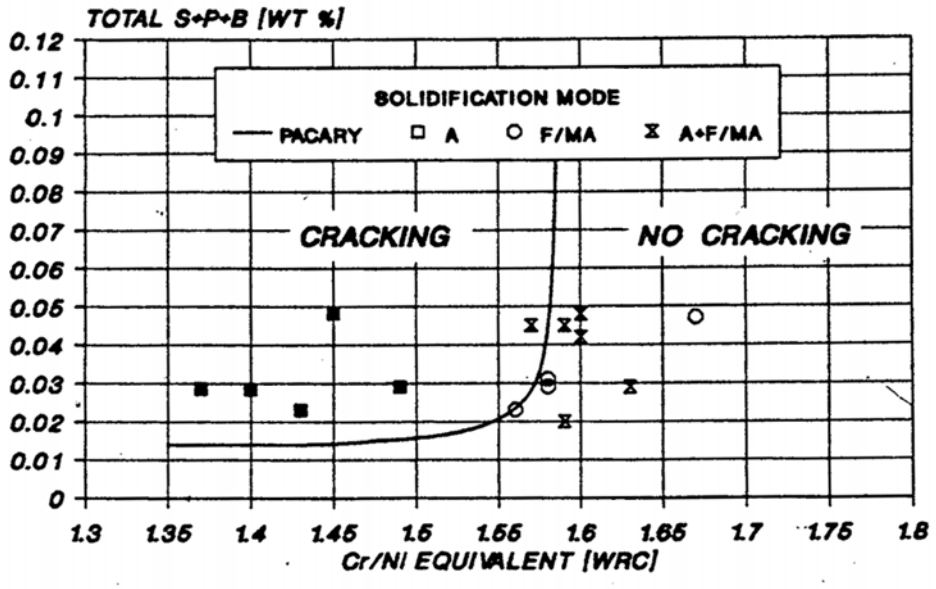


(b)

$Cr_{eq} = Cr + Mo + 0.7Nb$

$Ni_{eq} = Ni + 35C + 20N$

Figure 2.19 Modified Suutala diagram [29]
(a)-with Suutala equivalents; (b)-with WRC equivalents.
Filled symbols=cracking, Open symbols=no cracking,
filled/open symbols=variable.

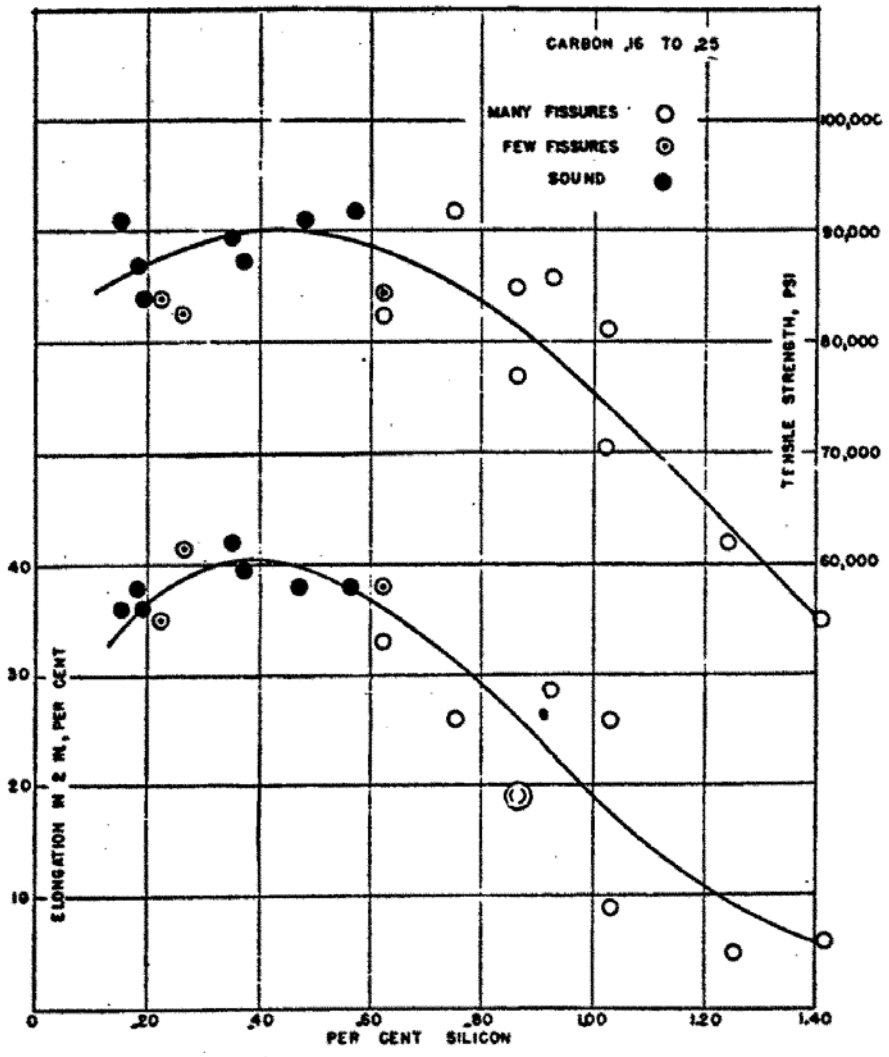


Figure 2.20 Effect of silicon on microfissures and mechanical properties of 15Cr35Ni type weld metal [50].

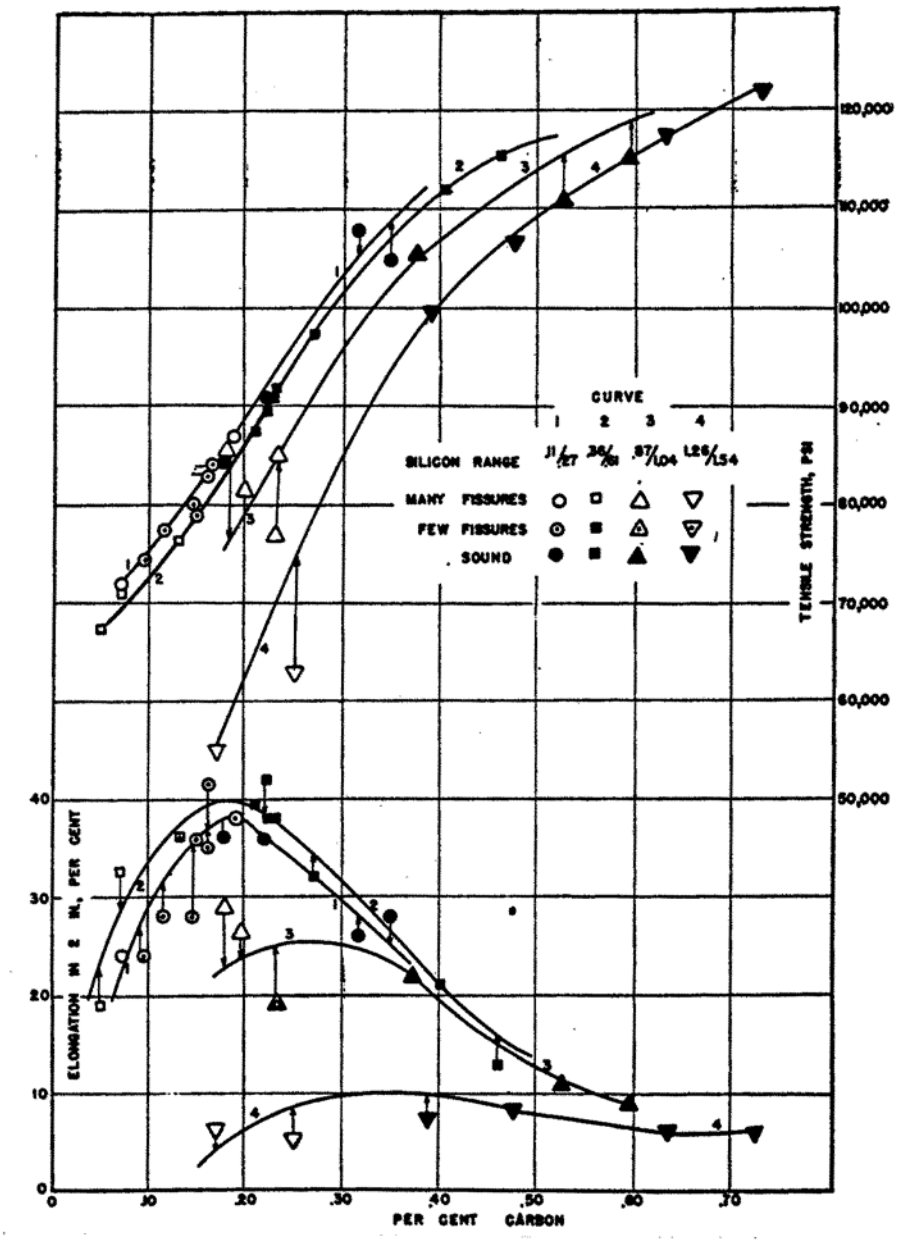


Figure 2.21 Effect of carbon on microfissuring and mechanical properties of 15Cr35Ni type weld metal [48].

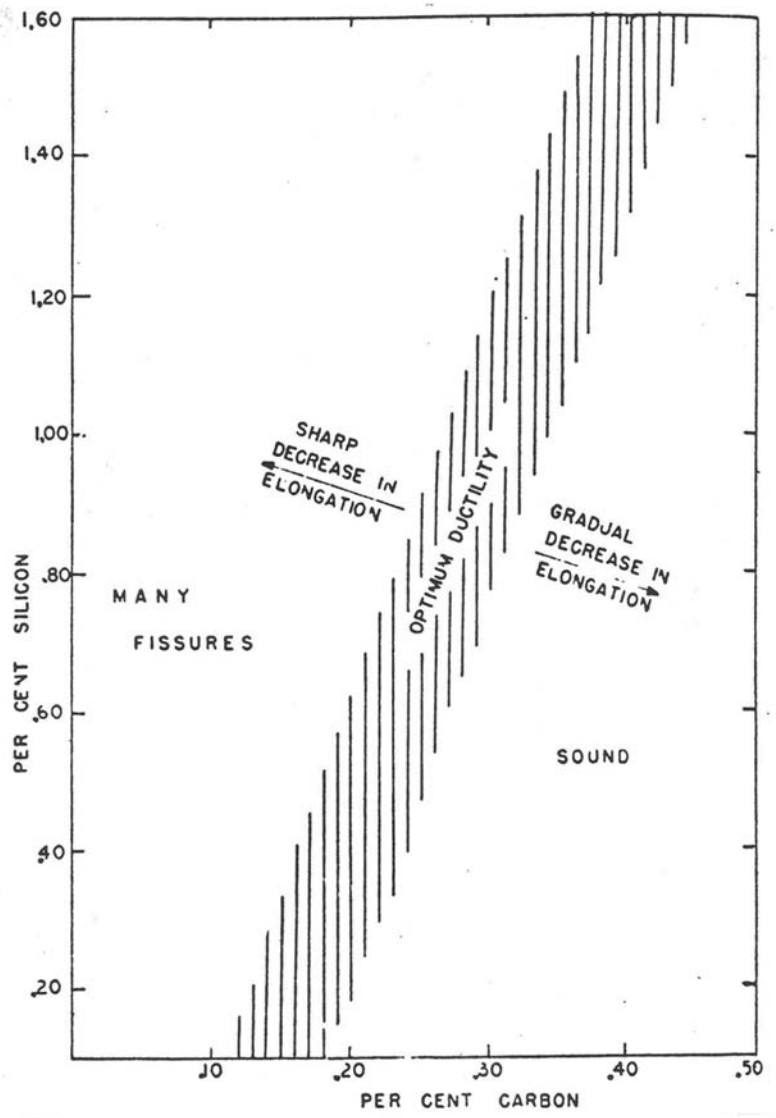


Figure 2.22 Effect of carbon and silicon on microfissuring and ductility of 15Cr35Ni type weld metal [48].

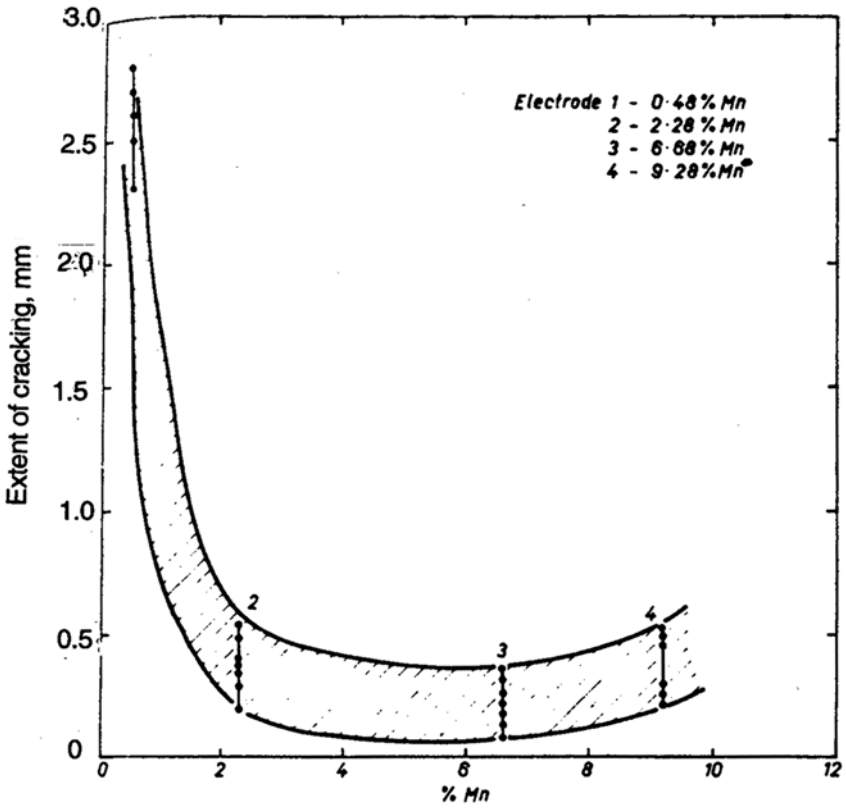


Figure 2.23 Relationship between incidence of cracking in weld pads and manganese content [56].

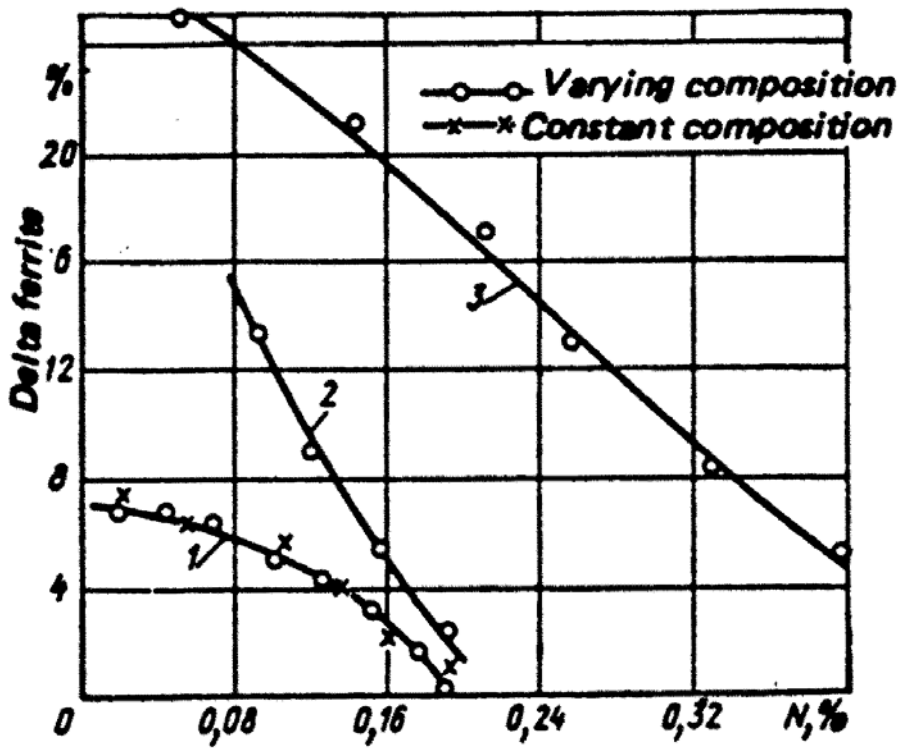


Figure 2.24 Effect of nitrogen content on the delta ferrite content of deposited weld metal of type (1) Cr18-Ni9-Ti (2) Cr20-Ni6 (3) Cr25-Ni12-Mn2-Ti [57].

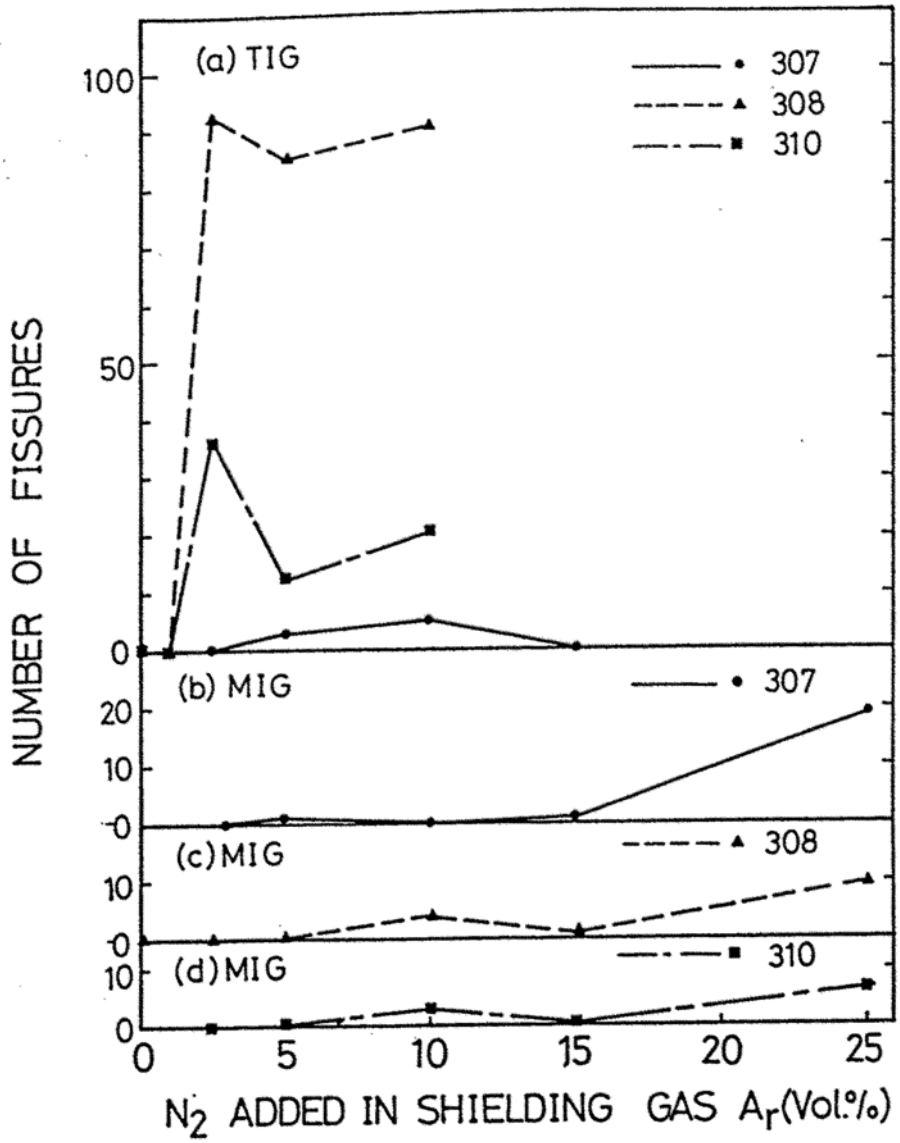


Figure 2.25 Effect of nitrogen addition in the shielding gas on the number of hot cracking in stainless steel weld [62].

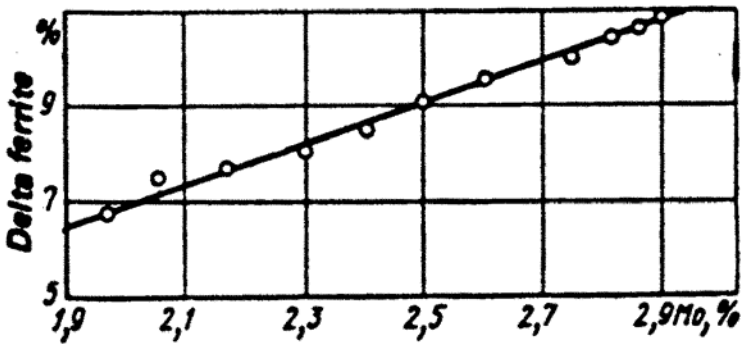


Figure 2.26 Effect of molybdenum content on the delta ferrite content of type OKH16N6M2 weld metal [57].

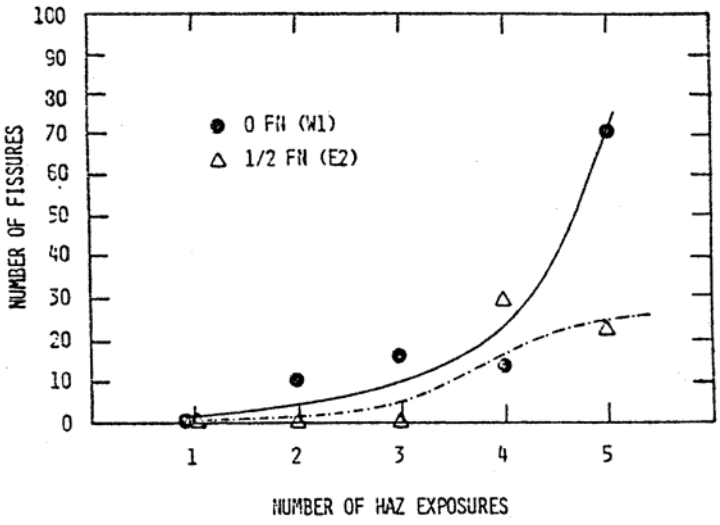


Figure 2.27 Microfossire count as a function of multiple HAZ thermal cycle [39].

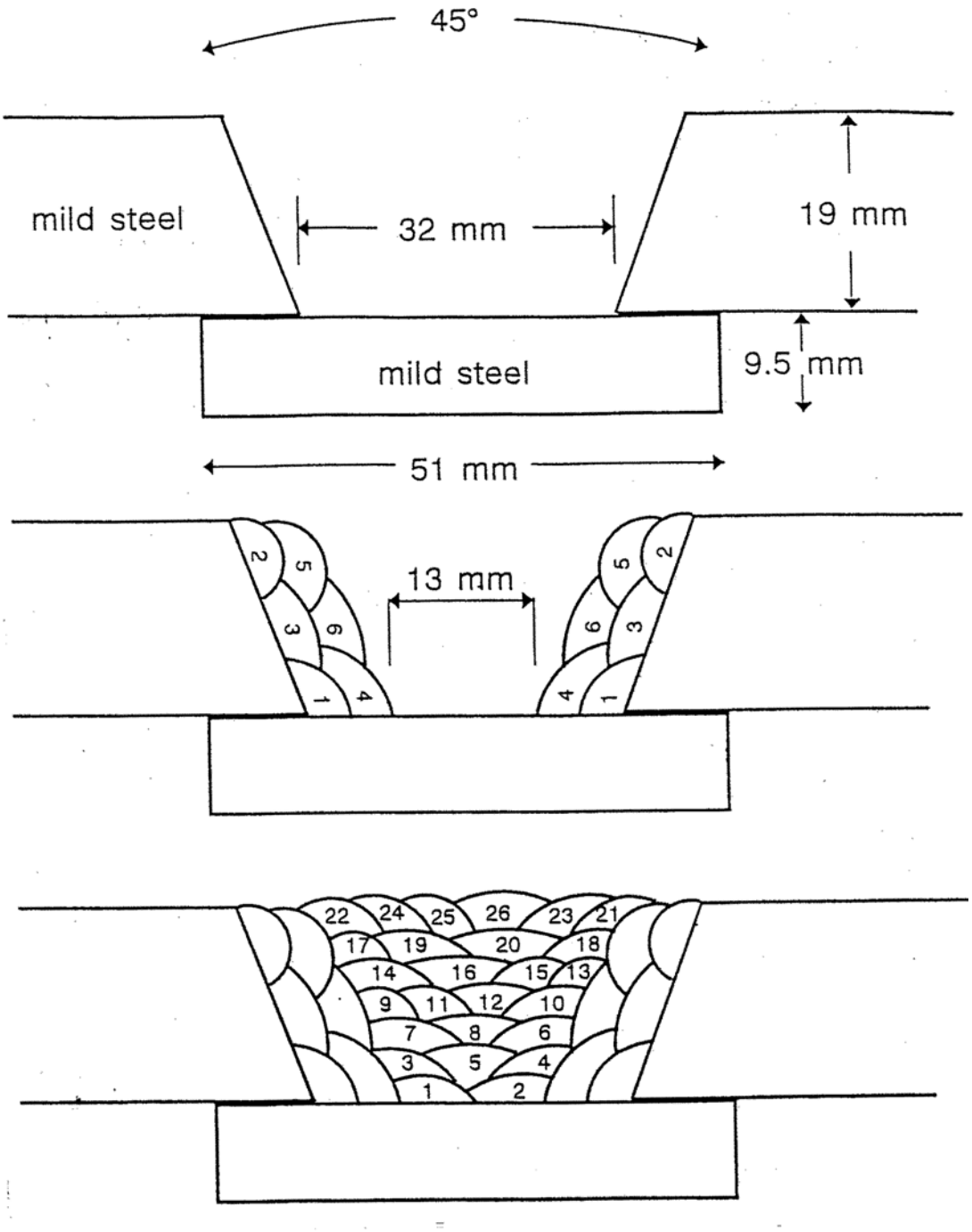


Figure 2.28 Weldment for microfissure determination [73].
Top-initial joint before buttering
Central-joint after buttering
Bottom-completed joint.

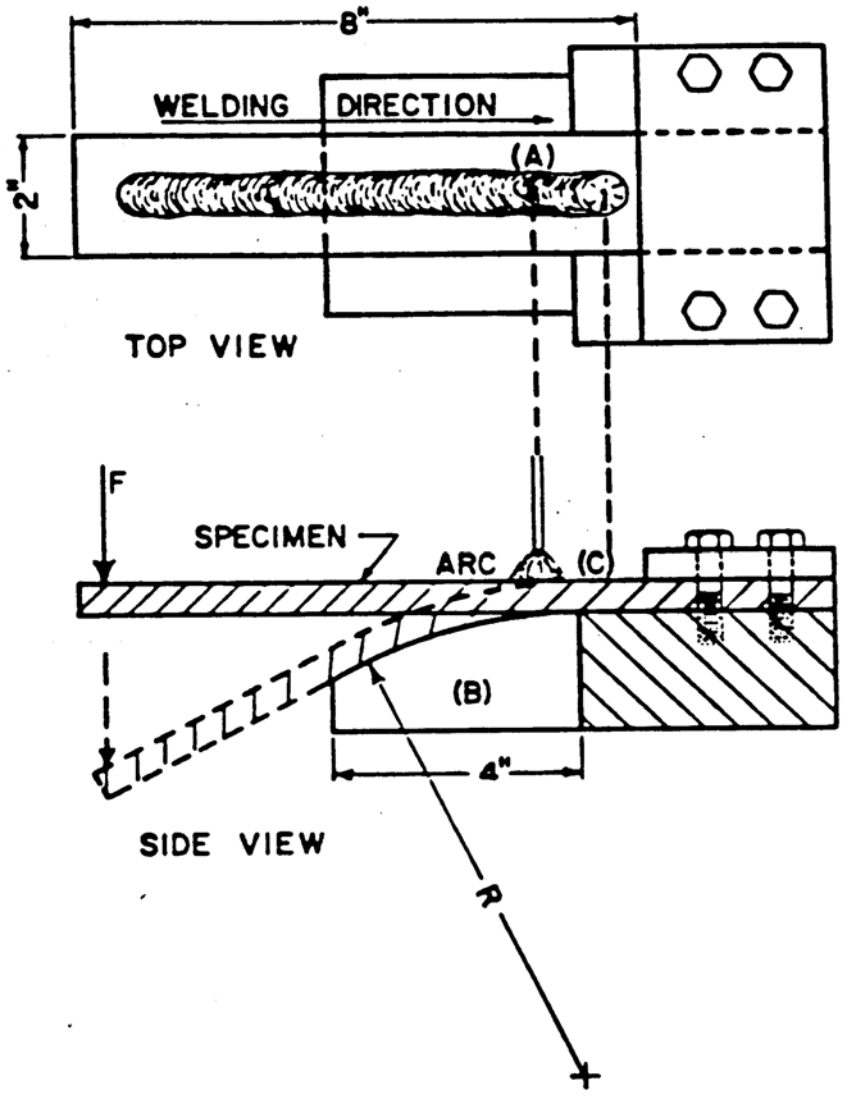


Figure 2.29 Schematic showing principle of varestraint testing [74].

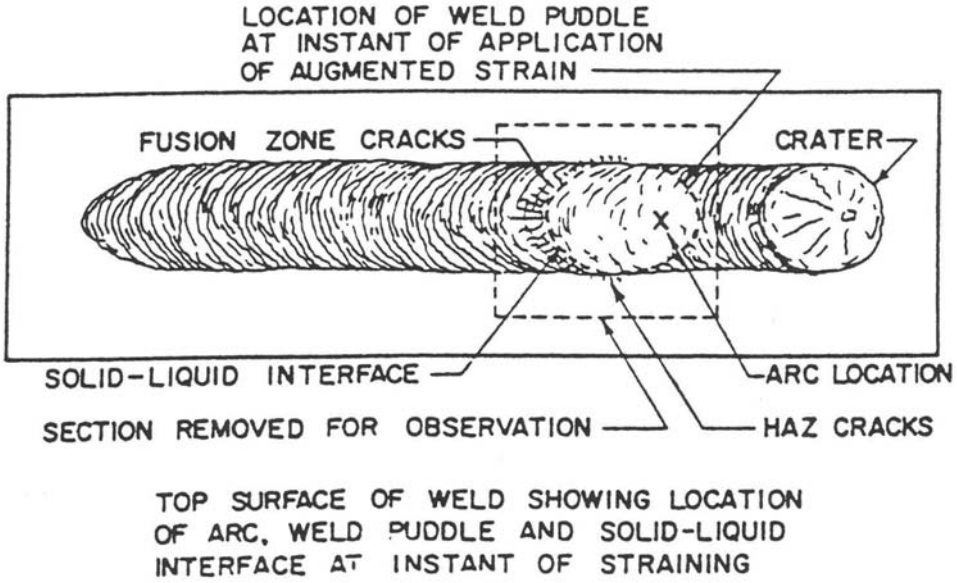


Figure 2.30 Schematic representation of the section of the weld removed for metallographic observation [75].

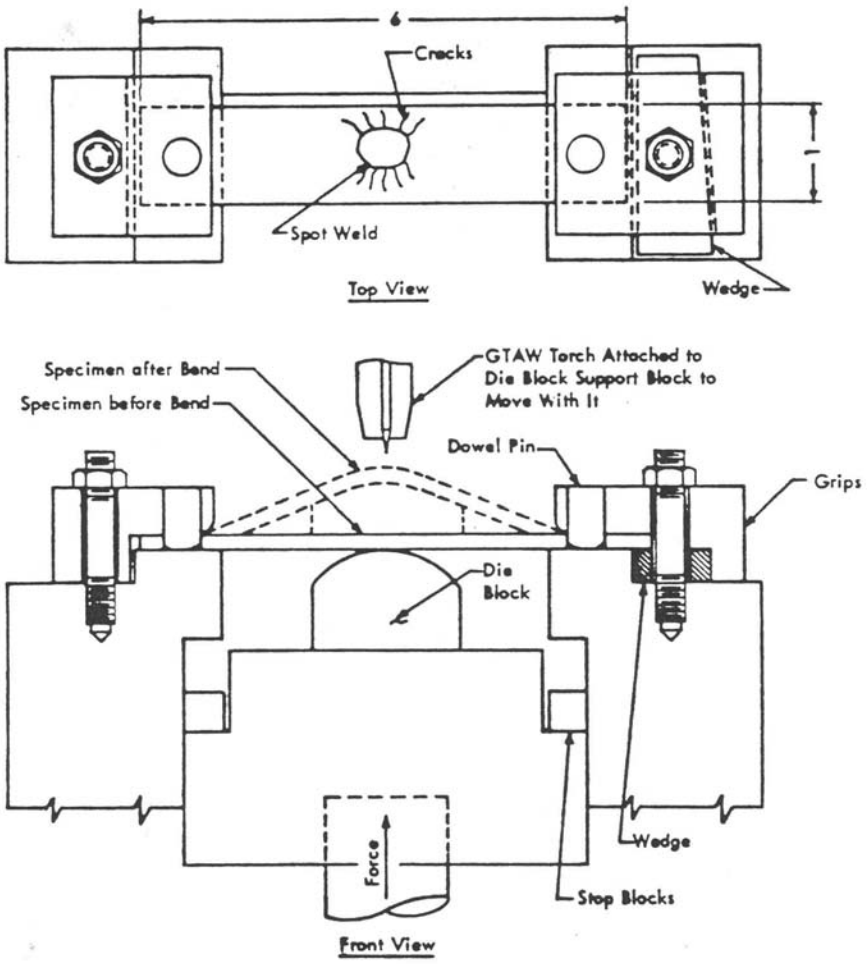


Figure 2.31 Spot varestraint test device showing the methodology by which a specimen is tested [69].

(a)

(b)

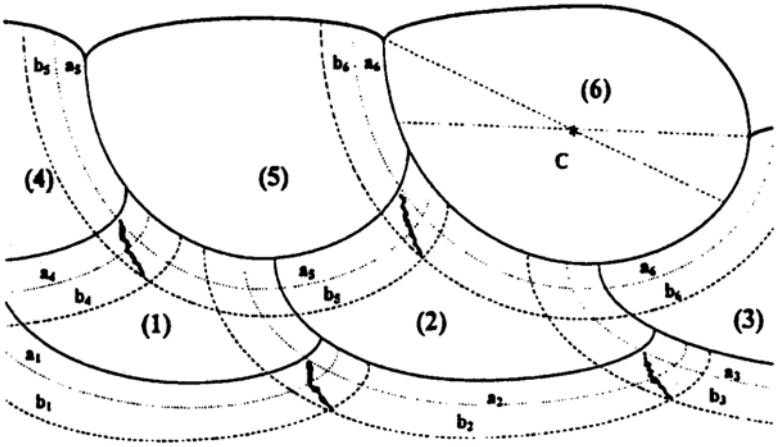


(c)

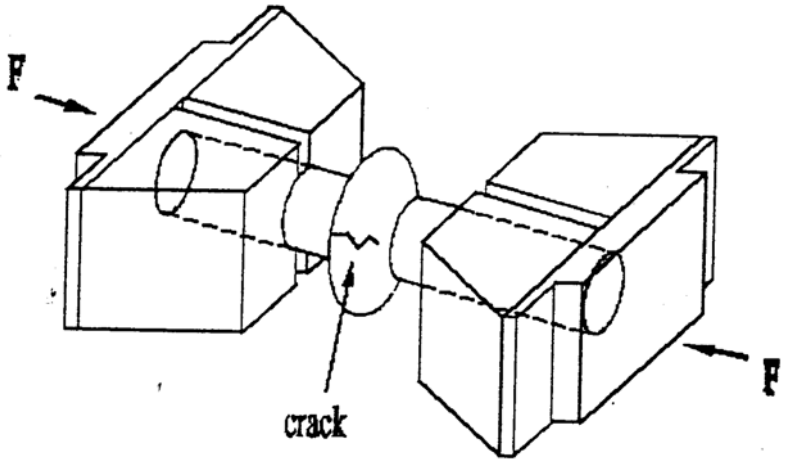


Figure 2.32 (a) Extraction of SICO testing specimens from a weld plate;
(b) Bead sequence;
(c) Mcirofissures initiate at the equatorial surface of the bulge zone.

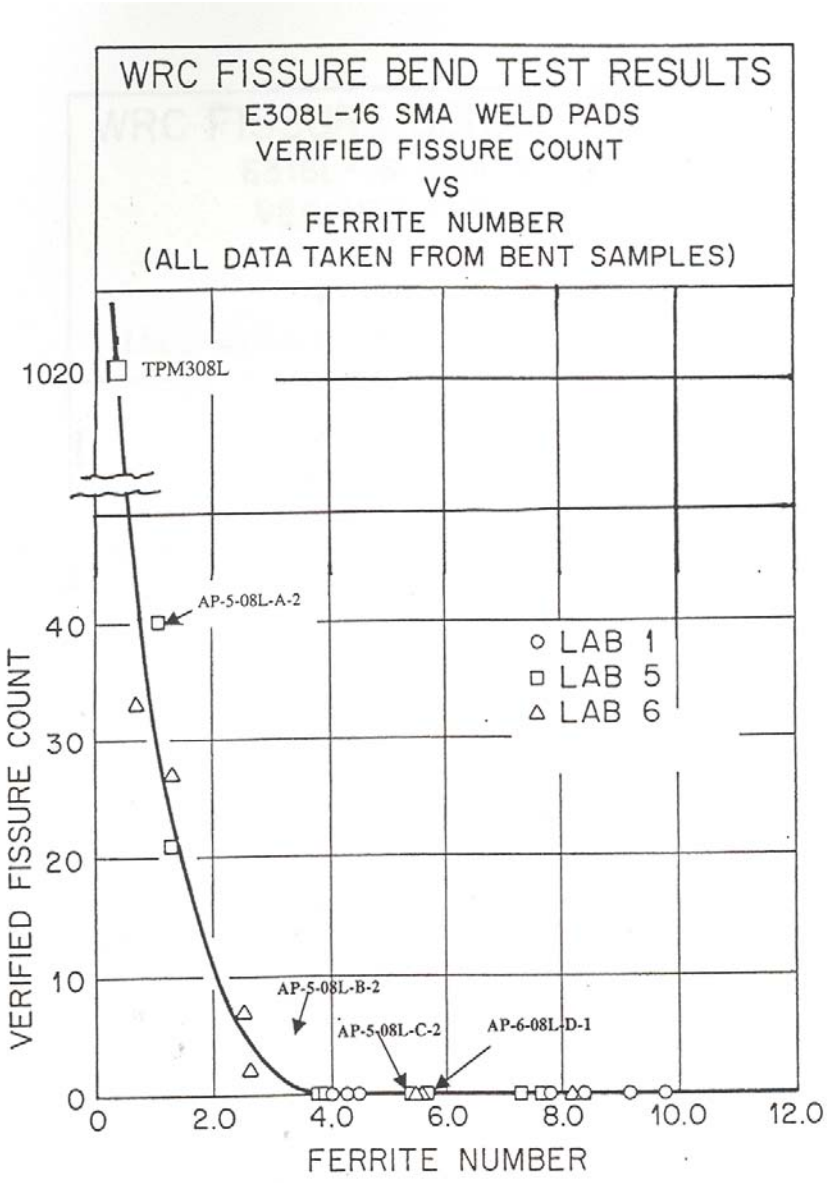


Figure 3.1 Microfissure distribution of 308L used in the project of Fissure Bend Test.

Note:
AP-5-08L-A-2 is labeled as 308L-A in this project;
AP-5-08L-B-2 is labeled as 308L-B in this project
AP-5-08L-C-2 is labeled as 308L-C in this project
AP-6-08L-CD-1 is labeled as 308L-D in this project.

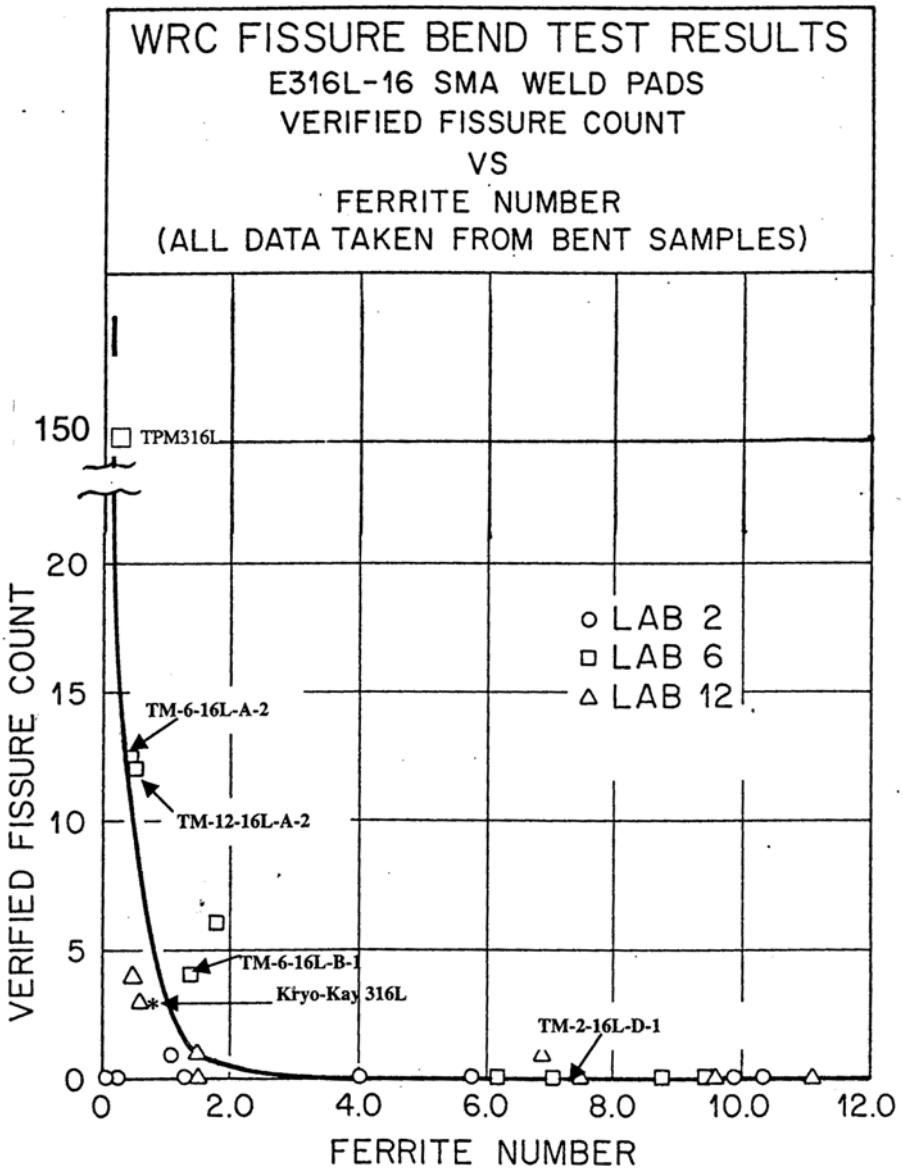


Figure 3.2 Microfissure distribution of 316L used in the project of Fissure Bend Test.

Note:
TM-6-16L-A-2 and TM-12-16L-A-2 are labeled as 316L-A in this project;
TM-6-16L-B-1 is labeled as 316L-B;
Kro-Kay 316L is labeled as KK316L;
TM-2-16L-D-1 is labeled as 316L-D.

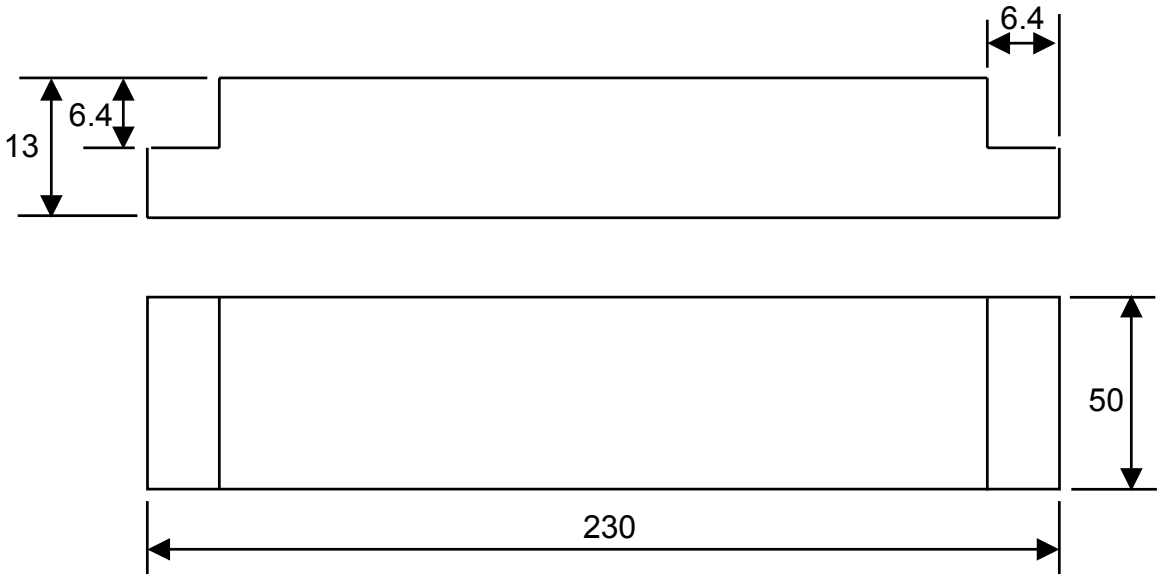


Figure 3.3 Schematic diagram of a welding coupon.

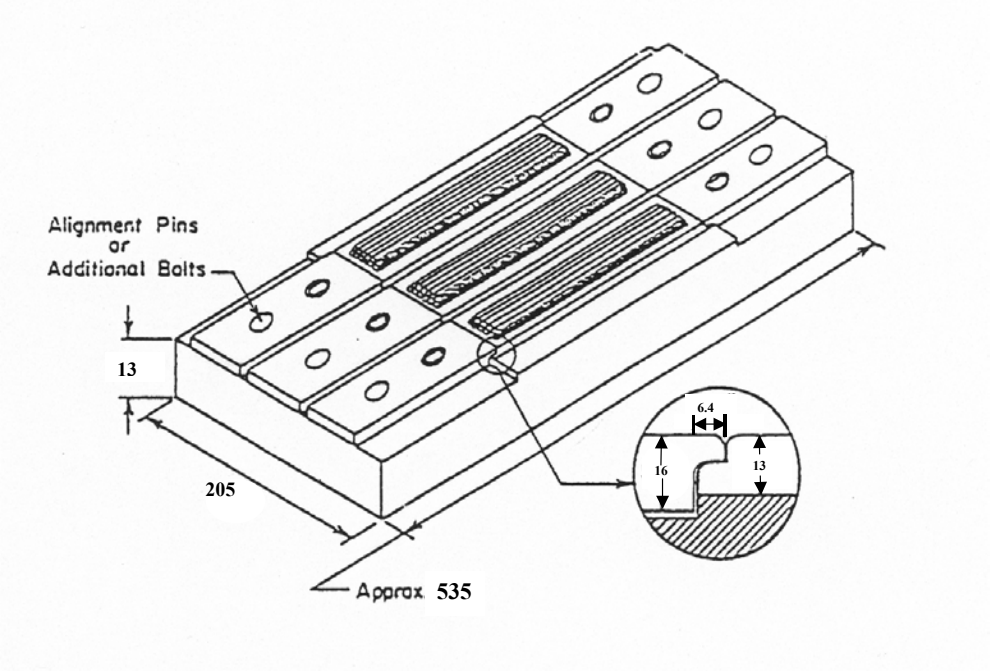


(a)

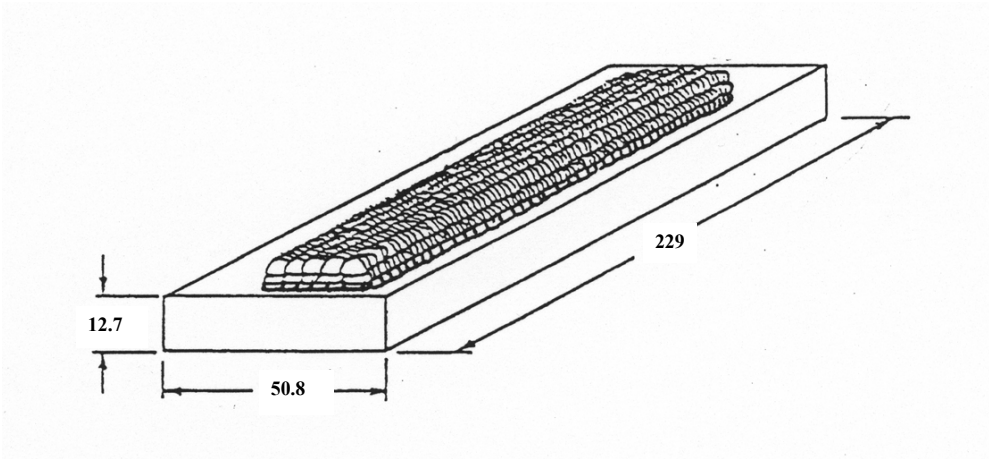


(b)

All units are in mm.

Figure 3.4 (a) Schematic drawing of the clamping fixture, (b) pad configuration.

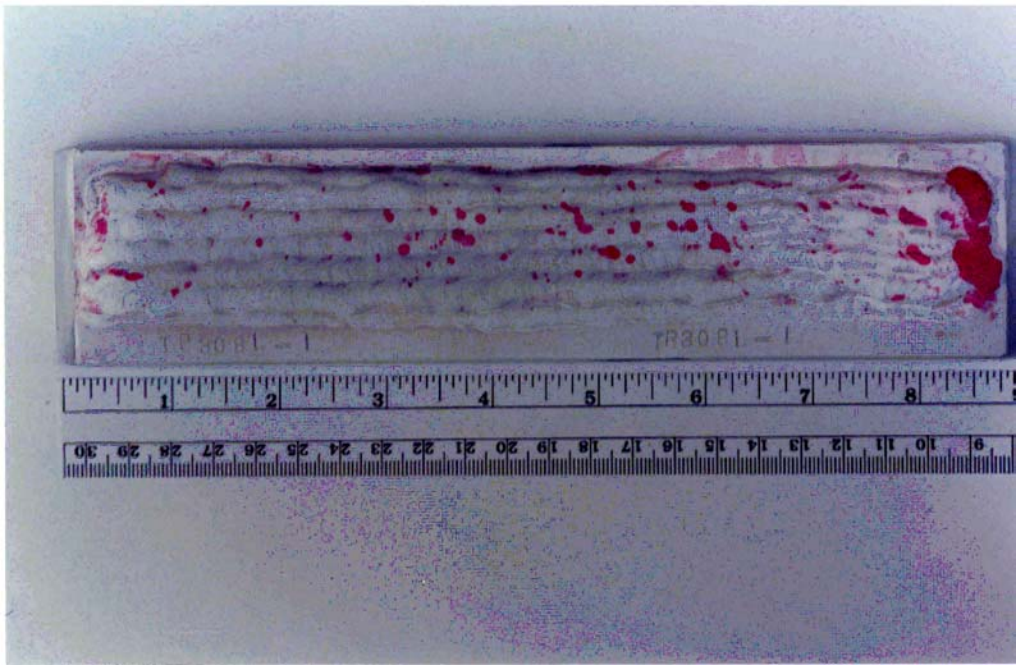

Figure 3.5 Typical morphology detected using dye penetrate testing.

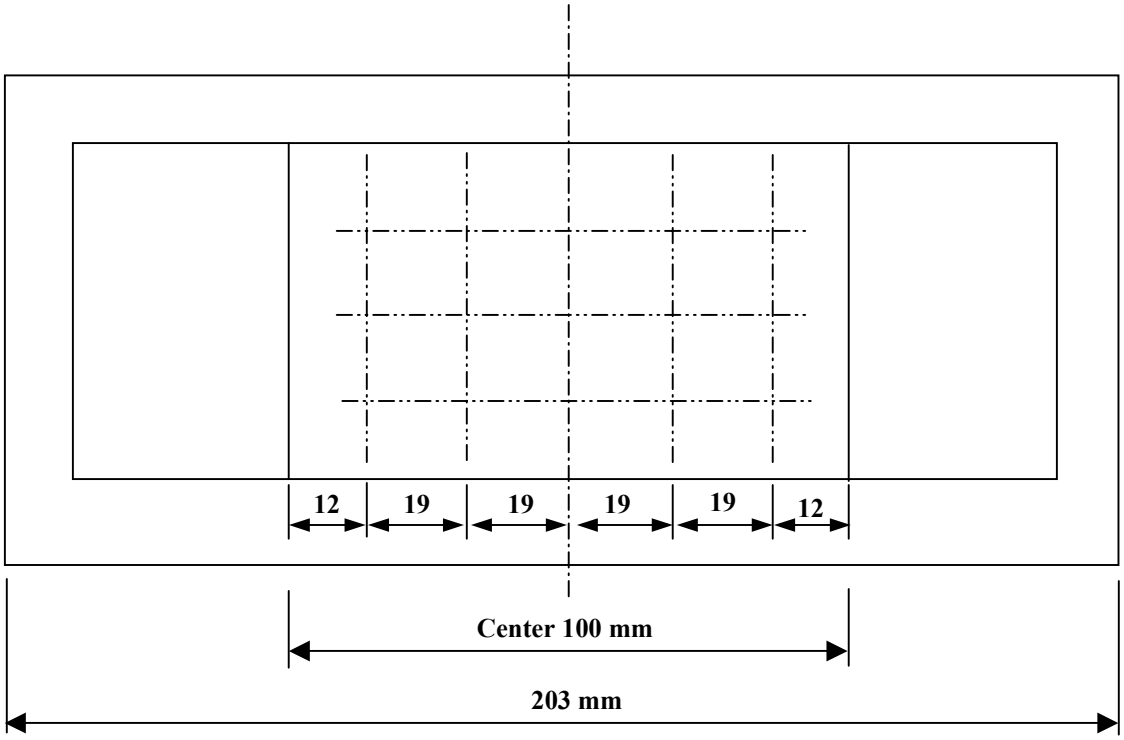


(a)


(b)

Figure 3.6 (a) Schematic diagram for Ferrite Number determination; (b) Feritscope.

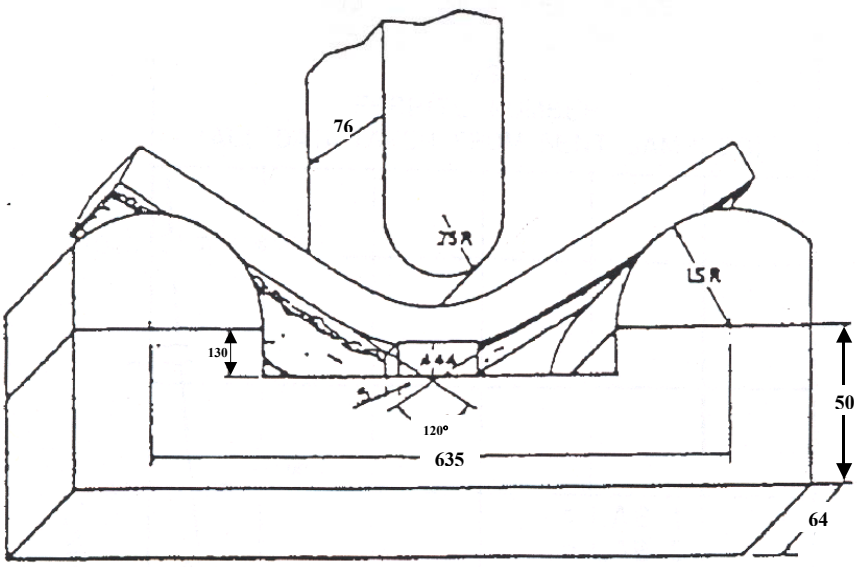


All units are in mm.

Figure 3.7 Fissure Bend Test fixture.

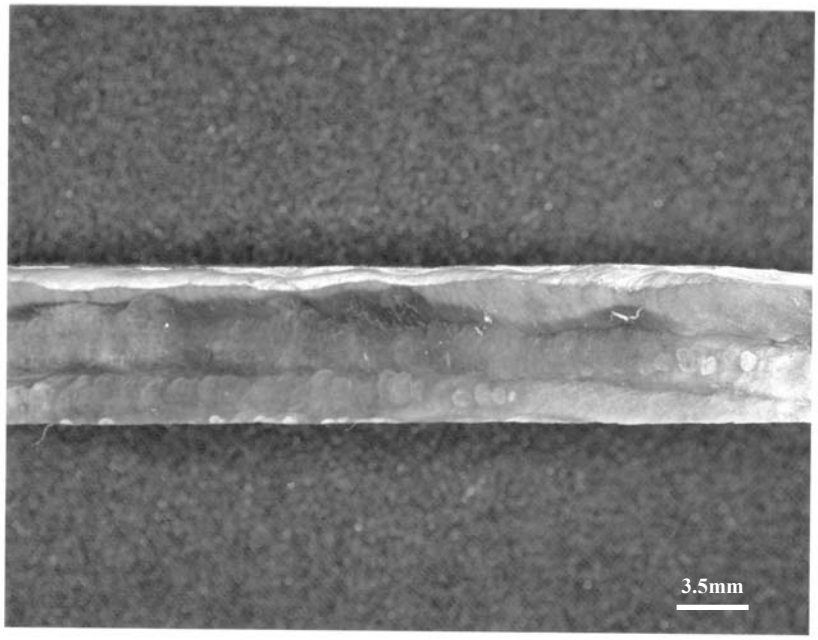


Figure 3.8 Sample extracted from the unbend sample for SEM evaluation.

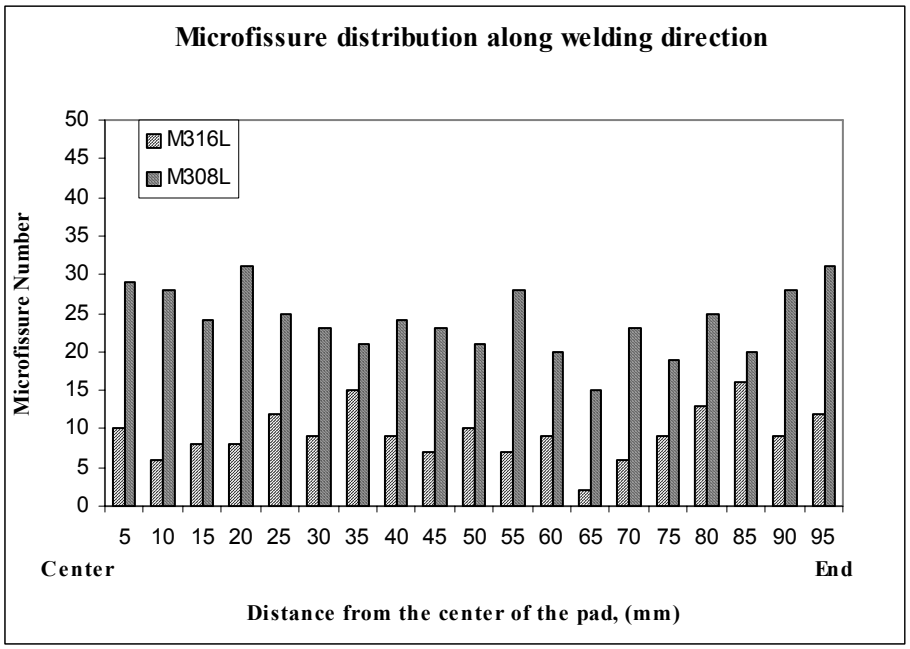


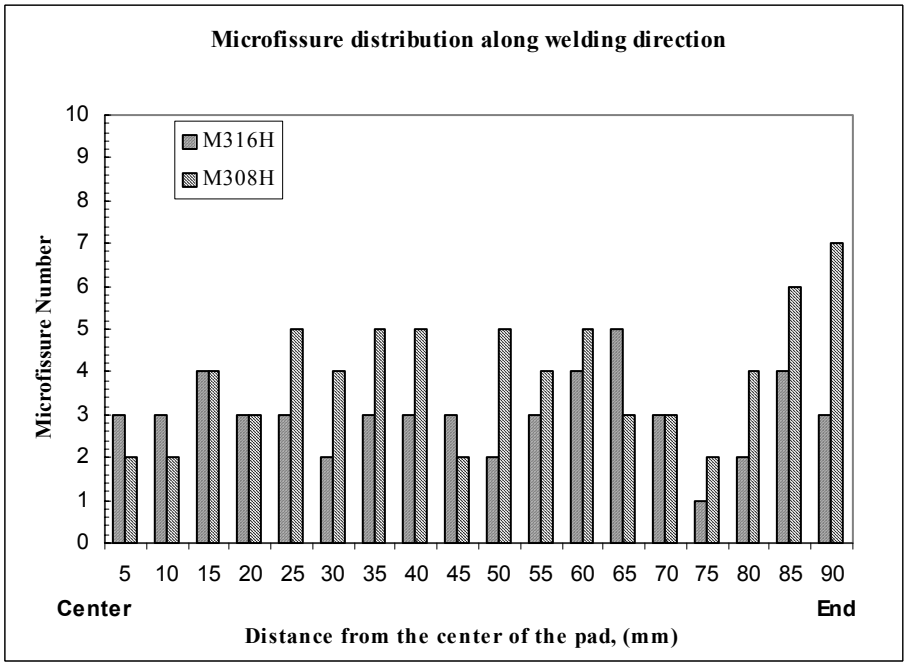


Figure 3.9 Microfissure distribution determined on sample top surface along welding direction.


(a)-50X

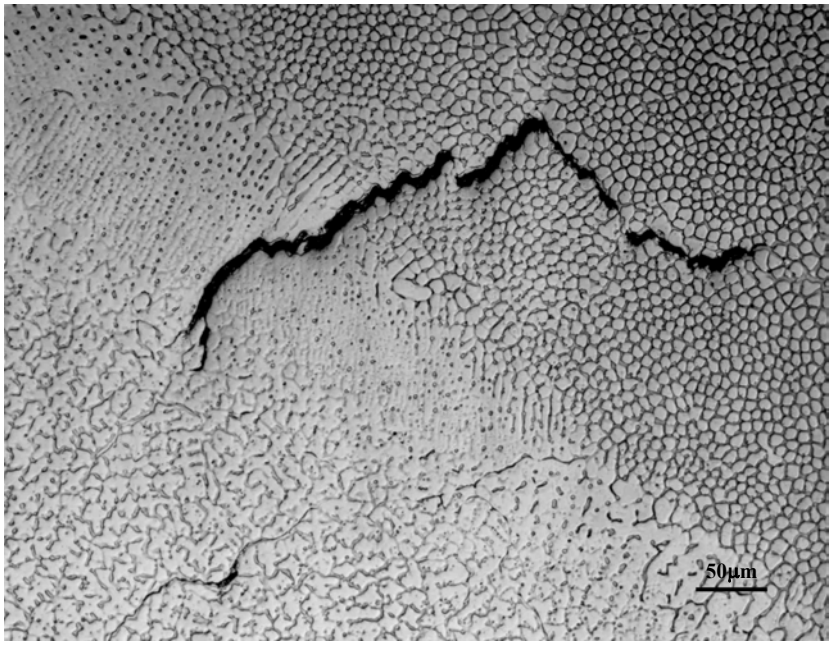


(b)-400X

Figure 3.10 Microfissure morphology of modified F316L sample surface along welding direction.

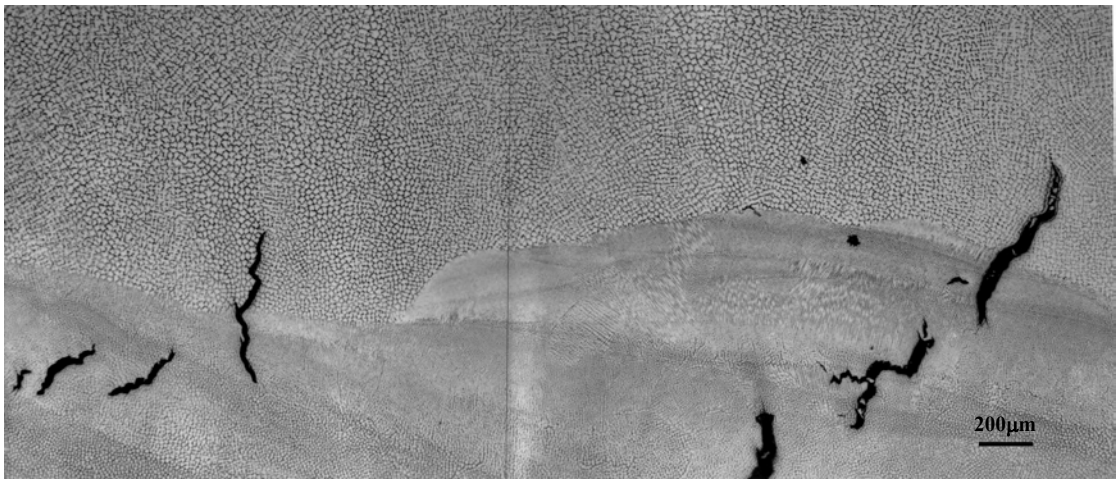


Figure 3.11 Microfissure morphology of modified 316H sample surface along welding direction.

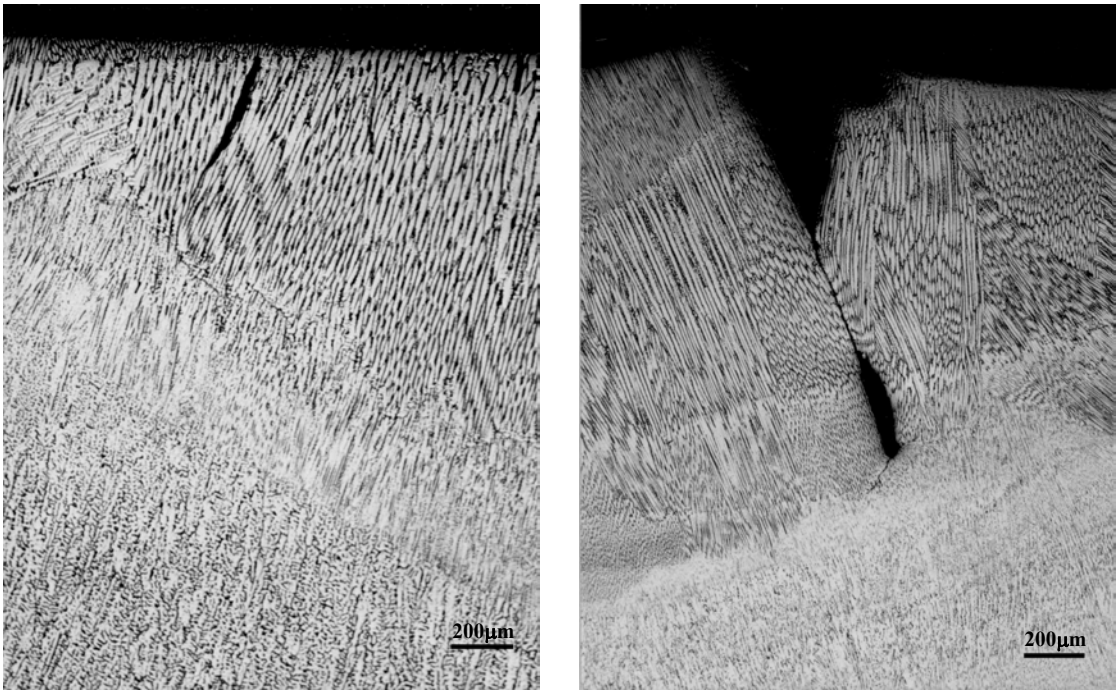


(a) (b)

Figure 3.12 Microfissure morphology of modified 308L transverse section, 50X.

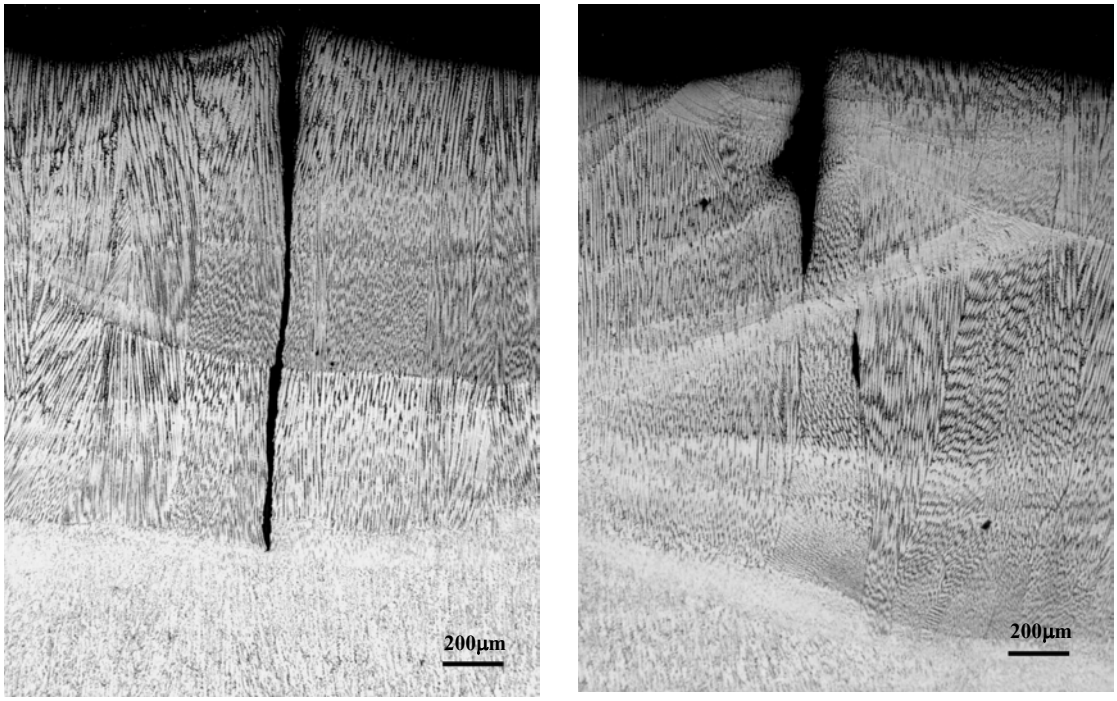


(a) (b)

Figure 3.13 Microfissure morphology of modified 308L transverse section, 50X.

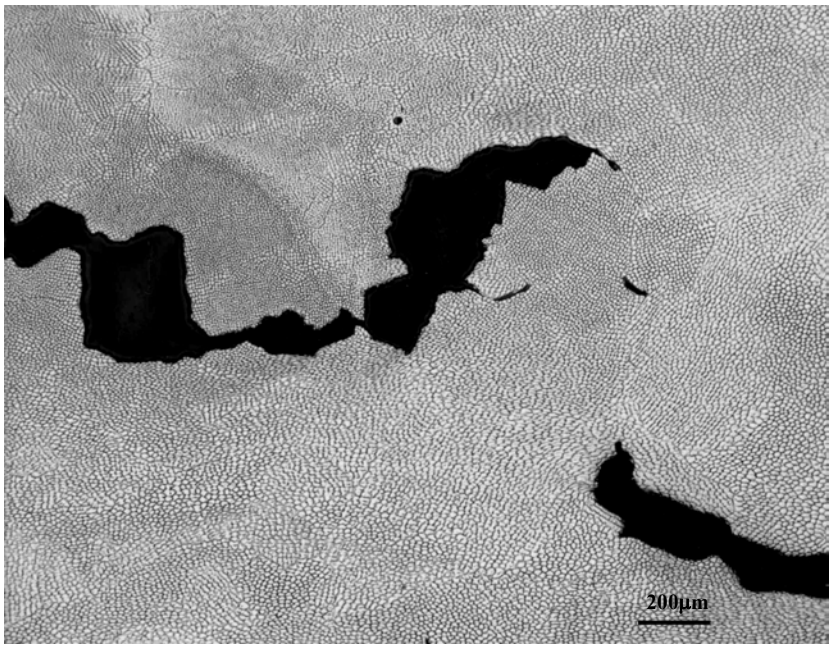


(a)

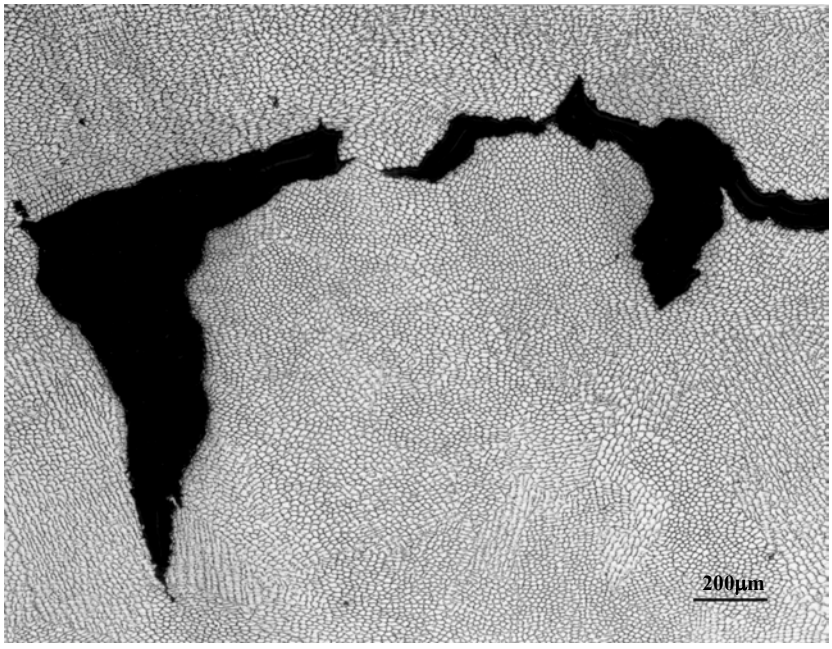


(b)

Figure 3.14 Microfissure morphology of modified 308L sample surface after Fissure Bend Testing, 50X.

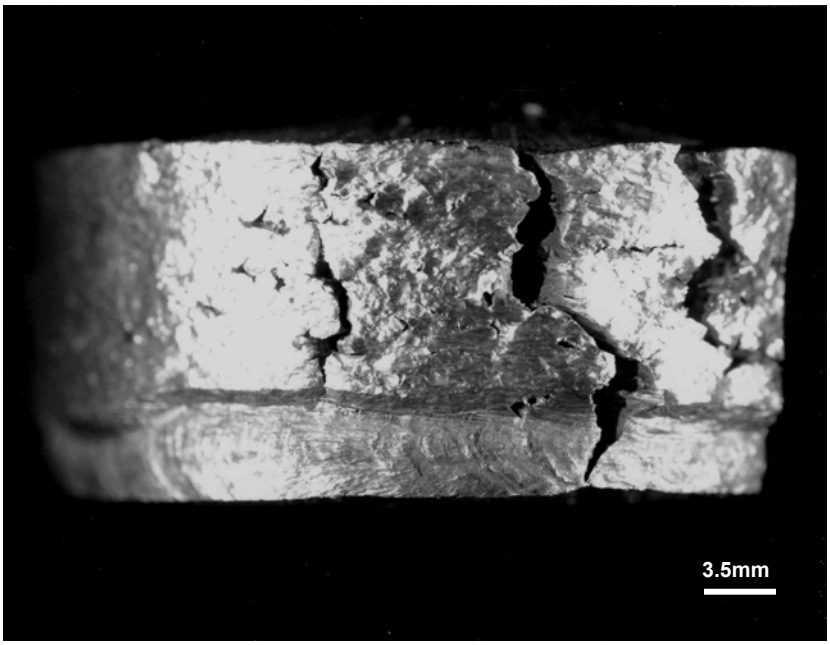


Figure 3.15  Sample extracted from bent M308L for SEM evaluation.

(a)

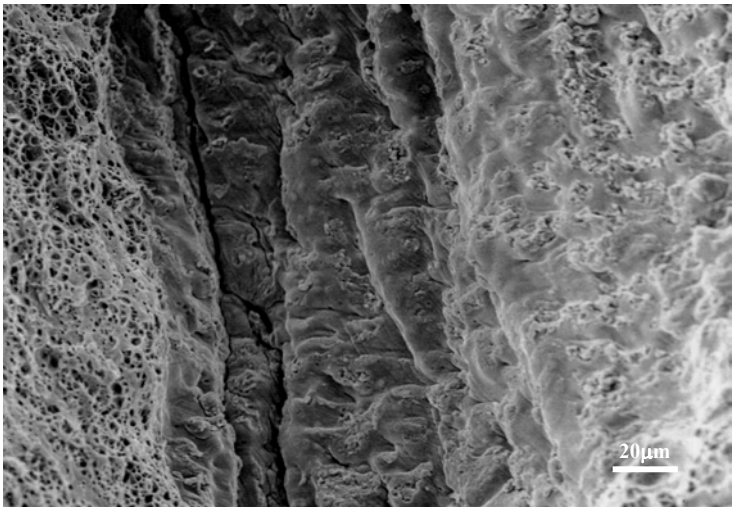


(b)

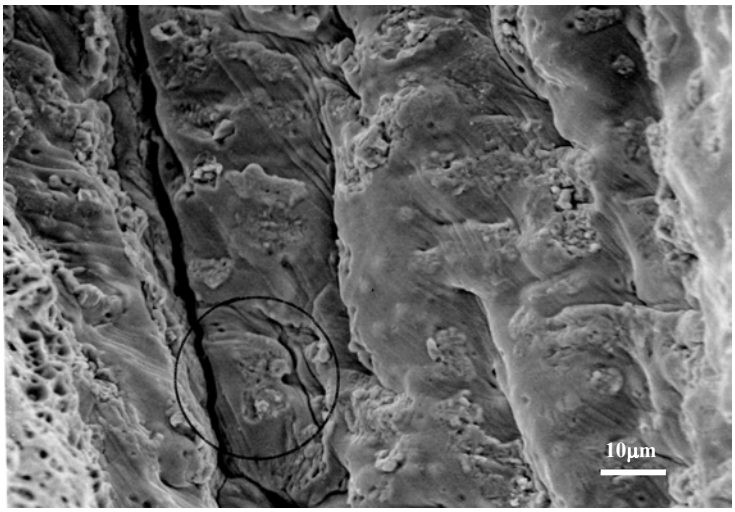


(c)

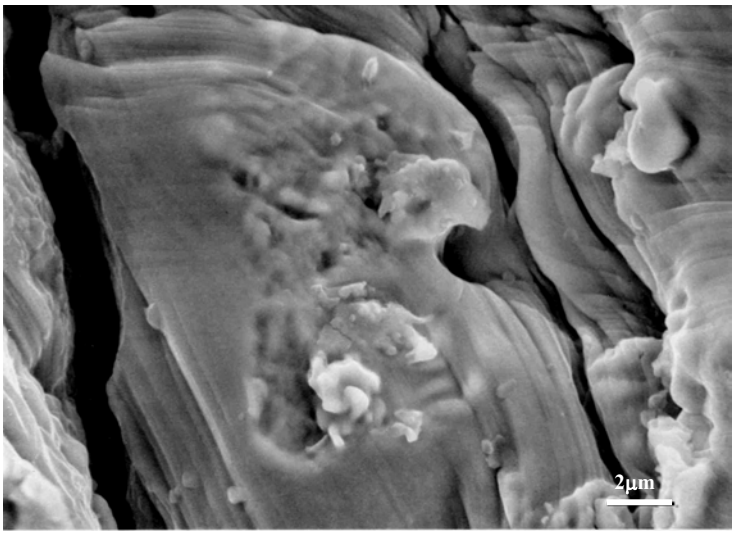


Figure 3.16 SEM fracture surface morphology of microfissures in M308L weld pad.

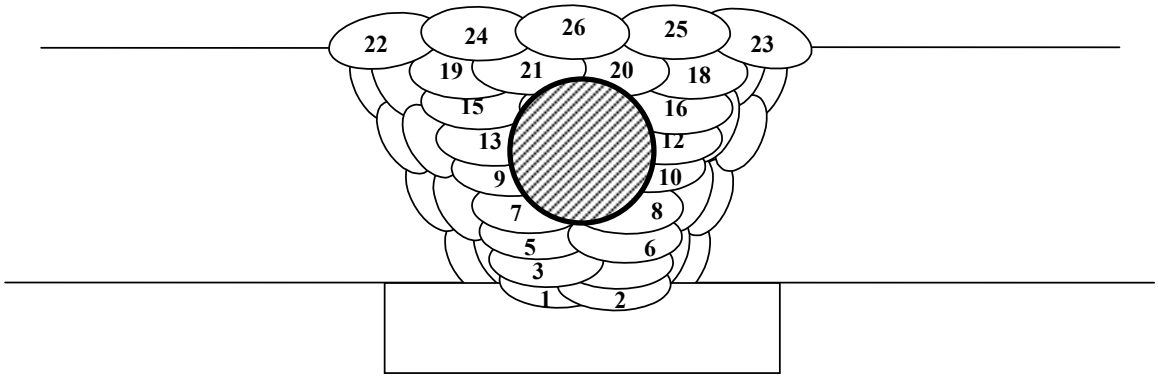


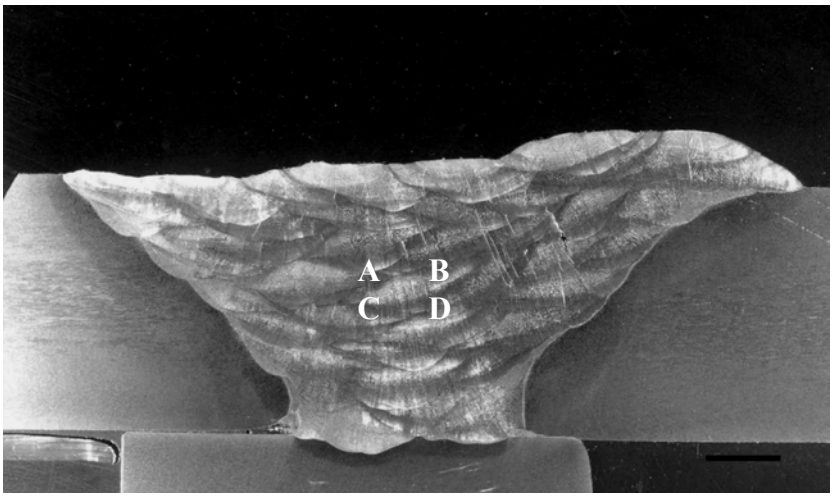


Figure 3.17 Weldment preparation for tensile test.

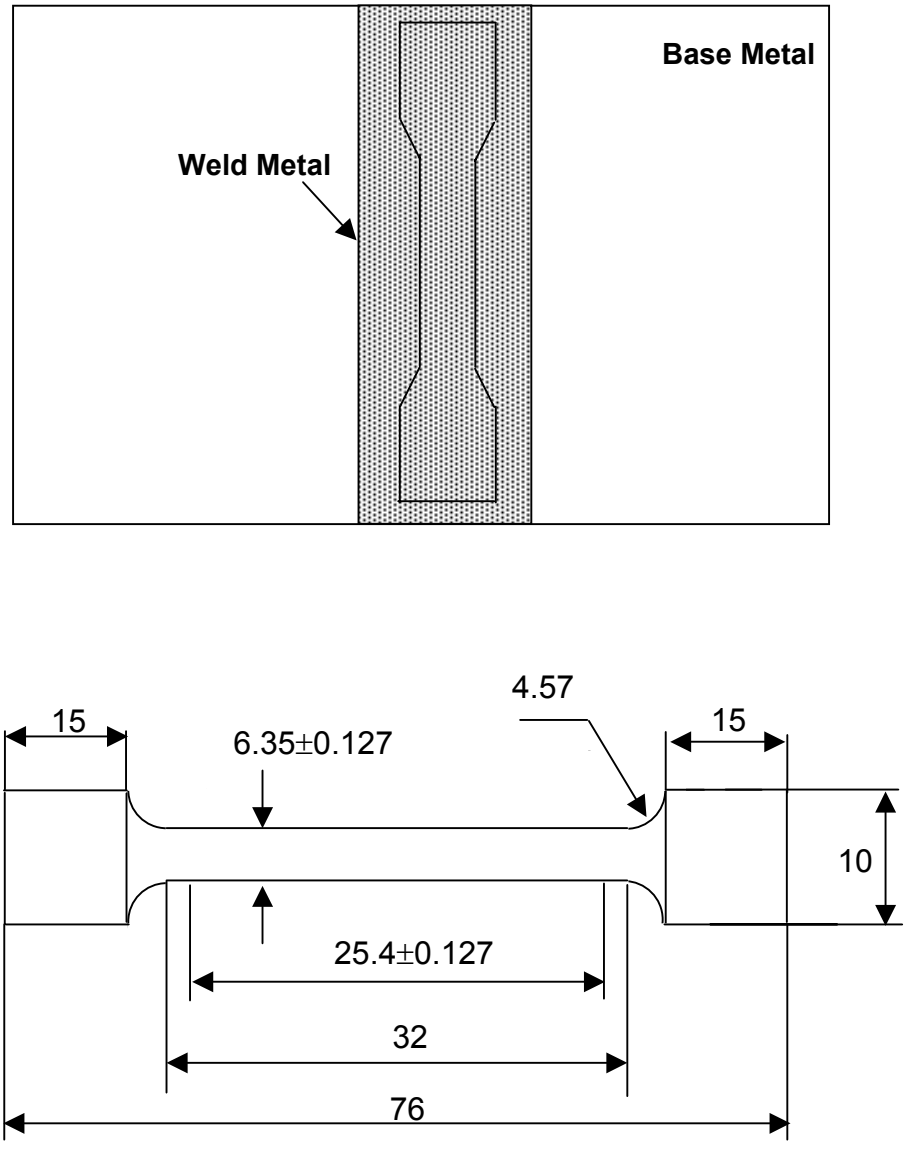


Figure 3.18 Schematic drawing of grove weld test pad for tension test specimen.

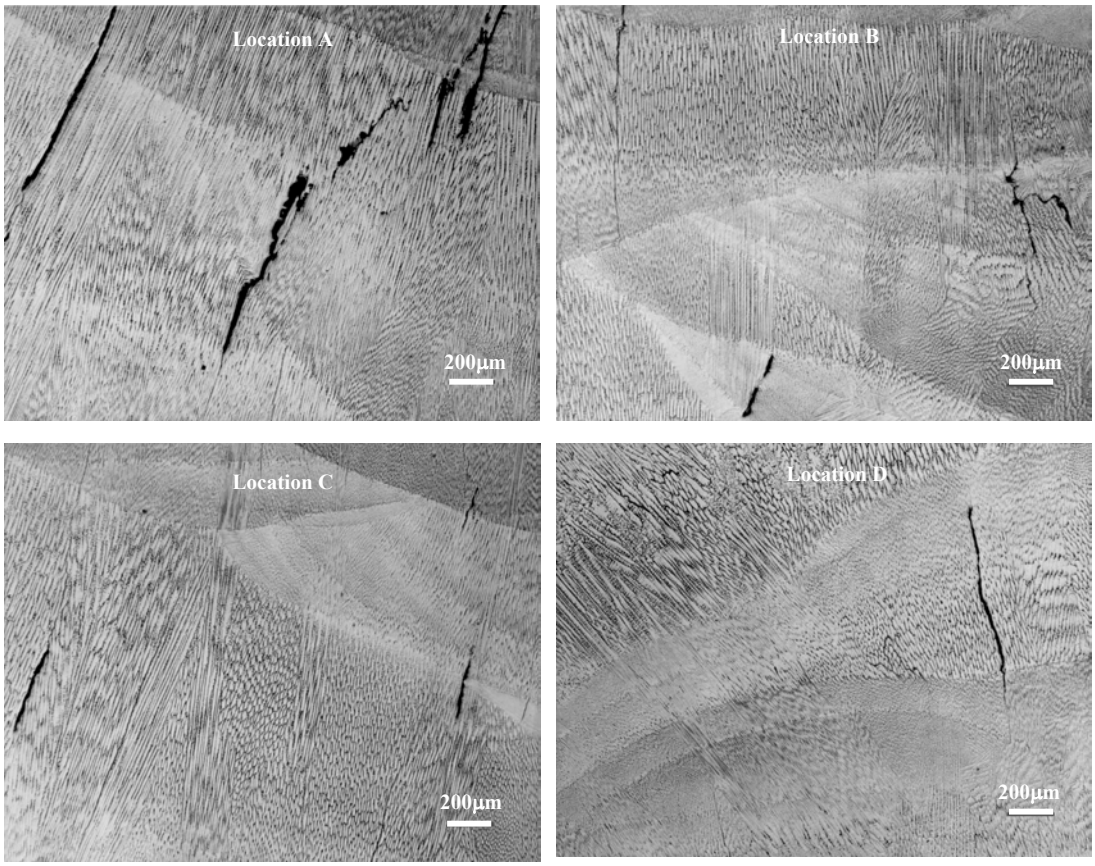


Figure 3.19 Microfissure morphologies on the transverse section of E308L coupon shown in Figure 3.17 for extraction of tensile sample.

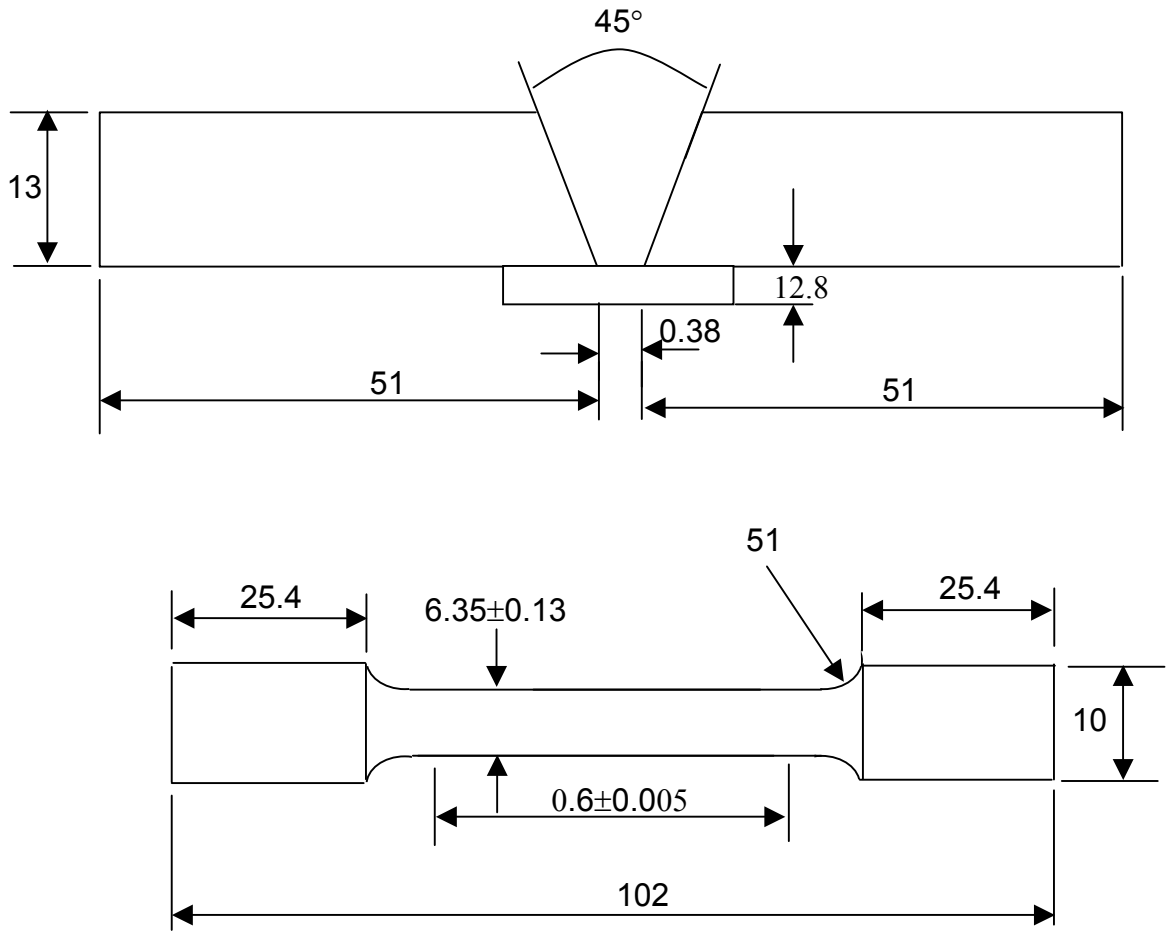


Note: All dimensions are in mm

Figure 3.20 Schematic sketch of weld coupon and the fatigue sample with circular section.

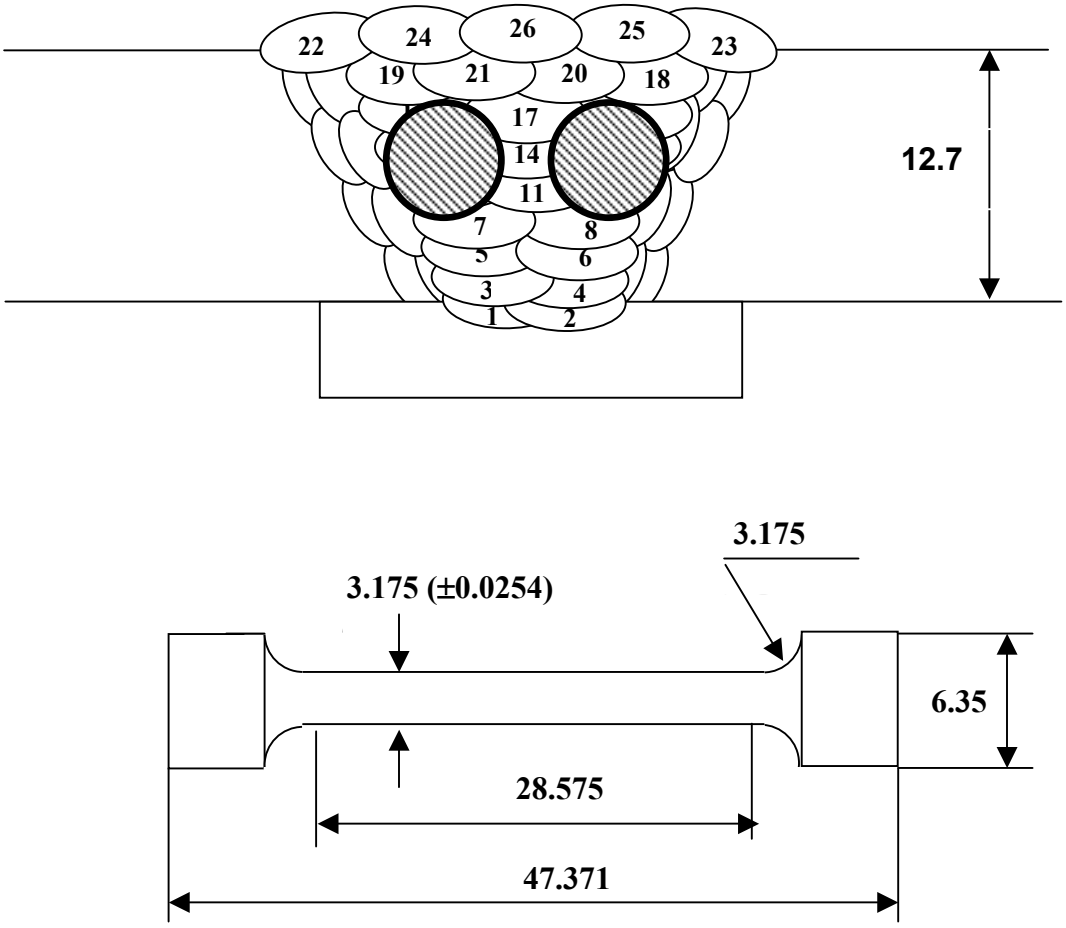


All units are in mm.

Figure 3.21 Weldment preparation and schematic drawing of creep sample.

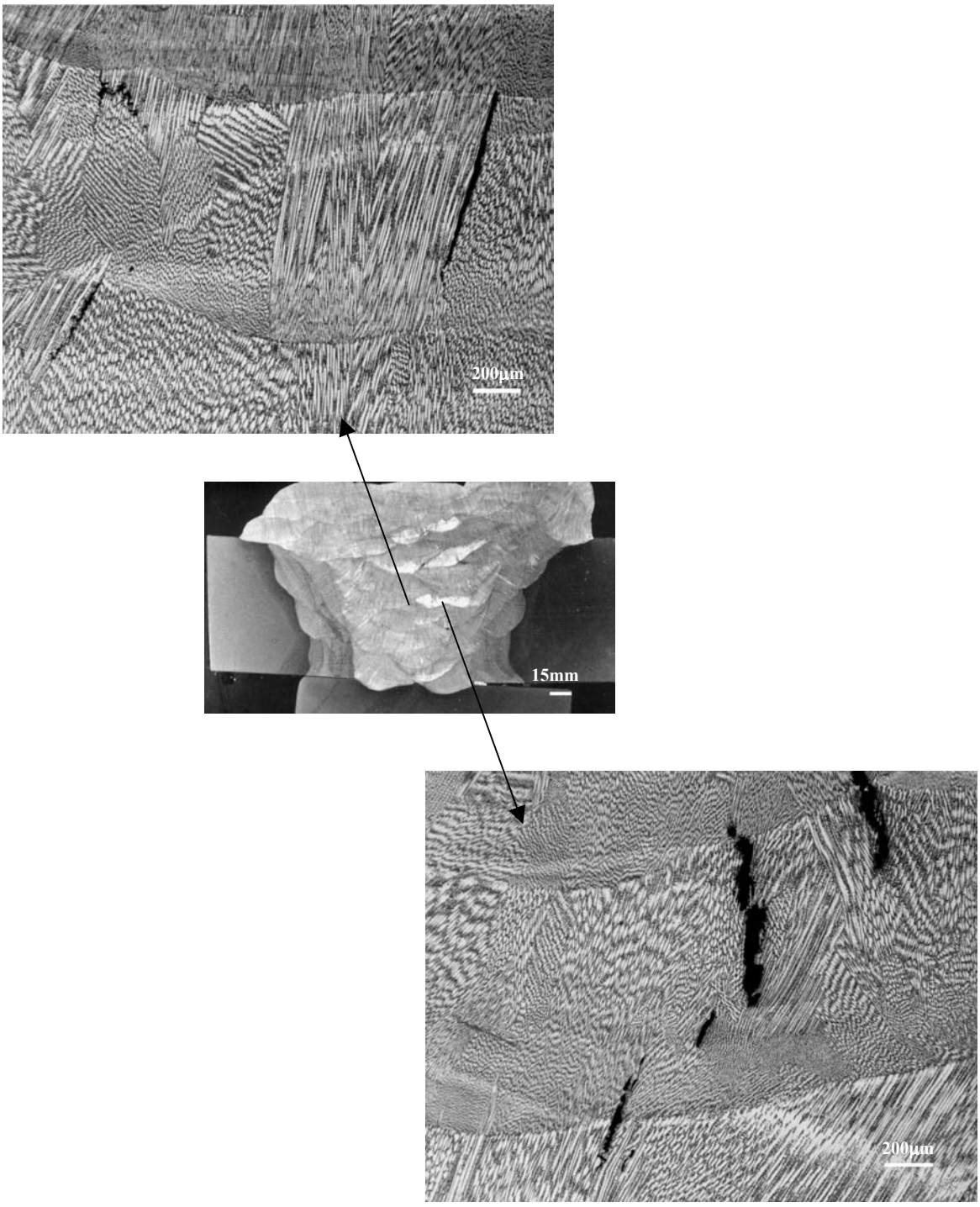


Figure 3.22 Microfissure morphologies on a transverse section of modified E316H coupon.

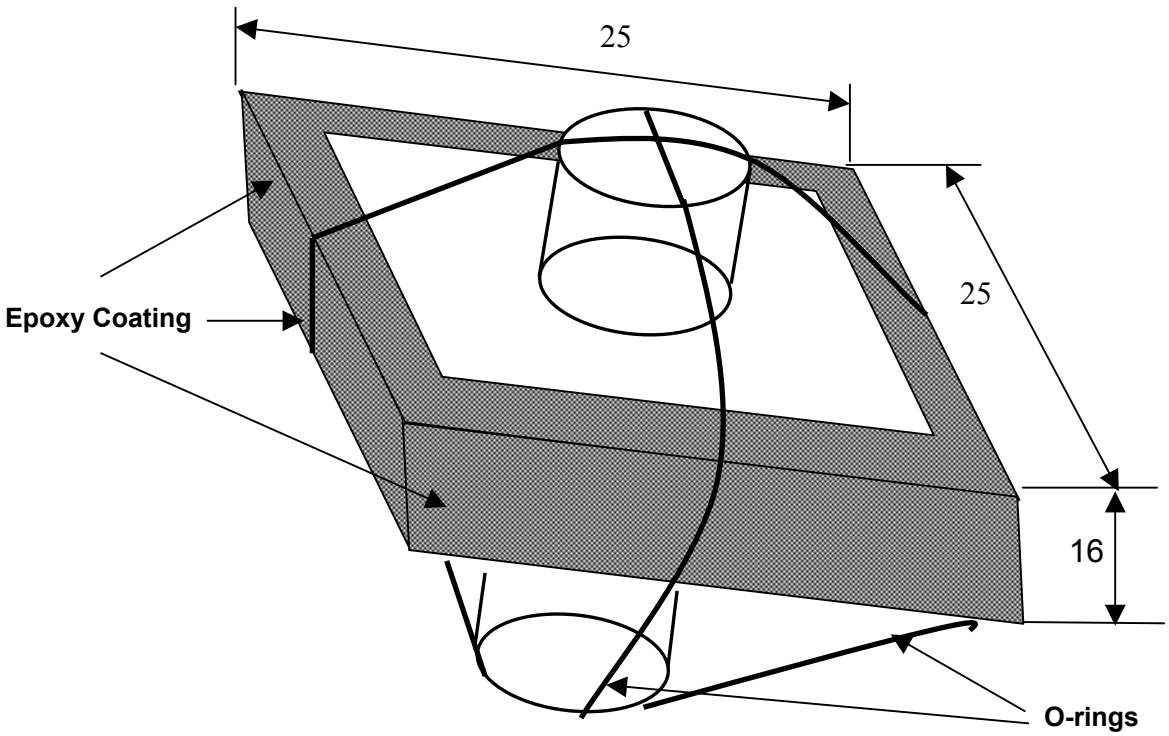


All units are in mm

Figure 3.23 Crevice corrosion test specimen.


Figure 3.24  Temperature controlled water bath.

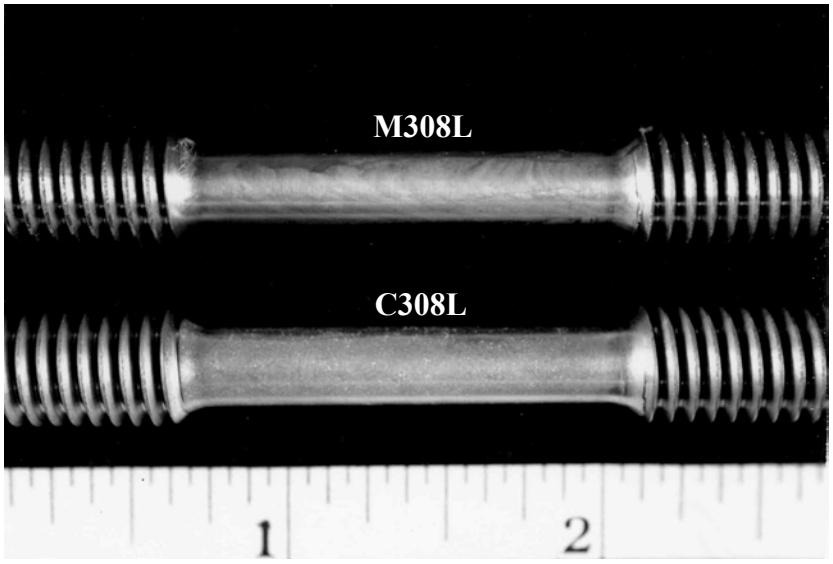


(a) M308L & C308L

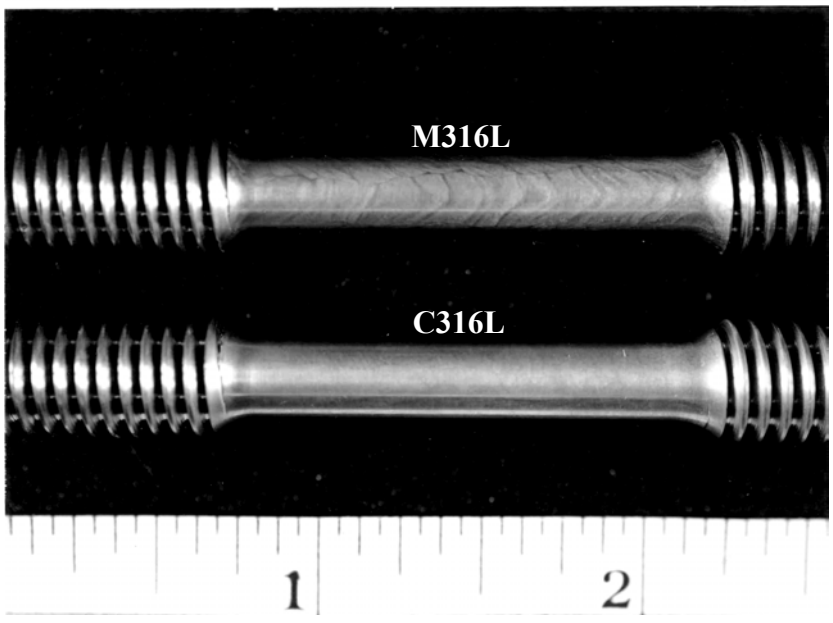


(b) M316L & C316L

Figure 3.25 Modified and commercial 316L samples polished and etched with 10% oxalic acid before tensile testing.

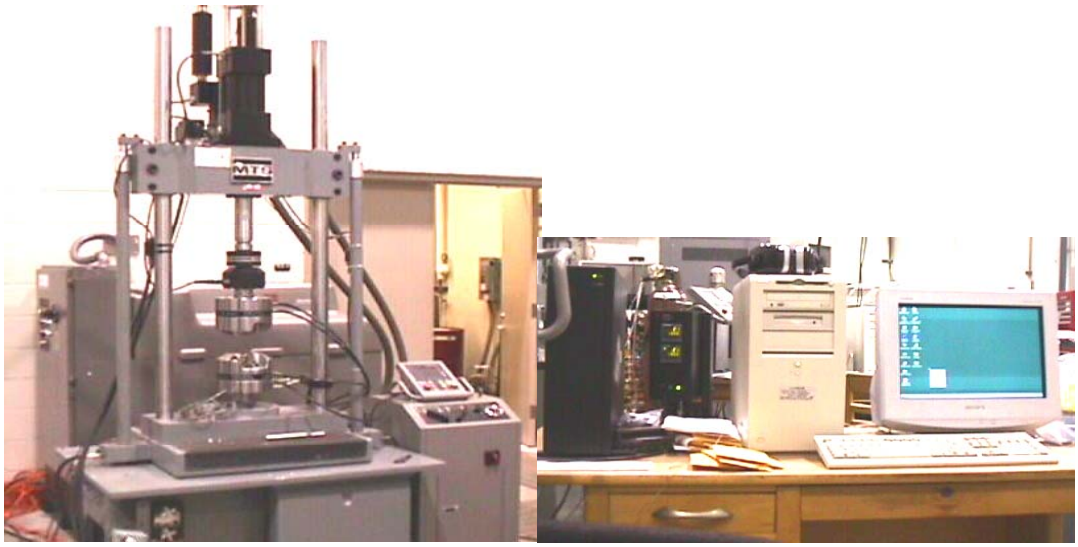


Figure 3.26 A computer-controlled Material Test System (MTS) servohydraulic fatigue testing machine.

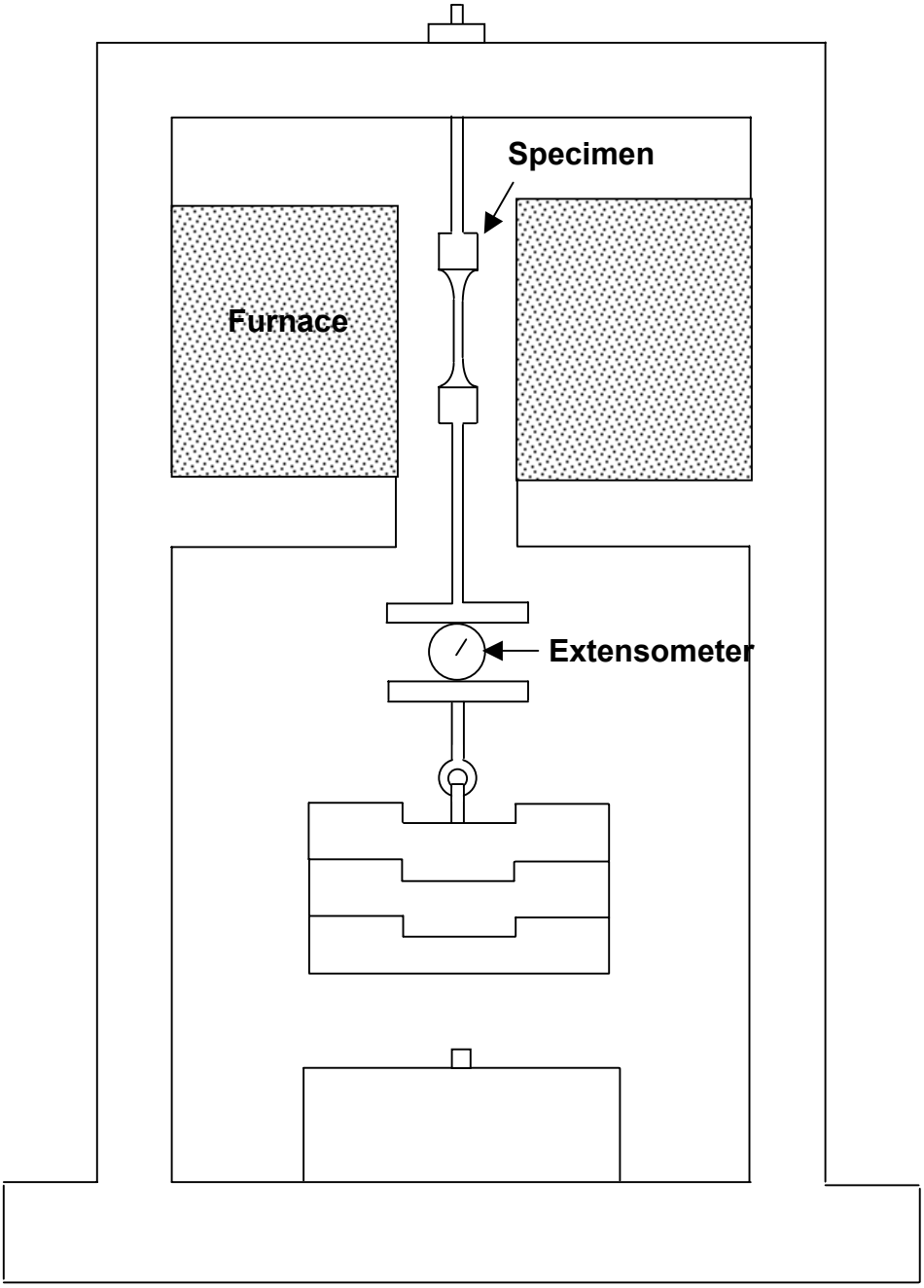


Figure 3.27 Schematic of creep frame.

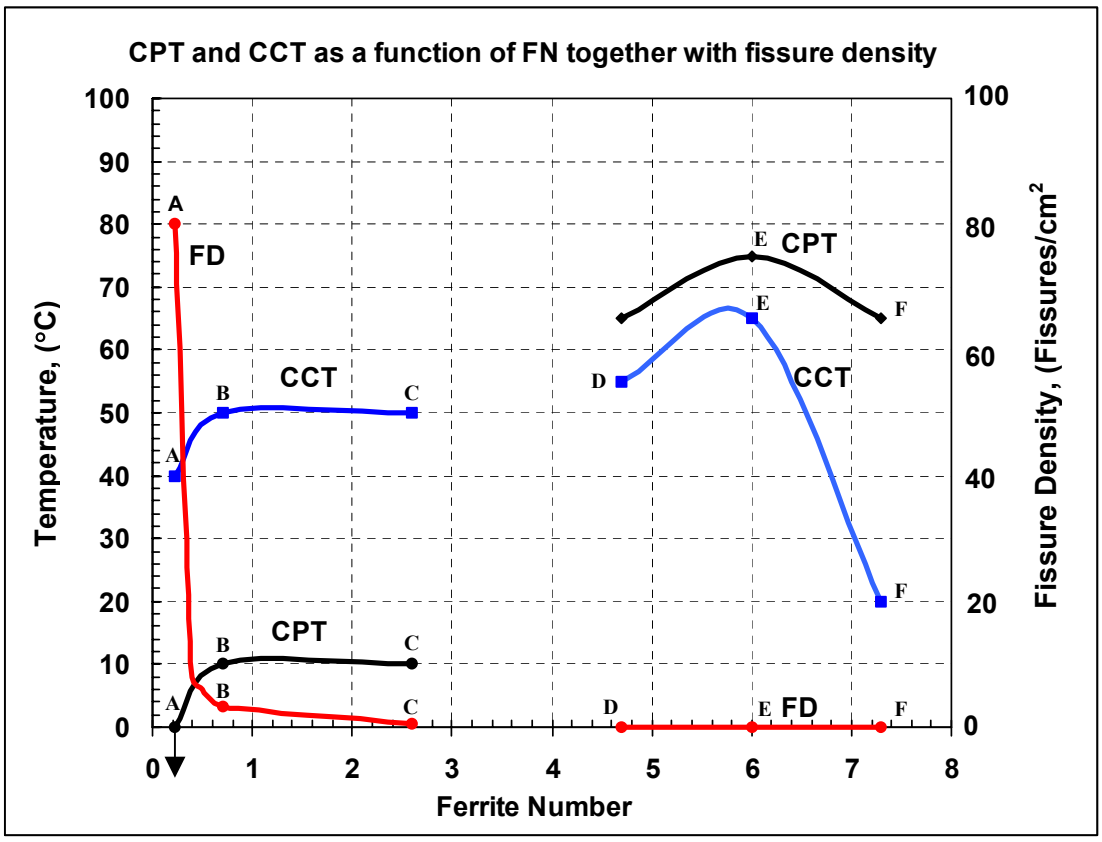


Figure 4.1 CPT and CCT as a functiion of Ferrite Number together with the corresponding microfissure density for E308L weld deposits in 1% $FeCl_3$.

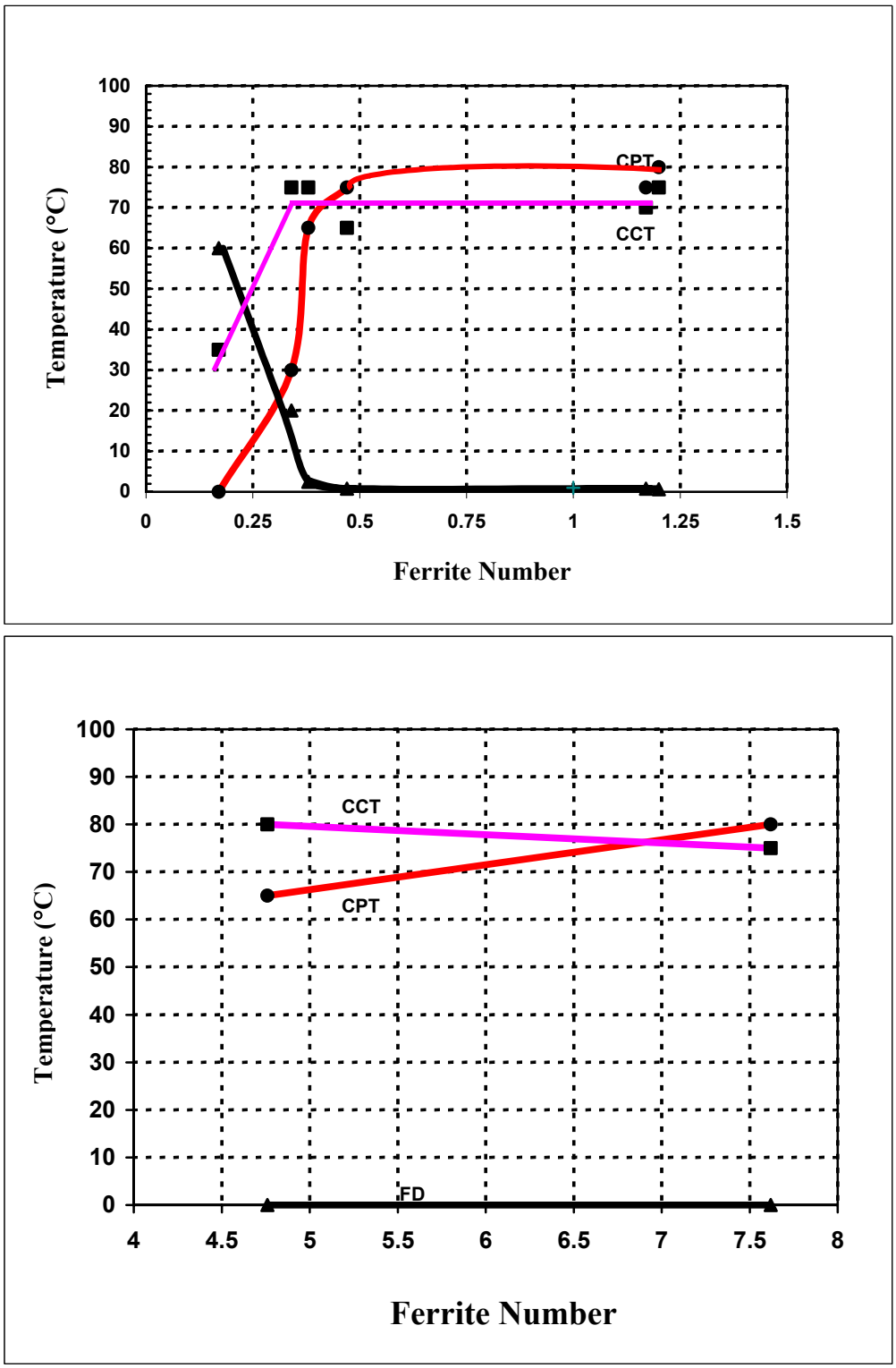


Figure 4.2 CPT and CCT as a functiion of Ferrite Number together with the corresponding microfissure density for E308L weld deposits in 3% $FeCl_3$.

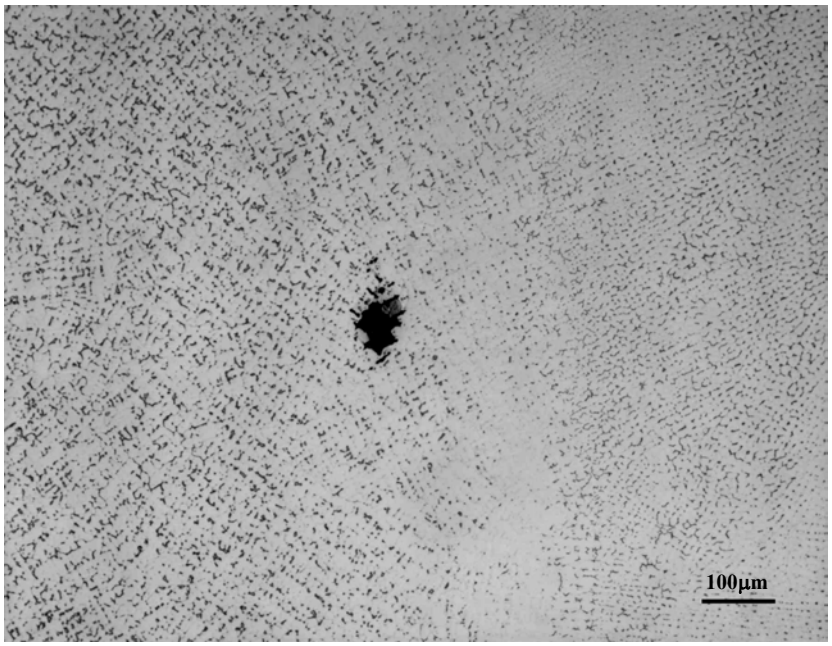


(a)

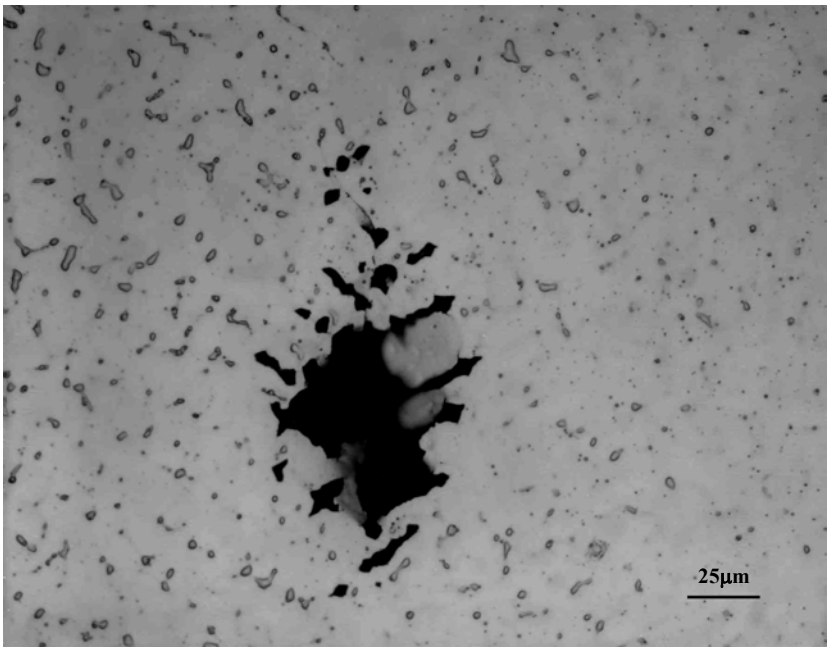


(b)

Figure 4.3 Pits initiated at the tip of microfissure of 316L (KK316L) at CPT (80°C) [FN=1.2, Microfissure Density=0.12 microfissures/cm$^2$], (a)-100X, (b)-400X.

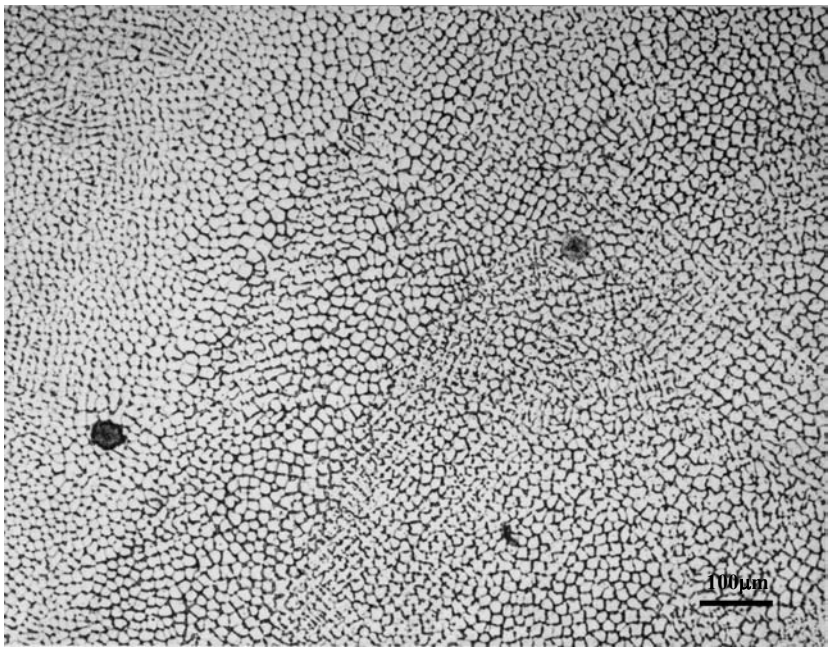


(a)

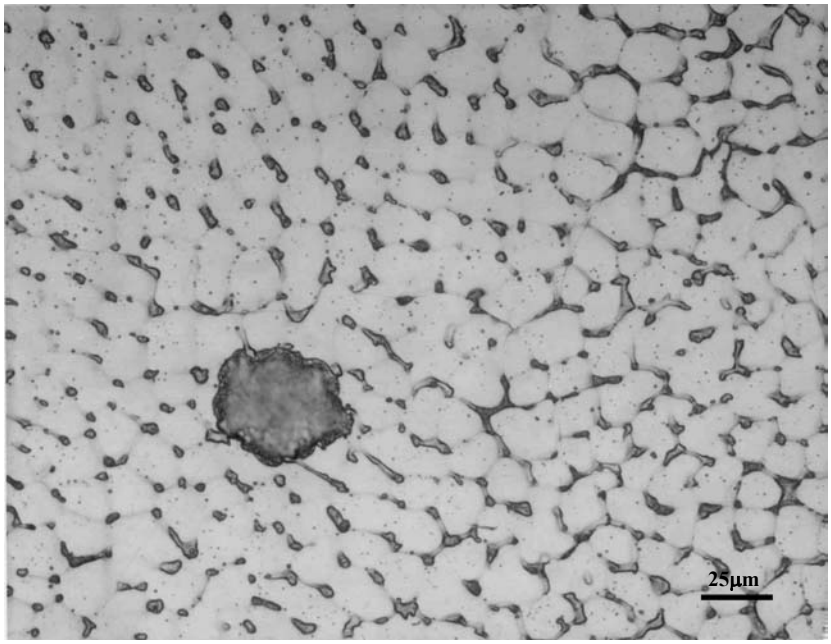


(b)

Figure 4.4 Pits morphologies of 316L (316L-A) at CPT (65°C) [FN=0.47, Microfissure Density=0.5 microfissures/$cm^2$], (a)-100X, (b)-400X.

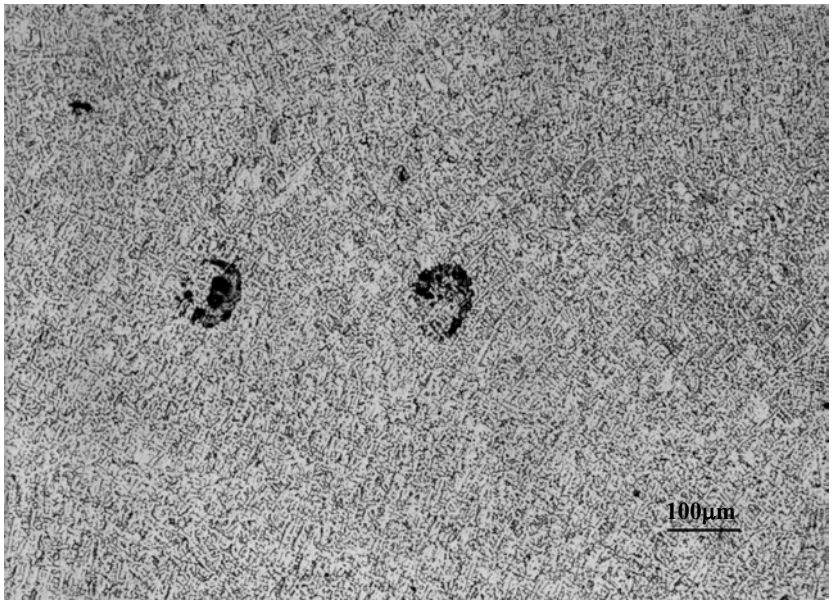


(a)

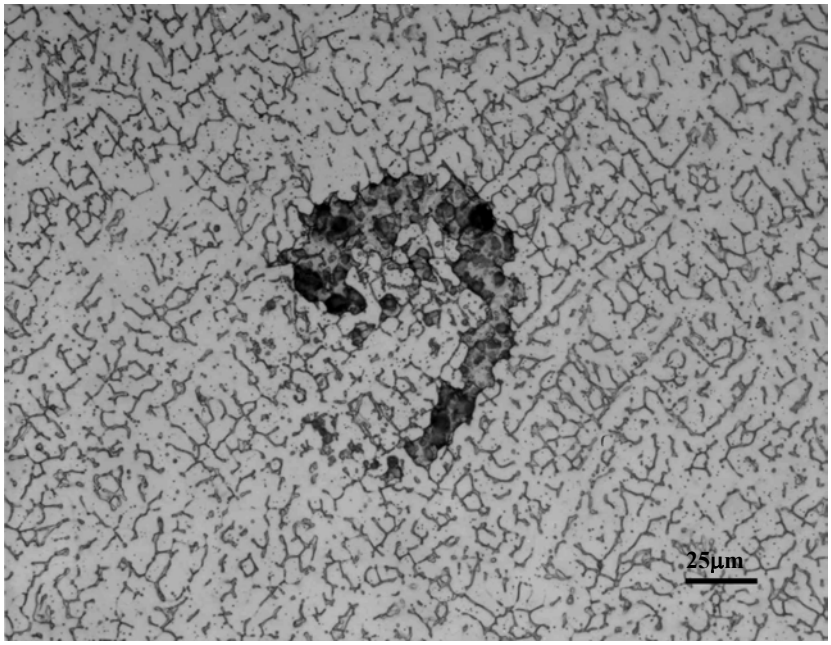


(b)

Figure 4.5 Pits morphology of 316L-D at CPT (80°C), Microfissure Density=0, (a)-100X, (b)-400X.

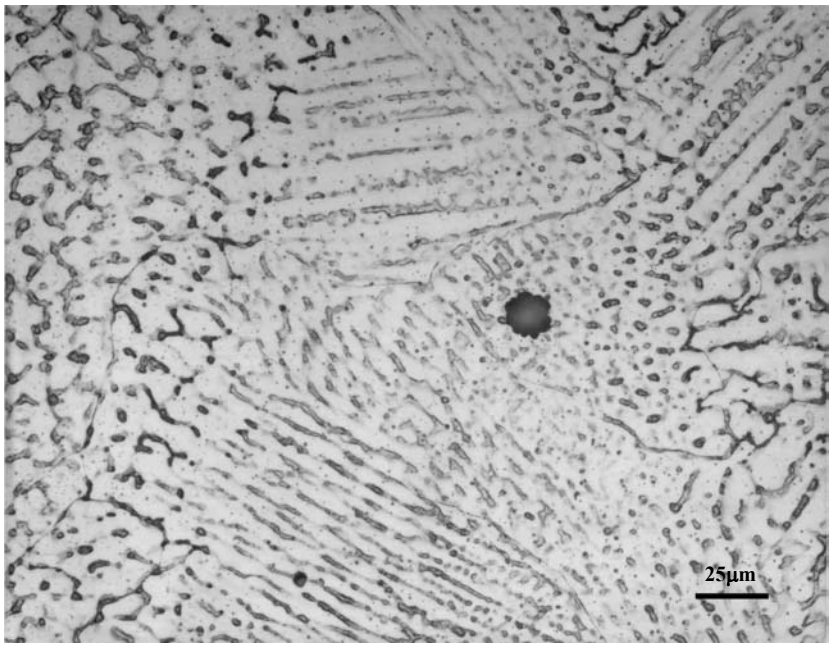


Figure 4.6 Pit morphology of 316L (316L-B-) at CPT (75°C), [FN=1.17, Microfissure Density=0.16 microfissures/cm$^2$], 400X.

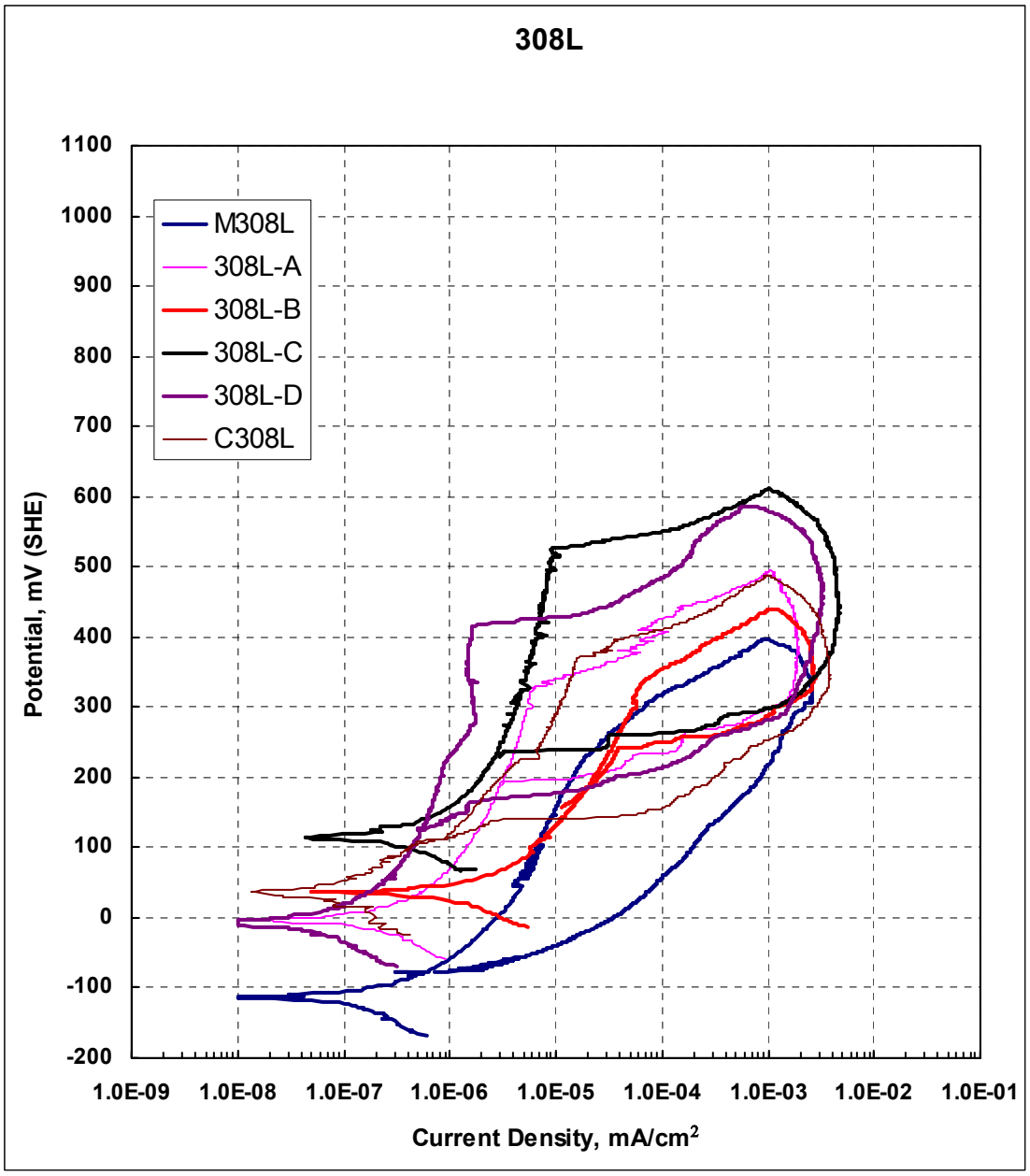


Figure 4.7 Typical cyclic polarization curves of E308L samples in 3.5% sodium chloride solution.

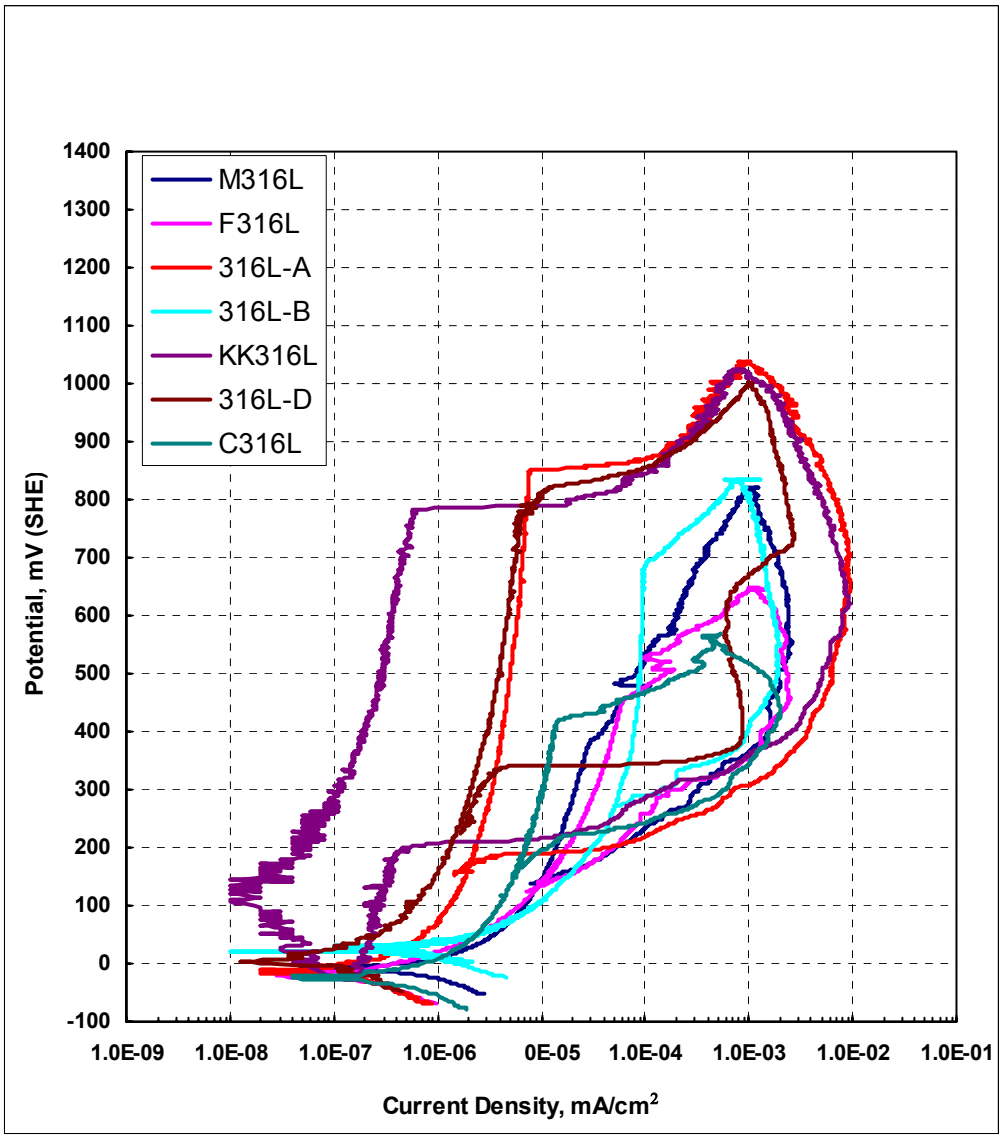


Figure 4.8 Typical cyclic polarization curves of E316L samples in 3.5% sodium chloride solution.

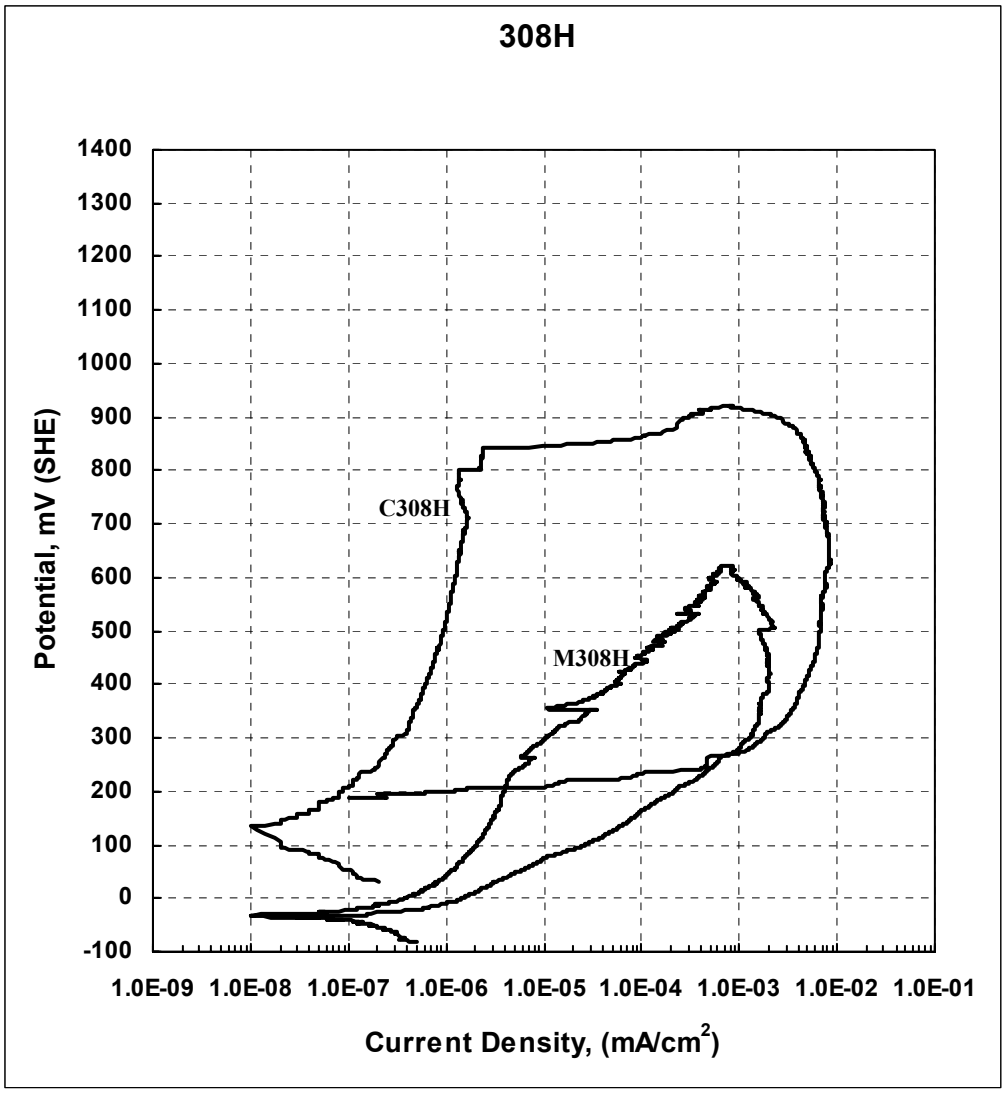


Figure 4.9 Typical cyclic polarization curves of E308Hsamples in 3.5% sodium chloride solution.

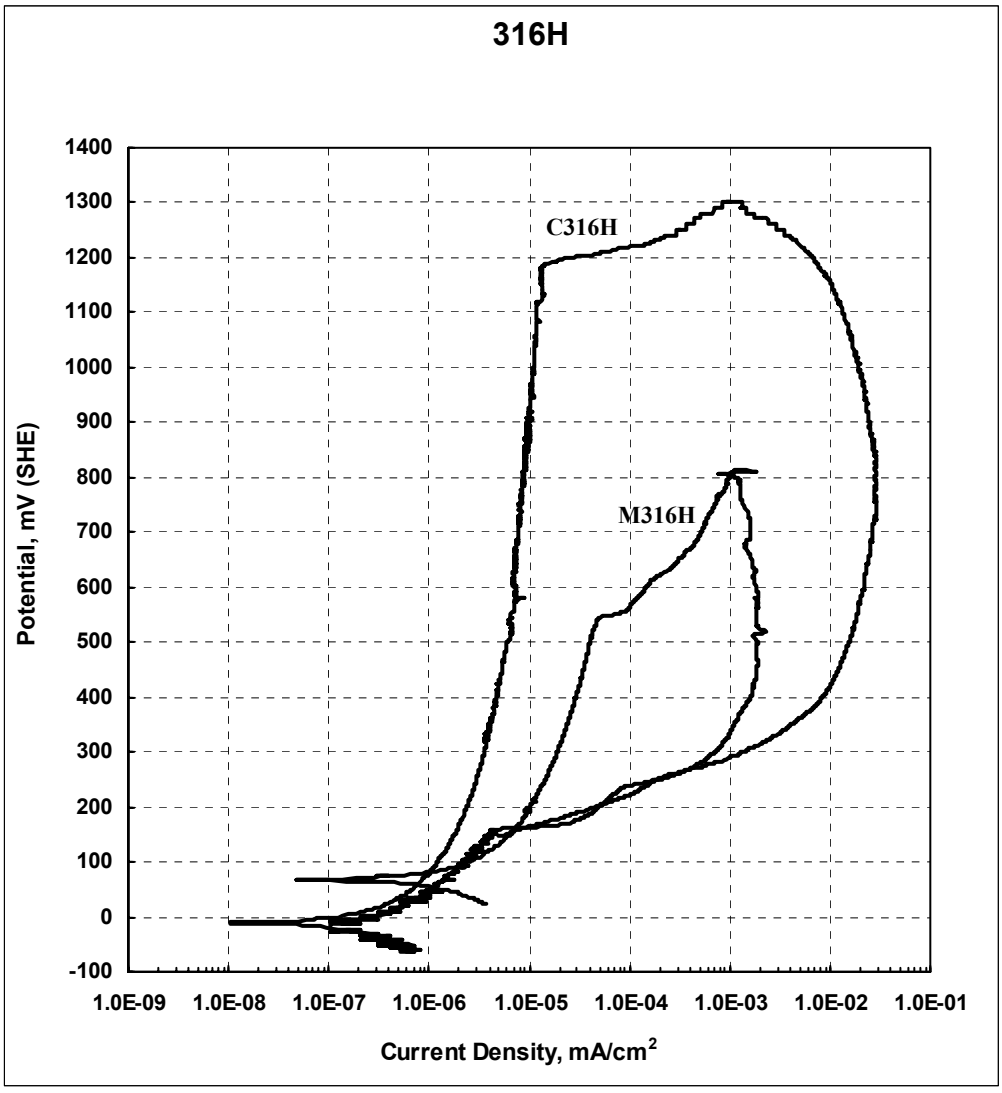


Figure 4.10 Typical cyclic polarization curves of E316H samples in 3.5% sodium chloride solution.

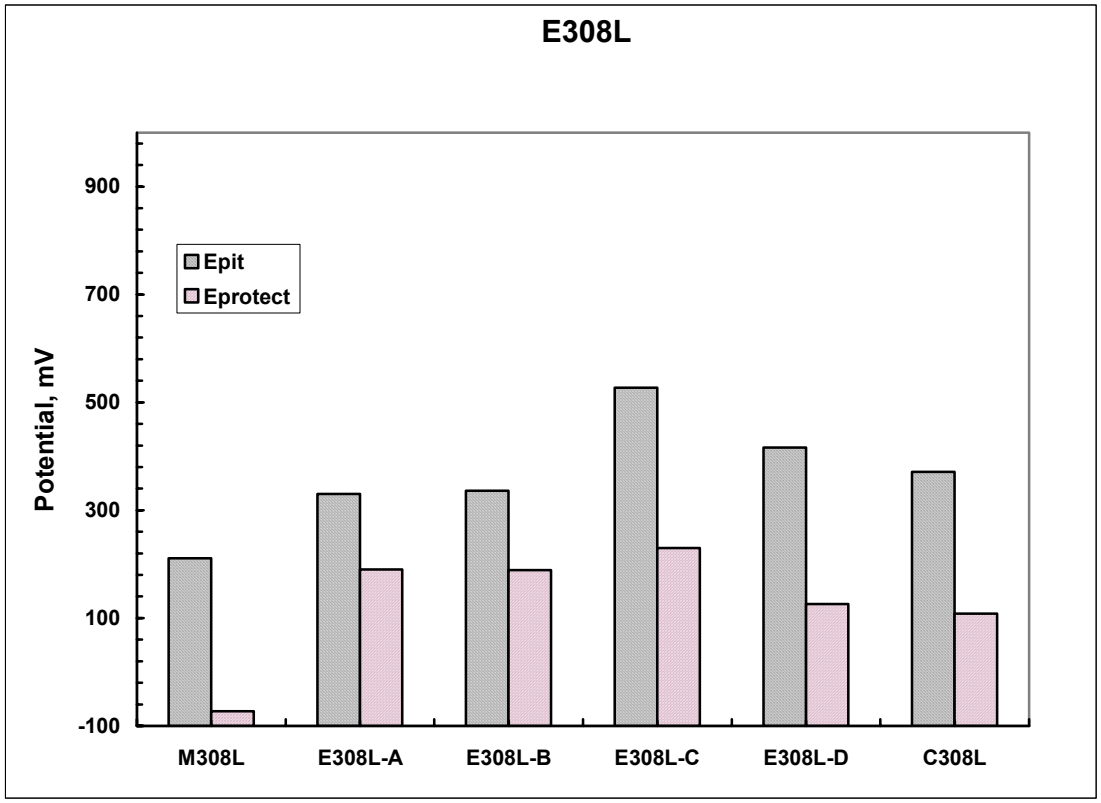


Figure 4.11 $E_{pit}$ and $E_{prot}$ of E308L in cyclic polarization test in 3.5% sodium chloride.

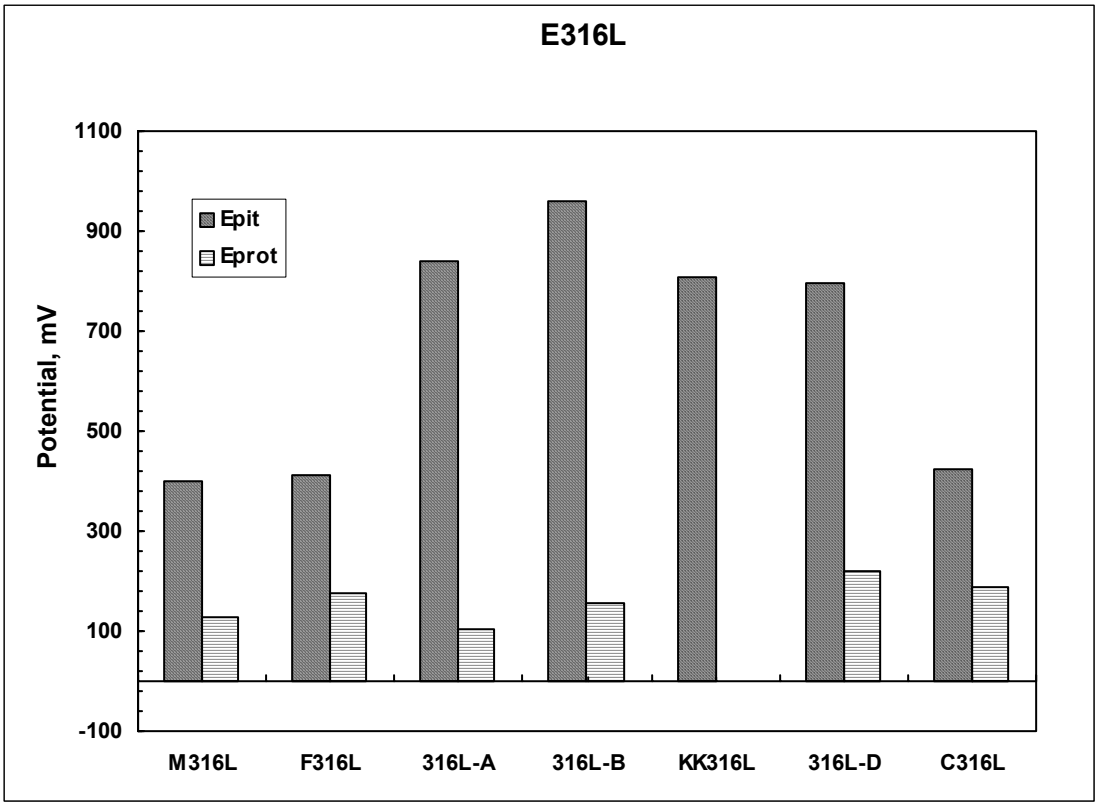


Figure 4.12 $E_{pit}$ and $E_{prot}$ of E316L in cyclic polarization test in 3.5% sodium chloride solution.

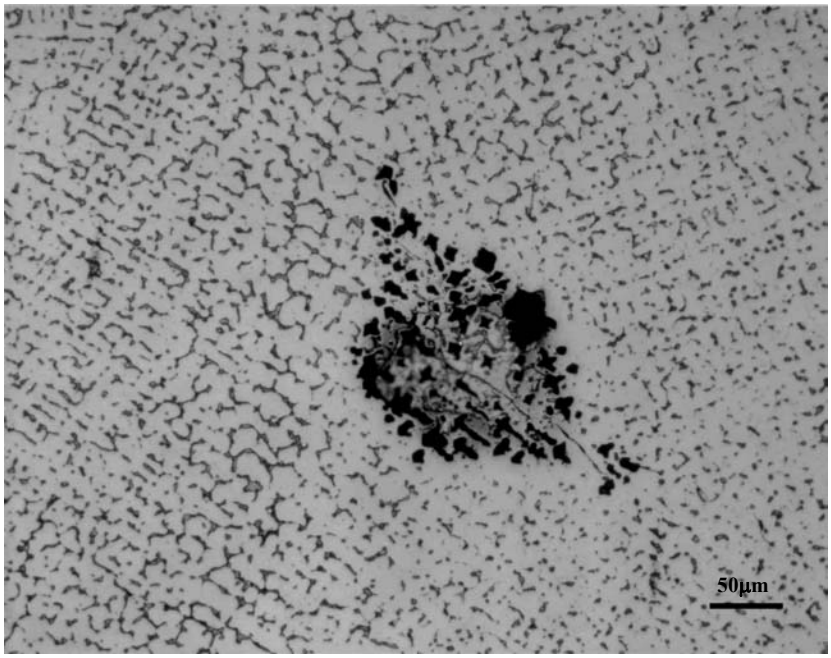


Figure 4.13 Pits initiated along the microfissure of 316L-A at CPT (65°C) [FN=0.47, Microfissure Density=0.38 microfissures/cm$^2$], 200X.

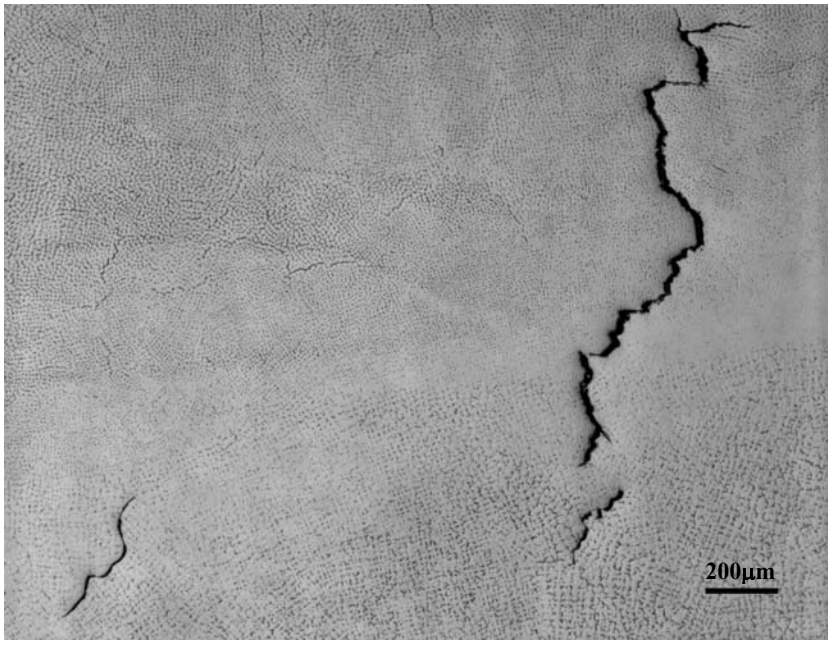


(a) Before Pitting Immersion testing

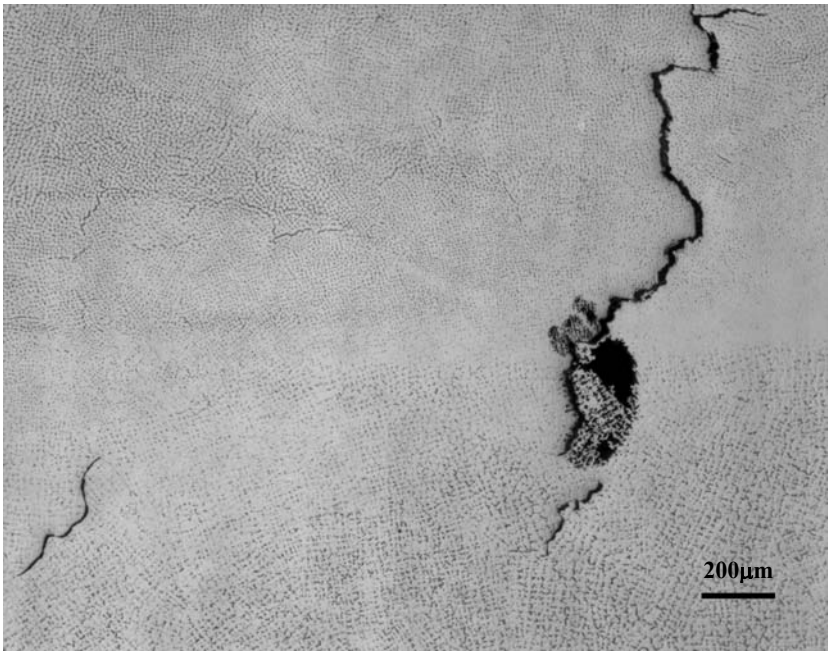


(b) After Pitting Immersion testing

Figure 4.14 Photomicrographs of modified 316L before and after pitting immersion testing at CPT (1°C) in 3% ferric chloride solution, 50X.

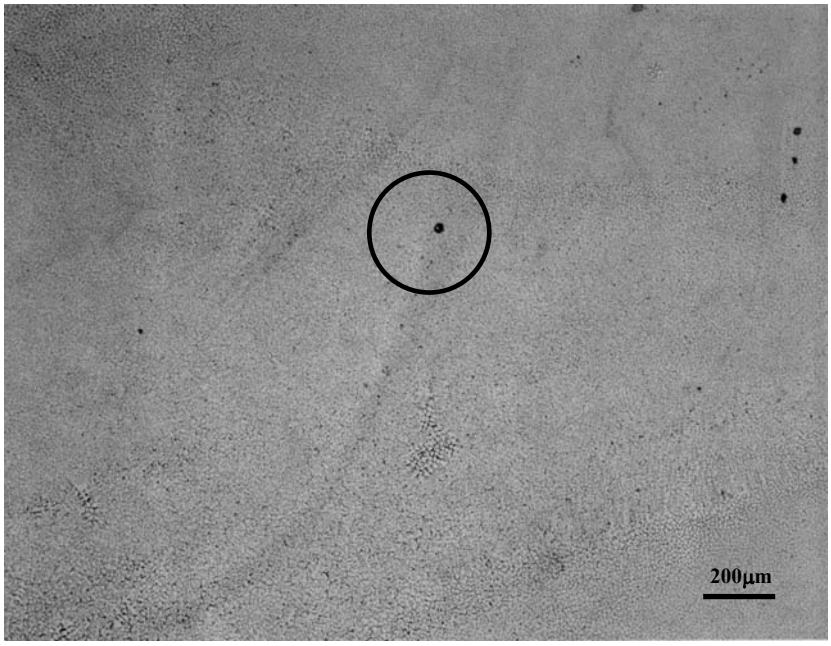


(a)

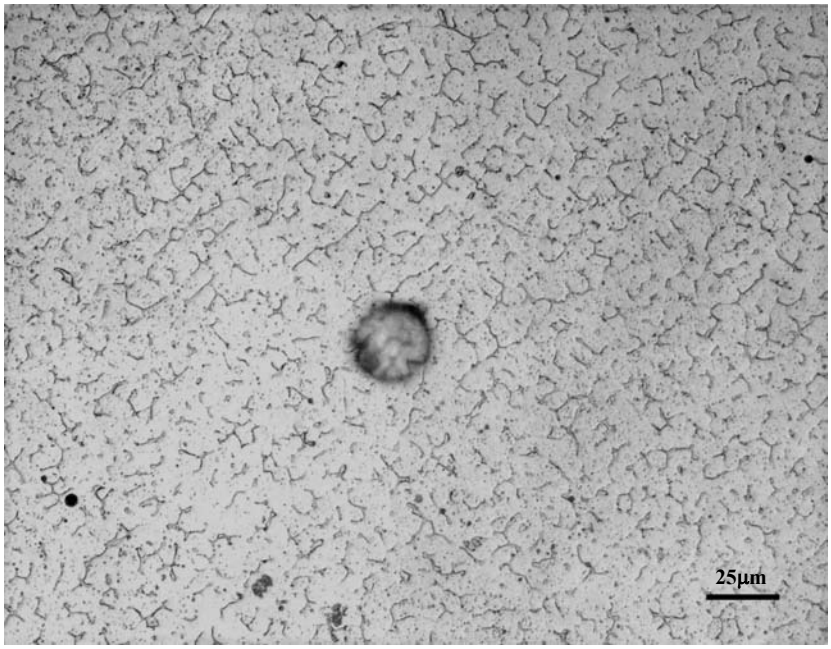


(b)

Figure 4.15 Pitting initiated at the fusion line of C316L sample in pitting immersion corrosion testing at CPT, 65°C, (a)-50X, (b)-400X.

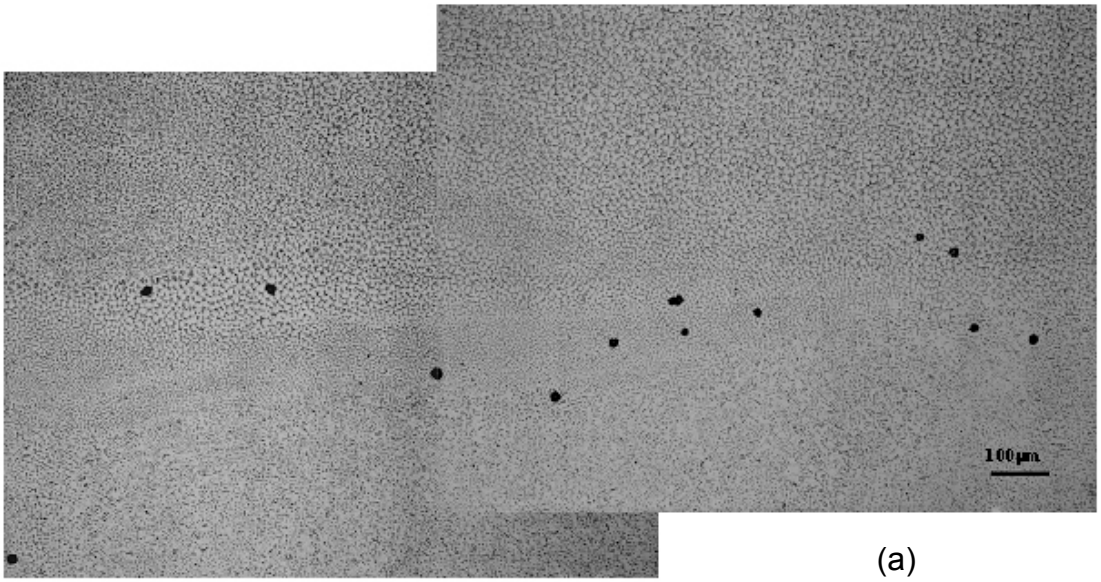


(a)

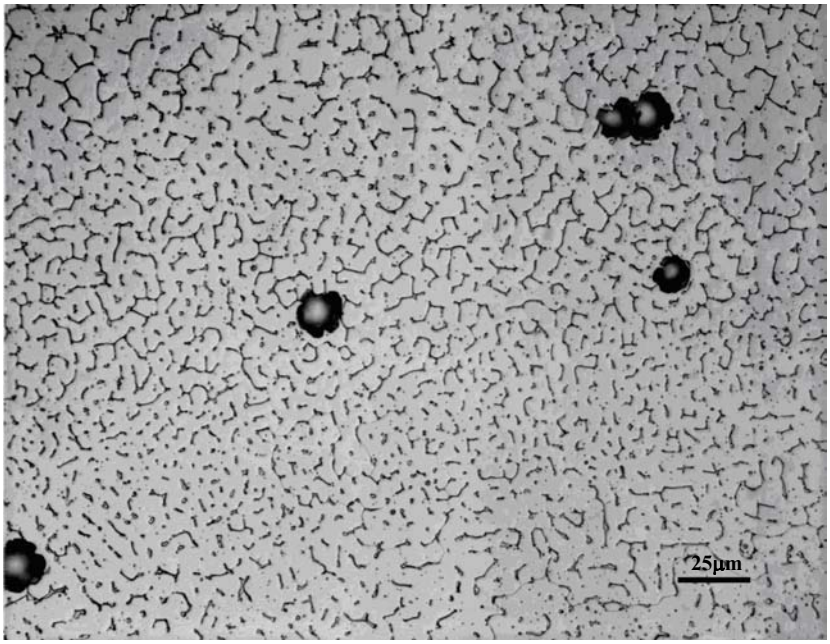


(b)

Figure 4.16 Pitting morphology of commercial 316L (fissure-free) at the overlap region in pitting immersion testing at 80°C, (a)-100X, (b)-400X.

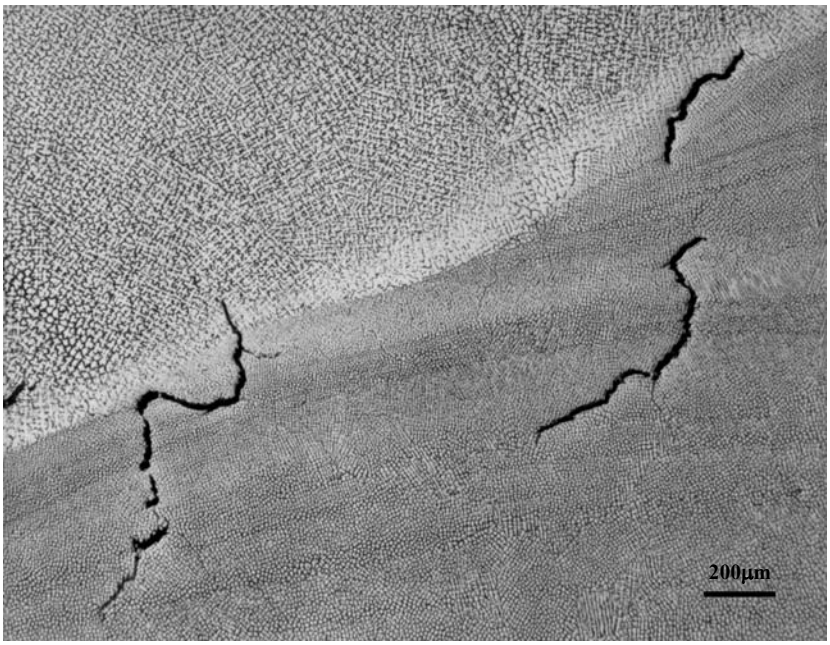


(a) Before Cyclic Polarization Test

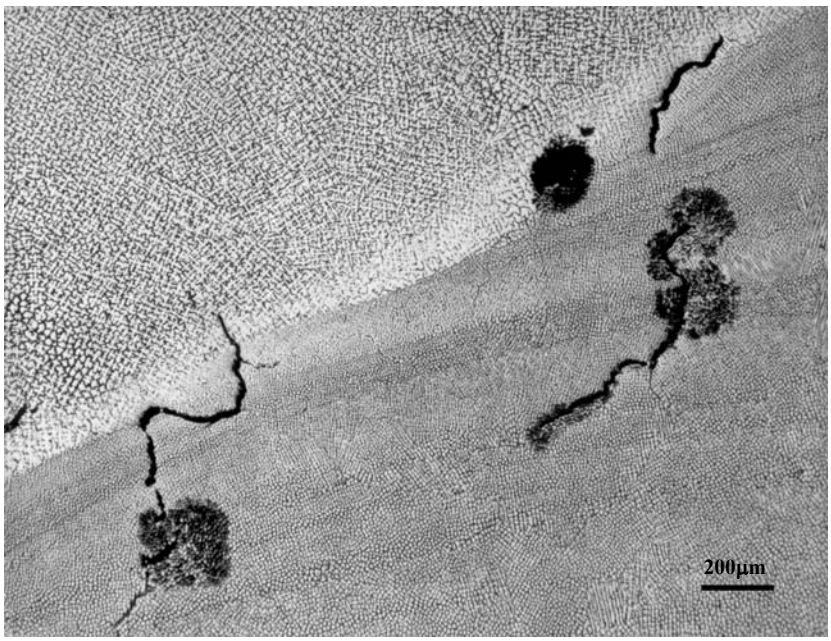


(b) After Cyclic Polarization Test

Figure 4.17 Photomicrographs of M316L before and after cyclic polarization test (3.5% sodium chloride at 22°C in deaerated conditions), 50X.

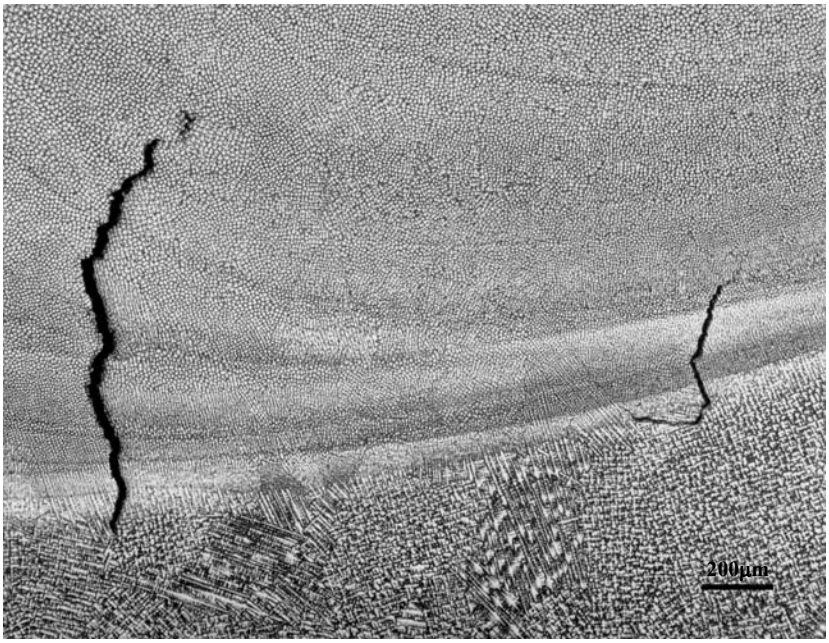


(a) Before Cyclic Polarization Test

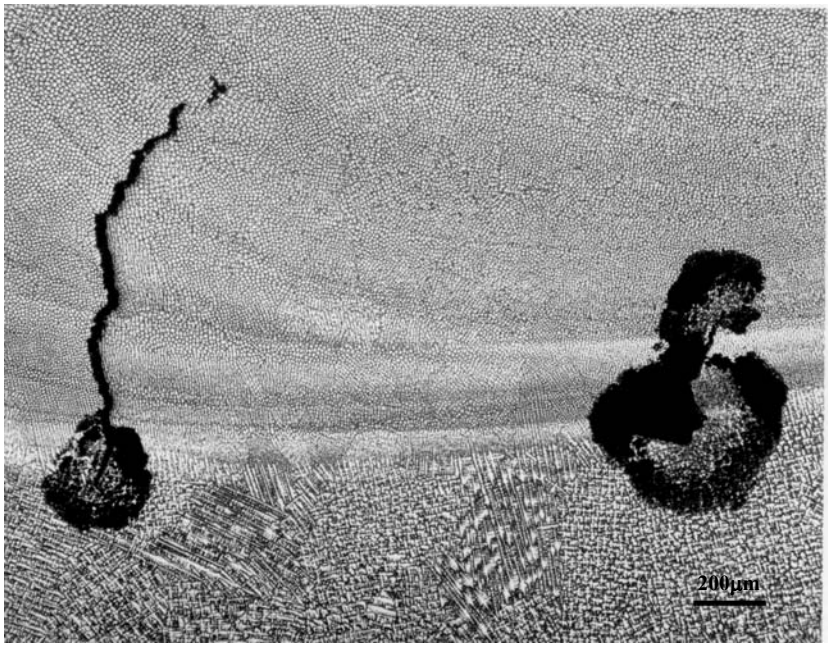


(b) After Cyclic Polarization Test

Figure 4.18 Photomicrographs of M316H before and after cyclic polarization test (3.5% sodium chloride at 22°C in deaerated conditions), 50X.

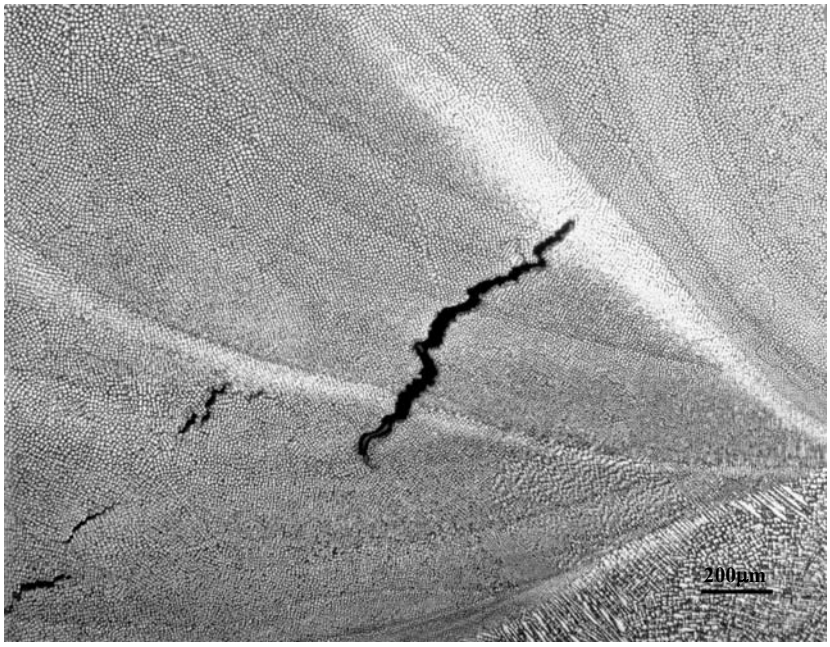


(a) Before Cyclic Polarization Test

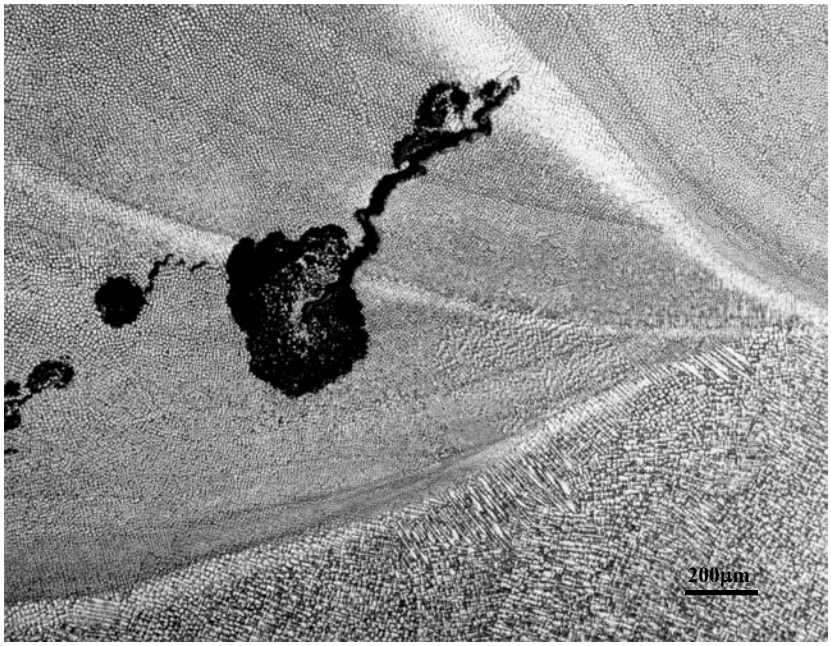


(b) After Cyclic Polarization Test

Figure 4.19 Photomicrographs of M316H before and after cyclic polarization test (3.5% sodium chloride at 22°C in deaerated conditions), 50X.

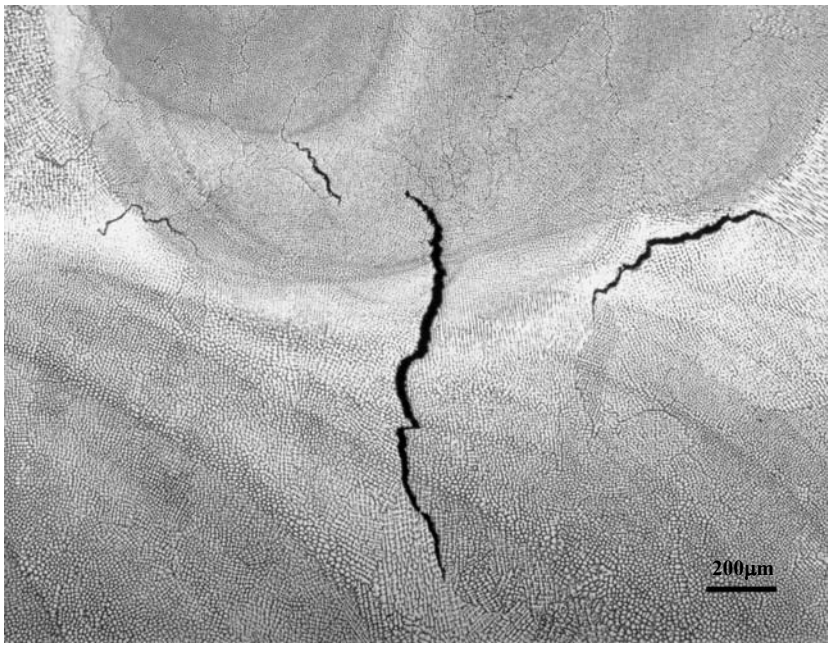


(a) Before cyclic polarization test

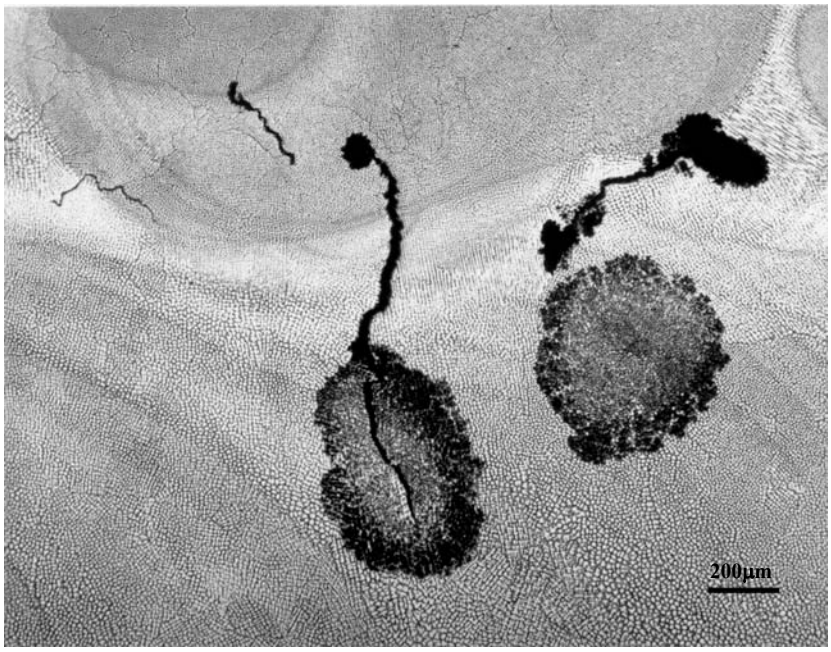


(b) After cyclic polarization test

Figure 4.20 Photomicrographs of M316H before and after cyclic polarization test (3.5% sodium chloride at 22°C in deaerated conditions), 50X.

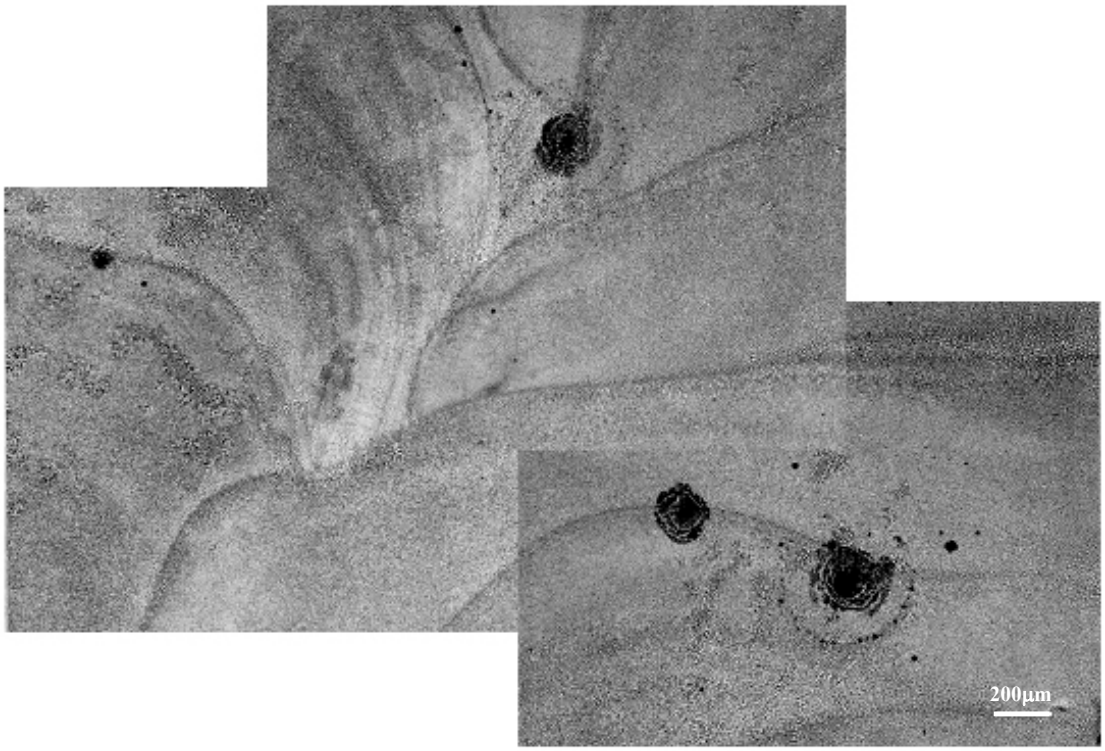


Figure 4.21 Typical pitting morphology of commercial 316H (fissure-free) deposit after cyclic polarization test (3.5% sodium chloride at 22°C, 50X.

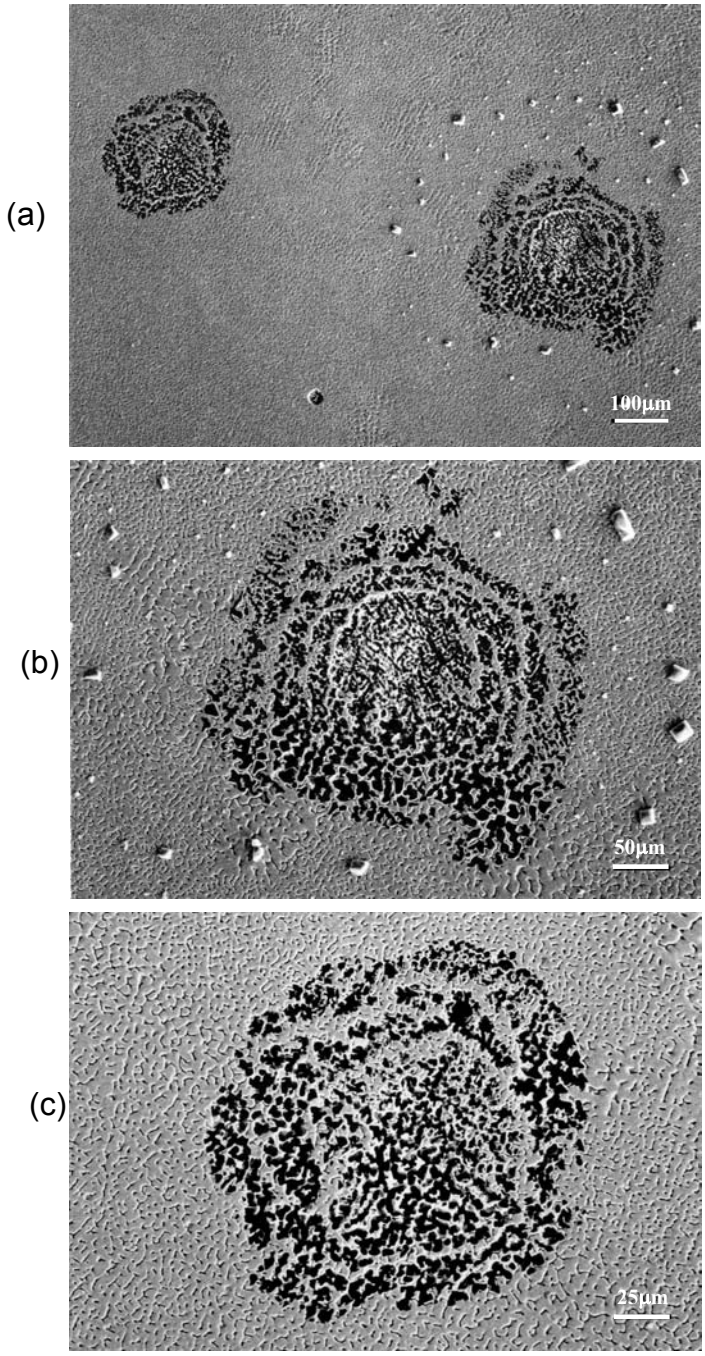


Figure 4.22 Typical pitting morphology of commercial 316L (fissure-free) deposit in location A in Figure 4.21 after cyclic polarization test in SEM (3.5% sodium chloride at 22°C, (a)-100X, (b)-200X, (c)-400X.

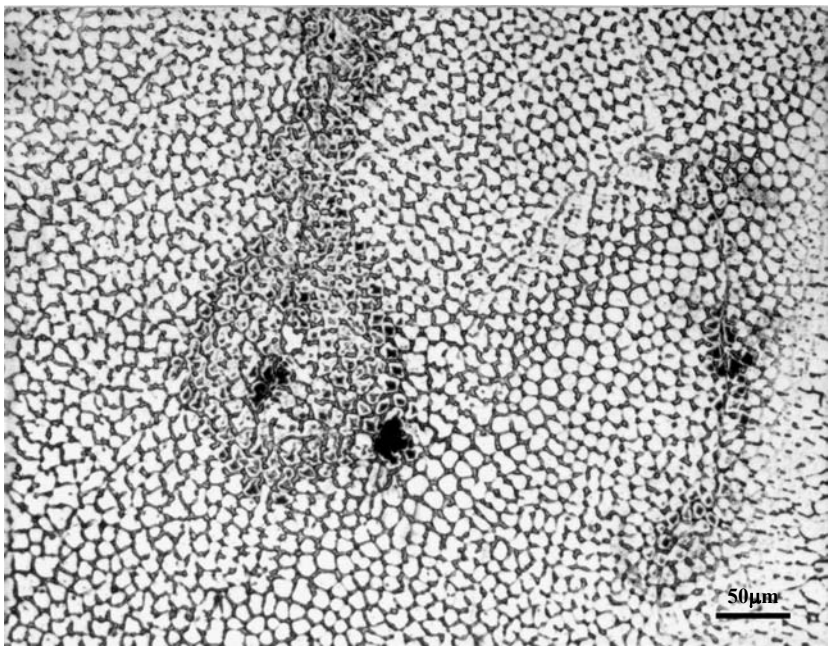


(a)

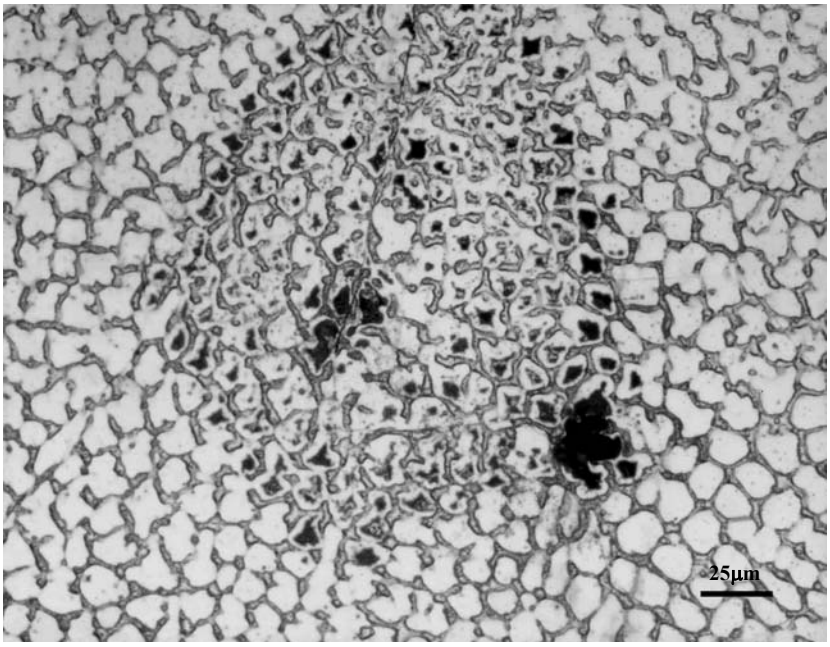


(b)

Figure 4.23 Pits initiated from austenite of 316L-B sample at CPT (75°C-3% FeCl3) [FN=1.2], (a)-200X, (b)-400X.

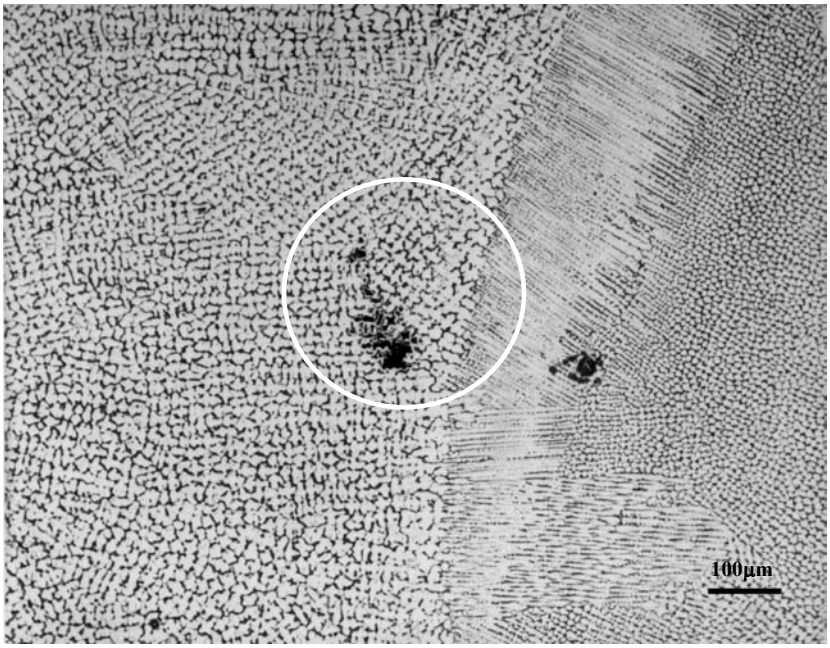


(a)

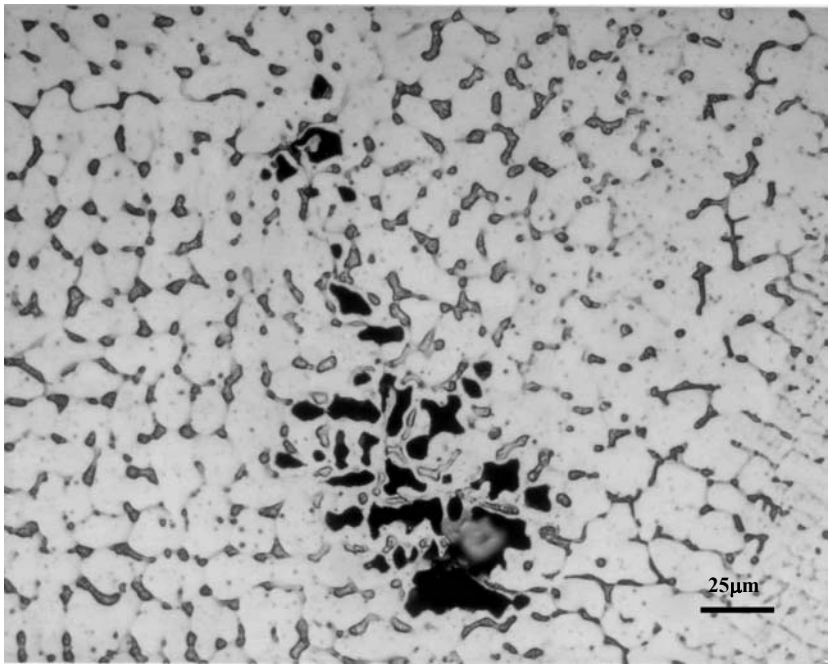


(b)

Figure 4.24 Pits initiated from austenite of 316L-A sample at CPT (65°C-3% FeCl3). [FN=0.47], (a)-100X, (b)-400.

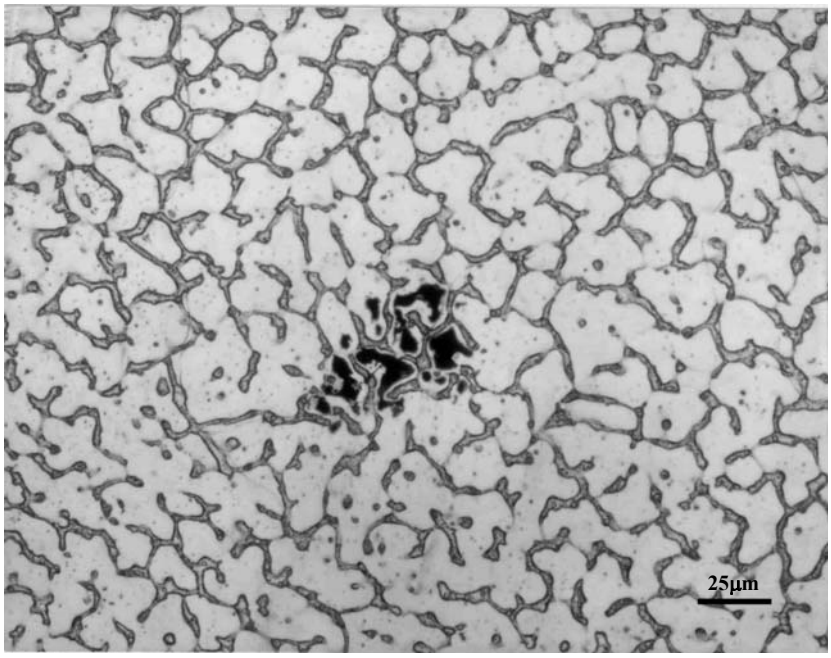


Figure 4.25 Pits initiated from austenite of 316L-B sample at CPT (75°C-3% $FeCl_3$) [FN=1.17, Microfissure Density=0.16 microfissures/$cm^2$], 400X.

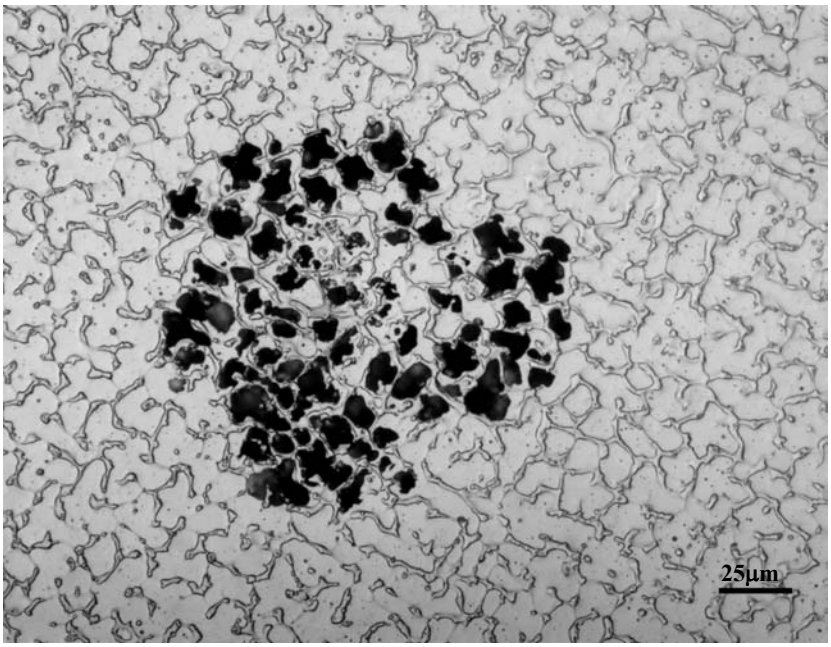


Figure 4.26 Pits initiated from austenite of 316H sample at CPT (75°C-6% $FeCl_3$) [FN=4.5], 400X.

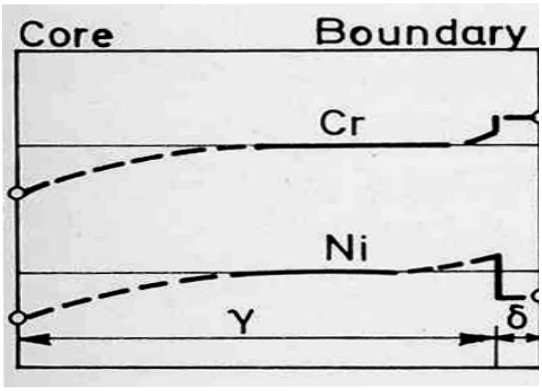


Figure 4.27 Schematic representation of the segregations and the distributions of chromium and nickel during AF mode solidification of an austenitic weld metal [91].

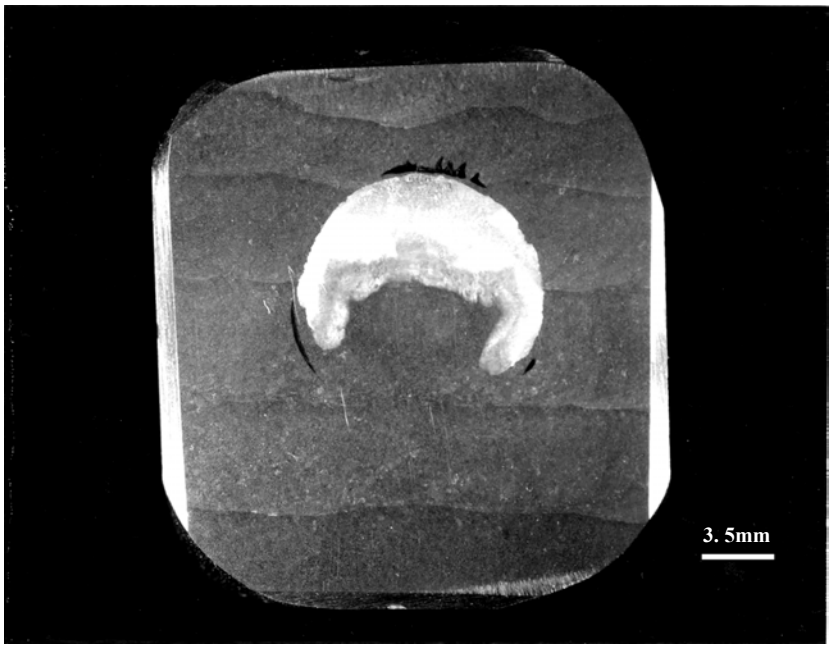


(a) 75°C

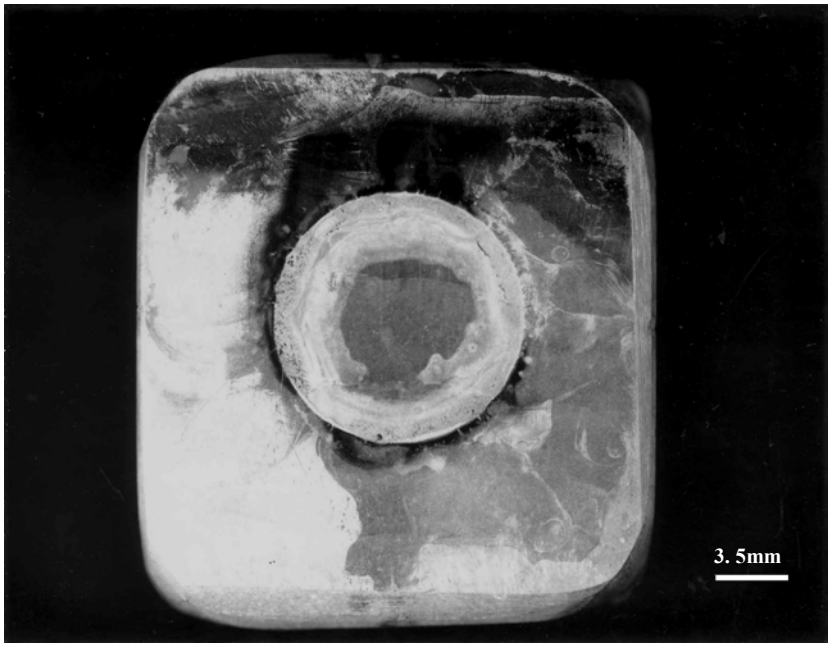


(b) 80°C

Figure 4.28 Surface morphology of C316H after crevice corrosion test at (a) 75 °C , 2.8X and (b) 80°C, 2.8X.

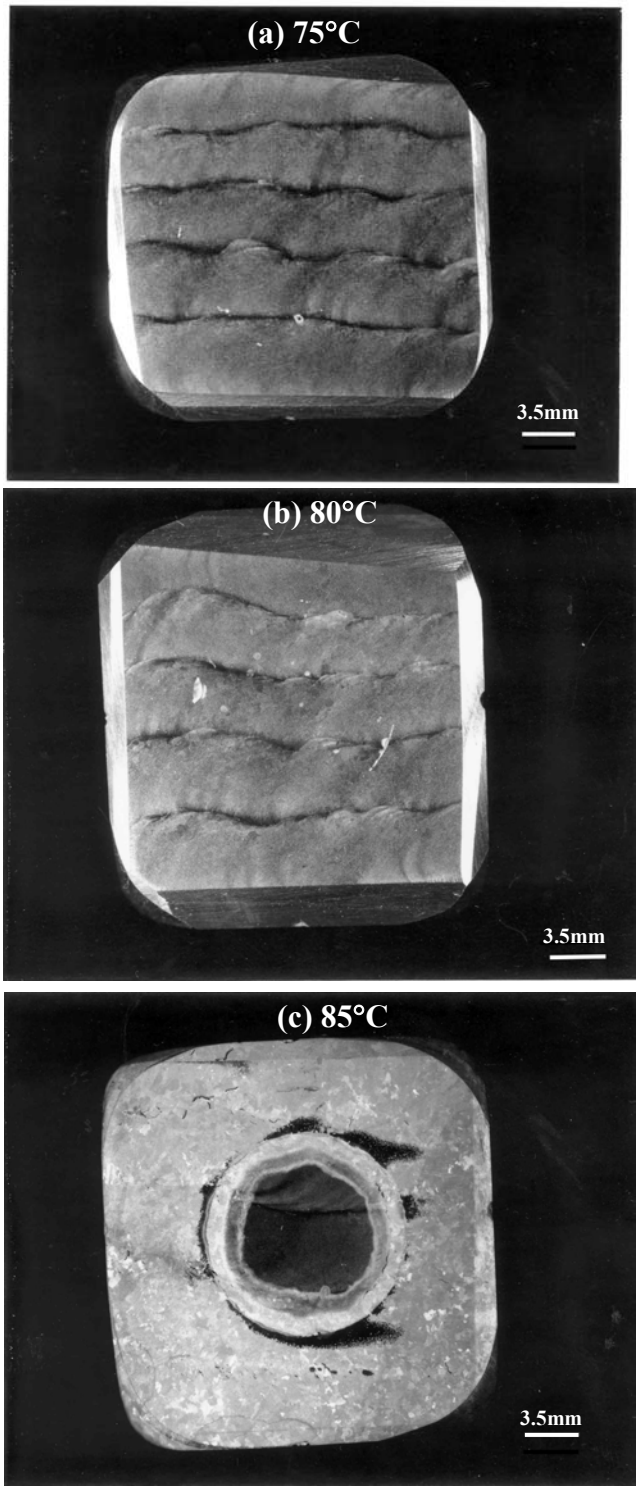


Figure 4.29 Surface morphology of M316H after crevice corrosion test at 75°C, 80°C and 85°C.


(a) M308L before & after tensile test

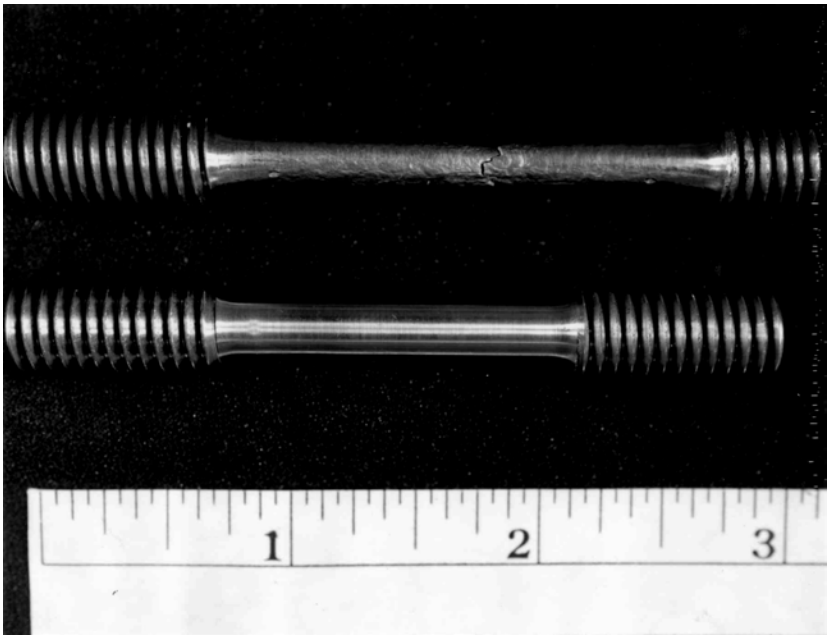


(b) C308L before & after tensile test

Figure 4.30 Modified and commercial 308L samples before and after tensile testing.

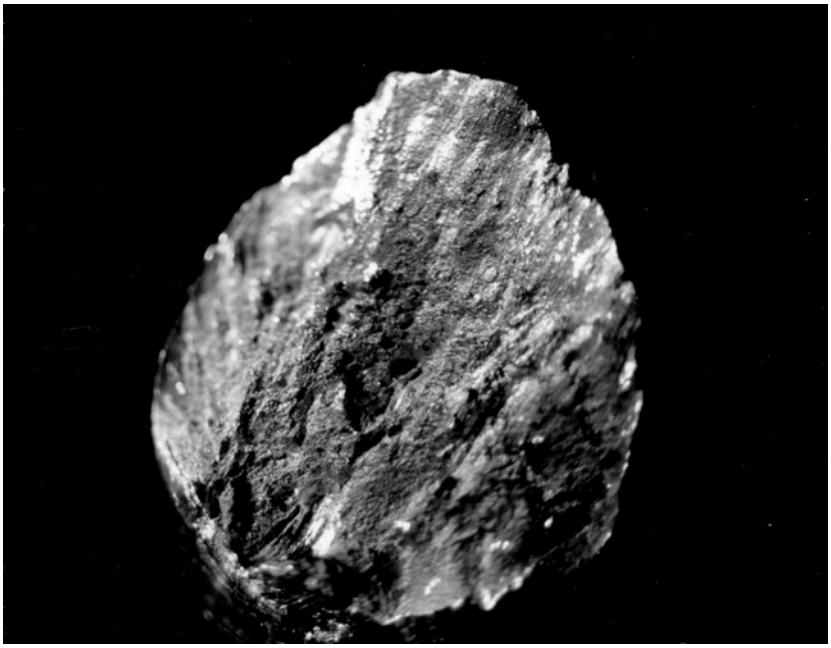

(a) M308L

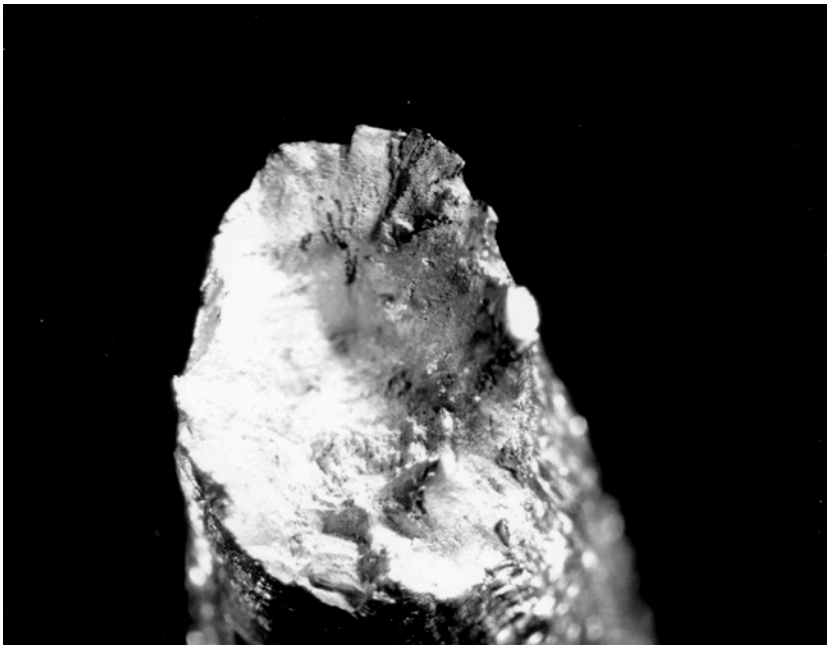

(b) M316L

Figure 4.31 Morphologies of fracture surfaces of modified E308L and E316L samples after tensile test, (a)-3X and (b)-3X.

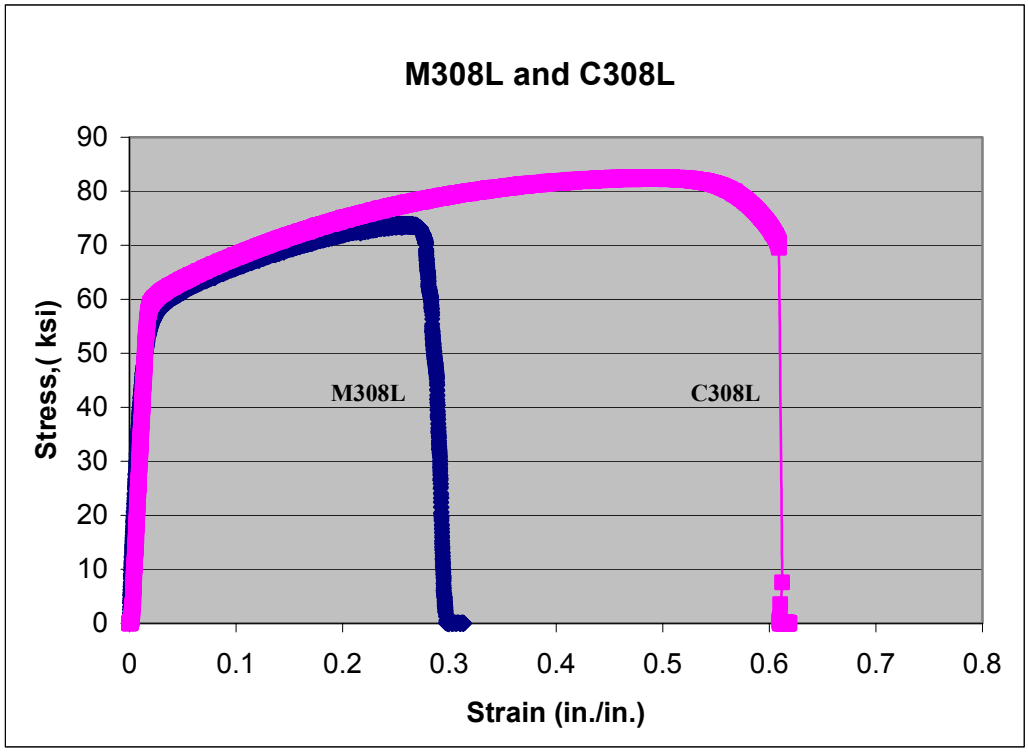


Figure 4.32 Stress-strain curves for modified and commercial E308L weld deposits.

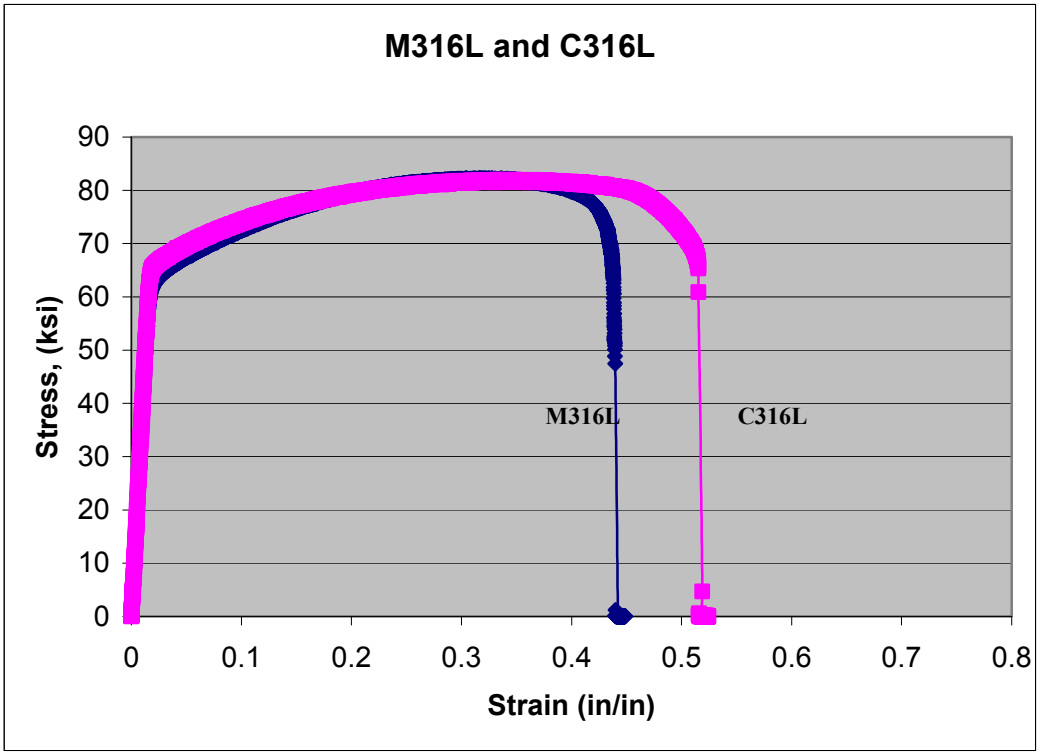


Figure 4.33 Stress-strain curves for modified and commercial E316L weld deposits.

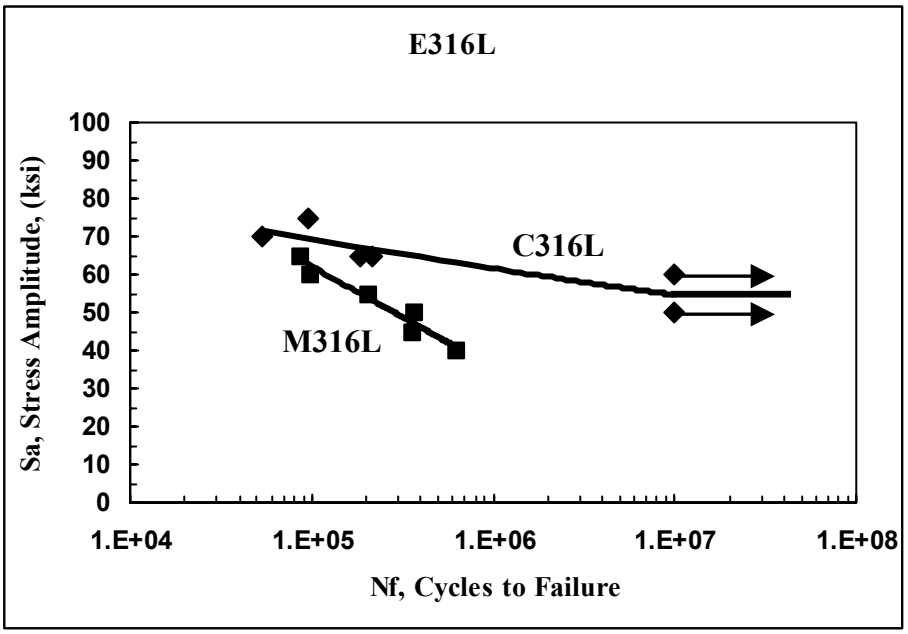


Figure 4.34 S-N curve for E316L weld specimens.

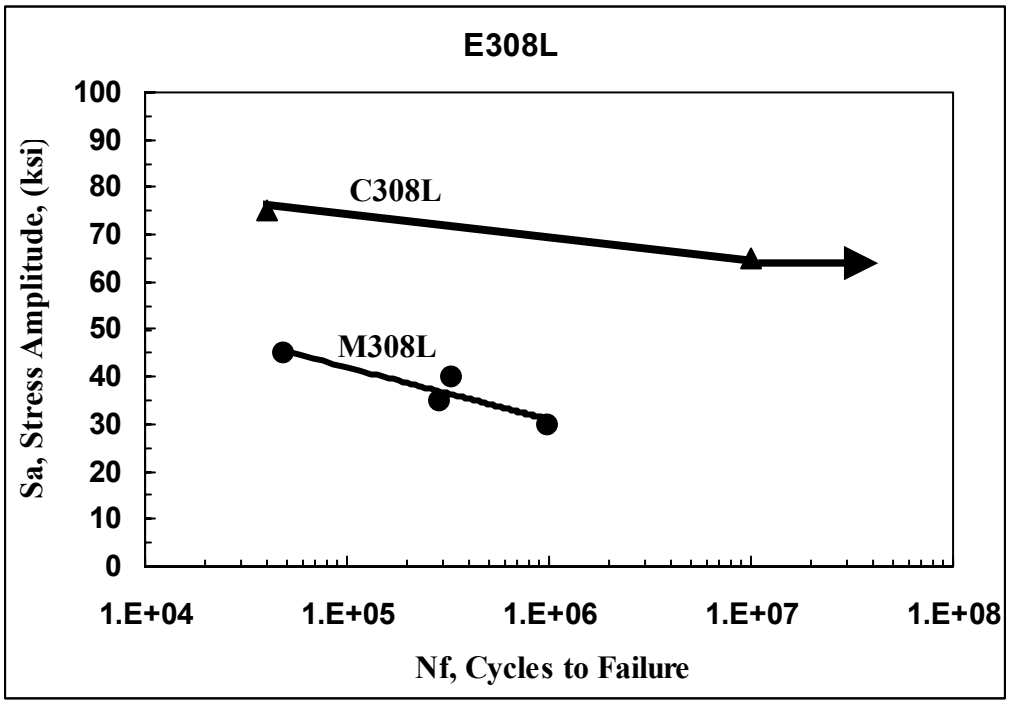


Figure 4.35 S-N curve for E308L weld specimens.

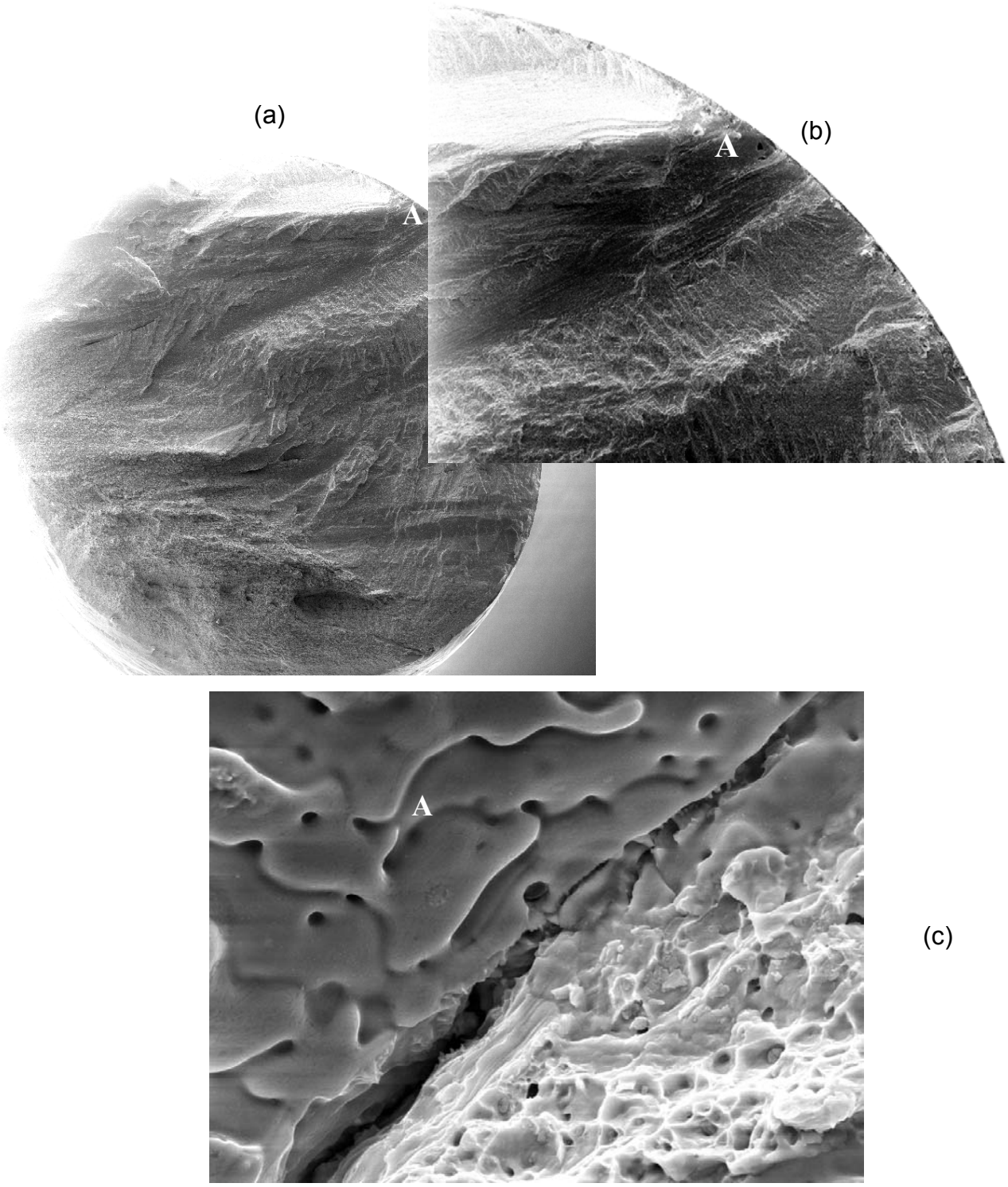


Figure 4.36 (a) and (b) Fractograph of modified 316L fracture surface after fatigue testing, (a) 18-X and (b)-100X. (c) Initial fracture surface at location A in Figures (a) and (b), 3000X.

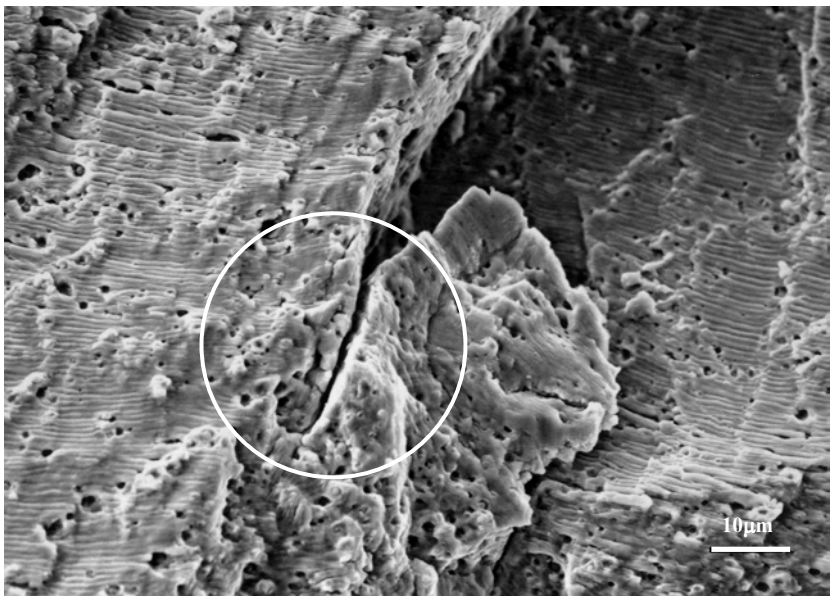


(d)

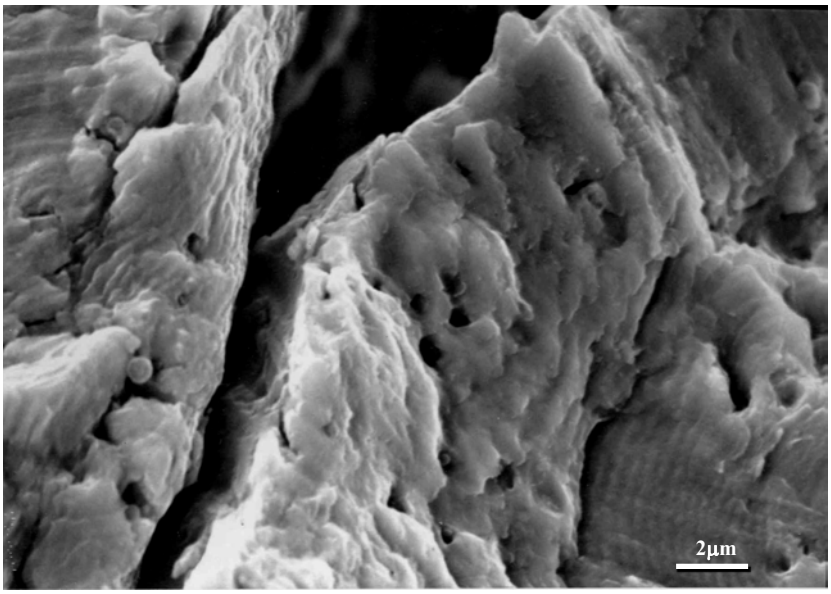


(e)

Figure 4.36 (d) and (e) SEM fractographic of modified E316L in Location B in Figure 4.37 (a) showing fine striations on fracture surface, (d)-1000X, (e)-5000X.

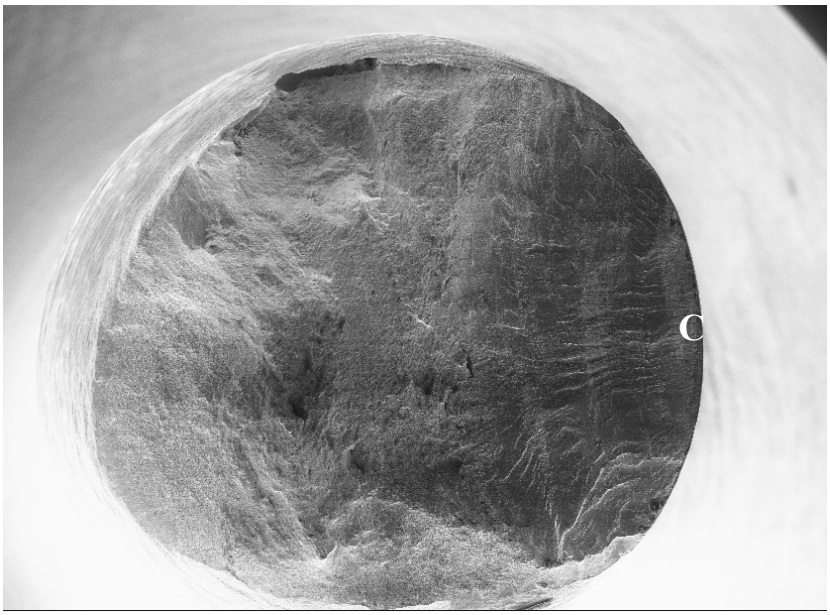


(a)

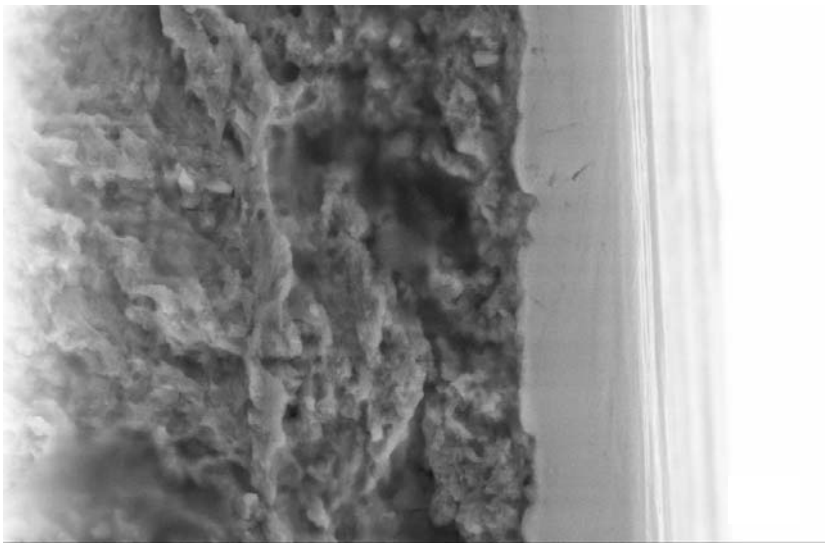

(b)

Figure 4.37 (a) Fractograph of commercial 316L fatigue sample, 18X,
(b) Initial fracture surface at location C in Figure (a), 3000X.

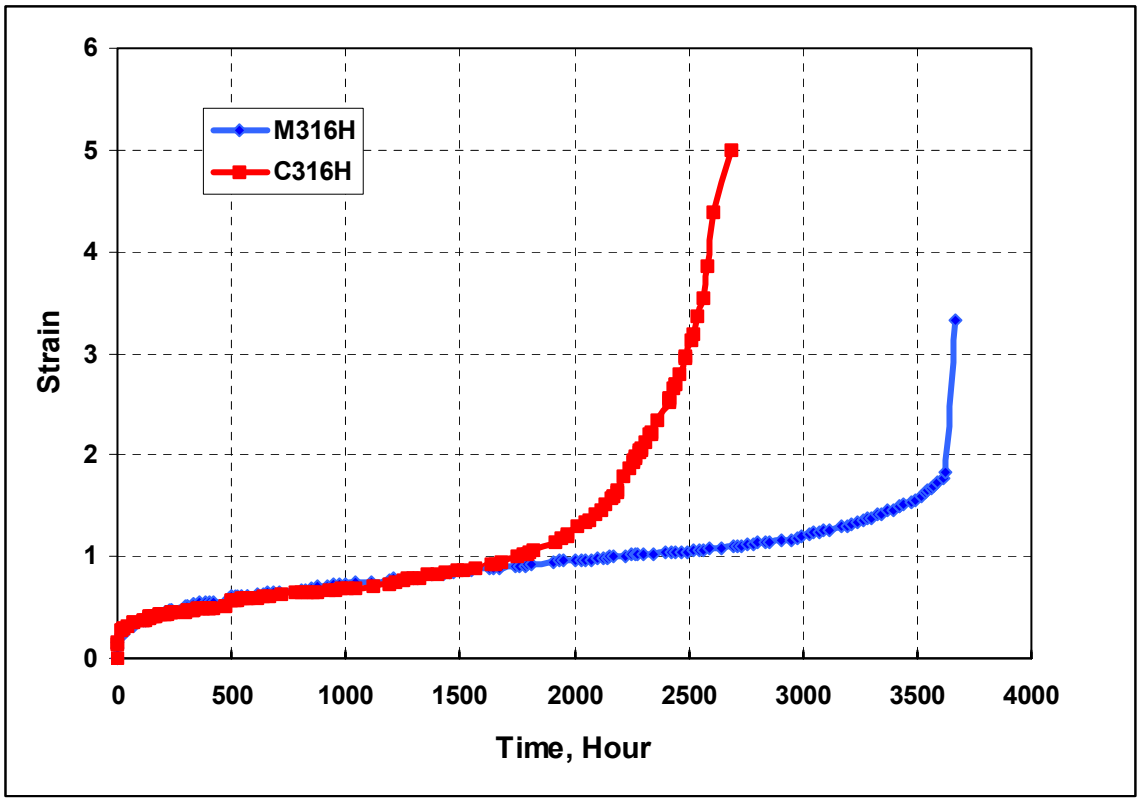


Figure 4.38 Typical creep curves (strain vs. time to rupture) for fissure containing and fissure-free 316H samples under the same testing condition, 117 MPa and 660°C.

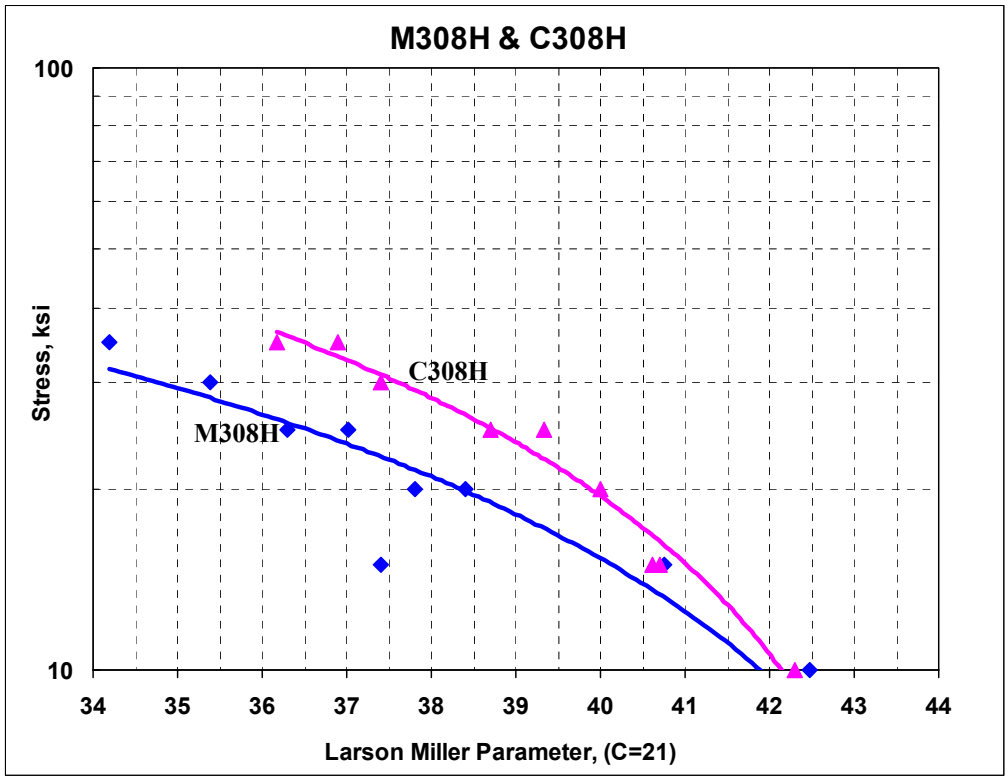


Figure 4.39 Creep rupture behavior for E308H welds.

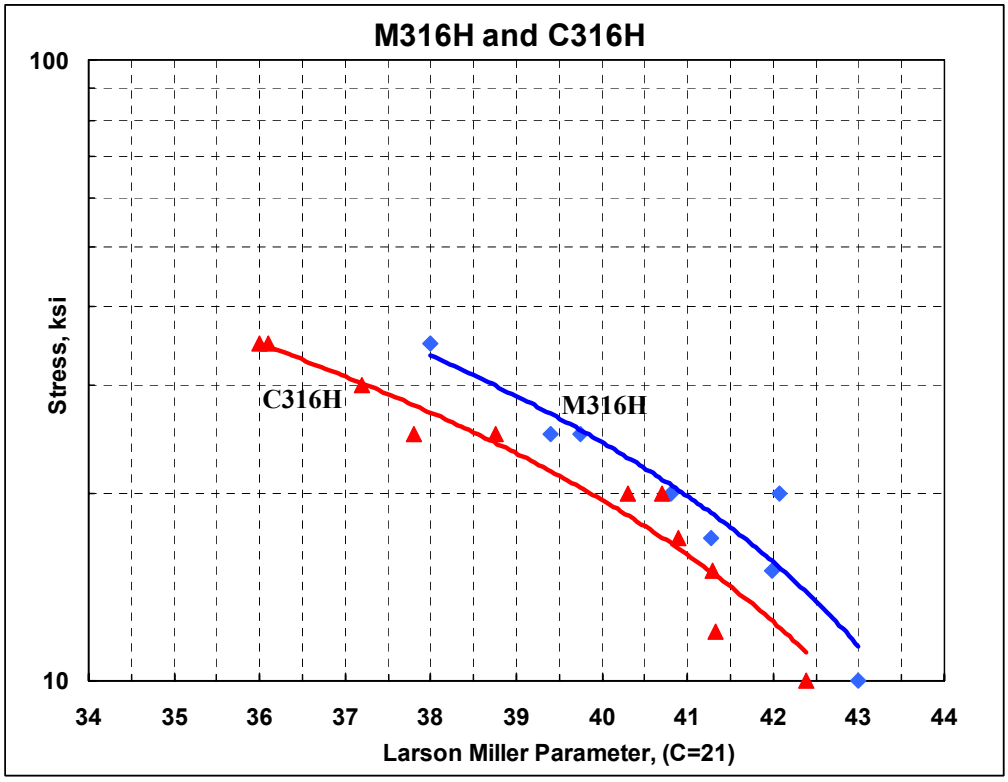


Figure 4.40 Creep rupture behavior for M316H and C316H welds.

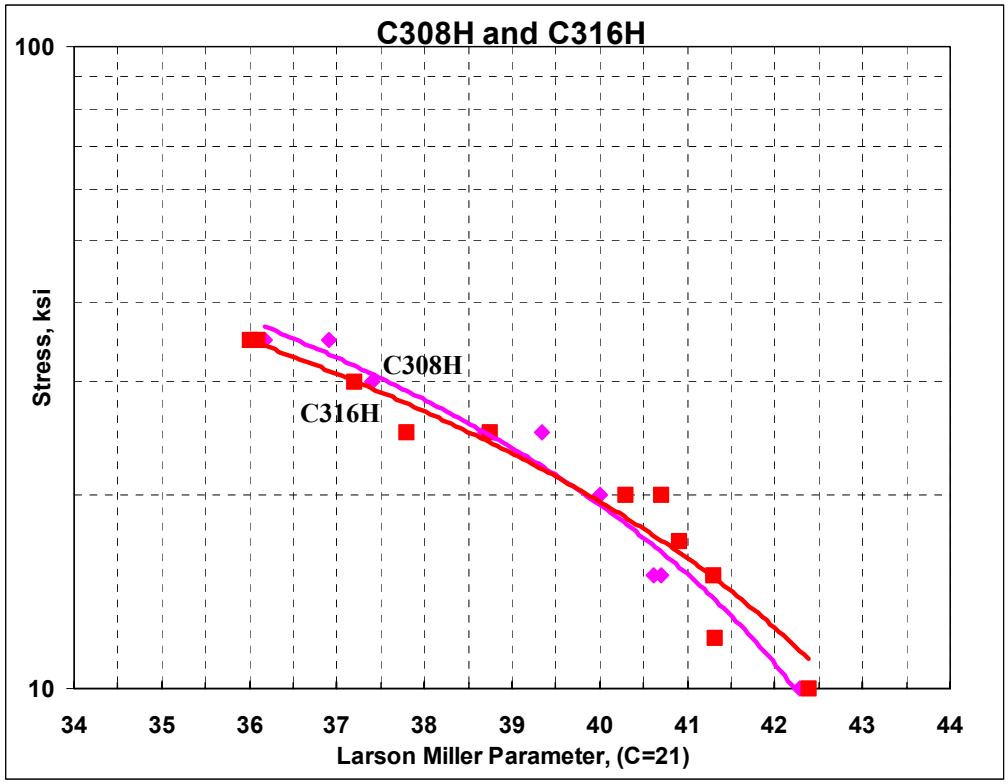


Figure 4.41 Creep rupture behavior for C308H and C316H welds.

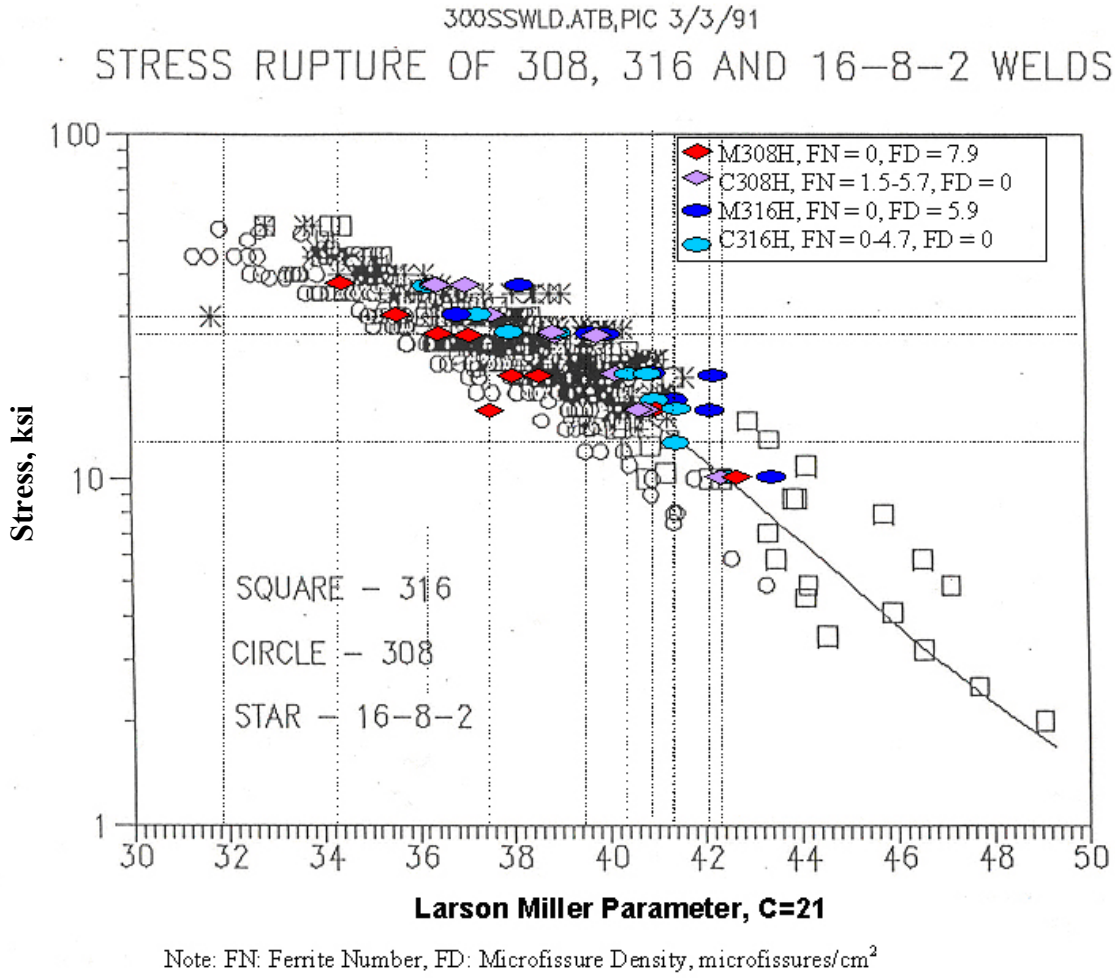


Figure 4.42 Stress rupture of 308 and 316 welds.

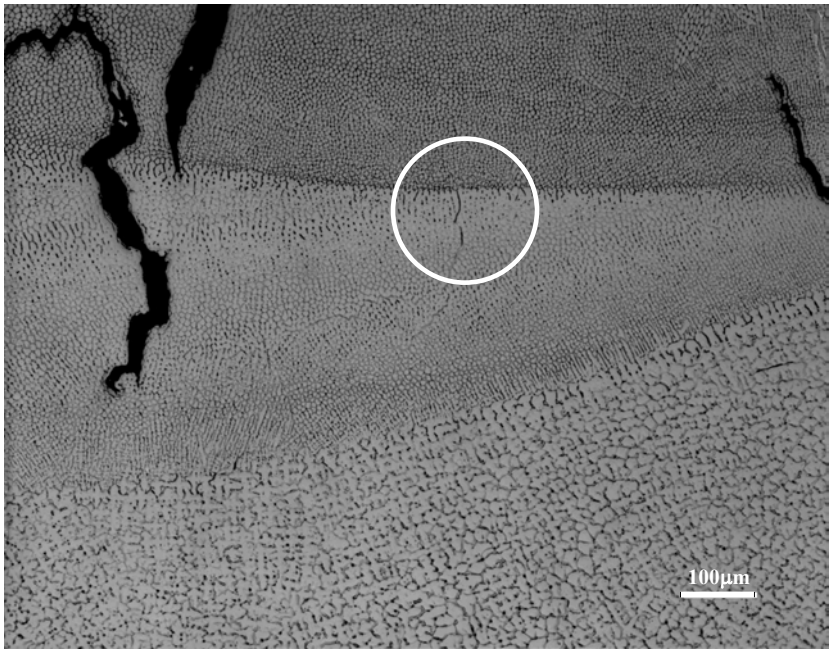


(a)

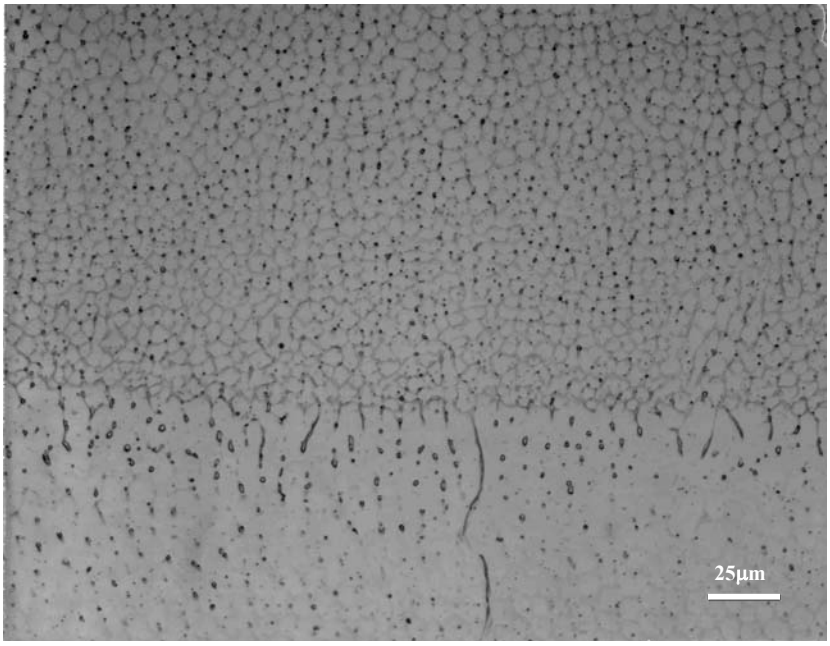


(b)

Figure 4.43 Microstructure of modified 308H before creep testing, (a)-100X, (b)-400X.

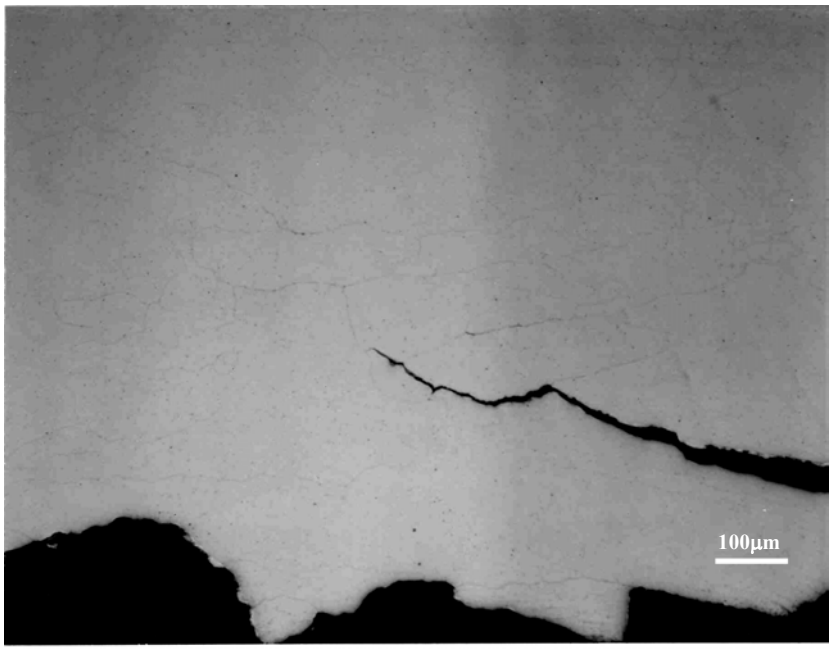


(a)

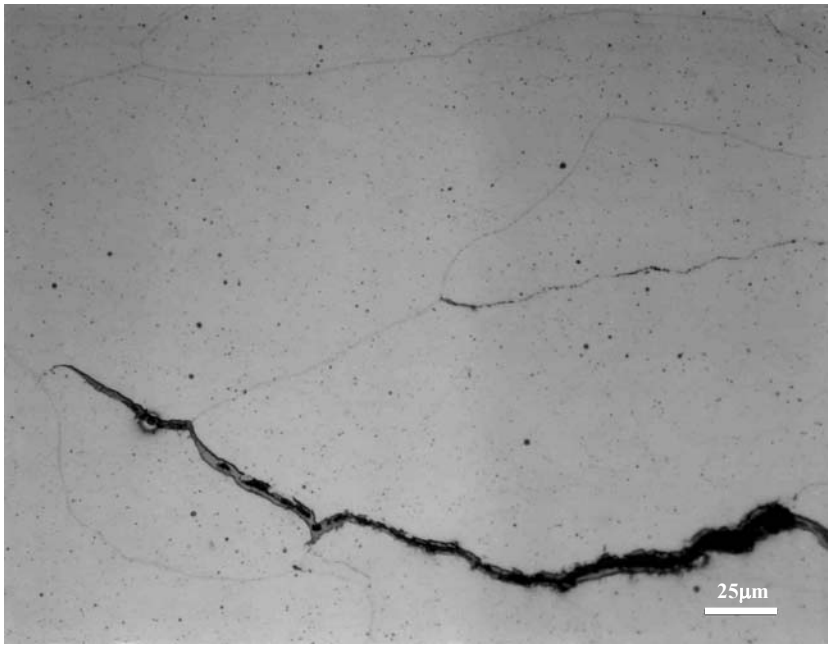


(b)

Figure 4.44 Microstructure of modified 308H after creep testing, (138 MPa, 620°C, 746 hours), (a)-100X, (b)-400X.

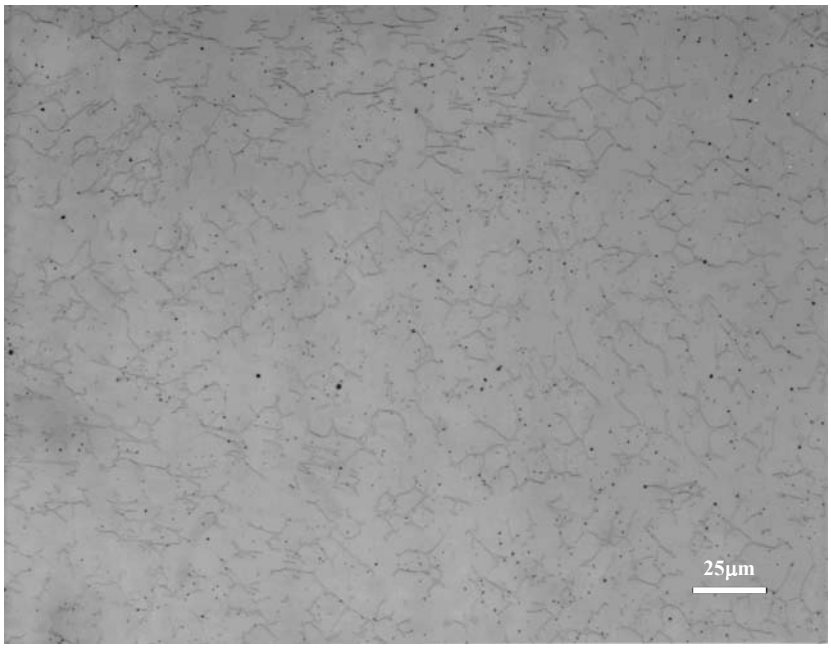


(a)

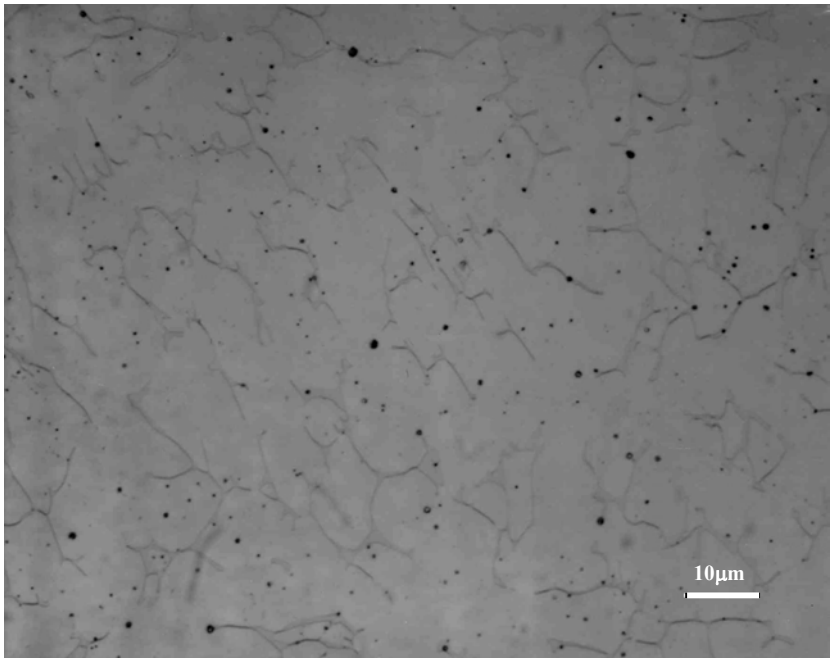


(b)

Figure 4.45 Microstructure of commercial 308H before creep testing, (a)-400X, (b)-1000X.

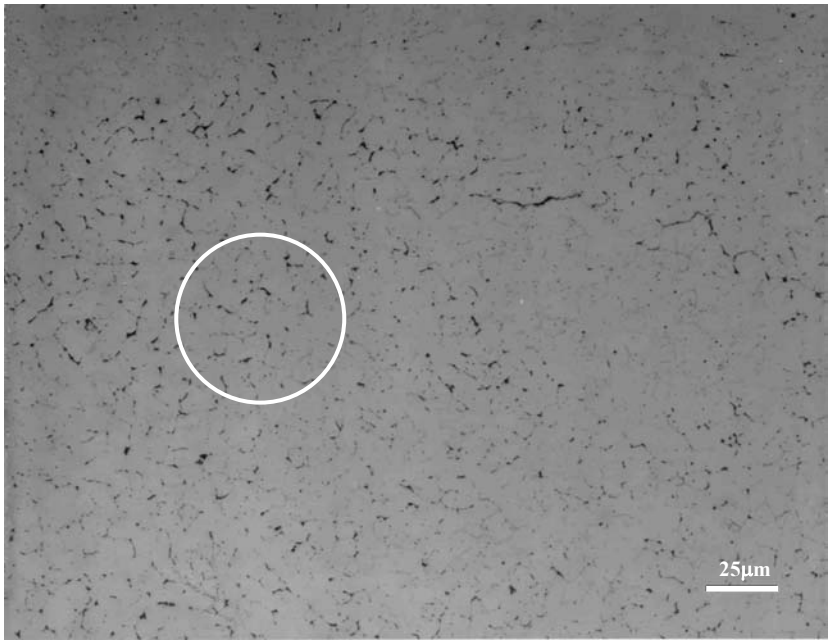


(a)

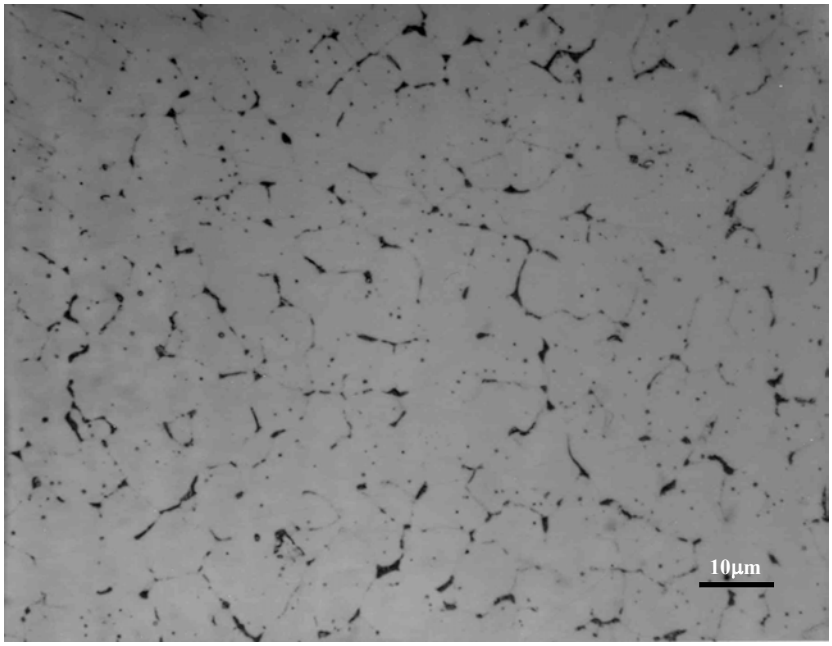


(b)

Figure 4.46 Microstructure of commercial 308H after creep testing (138 MPa, 645°C, 754 hours), (a)-400X, (b)-1000X.

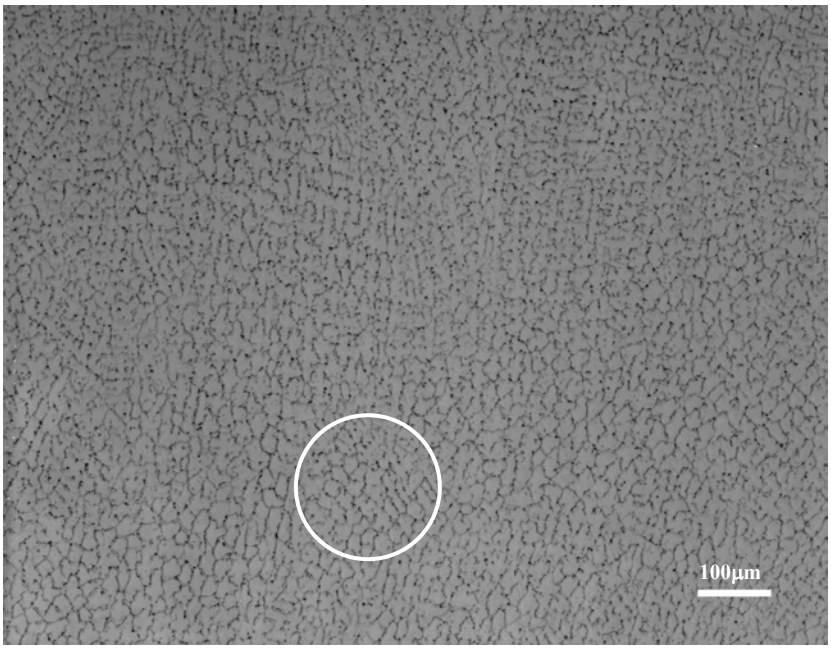


(a)

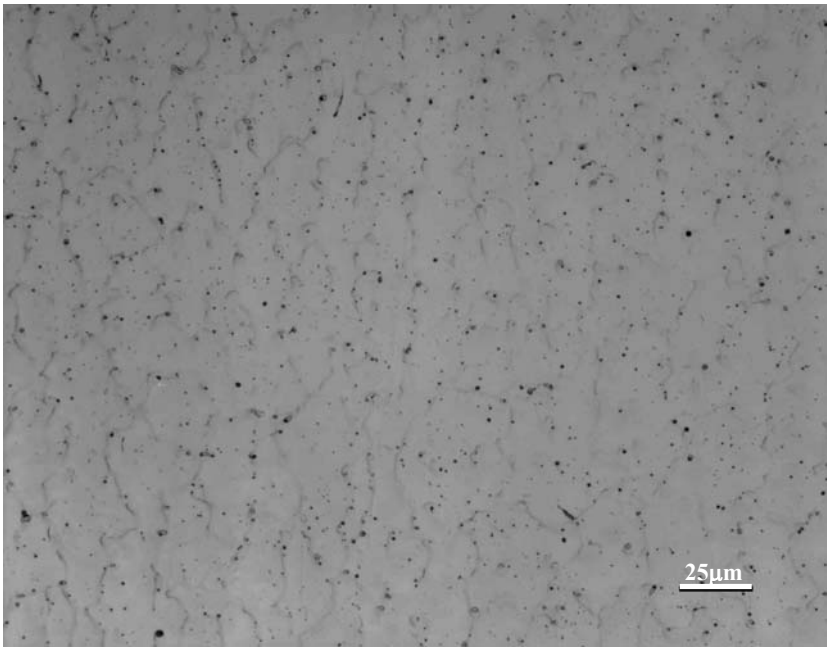


(b)

Figure 4.47 Microstructure of modified 316H before creep testing, (a)-100X, (b)-400X.

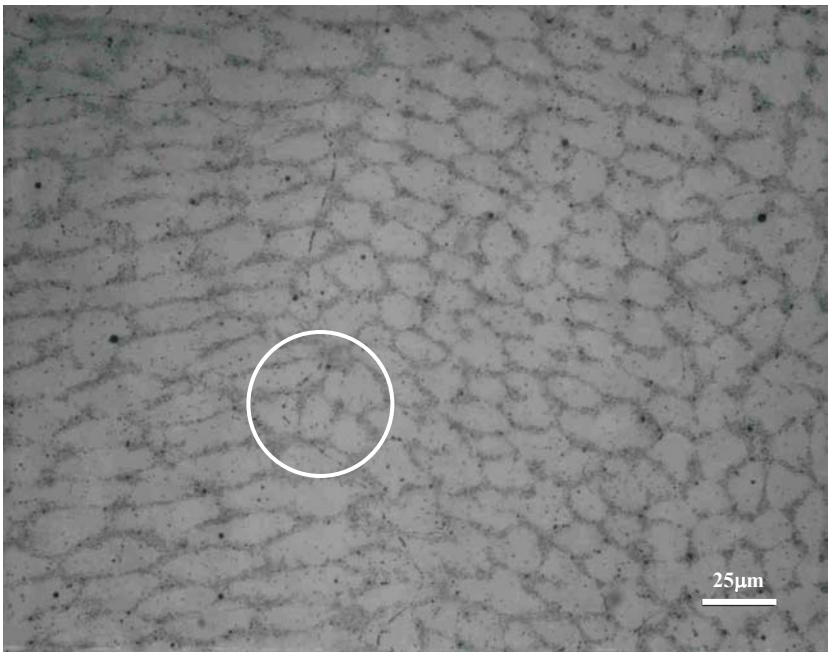


(a)

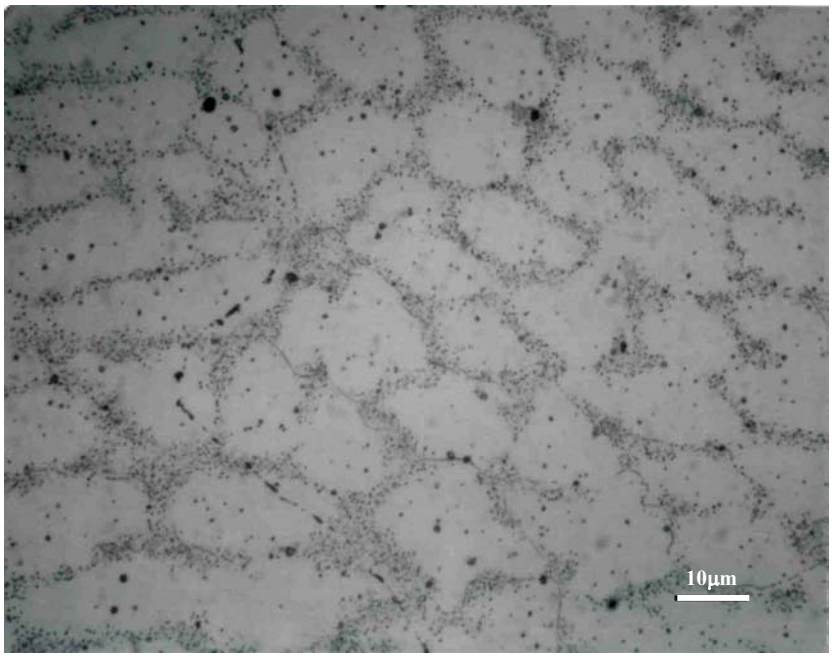


(b)

Figure 4.48 Microstructure of modified 316H after creep testing (117 MPa, 660°C, 3671 hours), (a)-400X, (b)-1000X.

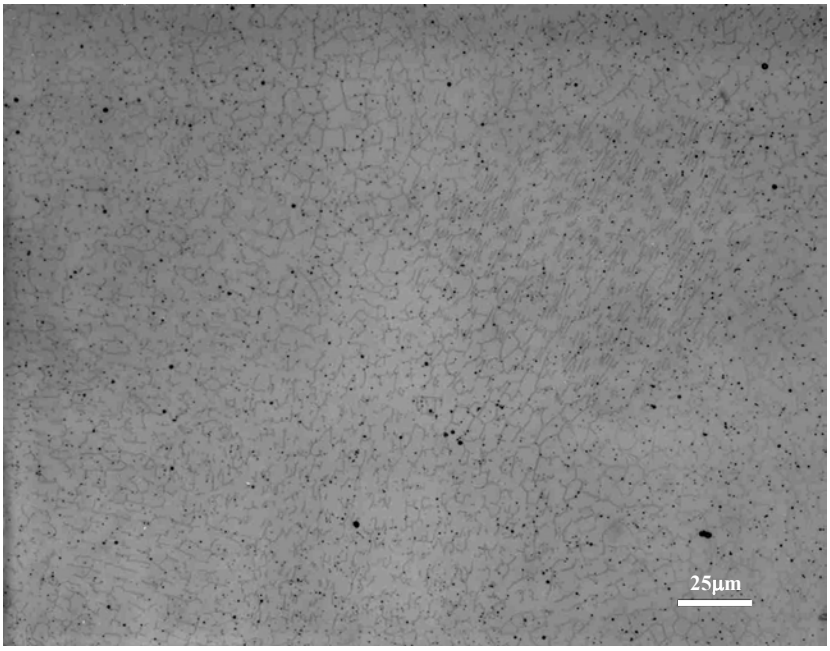


(a)

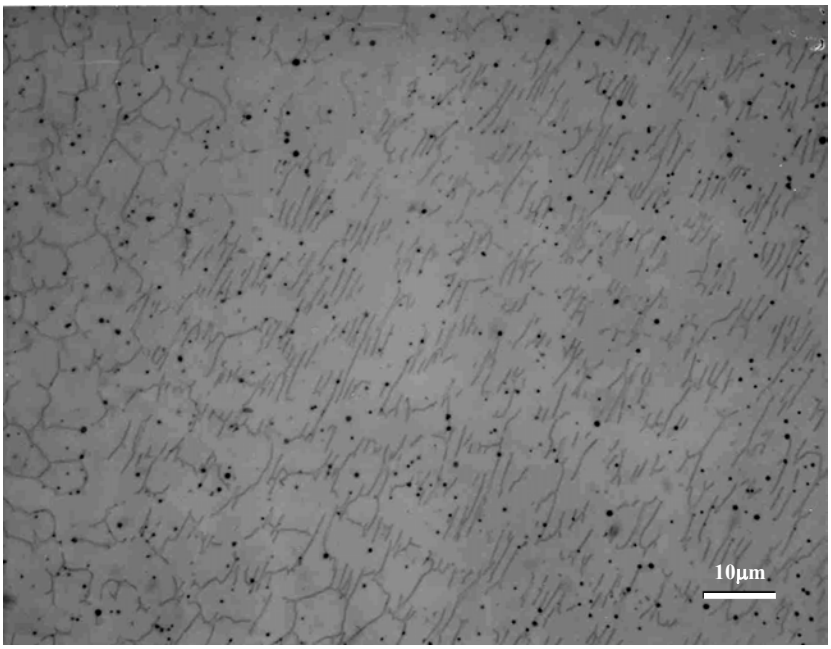


(b)

Figure 4.49 Microstructure of commercial 316H before creep testing, (a)-400X, (b)-1000X.

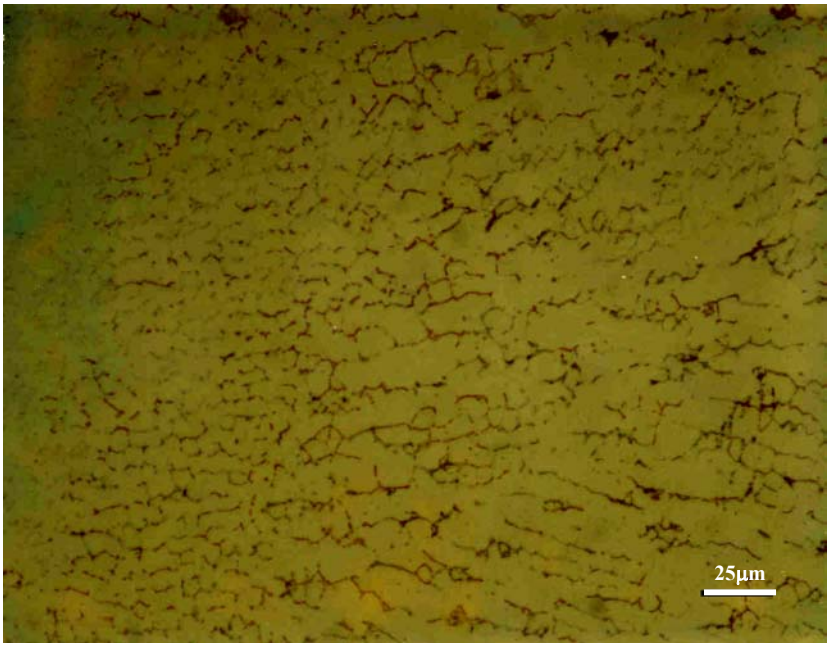


(a)

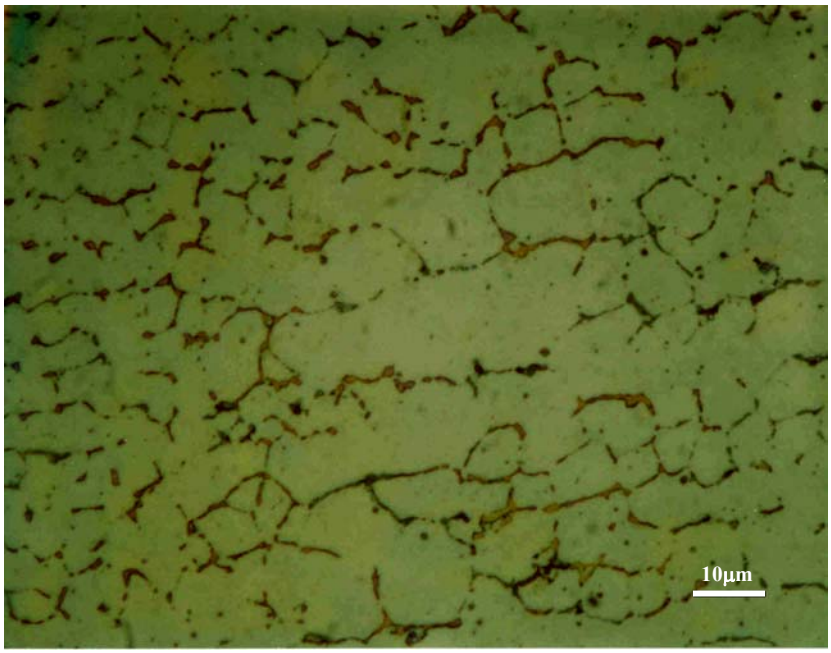


(b)

Figure 4.50 Microstructure of commercial 316H after creep testing (117 MPa, 660°C, 2685 hours), (a)-400X, (b)-1000X.

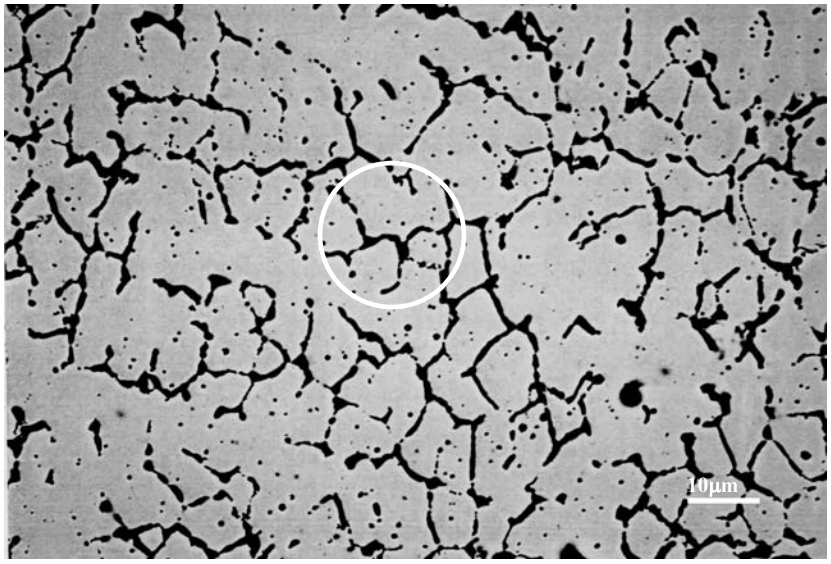


(a)

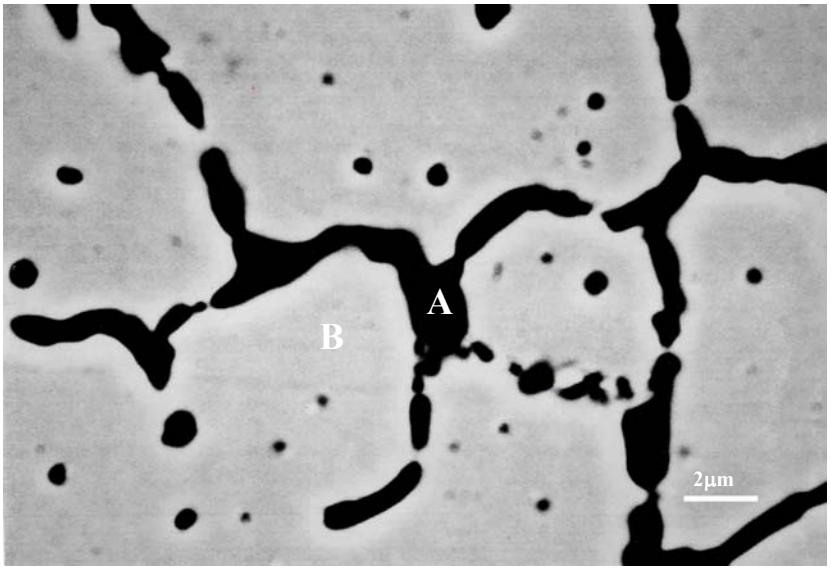


(b)

Figure 4.51 SEM microstructural morphology of commercial E316H samples after creep testing (117 MPa, 660°C, 2685 hours), as a back scattered image, (a)-1000X, (b)-5000X.

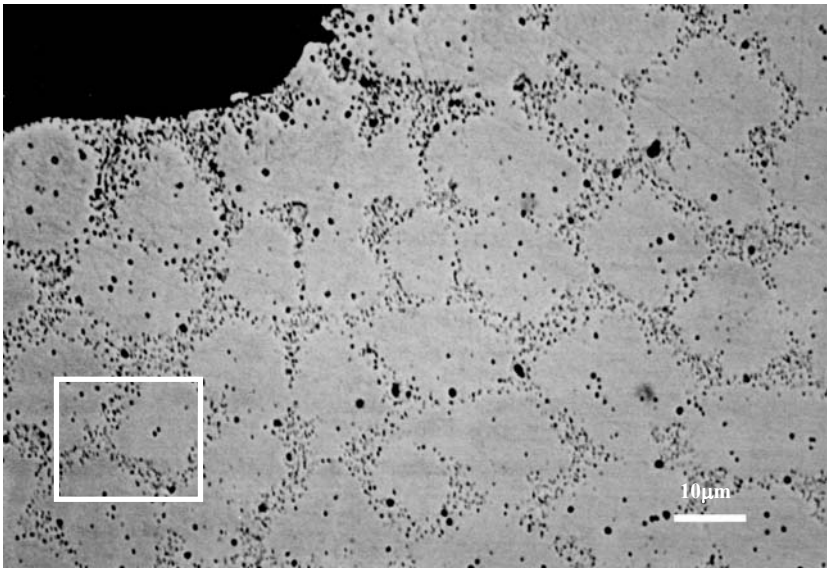


(a)

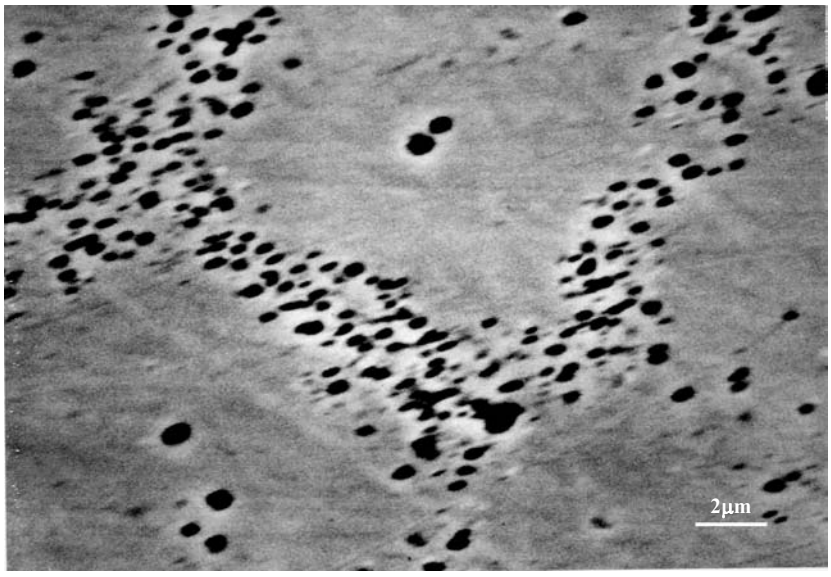


(b)

Figure 4.52 SEM microstructural morphology of modified E316H samples after creep testing (117 MPa, 660°C, 3671 hours), as a back scattered image, (a)-1000X, (b)-5000X.

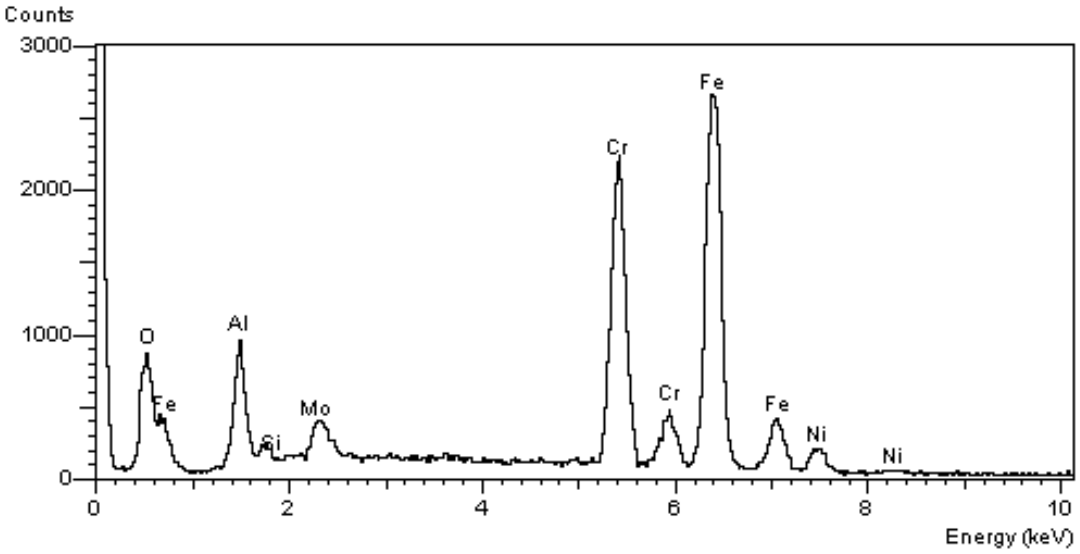


(a)

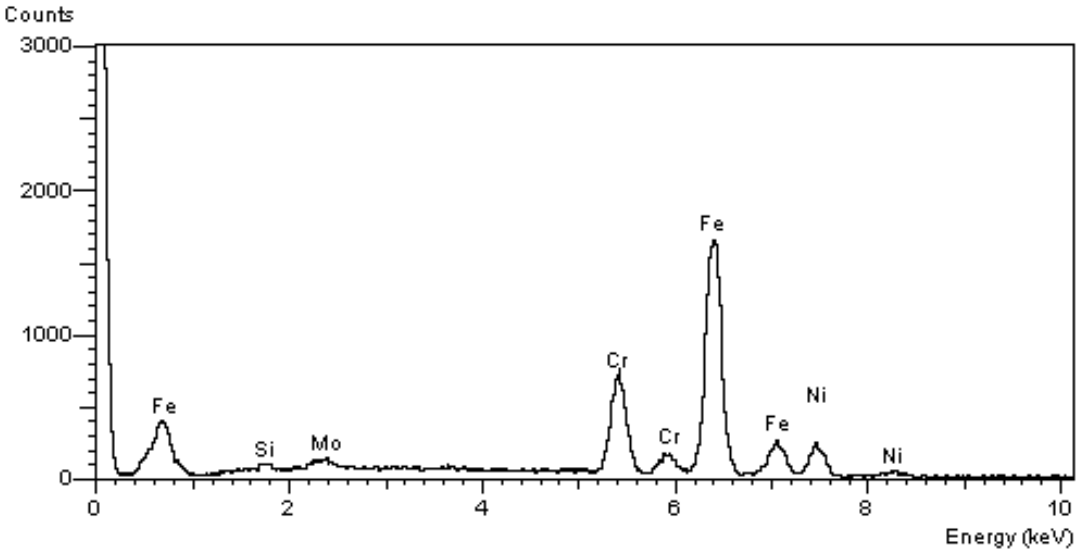


(b)

Figure 4.53 EDS spectra for locations A (a) and B (b) in Figure 4.51.

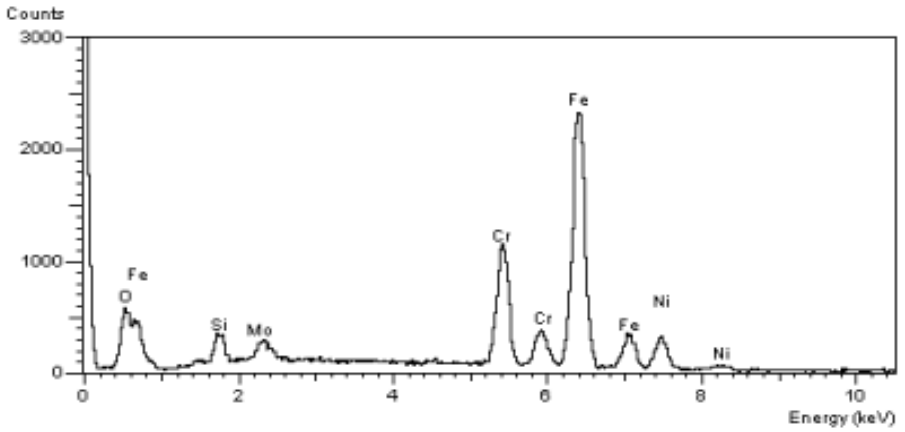


(a) Carbides

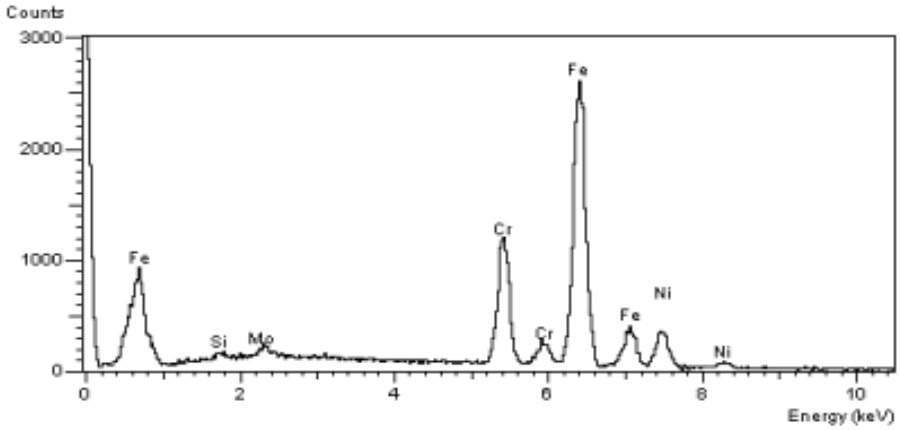


(b) Matrix

Figure 4.54 EDS spectra from carbides in Figure 4.52 (a) and matrix (b) showing the difference in Mo content.

Figure 4.55 X-ray diffraction lab.

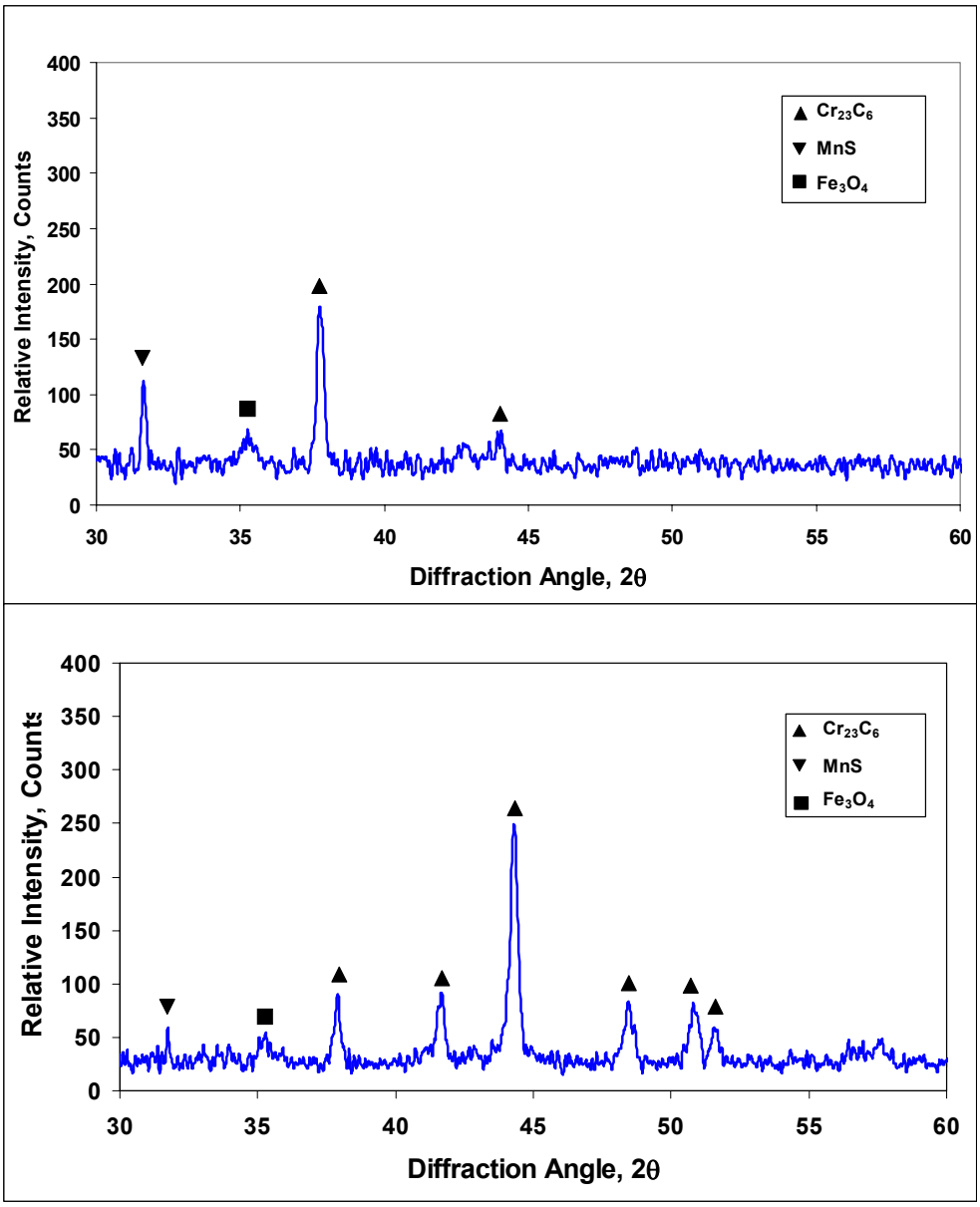


Figure 4.56 X-ray diffraction patterns obtained from modified M308H weld deposit (a) before and (b) after creep testing.

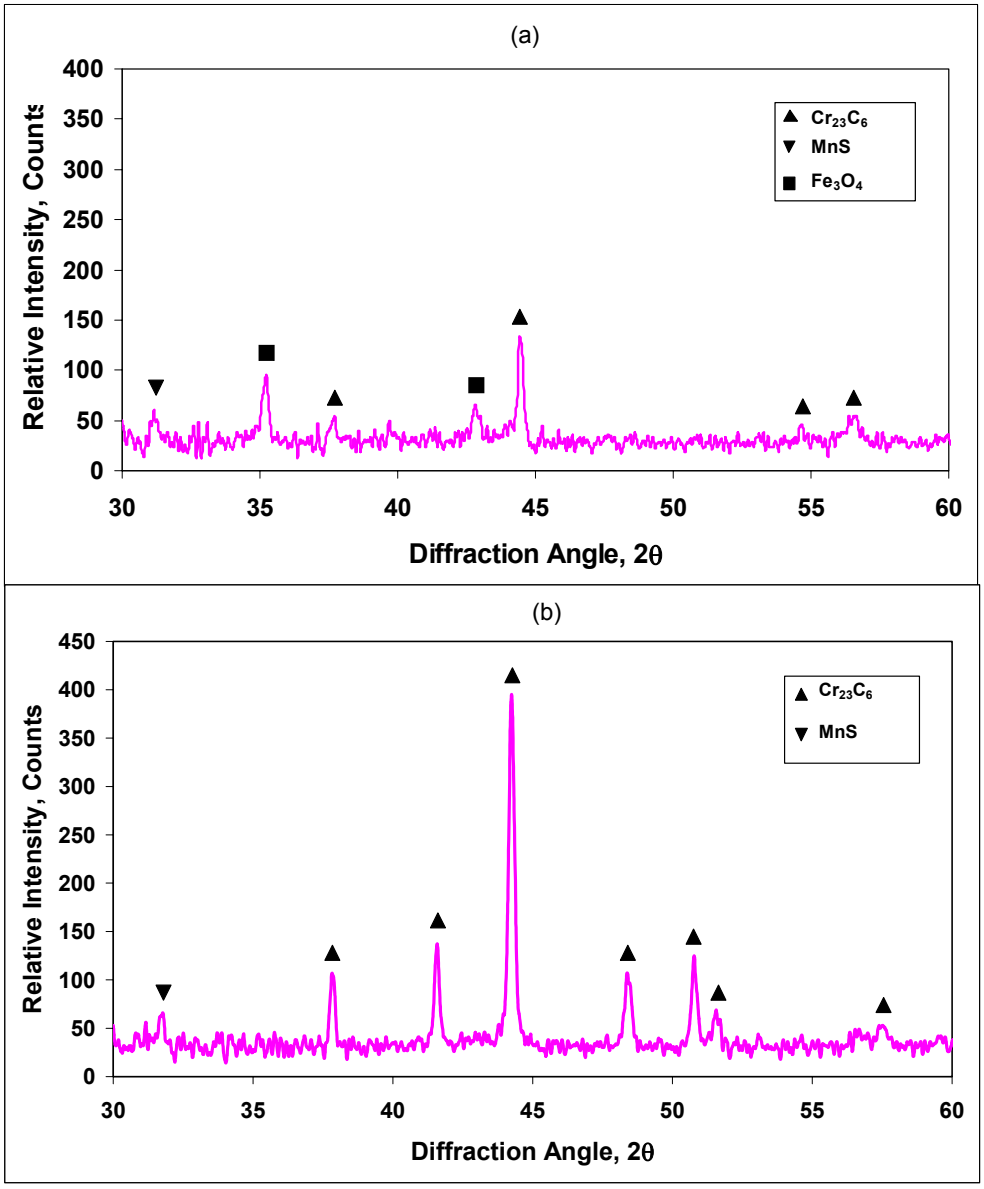


Figure 4.57 X-ray diffraction patterns obtained from commercial C308H weld deposit (a) before and (b) after creep testing.

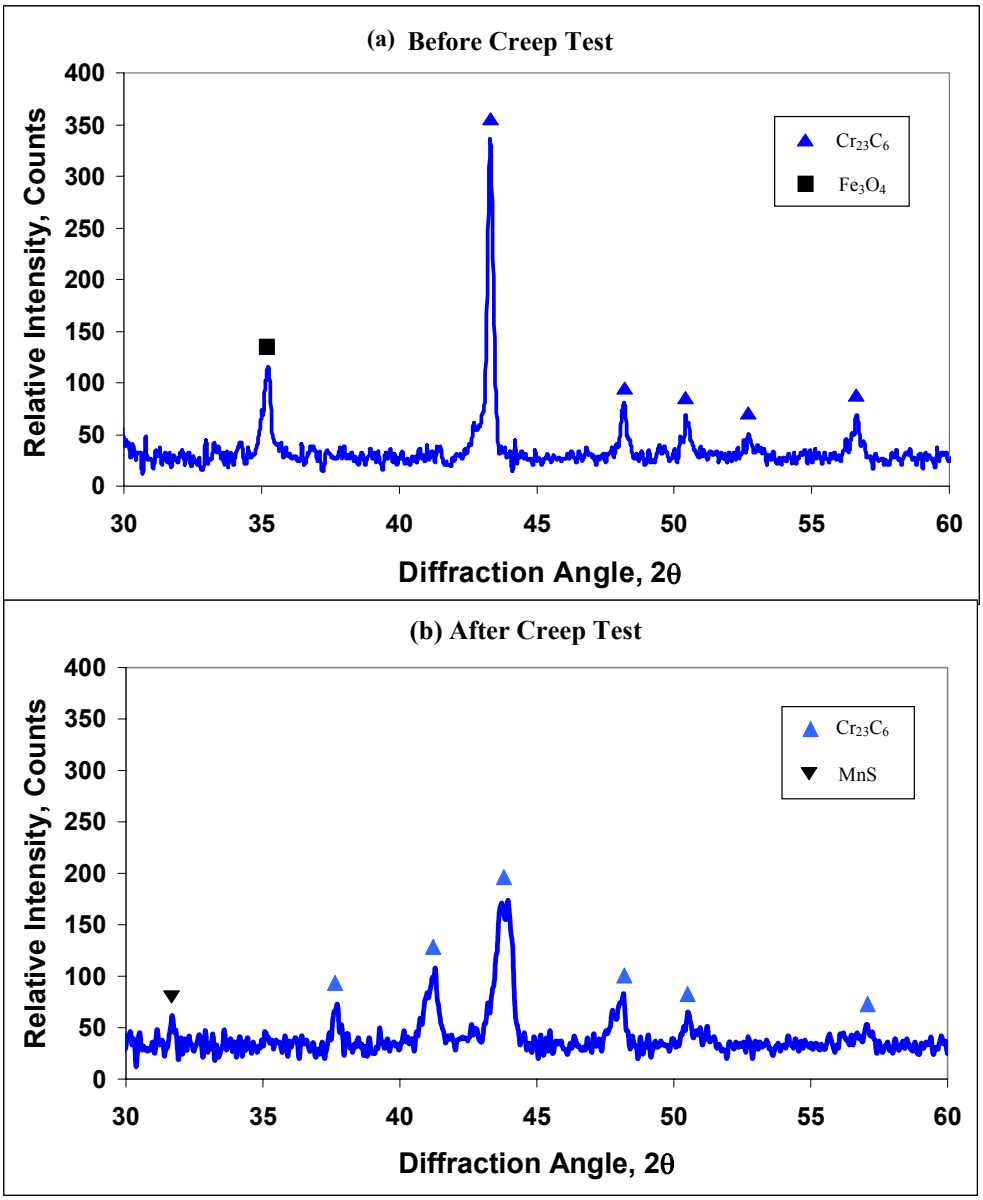


Figure 4.58 X-ray diffraction patterns obtained from modified M316H weld deposit (a) before and (b) after creep testing.

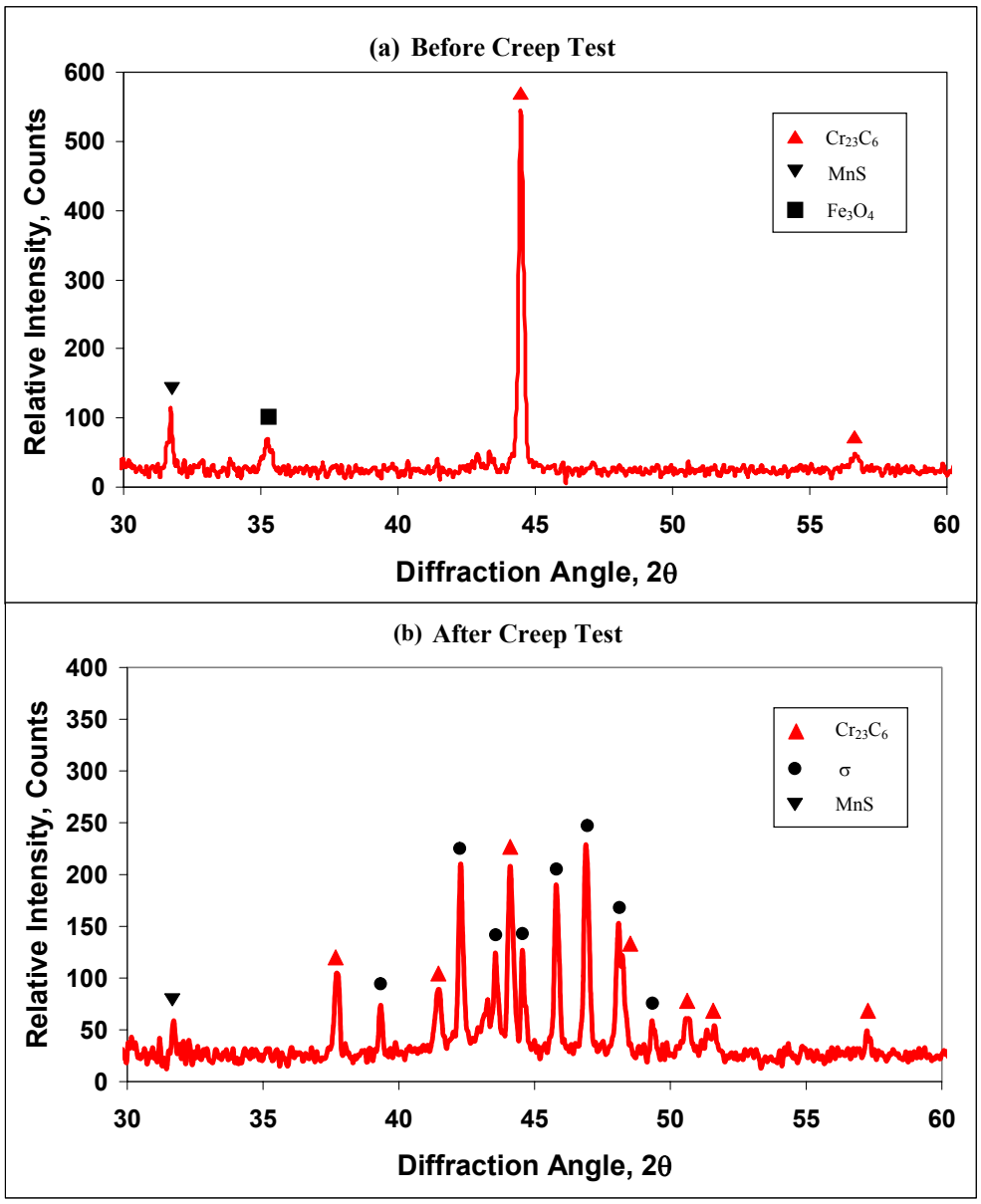


Figure 4.59 X-ray diffraction patterns obtained from commercial C316H weld deposit (a) before and (b) after creep testing.

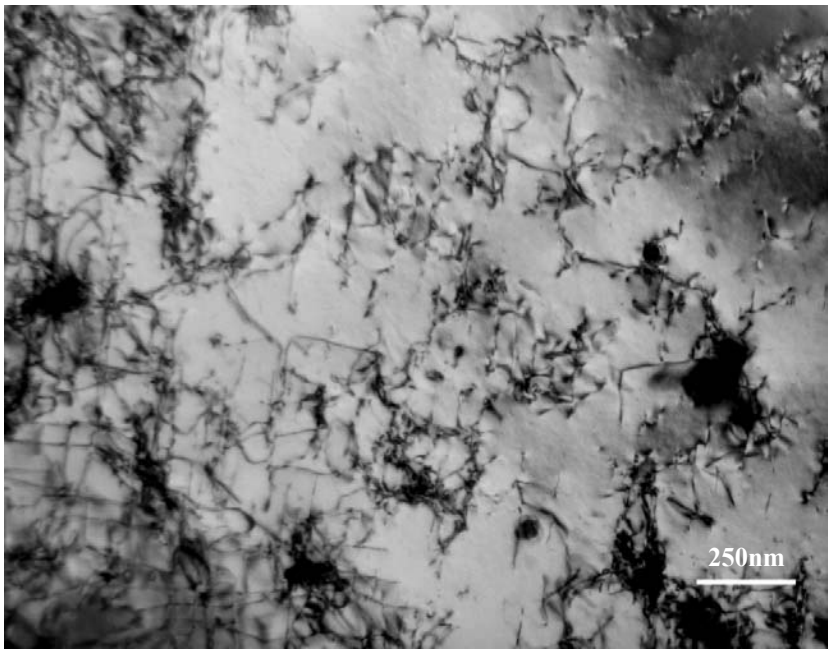


(a)

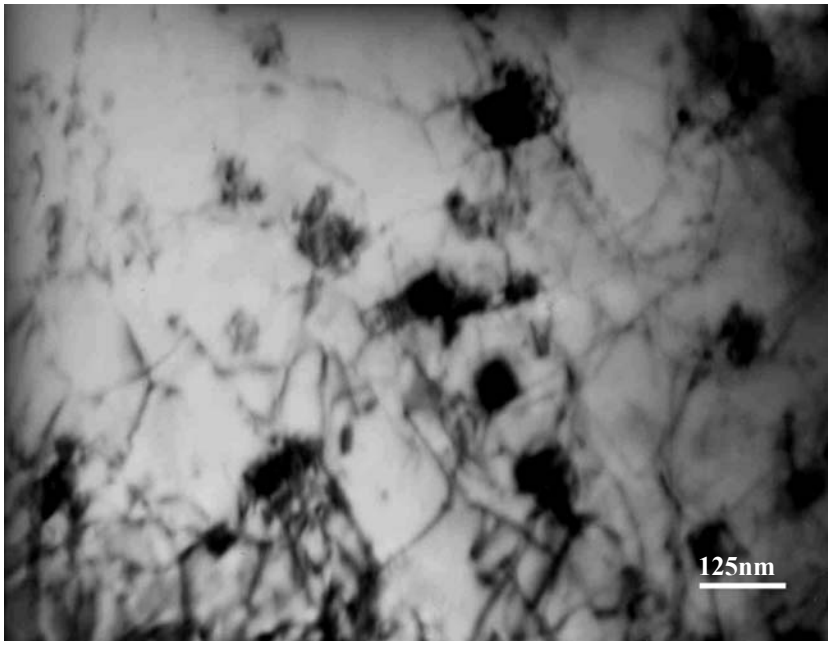


(b)

Figure 4.60 Typical TEM microstructural morphology of modified E316H after creep testing under 70 MPA, 700°C, and 4560 hours.

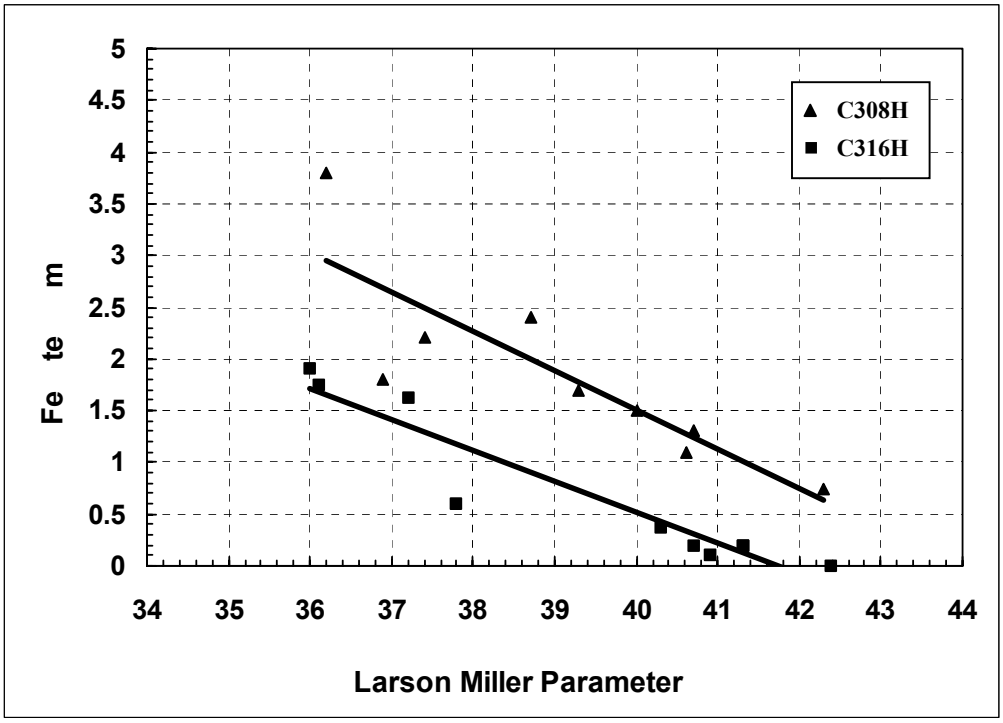


Figure 4.61 Ferrite Number of commercial E308H and E316H weld deposits after creep testing as a function of Larson Miller Parameter.

# VITA

Yan Cui was born in Shenyang, Liaoning Province, People's Republic of China. He received Bachelor degree from Shenyang Polytechnical University in 1986 and Master degree from Institute of Metal Research, Chinese Academy of Sciences in 1994. He enrolled to the University of Tennessee in 1999 and received the Doctoral of Philosophy degree in August 2004.